uc3m | Universidad Carlos III de Madrid
Escuela Politécnica Superior

Polymer Exchange Membrane Fuel Cells modeling: from kinetic models to water management

Tesis Doctoral

Autor
Juan Sánchez Monreal

Director
Marcos Vera Coello

DEPARTAMENTO DE INGENIERÍA TÉRMICA Y DE FLUIDOS

Leganés, septiembre 2017

TESIS DOCTORAL

POLYMER EXCHANGE MEMBRANE FUEL CELLS MODELING: FROM KINETIC MODELS TO WATER MANAGEMENT

Autor: Juan Sánchez Monreal

Director de Tesis: Marcos Vera Coello

Firma del Tribunal Calificador:

Firma

Presidente: Dr. Antonio L. Sánchez Pérez

Vocal: Dr. Alexandra Maria Pinheiro da Silva Ferreira Rodrigues Pinto

Secretario: Dr. Alfredo Iranzo Paricio

Suplente: Dr. Pedro L. Garcia Ybarra

Calificación:

Leganés, 6 de septiembre de 2017

DEPARTAMENTO DE INGENIERÍA TÉRMICA Y DE FLUIDOS
Escuela Politécnica Superior

Polymer Exchange Membrane Fuel Cells modeling: from kinetic models to water management

Autor
Juan Sánchez Monreal

Director de Tesis
Marcos Vera Coello

Leganés, septiembre 2017

To those who support

"You just have to know what the right laws are under the right circumstances,
and design the device with the correct laws.
You cannot expect old designs to work in new circumstances.
But new designs can work in new circumstances "

– Richard P. Feynman
The Computing Machines in the Future,
Nishina Memorial Lecture at Gakushuin University (Tokyo),
August 9, 1985 .

Abstract

Polymer electrolyte fuel cells, based on proton exchange membranes, also known as PEM fuel cells (acronym for polymer electrolyte membrane or proton-exchange membrane), constitute a real alternative for the generation of sustainable energy. Their versatility allows them to be used in mobile systems (from small portable electronic devices to vehicles) or in fixed stations (auxiliary power generators for buildings or small remote unattended stations). The biggest attraction of this type of fuel cells is that they can operate at low temperatures (0-100 C), which requires the use of catalysts based nobel metals such as platinum, which allows then even to start from freezing temperatures.

The operation of a PEM fuel cell is based on the electrooxidation of the fuel at the anode and the electroreduction of the oxygen at the cathode. The anodic and cathodic reactions take place independently, with both electrodes separated by a polymer membrane that allows only the transfer of protons. This forces the electrons to travel through an external circuit generating an electric current. The proton conductivity of the membrane depends strongly on the water content of the membrane. For a correct operation of the cell, the electrochemical reactions and the water management appear therefore as fundamental aspects in its modeling and operation.

Depending on the fuel used, there are two types of PEM fuel cells: those fueled with hydrogen and those fed with alcohols. Hydrogen fuel cells stand out because of their high power density, which makes them ideal for the automotive industry. When operating at full load, the performances of this type of batteries are dominated by the water management in the membrane. By contrast, direct alcohol fuel cells (DAFCs) generate currents that are significantly lower, making them a possible alternative to hydrogen fuel cells as power sources for small portable devices. However, DAFC batteries still have two major drawbacks: the slow kinetics of the electrooxidation of alcohol molecules and the crossover of water and alcohol from anode to cathode through the membrane. Both phenomena severely limit the performances of this type of fuel cells.

The aim of this thesis is to study the influence of both electrochemistry and water management on the behavior of PEM type cells using simplified mathematical models. The theoretical framework that supports fuel cell modeling is presented first: this includes thermodynamic considerations, electrochemical reactions, mass transport, and membrane behavior are summarized. Next, a kinetic model for the description of the ethanol electrooxidation reaction in direct ethanol fuel cells is proposed. The kinetic model is then integrated into a 1D across-the-channel model for the anode of a direct ethanol fuel cell that is able to accurately predict the generated current and product selectivity data. The anode model is further extended to a full-length 1D Across-the-channel + 1D Along-the-channel model including a simple advective description for transport along the channels.

In the second part of the thesis, an experimental and theoretical analysis of the water balance in a hydrogen fuel cell is performed. The testing campaign presented was conducted at the DLR-Stuttgart facility during a couple of quarterly stays during the years 2013 and 2014. The tests consisted in subjecting the operation of a segmented hydrogen cell to different relative humidity conditions of the feeding streams in order to identify stable working conditions at the lowest possible relative humidity at different temperatures. After the presentation of the experimental results, a global water balance model is proposed to correlate the operational stability of a fuel cell with the global water balance in the interior. After validating the global model with the experimental results, a parametric study is carried out to extract information about the dependencies of the stability frontier with the flow, relative humidity and stoichiometry of the feed currents for different operating temperatures.

Resumen

Las pilas de combustible de electrolito polimérico, basadas en membranas de intercambio protónico, también conocidas como pilas de combustible PEM (acrónimo de *polymer electrolyte membrane* o *proton-exchange membrane*), constituyen una alternativa real para la generación de energía sostenible. Su versatilidad les permite ser utilizadas tanto en sistemas móviles (desde pequeños dispositivos electrónicos portátiles hasta vehículos) como en estaciones fijas (generadores de energía auxiliares para edificios o pequeñas estaciones remotas desatendidas). El mayor atractivo de este tipo de pilas es que pueden operar a bajas temperaturas (0-100°C), para lo cual se requiere el uso de catalizadores basados en platino, pudiendo incluso arrancar desde temperaturas bajo cero.

El funcionamiento de una pila de combustible PEM se basa en la electrooxidación del combustible en el ánodo y la electroreducción del oxígeno en el cátodo. Las reacciones anódica y catódica tienen lugar de forma independiente, con ambos electrodos separados por una membrana polimérica que permite únicamente la transferencia de protones. Esto fuerza a los electrones a recorrer un circuito externo generando una corriente eléctrica. La conductividad protónica de la membrana depende fuertemente del contenido en agua de la misma. Para un correcto funcionamiento de la pila, la cinética de las reacciones electroquímicas y la gestión del agua aparecen por tanto como aspectos fundamentales en su modelado y operación.

En función del combustible utilizado existen dos tipos de pilas PEM: las alimentadas con hidrógeno y las alimentadas con alcoholes. Las pilas de hidrógeno destacan por su gran densidad de potencia, lo que las hace ideales para el campo de la automoción. Cuando operan a plena carga, las actuaciones de este tipo de pilas están dominadas por la gestión del agua en la membrana. Por el contrario, las pilas de combustible de alcohol directo (DAFC) generan corrientes sensiblemente más bajas, por lo que constituyen una posible alternativa a las pilas de hidrógeno como fuentes de potencia para pequeños aparatos portátiles. No obstante, las pilas DAFC aún presenta dos grandes inconvenientes: la lenta cinética de electrooxidación de los alcoholes y el *crossover* de agua y alcohol desde el ánodo al cátodo a través de la membrana. Ambos fenómenos limitan severamente las actuaciones de este tipo de pilas.

El objetivo de esta tesis consiste en estudiar la influencia de la electroquímica y de la gestión del agua en el comportamiento de pilas tipo PEM por medio de modelos matemáticos simplificados. En primer lugar se resume el marco teórico en el que se basa el modelado de pilas de combustible: consideraciones termodinámicas, reacciones electroquímicas, transporte de masa y comportamiento de la membrana. A continuación se presenta un modelo cinético para la descripción de la reacción de electrooxidación del etanol en pilas de combustible de etanol directo. El modelo cinético se integra en un modelo unidimensional de tipo 1D *across-the-channel* para el ánodo de una pila de etanol directo que es capaz de predecir con precisión la corriente generada y la selectividad de

los productos. Seguidamente, el modelo del ánodo se extiende a un modelo de celda completa de tipo 1D *across-the-channel* + 1D *along-the-channel* incluyendo un modelo advectivo sencillo para el transporte a lo largo de los canales.

Por ultimo se realiza un análisis experimental y teórico del balance de agua en una pila de combustible de hidrógeno. La campaña de ensayos presentada se realizó en las instalaciones del DLR-Stuttgart durante un par de estancias trimestrales realizadas durante los años 2013 y 2014. Los ensayos consistieron en someter el funcionamiento una celda segmentada de hidrógeno a diferentes condiciones de humedad relativa a la entrada para identificar las condiciones de trabajo estables a la menor humedad relativa posible a diferentes temperaturas. Tras la presentación de los resultados experimentales se desarrolla un modelo de balance de agua global para correlacionar la estabilidad de funcionamiento de una pila de combustible con el balance de agua global en su interior. Tras validar el modelo global con los resultados experimentales, se realiza un estudio paramétrico que permite extraer información sobre las dependencias de la frontera de estabilidad con el caudal, la humedad relativa y la estequiometría de las corrientes de alimentación para diferentes temperaturas de operación.

Contents

CHAPTER

ONE

Introduction

Contents

1.1 Fuel cells

A fuel cell is an electrochemical device that converts the chemical energy stored in a fuel and an oxidant directly into electricity and heat. The electric current is generated by a pair of *redox* reactions that occur separated by an *electrolyte*. At the anode, the fuel is oxidized generating electrons and ions, while at the cathode the oxidant is reduced, consuming the electrons and ions generated at the anode. The electrolyte is specifically designed so that it cannot conduct electrons, which must therefore flow through an external circuit where they perform electric work, whereas it allows the flow of ions needed to maintain global electrical neutrality. Unlike conventional batteries, fuel cells require that the fuel and the oxidant be supplied continuously to sustain the electrochemical reactions.

The operation of a fuel cell is driven by chemical processes. As a result, they circumvent the Carnot cycle limitations of thermal devices and the mechanical limitations of systems with moving parts. In addition, the amount of electrical energy that can be generated by a fuel cell is only limited by the capacity of the fuel and oxidant reservoirs. This eliminates the long recharge times characteristic of conventional batteries.

The discovery of the fuel cell operating principle is commonly attributed to Sir William R. Grove (Grove, 1839), who also invented a practical device based on this principle: the so-called *gaseous voltaic battery* (Grove, 1842). Recent publications, however, attribute the discovery to Christian Friedrich Schöenbein, the well-known German-Swiss chemist who also discovered guncotton and ozone, a year before Sir William R. Grove (Bossel,

2000). It is known that both scientist maintained a lively scientific correspondence, which may be the origin of the confusion. Nevertheless, until the introduction of PTFE (Teflon) in the 1950s the fuel cell was rather a scientific curiosity than a practical system.

The first practical application of fuel cells was in space. The National Aeronautics and Space Administration (NASA) used them in the Gemini program during the 1950s and later in the Apollo program. The first mission that used a fuel cell was an unmanned suborbital flight on 30 October 1960. The Gemini module mounted the first alkaline fuel cell developed by General Electric, which generated 1 kW power with 29 kg weight and provided a potable water source for the crew. During the Apollo program NASA used the alkaline fuel cells developed by Pratt & Whitney based on Sir Francis T. Bacon patents (Appleby, 1990; Perry & Fuller, 2002). However, it was not until the 1990s when the industry (Ballard, Plug Power, etc.) started the development of commercial fuel cells, mainly for automotive and backup power applications, and the US Department of Energy included fuel cells among their research interest.

According to the Fuel Cell Technologies Office Multi-Year Research, Development, and Demonstration (MYRD&D) Plan (Fuel Cells Technologies Office, 2016), the largest markets for fuel cells today are in stationary power, portable power, auxiliary power units, backup power, and material handling equipment. Among fuel cell end-users, the automotive sector stands out as one of the most relevant ones (Cipriani *et al.*, 2014; Wang *et al.*, 2011). It is important to highlight that car manufacturers have already begun to commercialize fuel cell electric vehicles (FCEVs). Hyunday and Toyota have already FCEVs in the marketplace; Honda is close to the commercialization of its FCEV, and Daimler and other manufacturers are also set to begin commercialization (Department of Energy, 2015).

However, there are still some barriers for the development of fuel cells, both technical and economical (Fuel Cells Technologies Office, 2016). The use of catalysts is mandatory to reach competitive power densities, as they significantly accelerate the electrochemical reactions. In low temperature fuel cells the catalysts are usually based on noble metals, such as platinum, which are scarce and very expensive. The electrolyte is also one of the main challenges. It often requires strict working conditions (in terms of temperature, humidity, etc.) to work properly. As well, fuels and oxidants are not always easy to manage or store, which significantly increases system complexity.

Fuel cells are often classified by the type of electrolyte they use. The charge transport process that occurs in the electrolyte determines drastically the electro-chemical reactions that take place in the cell, the kind of catalysts required, the temperature range in which the cell operates, the fuel required, and other factors. These characteristics, in turn, affect the applications for which the different types of fuel cells are most suitable. The following list describes the different types of fuel cells, indicating the operating temperature, the typical applications, and main advantages of each type (Barbir, 2005):

Polymer Electrolyte (or Proton Exchange) Membrane Fuel Cells (PEMFC): They use

a proton conducting polymer membrane as electrolyte. The operating temperatures lie typically between 60°C and 90°C, although air-breathing systems may operate even at room temperature. This cells are usually operated with hydrogen or diluted aqueous alcohol solutions (methanol, ethanol, etc.). Their applications include backup power, portable power, small distributed generation, transportation and specialty vehicles. Their main advantages are the low temperatures of operation and the quick start-up.

Alkaline Fuel Cells (AFC): They use KOH immobilized in a matrix as electrolyte. The electrolyte operates in a temperature range between 50°C and 250°C depending on the concentration of KOH. In AFCs the ions that move in the electrolyte are OH^- groups. These fuel cells, also known as anion exchange membrane fuel cells (AEMFC), can be operated with organic compounds. They are used for military and space applications. The cathode reaction is faster in alkaline electrolyte, which leads to higher performance.

Phosphoric acid fuel cells (PAFC): They use as electrolyte a highly concentrated or pure liquid phosphoric acid (H_3PO_4) saturated in a silicon carbide matrix (SiC). The electrolyte operates roughly at 200°C and is permeable to protons, just like the polymeric membrane in PEMFCs. They are mostly used for distributed generation, and exhibit a high overall efficiency when used in combined heat and power (CHP) systems. The high temperature of operation increases the tolerance to impurities in hydrogen.

Molten Carbonate Fuel Cells (MCFC): They use as electrolyte a combination of alkali (Li, Na, K) in a ceramic matrix made of $LiAlO_2$. The operating temperatures are between 600°C and 700°C. In this case the electrolyte is permeable to CO_3^{2-} groups. They are used for electric utility and large distributed generation. Their advantages include high efficiency, fuel and catalyst flexibility, and suitability for CHP.

Solid Oxide Fuel Cells (SOFC): They use a solid oxide or ceramic electrolyte to conduct negative oxygen ions O^{2-} from cathode to anode. The operating temperatures are between 600°C and 1000°C. They are used for auxiliary power, electric utility, and large distributed generation. Like MCFCs, their high temperature of operation yields high efficiency, fuel and catalyst flexibility, and suitability for CHP.

1.2 Polymer exchange membrane fuel cells (PEMFC)

A polymer exchange membrane fuel cell (PEMFC) uses a polymeric electrolyte membrane to separate the anode from the cathode. As previously discussed, the polymer electrolyte membrane allows the transport of protons. The membrane is made of ionomers (synthetic polymers with ionic properties), the most extended one being Nafion®, discovered in the late 1960s by Walther Grot of DuPont. It contains perfluorovinyl ethers terminated by

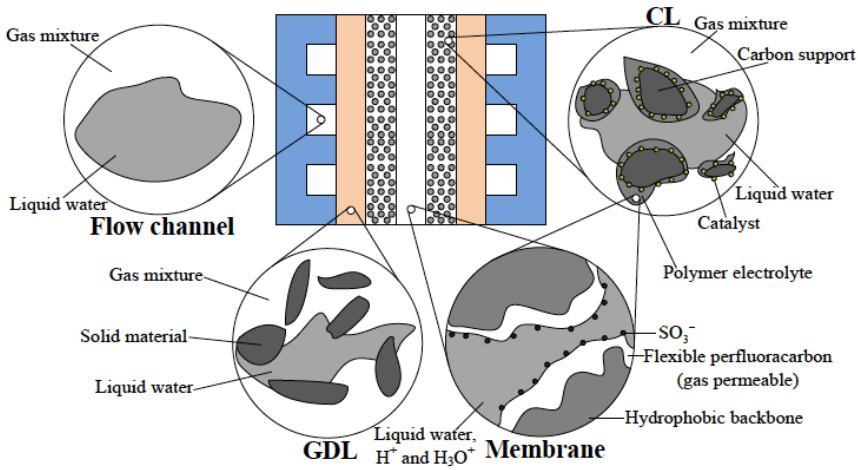

Figure 1.1: Cross section scheme of a hydrogen PEMFC. Details show the micro structure of different parts of the cell under normal operation with the presence of liquid water (Jiao, 2011; Jiao & Li, 2011).

sulfonic acids with hydrophobic tetrafluoroethylene (Teflon) flexible structures. So the proton conductivity is achieved because the water into the membrane ionizes the acidic groups (Jiao, 2011; Jiao & Li, 2011). The sulfonic groups $-SO_3H$ (with general formula $R-S(=O)_2-OH$, where R represents the generic chain where the group is attached) are highly hydrophilic and can adsorb large amounts of water, creating hydrated regions. In these regions, the H^+ are weakly attracted by the SO_3^- groups, which are rigidly attached to the Teflon structure, and they are able to move easily. The hydrated hydrophilic regions thus behave as dilute acids, explaining why the membrane needs to be well hydrated for the proton conductivity to be appreciable. Both the polymeric nature of the membrane and the requirement of membrane hydration restrict the operational temperature range between 60 and 90°C.

The transport of protons in the membrane forces the electrochemical reactions to produce or consume protons as charge carriers. At the anode side, the most extended fuel in PEMFCs is hydrogen (Wang *et al.*, 2011), although alcohols can also be used in direct alcohol fuel cells (DAFC). The use of alcohols generates significantly less power than hydrogen, but they offer safer operation for unattended low-power missions. At the cathode side, oxygen is reduced with the protons and electrons released in the anode to generate water as only reaction product. As previously discussed, the protons reach the cathode crossing the membrane, whereas the electrons are conducted through an external circuit generating current. The oxygen can be supplied as a pure gas or diluted as part of an air stream feed directly to the cell.

To optimize the power output of PEMFCs, adequate operating conditions are needed. Most PEMFCs operate between 60°C and 80°C to exploit the proton conductivity of the

membrane. Humidification of the gas feed streams is often used to guarantee an adequate membrane water content. The hydrogen and air streams are usually pressurized (typically at 0.5 bar gauge pressure) to improve water management (Barbir, 2005). To provide these cell conditions, additional systems are required. However, other operating conditions have also been investigated to try to eliminate auxiliary systems. Passive fuel cells rely on natural mechanisms, such as capillary forces, diffusion, convection, and evaporation, to achieve cell feeding without extra power consumption. Among the passive systems used one finds air-breathing systems for the anode electrode (O'Hayre *et al.*, 2007), pressurized cannisters (Kelley *et al.*, 2001), and capillary liquid systems (Guo & Cao, 2004). There are also passive cells feed running on different fuels, such as hydrogen (Chu & Jiang, 1999; Fabian *et al.*, 2006; O'Hayre *et al.*, 2007), methanol (Chen & Yang, 2003), and ethanol (Pereira *et al.*, 2014). In general, passive systems are more suitable for portable power sources (Kamarudin *et al.*, 2009). In the last decade, microbial fuel cells (MFCs), which use bacteria as the catalysts to oxidize organic and inorganic matter, have also been developed with application to micro devices (Logan *et al.*, 2006)

High temperature polymer exchange membrane fuel cells (HT-PEMFC) are another variant of PEMFCs. They operate between 100°C and 200°C, are able to run in dry conditions, tolerate impure fuel streams (e.g., hydrogen obtained from reforming gases), and the excess heat can be used for cogeneration. These characteristics can be exploited to simplify the system design, which increases its overall efficiency. Nevertheless, materials other than Nafion® must be used for the membrane (PBI, SPEEK, SPI, or SPSV) and the proton carrier (phosphoric acid or ionic liquids) (Chandan *et al.*, 2013; Yang *et al.*, 2001). High temperature operation has also been considered for DAFCs (Lamy *et al.*, 2001, 2002, 2004) to improve the effectiveness of the C–C bond breaking step in longer alcohols such as ethanol.

The structure of a single PEM fuel cell is outlined in Figure 1.2. As can be seen, the polymer exchange membrane (mem) is wrapped between the anode and cathode catalyst layers (cl), which are, in turn, covered by the gas diffusion layers (gdl). The gas diffusion layers are fibrous macroporous layers that are typically coated with highly hydrofobic microporous layers (mpl) on the side facing the catalyst for improved water management in PEM fuel cells operating with hydrogen. This tight layered pack constitutes the so-called *Membrane Electrode Assembly*, or MEA. Both the eletrochemical reactions and most of the performance limiting mass and charge transport phenomena occur within the MEA. The MEA is further sandwiched between the bipolar, or end, plates, whose purpose is to collect the current generated by the cell and to enable the distribution of reactants and the evacuation of products through the flow channels grooved on them.

The PEMFC work flow can be divided into four main processes:

1. **Fuel/oxidant supply:** Fuel and oxidant are supplied to the cell and distributed all over the MEA by the channels grooved on the bipolar plates. The reactants are transported to the catalyst layers by molecular diffusion and convection across the gass diffusion layers. These also homogenize the transport of reactants, whose

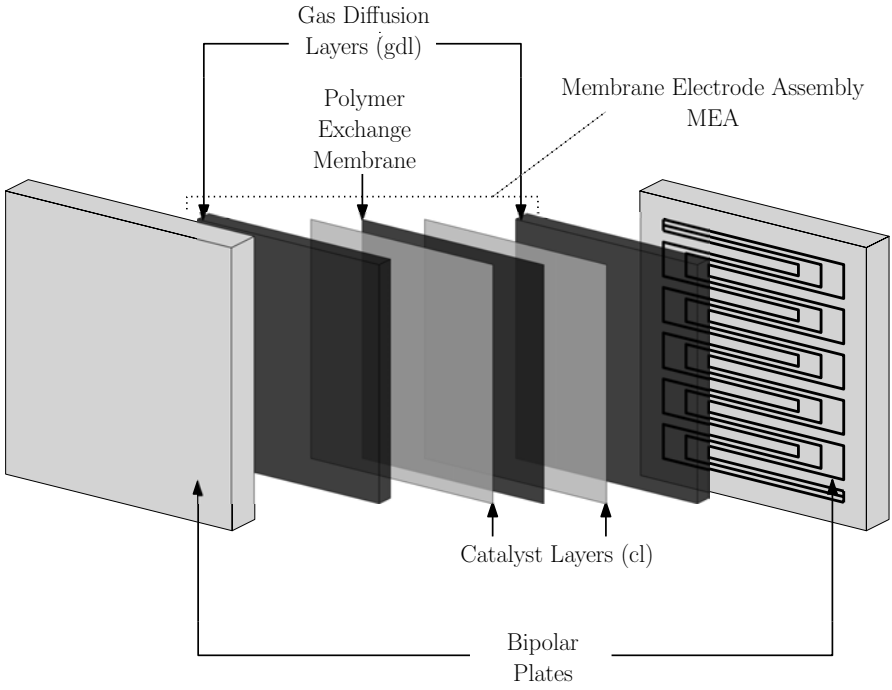

Figure 1.2: Scheme of a single fuel cell assembly.

concentrations are redistributed below the rib and the channels to provide as uniform a supply as possible to the catalyst layer.

2. **Electrochemical reactions:** The electrochemical reactions occur at the catalyst layers. The catalyst layers are composed by a mixture of a carbonacous porous media, ionomers, and catalyst particles. In the anode catalyst layer (acl), the reaction generates the protons an the electrons. Protons are conduced to the polymeric membrane by the ionomers while electrons are collected by the carbon web of the porous media and conduced to the bipolar plates. At the cathode catalyst layer (ccl) the electrons provided by the bipolar plate, the protons provided by the membrane and the oxygen supplied by the flow channels across the gass diffusion layer react in a electroreduction reaction generating water.

3. **Charge conduction:** The membrane is only permeable to protons. This fact forces electrons to travel through the external electric circuit to reach the cathode.

4. **Evacuation of reaction products:** Anode and cathode reactions generate products that are transported through the gass diffusion layers to the channels to be removed from the cell. The cathode reaction generates water but the anode has different products depending on the fuel. While hydrogen PEMFCs do not generate any product at the anode (the diatomic hydrogen molecule splits into two protons and

two electrons, effectively dissapearing at the anode catalyst layer), a DAFC produces carbonated compounds (CO_2, acetaldehyde, acetic acid, methane, etc.) that must be evaquated either in gaseous of diluted form.

To enable these four processes, the fuel cell is made up of the following components:

Bipolar Plates: They main tasks of the bipolar plates are to conduct electrons to and from the external electrical circuit and to manage the reactants and products flows. They are made of electron conductor materials, such as metallic alloys or graphite, onto which flow channels are engraved to guarantee reactant supply and product removal. While the solid part conducts the electrons out of the gdl at the anode side and into the gdl in cathode side, the engraved flow channels create a characteristic channel-rib pattern. Several designs have been proposed to ensure homogeneous distributions of reactants and current (single/multiple serpentine, parallel channels, or interdigitated channels, see Fig. 1.3). The relative orientation of anode and cathode flows (co-flow, counter-flow, or co-counterflow channels, see Fig.1.4) is also used to guarantee a uniform cell operation.

Gas diffusion layers: The gas diffusion layers are made of a macroporous carbon fiber structure with an uncompressed porosity between 0.7 and 0.9. The thickness is in the range of 100-400 μm. The two main pourposes of the gdl are to allow transportation of reactants and products from the channel to the catalys layers and vice-versa and to conduct the electric current and heat through the solid phase. The face in contact with the catalyst layer is usually coated with a thin microporous layer (mpl) made of a fine mixture of carbon black particles and hydrophobic Teflon. The porosity of this layer is between 0.4 and 0.6 and its thickness about 20-60 μm. The presence of the microporous layer reduces the contact losses between the gas diffusion layer and the catalyst layer and helps to alleviate water management problems such as cathode flooding (Gostick *et al.*, 2009; Pasaogullari *et al.*, 2005). In DAFCs the mpl also reduces fuel crossover (Kang *et al.*, 2012; Park *et al.*, 2008).

Catalyst layers: Also known as electrodes, they are thin layers that contain a porous combination of catalyst particles, ionomer and conductive phase (usually carbon). The electrochemical reactions occur in the so-called triple points, where the three phases are present. The catalyst (often Pt-based) favours the reactions, as its surface has places where the molecules are adsorbed and react catalytically. In the electrochemical reactions, species and charge carriers are involved. The void space acts as species supplier and product drainage, whereas the ionomer allows the movement of the protons and the electric conductor allows the movement of the electrons. At the anode catalyst layer the electro-oxidation reaction generates protons and electrons that are conduced by their respective phases. On the other hand, at the cathode catalyst layers protons and electrons are supplied to the electro-reduction reaction.

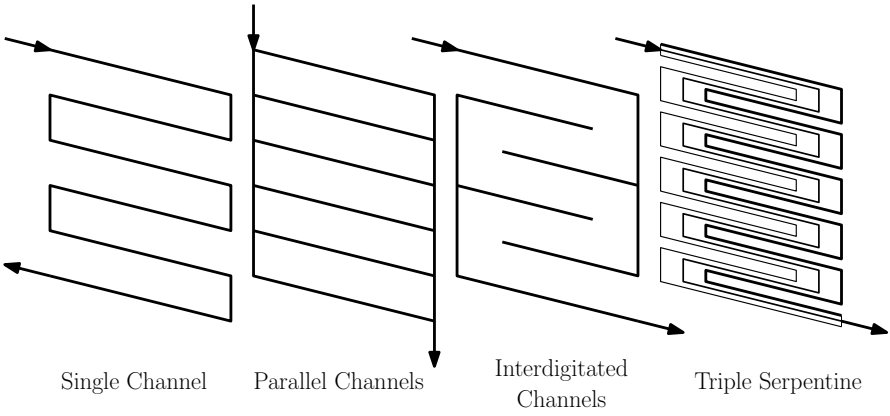

Figure 1.3: Schemes of the most common flow patterns in bipolar plates: Single channels, parallel channels, interdigitated channels and multiple channel serpentine.

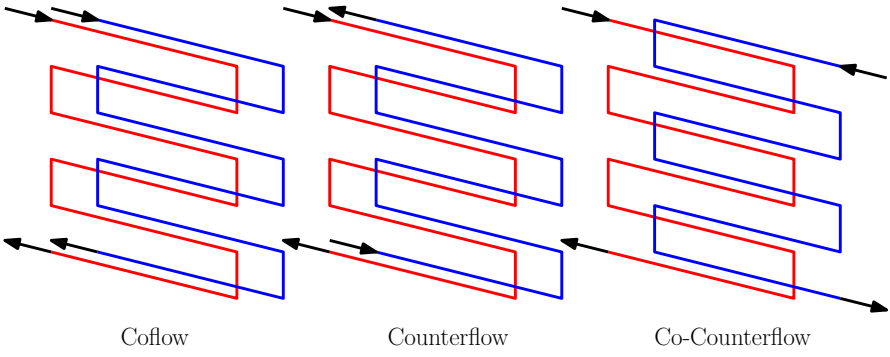

Figure 1.4: Schemes of the most typical orientation of flow fields in fuel cells: Coflow, counterflow and co-counterflow. The channel serpentines can be multiple channel serpentines.

Membrane: The main goal of the membrane is to allow the transport of protons from anode to cathode. Moreover, it has to keep the fuel and the oxidant separated. On top of this, the membrane has to be chemically an mechanically stable at the cell operating conditions (pressure, temperature, mechanical stresses, etc.). DuPont™ Nafion® PFSA membranes are the most commonly used in the fuel cell industry. However, there are several alternatives such as organic and inorganic variations of Nafion®, fluorinated compounds, etc. (Corti, 2014).

1.2.1 Direct alcohol fuel cells (DAFC)

In addition to hydrogen, several liquid organic and inorganic compounds can be used as fuels in PEMFC (Soloveichik, 2014). Common inorganic compounds tested for use are

ammonia, hydrazine, borohydrides and ammonia borane. Among the organic compounds used there are alcohols, hydrocarbons, acids and glycol compounds. Most of the organic compounds tested are produced by renewable biomass sources, which makes them a suitable clean option. Besides PEM membranes, also anion exchange membranes (AEM) are used in alkaline cells (Kamarudin *et al.*, 2013). Liquid fuels can be used either pure or diluted for safety reasons. Water is the most used solvent due to its natural properties and because of its importance for the correct operation of the membrane. However, other solvents have also been tested (e.g., sodium borohydride).

Alcohols are considered a promising source fuel to fuel cells (Corti & Gonzalez, 2014). Light alcohols, such as methanol or ethanol, are able to electrooxidate at relative low temperatures (less than 90°C). They also have a higher energy density than hydrogen. The electro-oxidation of alcohols consumes water, which makes water an optimum solvent for the fuel supply. In addition, aqueous alcohol solutions are typically feed at low concentrations (0.5–2M) which makes their operation and storage safer. These advantages makes DAFCs an alternative option for low power applications such as portable devices or unattended remote stations. Furthermore, more complex alcohols (e.g., propanol isomers, 2-methylpropan-2-ol, and butan-2-ol) may be an option at higher temperatures (up to 300°C). Nacef & Affoune (2011) carried out an extensive thermodynamic study about the potential performances of several alcohols used in PEM fuel cells.

Nevertheless, some disadvantages arise when alcohols are used in PEM fuel cells. Contrary to hydrogen, alcohol electro-oxidation is a sluggish process that involves many elementary reactions generating high activation overpotentials. This results in a severe reduction of fuel cell performance. Besides that, since the alcohols are supplied as aqueous dilutions and the membrane is highly permeable to water, a *crossover* flux of fuel is established across the membrane. The fuel that crosses the membrane is electrooxidized at the cathode electrode, generating an undesired parasitic current that also results in larger cathode activation losses (Andreadis *et al.*, 2008; Andreadis & Tsiakaras, 2006; Gurau & Smotkin, 2002; Heinzel & Barragán, 1999; James & Pickup, 2010; Ravikumar & Shukla, 1996; Song *et al.*, 2005*a*,*c*).

The electrooxidation of organic compounds is not straightforward, as it proceeds as a branched, multi-step, reaction (Braunchweig *et al.*, 2013; Kutz *et al.*, 2011). Due to the large number of chemical bonds of the compounds, several reactions can be expected. Unfortunately, poisoning species such as carbon monoxide are found among the reaction intermediates that are formed in the reaction path. The CO groups remain adsorbed to the catalyst, blocking the active reactions sites. This produces a sharp reduction of the effective catalyst surface area, which also reduces cell performance (Gonzalez & Mota-Lima, 2014; Lamy *et al.*, 2004; Morimoto & Yeager, 1998; Vigier *et al.*, 2004*a*). To mitigate this effect, binary Pt-based catalysts include a secondary metal, such as Sn or Ru (Akhairi & Kamarudin, 2016; Antoniassi *et al.*, 2013; Bach Delpeuch *et al.*, 2016; Colmati *et al.*, 2006; Fatih *et al.*, 2010; Kavanagh *et al.*, 2012; Kim *et al.*, 2011; Li *et al.*, 2007;

Rousseau *et al.*, 2006; Vigier *et al.*, 2004*a*; Wang & Liu, 2008); the blockage of active sites is alleviated via a bifunctional mechanism that allows the absorption of hydroxyl groups at lower potentials on the secondary metal, thus favoring further oxidation of Pt-adsorbates blocking the active catalyst sites. (Vigier *et al.*, 2004*b*, 2006; Watanabe & Motoo, 1975). It is interesting to note that the problem of CO poisoning is not unique to DAFCs; low temperature PEMFCs running on hydrogen have very low tolerance to impurities (e.g., CO) in the fuel, requiring very high purity hydrogen that is costly to produce. Fuel cells operated with reformate gas also exhibit this problem (Springer *et al.*, 2001).

DAFCs are suitable for portable power applications (e.g., battery chargers, consumer electronics, handheld terminals, unattended security devices, notebook PCs, emergency response mobile communications, or even auxiliary power units) and material handling equipment. The power requirements for these applications are low and the cost targets and infrastructure requirements are not as challenging as for transportation applications (Franceschini & Corti, 2014; Fuel Cells Technologies Office, 2016).

Considering all the types of DAFCs currently under development, those running on methanol and ethanol are, in this order, the ones that have reached further progress. Below we describe the particularities of these fuel cells, indicating the main advantages and disadvantages of both:

Direct methanol fuel cells (DMFC): Methanol is the simplest alcohol. Due to the lack of the C–C bond present in higher alcohols, methanol is the alcohol with the largest number of hydrogens per carbon (Olah *et al.*, 2006), which makes it a good hydrogen carrier. However, reforming methanol to H_2 is still under study. By contrast, a DMFC uses methanol as fuel without producing H_2 during the process. The device operates with diluted methanol (1—2M) and only a fraction of the diluted fuel is used. The device recycles the outlet and replenishes it to keep methanol concentration (Carrette *et al.*, 2001). Platinum based catalysts show the best results (Kobayashi *et al.*, 2003); additionally, secondary metals are included to reduce the impact of CO poisoning (Braunchweig *et al.*, 2013; Carrette *et al.*, 2001; Léger *et al.*, 2005; Liu *et al.*, 2006). The main applications of DMFCs are on small portable devices: battery chargers, consumer electronics, notebook PCs and portable generators (Carrette *et al.*, 2001; Franceschini & Corti, 2014; Ren *et al.*, 2000). Actual challenges for DMFCs marked by DOE include reducing Pt loading, reducing methanol crossover to increase efficiency, simplifying the side-on systems to increase energy and power density, improve reliability, and reduce cost (Fuel Cells Technologies Office, 2016).

Direct ethanol fuel cells (DEFC): Ethanol is a fully renewable alcohol that can be readily obtained from the fermentations of biomass and is much less toxic than methanol (Kamarudin *et al.*, 2013; Wang *et al.*, 1995). FCTS plans (Fuel Cells Technologies Office, 2016) include ethanol tolerance for liquid-feed fuel cells operated with fuel blends. The number of patents in DEFC is steadily growing

since 2002, which suggests that DEFC technology is still under development and further progress can be expected (Franceschini & Corti, 2014). The complete electrooxidation of ethanol to CO_2 would make DEFCs useful even for automotive purposes (Kamarudin *et al.*, 2013). But the sluggish kinetics of the ethanol electro-oxidation reaction hinders this achievement (Brouzgou *et al.*, 2013; Friedl & Stimming, 2013; Kamarudin *et al.*, 2013; Song & Tsiakaras, 2006). By way of contrast, due to its larger molecular structure ethanol has a lower crossover rate than methanol, which together with its slower electrochemical oxidation kinetics produces a lesser effect on the cathode performance (Ekdharmasuit *et al.*, 2013; Song *et al.*, 2005*b*). The complexity of ethanol electooxidation is originated by the difficulty of breaking the C–C bond (Antolini, 2007; Antoniassi *et al.*, 2013; Brouzgou *et al.*, 2013; Hitmi *et al.*, 1994; Iwasita & Pastor, 1994; Léger *et al.*, 2005; Li & Pickup, 2006; Meyer *et al.*, 2011; Shao & Adzic, 2005; Wang *et al.*, 2004, 2006), a problem that is shared with other higher alcohols.

1.2.2 Water Management

Water management is one of the main active areas in PEMFC research, as it constitutes one of the key engineering challenges to overcome in the commercialization of fuel cells in transport application; including operation at subzero ambient temperatures (Fuel Cells Technologies Office, 2016). Proper membrane hydration is a key factor to ensure good proton conductivity across the membrane. On one hand, insufficient membrane hydration leads to a severe conductivity drop and is known to affect membrane aging (Collier *et al.*, 2006; Knights *et al.*, 2004; Wu *et al.*, 2008; Yousfi-Steiner *et al.*, 2008). On the other hand, an excess of water causes flooding, which is a major obstacle to the mass transport of reactants and products (Barbir *et al.*, 2005; Li *et al.*, 2008; Tüber *et al.*, 2003; Yousfi-Steiner *et al.*, 2008). Water accumulation produces liquid water clusters that fill the voids of the porous media, thereby increasing mass transport losses and leading to reactant starvation at the catalyst layer. Excess liquid water can also lead to the obstruction of the flow channels leading to flow maldistribution. When combined together, these effects may cause inhomogeneous or intermittent cell operation, leading to hot spots or sharp transient currents that lead to a severe reduction of the membrane life.

PEMFCs operated with hydrogen are particularly sensitive to water management. The gas feed streams are able either to hydrate or dehydrate the cell, depending on their temperature and relative humidity. Even though water is produced at the cathode electrode, additional water supply is often needed at the anode to ensure a correct water distribution throughout the membrane. This water is provided by a proper humidification of the inlet gases. The water management strategy differs significantly in liquid-feed direct alcohol fuel cells. Since these cells are fully hydrated at the anode, they are more stable under dry cathode operation (Chen & Yang, 2003; Kamarudin *et al.*, 2009; Pereira

et al., 2014). On the other hand, at the anode side gas (e.g., CO_2) bubbles may appear, generating a problem analogous to the presence of water drops in gas-feed fuel cells (García-Salaberri *et al.*, 2015*a*,*b*, 2014).

1.2.3 PEMFC performance

The overall performance of a fuel cell is usually represented by the current density (i.e., current per unit surface) vs. voltage curve, often referred to as the *polarization curve*. Thermodynamics teaches us that, in an ideal process in which mass and charge transport phenomena occur in a reversible manner, the output voltage should remain constant independently of the current density. Such an ideal reversible voltage, E_0, is determined by the electrochemical reactions that occur in the cell, and therefore is directly related to the redox pair. Operational parameters such as temperature and pressure also influence the ideal thermodynamic voltage.

The deviations between the ideal equilibrium potential of the redox pair and the polarization curve provide a measure of the fuel cell efficiency. The actual current density vs. voltage curve for a particular fuel cell (geometry, catalyst/electrode characteristics, and electrolyte properties) and operating conditions (reactant concentrations, flow rates, pressures, temperature, and relative humidity) is dependent on both activation (i.e., kinetic), ohmic, and mass transport losses, to be described below:

Activation loses are originated by the finite rate of the electrochemical reactions that take place in the cell electrodes.

Mass transport looses arise when the reactants are not supplied at the same rate than they can be consumed. Mass transport losses are dominated by the gas diffusion layers and interfacial phenomena (Weber *et al.*, 2014). As previously discussed, one of the main tasks of the gas diffusion layers is to smooth the channel-rib pattern of the bipolar plates to provide an as homogeneous as possible supply of reactants to the catalyst layers. However, this task entails a certain mass transfer resistance that produces significant mass transport losses at large current densities.

Ohmic looses are generated by the irreversible charge transport processes associated with finite charge transport conductivities. Electrons move through the solid phase of the gas diffusion layers and other elements of the cell and their interfaces, while protons are conducted through the polymeric membrane. Although the charge transport mechanisms are different, both result in finite voltage drops. These looses grow linearly with the current density as stated by Ohm's law.

The actual cell voltage at a given current density can then be expressed as the idel reversible voltage, E_0, minus the so-called activation (act), transport (trp), and ohmic (ohm) overpotentials

$$V = E_0 - \eta_{\text{act}} - \eta_{\text{trp}} - \eta_{\text{ohm}} \tag{1.1}$$

For modeling purposes, the voltage losses are separated by regions rather than processes. The voltage is therefore

$$V = E_0 - \eta_a - \eta_c - \eta_{mem} \tag{1.2}$$

where η_a, η_c, and η_{mem} denote the voltage losses (including activation, mass transport and ohmic contributions) at the anode, the cathode, and the membrane.

1.3 Scope of the thesis

As presented above, PEMFC operation is based in two main processes, electrochemical reaction at the catalyst layers and charge transportations through the membrane. This thesis aims to contribute to the understanding of those two processes.

Electrooxidation reaction arises as crucial issue in DAFC. The incomplete electrooxidation of ethanol hinders the theoretical maximum energy release while at the same time generates a variety of compounds. An accurate DAFC model therefore has to predict current density and overpotentials as well as a detailed description of the residual product. For this purpose, a systematic formulation of the kinetic models is needed.

Charge transportation through acidic membranes is caused by water absorption. Stable behavior of a PEMFC is direcly related with the appropriate hydration level of the membrane. A global balance for the water inlet, outlet and production into the cell can be used to identify and predict unfeasible working conditions.

The specific goals of this dissertation are:

Goal 1: To develop a complete kinetic eletrooxidation scheme in binary Pt based catalyst for a DEFC anode including free and adsorbed intermediate species. In order to fit kinetic constants, experimental result of product selectivity. In addition this work aims to establish a systematic methodology to determine kinetic constants values from product selectivity analysis.

Goal 2: To integrate the previous anode model into a complete DEFC model. The model will include across-the-channel and along-the-channel to evaluate the evolution of the full range of final products keeping the model as simple as possible.

Goal 3: To correlate qualitative behavior of a PEMFC with the balance of water at different relative humidity inlet conditions

1.4 Outline of the thesis

This dissertation is divided in six chapters. Chapter 1 provides a general introduction to the field PEM fuel cells and gives information about the objectives and scope of the thesis. Chapter 2 presents an overview of the basic theoretical framework underlying

fuel cell modeling. It includes an overview of the thermodynamic analysis of fuel cells, the modeling of electrochemical reactions, and the transport processes involved in the porous media and in the membrane. The rest of the thesis has been divided into two parts, corresponding to different types of fuel cells and phenomena under study.

Part I, which includes Chapters 3 and 4, is devoted to direct ethanol fuel cell modeling. Chapter 3 presents a 1D across-the-channel model for the anode of a DEFC accounting for a multi-step kinetic mechanism for the ethanol electrooxidation reaction. The model considers free and adsorbed intermediate species, and the reaction constants are optimized using a genetic algorithm to fit overpotential and product selectivity data taken from the literature. In Chapter 4, an extended 1D+1D model for DEFCs is proposed. The 1D across-the-channel model developed previously is coupled to a simplified 1D along-the channel advection model to account for the consumption of reactants along the flow channels. The extended model includes also the cathode electrode and accounts for ethanol and acetaldehyde crossover.

Part II, which includes chapters 4 and 5, addresses the problem of water management in hydrogen PEMFCs from the experimental and modeling perspectives. Chapter 4 reports the experimental results obtained in a thorough experimental campaign carried out during two short stays a DLR-Stuttgart. A segmented cell was operated at different temperatures and gas feed humidifications to plot qualitative maps of stable and unstable operating conditions. In order to explain the obtained results, Chapter 5 presents a global (i.e., zero-dimensional) water management model that is able to predict the qualitative stability of the cell from first principles. A simple energy analysis of the cell gas conditioning system is also included.

Finally, chapter 7 summarizes the main conclusions of the thesis and suggests further work.

References

AKHAIRI, M. A. F. & KAMARUDIN, S. K. 2016 Catalysts in direct ethanol fuel cell (DEFC): An overview. *Int. J. Hydrogen Energy* **41** (7), 4214–4228.

ANDREADIS, G. M., PODIAS, A. K. M. & TSIAKARAS, P. E. 2008 The effect of the parasitic current on the Direct Ethanol PEM Fuel Cell Operation. *J. Power Sources* **181** (2), 214–227.

ANDREADIS, G. M. & TSIAKARAS, P. E. 2006 Ethanol crossover and direct ethanol PEM fuel cell performance modeling and experimental validation. *Chem. Eng. Sci.* **61** (22), 7497–7508.

ANTOLINI, E. 2007 Catalysts for direct ethanol fuel cells. *J. Power Sources* **170** (1), 1–12.

ANTONIASSI, R. M., OLIVEIRA NETO, A., LINARDI, M. & SPINACÉ, E. V. 2013 The effect of acetaldehyde and acetic acid on the direct ethanol fuel cell performance using PtSnO2/C electrocatalysts. *Int. J. Hydrogen Energy* **38** (27), 12069–12077.

APPLEBY, A. J. 1990 From Sir William Grove to today: fuel cells and the future. *J. Power Sources* **29** (1-2), 3–11.

BACH DELPEUCH, A., MAILLARD, F., CHATENET, M., SOUDANT, P. & CREMERS, C. 2016 Ethanol oxidation reaction (EOR) investigation on Pt/C, Rh/C, and Pt-based bi- and tri-metallic electrocatalysts: A DEMS and in situ FTIR study. *Appl. Catal. B Environ.* **181**, 672–680.

BARBIR, F. 2005 *PEM Fuel Cells: Theory and practice*. Elsevier Academic.

BARBIR, F., GORGUN, H. & WANG, X. 2005 Relationship between pressure drop and cell resistance as a diagnostic tool for PEM fuel cells. *J. Power Sources* **141** (1), 96–101.

BOSSEL, U. 2000 *The Birth of the Fuel Cell, 1835-1845: Including the First Publication of the Complete Correspondence from 1839 to 1868 Between Christian Friedrich Schoenbein (discoverer of the Fuel Cell Effect) and William Robert Grove (inventor of the Fuel Cell)*. European Fuel Cell Forum.

BRAUNCHWEIG, B., HIBBITTS, D., NEUROCK, M. & WIECKOWSKI, A. 2013 Electrocatalysis: A direct alcohol fuel cell and surface science perspective. *Catal. Today* **202** (1), 197–209.

BROUZGOU, A., PODIAS, A. K. M. & TSIAKARAS, P. 2013 PEMFCs and AEMFCs directly fed with ethanol: A current status comparative review. *J. Appl. Electrochem.* **43** (2), 119–136.

CARRETTE, L., FRIEDRICH, K. A. & STIMMING, U. 2001 Fuel Cells - Fundamentals and Applications. *Fuel Cells* **1** (1), 5–39.

CHANDAN, A., HATTENBERGER, M., EL-KHAROUF, A., DU, S., DHIR, A., SELF, V., POLLET, B. G., INGRAM, A. & BUJALSKI, W. 2013 High temperature (HT) polymer electrolyte membrane fuel cells (PEMFC) – A review. *J. Power Sources* **231**, 264–278.

CHEN, C.Y & YANG, P 2003 Performance of an air-breathing direct methanol fuel cell.

CHU, D. & JIANG, R. 1999 Performance of polymer electrolyte membrane fuel cell (PEMFC) stacks. *J. Power Sources* **83** (1-2), 128–133.

CIPRIANI, G., DI DIO, V., GENDUSO, F., LA CASCIA, D., LIGA, R., MICELI, R. & RICCO GALLUZZO, G. 2014 Perspective on hydrogen energy carrier and its automotive applications. *Int. J. Hydrogen Energy* **39** (16), 8482–8494.

COLLIER, A., WANG, H., ZI YUAN, X., ZHANG, J. & WILKINSON, D. P. 2006 Degradation of polymer electrolyte membranes. *Int. J. Hydrogen Energy* **31** (13), 1838–1854.

COLMATI, F., ANTOLINI, E. & GONZALEZ, E. R. 2006 Effect of temperature on the mechanism of ethanol oxidation on carbon supported Pt, PtRu and Pt3Sn electrocatalysts. *J. Power Sources* **157** (1), 98–103.

CORTI, HORACIO R. 2014 Membranes for Direct Alcohol Fuel Cells. In *Direct Alcohol Fuel Cells*, pp. 121–230. Dordrecht: Springer Netherlands.

CORTI, HORACIO R. & GONZALEZ, ERNESTO R., ed. 2014 *Direct Alcohol Fuel Cells*. Dordrecht: Springer Netherlands.

DEPARTMENT OF ENERGY, DOE 2015 Fuel Cell Technologies Market Report 2014. *Tech. Rep.*. U.S. Department of Energy.

EKDHARMASUIT, P., THERDTHIANWONG, A. & THERDTHIANWONG, S. 2013 Anode structure design for generating high stable power output for direct ethanol fuel cells. *Fuel* **113**, 69–76.

FABIAN, T., POSNER, J. D., O'HAYRE, R., CHA, S.-W., EATON, J. K., PRINZ, F. B. & SANTIAGO, J. G. 2006 The role of ambient conditions on the performance of a planar, air-breathing hydrogen PEM fuel cell. *J. Power Sources* **161** (1), 168–182.

FATIH, K., NEBURCHILOV, V., ALZATE, V., NEAGU, R. & WANG, H. 2010 Synthesis and characterization of quaternary PtRuIrSn/C electrocatalysts for direct ethanol fuel cells. *J. Power Sources* **195** (21), 7168–7175.

FRANCESCHINI, ESTEBAN A. & CORTI, HORACIO R. 2014 Applications and Durability of Direct Methanol Fuel Cells. In *Direct Alcohol Fuel Cells*, pp. 321–355. Dordrecht: Springer Netherlands.

FRIEDL, J. & STIMMING, U. 2013 Model catalyst studies on hydrogen and ethanol oxidation for fuel cells. *Electrochim. Acta* **101**, 41–58.

FUEL CELLS TECHNOLOGIES OFFICE, FCTS(DOE) 2016 Multi-Year Research, Development, and Demonstration Plan. *Tech. Rep.*. U.S. Department of Energy.

GARCÍA-SALABERRI, P. A., GOSTICK, J. T., HWANG, G., WEBER, A. Z. & VERA, M. 2015*a* Effective diffusivity in partially-saturated carbon-fiber gas diffusion layers: Effect of local saturation and application to macroscopic continuum models. *J. Power Sources* **296**, 440–453.

GARCÍA-SALABERRI, P. A., HWANG, G., VERA, M., WEBER, A. Z. & GOSTICK, J. T. 2015*b* Effective diffusivity in partially-saturated carbon-fiber gas diffusion layers: Effect of through-plane saturation distribution. *Int. J. Heat Mass Transf.* **86**, 319–333.

GARCÍA-SALABERRI, P. A., VERA, M. & IGLESIAS, I. 2014 Modeling of the anode of a liquid-feed DMFC: Inhomogeneous compression effects and two-phase transport phenomena. *J. Power Sources* **246**, 239–252.

GONZALEZ, E. R. & MOTA-LIMA, A. 2014 Catalysts for Methanol Oxidation. In *Direct Alcohol Fuel Cells*, pp. 33–62. Dordrecht: Springer Netherlands.

GOSTICK, J. T., IOANNIDIS, M. A., FOWLER, M. W. & PRITZKER, M. D. 2009 On the role of the microporous layer in PEMFC operation. *Electrochem. commun.* **11** (3), 576–579.

GROVE, W. R. 1839 XXIV. On voltaic series and the combination of gases by platinum. *Philos. Mag. Ser. 3* **14** (86-87), 127–130.

GROVE, W. R. 1842 LXXII. On a gaseous voltaic battery. *Philos. Mag. Ser. 3* **21** (140), 417–420.

GUO, Z. & CAO, Y. 2004 A passive fuel delivery system for portable direct methanol fuel cells. *J. Power Sources* **132** (1), 86–91.

GURAU, B. & SMOTKIN, E. S. 2002 Methanol crossover in direct methanol fuel cells: a link between power and energy density. *J. Power Sources* **112** (2), 339–352.

HEINZEL, A. & BARRAGÁN, V.M. 1999 A review of the state-of-the-art of the methanol crossover in direct methanol fuel cells. *J. Power Sources* **84** (1), 70–74.

HITMI, H., BELGSIR, E. M., LÉGER, J.-M., LAMY, C. & LEZNA, R. O. 1994 A kinetic analysis of the electro-oxidation of ethanol at a platinum electrode in acid medium. *Electrochim. Acta* **39** (3), 407–415.

IWASITA, T. & PASTOR, E. 1994 A dems and FTir spectroscopic investigation of adsorbed ethanol on polycrystalline platinum. *Electrochim. Acta* **39** (4), 531–537.

JAMES, D. D. & PICKUP, P. G. 2010 Effects of crossover on product yields measured for direct ethanol fuel cells. *Electrochim. Acta* **55** (11), 3824–3829.

JIAO, K. 2011 Experimental and Modelling Studies of Cold Start Processes in Proton Exchange Membrane Fuel Cells .

JIAO, K. & LI, X. 2011 Water transport in polymer electrolyte membrane fuel cells. *Prog. Energy Combust. Sci.* **37** (3), 221–291.

KAMARUDIN, M. Z. F., KAMARUDIN, S. K., MASDAR, M. S. & DAUD, W. R. W. 2013 Review: Direct ethanol fuel cells. *Int. J. Hydrogen Energy* **38** (22), 9438–9453.

KAMARUDIN, S. K., ACHMAD, F. & DAUD, W. R. W. 2009 Overview on the application of direct methanol fuel cell (DMFC) for portable electronic devices. *Int. J. Hydrogen Energy* **34** (16), 6902–6916.

KANG, K., LEE, G., GWAK, G., CHOI, Y. & JU, H. 2012 Development of an advanced MEA to use high-concentration methanol fuel in a direct methanol fuel cell system. *Int. J. Hydrogen Energy* **37**, 6285–6291.

KAVANAGH, R., CAO, X. M., LIN, W. F., HARDACRE, C. & HU, P. 2012 Origin of low CO2 selectivity on platinum in the direct ethanol fuel cell. *Angew. Chem. Int. Ed. Engl.* **51** (7), 1572–5.

KELLEY, R. J., PRATT, S. D., LANDRETH, B. D., PENNISI, R. W., MUTHUSWAMY, S. & URBISH, G. F. 2001 Portable fuel cell power supply.

KIM, I., HAN, O. H., CHAE, S. A., PAIK, Y., KWON, S.-H., LEE, K.-S., SUNG, Y.-E. & KIM, H. 2011 Catalytic reactions in direct ethanol fuel cells. *Angew. Chem. Int. Ed. Engl.* **50** (10), 2270–4.

KNIGHTS, S. D., COLBOW, K. M., ST-PIERRE, J. & WILKINSON, D. P. 2004 Aging mechanisms and lifetime of PEFC and DMFC. *J. Power Sources* **127** (1), 127–134.

KOBAYASHI, T., OTOMO, J., WEN, C.-J. & TAKAHASHI, H. 2003 Direct alcohol fuel cell—relation between the cell performance and the adsorption of intermediate originating in the catalyst-fuel combinations. *J. Power Sources* **124** (1), 34–39.

KUTZ, R. B., BRAUNSCHWEIG, B., MUKHERJEE, P., BEHRENS, R. L., DLOTT, D. D. & WIECKOWSKI, A. 2011 Reaction pathways of ethanol electrooxidation on polycrystalline platinum catalysts in acidic electrolytes. *J. Catal.* **278** (2), 181–188.

LAMY, C., BELGSIR, E. M. & LÉGER, J.-M. 2001 Electrocatalytic oxidation of aliphatic alcohols: Application to the direct alcohol fuel cell (DAFC). *J. Appl. Electrochem.* **31** (7), 799–809.

LAMY, C., LIMA, A., LERHUN, V., DELIME, F., COUTANCEAU, C. & LÉGER, J.-M. 2002 Recent advances in the development of direct alcohol fuel cells (DAFC). *J. Power Sources* **105** (2), 283–296.

LAMY, C., ROUSSEAU, S., BELGSIR, E. M., COUTANCEAU, C. & LÉGER, J.-M. 2004 Recent progress in the direct ethanol fuel cell: development of new platinum–tin electrocatalysts. *Electrochim. Acta* **49** (22-23), 3901–3908.

LÉGER, J.-M., ROUSSEAU, S., COUTANCEAU, C., HAHN, F. & LAMY, C. 2005 How bimetallic electrocatalysts does work for reactions involved in fuel cells?: Example of ethanol oxidation and comparison to methanol. *Electrochim. Acta* **50** (25), 5118–5125.

LI, G. & PICKUP, P. G. 2006 Analysis of performance losses of direct ethanol fuel cells with the aid of a reference electrode. *J. Power Sources* **161** (1), 256–263.

LI, H., SUN, G., CAO, L., JIANG, L. & XIN, Q. 2007 Comparison of different promotion effect of PtRu/C and PtSn/C electrocatalysts for ethanol electro-oxidation. *Electrochim. Acta* **52** (24), 6622–6629.

LI, H., TANG, Y., WANG, Z., SHI, Z., WU, S., SONG, D., ZHANG, J., FATIH, K., ZHANG, J., WANG, H., LIU, Z., ABOUATALLAH, R. & MAZZA, A. 2008 A review of water flooding issues in the proton exchange membrane fuel cell. *J. Power Sources* **178** (1), 103–117.

LIU, H., SONG, C., ZHANG, L., ZHANG, J., WANG, H. & WILKINSON, D. P. 2006 A review of anode catalysis in the direct methanol fuel cell.

LOGAN, B. E., HAMELERS, B., ROZENDAL, R., SCHRÖDER, U., KELLER, J., FREGUIA, S., AELTERMAN, P., VERSTRAETE, W. & RABAEY, K. 2006 Microbial Fuel Cells: Methodology and Technology. *Environ. Sci. Technol.* **40** (17), 5181–5192.

MEYER, M., MELKE, J. & GERTEISEN, D. 2011 Modelling and simulation of a direct ethanol fuel cell considering multistep electrochemical reactions, transport processes and mixed potentials. *Electrochim. Acta* **56** (11), 4299–4307.

MORIMOTO, Y. & YEAGER, E.. B. 1998 CO oxidation on smooth and high area Pt, Pt-Ru and Pt-Sn electrodes. *J. Electroanal. Chem.* **441** (1-2), 77–81.

NACEF, M. & AFFOUNE, A.M. 2011 Comparison between direct small molecular weight alcohols fuel cells' and hydrogen fuel cell's parameters at low and high temperature. Thermodynamic study. *Int. J. Hydrogen Energy* **36** (6), 4208–4219.

O'HAYRE, R., FABIAN, T., LITSTER, S., PRINZ, F. B. & SANTIAGO, J. G. 2007 Engineering model of a passive planar air breathing fuel cell cathode. *J. Power Sources* **167** (1), 118–129.

OLAH, G. A., GOEPPERT, A. & PRAKASH, G. K. S. 2006 *Beyond oil and gas: the methanol economy*. Wiley-VCH, arXiv: arXiv:1011.1669v3.

PARK, J.-Y., LEE, J.-H., KANG, S., SAUK, J.-H. & SONG, I. 2008 Mass balance research for high electrochemical performance direct methanol fuel cells with reduced methanol crossover at various operating conditions. *J. Power Sources* **178**, 181–187.

PASAOGULLARI, U., WANG, C.-Y. & CHEN, K. S. 2005 Two-Phase Transport in Polymer Electrolyte Fuel Cells with Bilayer Cathode Gas Diffusion Media. *J. Electrochem. Soc.* **152** (8), A1574.

PEREIRA, J. P., FALCÃO, D. S., OLIVEIRA, V. B. & PINTO, A. M. F. R. 2014 Performance of a passive direct ethanol fuel cell. *J. Power Sources* **256**, 14–19.

PERRY, M. L. & FULLER, T. F. 2002 A Historical Perspective of Fuel Cell Technology in the 20th Century. *J. Electrochem. Soc.* **149** (7), s59–s67.

RAVIKUMAR, M. K. & SHUKLA, A. K. 1996 Effect of Methanol Crossover in a Liquid-Feed Polymer-Electrolyte Direct Methanol Fuel Cell. *J. Electrochem. Soc.* **143** (8), 2601.

REN, X., ZELENAY, P., THOMAS, S., DAVEY, J. & GOTTESFELD, S. 2000 Recent advances in direct methanol fuel cells at Los Alamos National Laboratory. *J. Power Sources* **86**, 111–116.

ROUSSEAU, S., COUTANCEAU, C., LAMY, C. & LÉGER, J.-M. 2006 Direct ethanol fuel cell (DEFC): Electrical performances and reaction products distribution under operating conditions with different platinum-based anodes. *J. Power Sources* **158** (1), 18–24.

SHAO, M. H. & ADZIC, R. R. 2005 Electrooxidation of ethanol on a Pt electrode in acid solutions: in situ ATR-SEIRAS study. *Electrochim. Acta* **50** (12), 2415–2422.

SOLOVEICHIK, G. L. 2014 Liquid fuel cells. *Beilstein J. Nanotechnol.* **5** (1), 1399–418.

SONG, S. & TSIAKARAS, P. 2006 Recent progress in direct ethanol proton exchange membrane fuel cells (DE-PEMFCs). *Appl. Catal. B Environ.* **63** (3), 187–193.

SONG, S., WANG, G., ZHOU, W., ZHAO, X., SUN, G., XIN, Q., KONTOU, S. & TSIAKARAS, P. 2005*a* The effect of the MEA preparation procedure on both ethanol crossover and DEFC performance. *J. Power Sources* **140** (1), 103–110.

SONG, S., ZHOU, W., LIANG, Z., CAI, R., SUN, G., XIN, Q., STERGIOPOULOS, V. & TSIAKARAS, P. 2005*b* The effect of methanol and ethanol cross-over on the performance of PtRu/C-based anode DAFCs. *Appl. Catal. B Environ.* **55** (1), 65–72.

SONG, S., ZHOU, W., TIAN, J., CAI, R., SUN, G., XIN, Q., KONTOU, S. & TSIAKARAS, P. 2005*c* Ethanol crossover phenomena and its influence on the performance of DEFC. *J. Power Sources* **145** (2), 266–271.

SPRINGER, T. E., ROCKWARD, T., ZAWODZINSKI, T. A. & GOTTESFELD, S. 2001 Model for Polymer Electrolyte Fuel Cell Operation on Reformate Feed: Effects of CO, H[sub 2] Dilution, and High Fuel Utilization. *J. Electrochem. Soc.* **148** (1), A11.

TÜBER, KLAUS, PÓCZA, DAVID & HEBLING, CHRISTOPHER 2003 Visualization of water buildup in the cathode of a transparent PEM fuel cell. *J. Power Sources* **124** (2), 403–414.

VIGIER, F., COUTANCEAU, C., HAHN, F., BELGSIR, E. M. & LAMY, C. 2004*a* On the mechanism of ethanol electro-oxidation on Pt and PtSn catalysts: electrochemical and in situ IR reflectance spectroscopy studies. *J. Electroanal. Chem.* **563** (1), 81–89.

VIGIER, F., COUTANCEAU, C., PERRARD, A., BELGSIR, E. M. & LAMY, C. 2004*b* Development of anode catalysts for a direct ethanol fuel cell. *J. Appl. Electrochem.* **34** (4), 439–446.

VIGIER, F., ROUSSEAU, S., COUTANCEAU, C., LEGER, J.-M. & LAMY, C. 2006 Electrocatalysis for the direct alcohol fuel cell. *Top. Catal.* **40** (1-4), 111–121.

WANG, H., JUSYS, Z. & BEHM, R. J. 2004 Ethanol Electrooxidation on a Carbon-Supported Pt Catalyst: Reaction Kinetics and Product Yields. *J. Phys. Chem. B* **108** (50), 19413–19424.

WANG, H., JUSYS, Z. & BEHM, R. J. 2006 Ethanol electro-oxidation on carbon-supported Pt, PtRu and Pt3Sn catalysts: A quantitative DEMS study. *J. Power Sources* **154** (2), 351–359.

WANG, H.-F. & LIU, Z.-P. 2008 Comprehensive mechanism and structure-sensitivity of ethanol oxidation on platinum: new transition-state searching method for resolving the complex reaction network. *J. Am. Chem. Soc.* **130** (33), 10996–1004.

WANG, J., WASMUS, S. & SAVINELL, R. F. 1995 Evaluation of Ethanol, 1-Propanol, and 2-Propanol in a Direct Oxidation Polymer-Electrolyte Fuel Cell. *J. Electrochem. Soc.* **142** (12), 4218.

WANG, Y., CHEN, K. S., MISHLER, J., CHO, S. C. & ADROHER, X. C. 2011 A review of polymer electrolyte membrane fuel cells: Technology, applications, and needs on fundamental research. *Appl. Energy* **88** (4), 981–1007.

WATANABE, M. & MOTOO, S. 1975 Electrocatalysis by ad-atoms. *J. Electroanal. Chem. Interfacial Electrochem.* **60** (3), 275–283.

WEBER, A. Z., BORUP, R. L., DARLING, R. M., DAS, P. K., DURSCH, T. J., GU, W., HARVEY, D., KUSOGLU, A., LITSTER, S., MENCH, M. M., MUKUNDAN, R., OWEJAN, J. P., PHAROAH, J. G., SECANELL, M. & ZENYUK, I. V. 2014 A Critical Review of Modeling Transport Phenomena in Polymer-Electrolyte Fuel Cells. *J. Electrochem. Soc.* **161** (12), F1254–F1299.

WU, J., YUAN, X. Z., MARTIN, J. J., WANG, H., ZHANG, J., SHEN, J., WU, S. & MERIDA, W. 2008 A review of PEM fuel cell durability: Degradation mechanisms and mitigation strategies. *J. Power Sources* **184** (1), 104–119.

YANG, C., COSTAMAGNA, P., SRINIVASAN, S., BENZIGER, J. & BOCARSLY, A. B. 2001 Approaches and technical challenges to high temperature operation of proton exchange membrane fuel cells. *J. Power Sources* **103** (1), 1–9.

YOUSFI-STEINER, N., MOÇOTÉGUY, PH., CANDUSSO, D., HISSEL, D., HERNANDEZ, A. & ASLANIDES, A. 2008 A review on PEM voltage degradation associated with water management: Impacts, influent factors and characterization. *J. Power Sources* **183** (1), 260–274.

CHAPTER

TWO

Physicochemical principles of Polymer Exchange Membrane Fuel Cells operation

Contents

2.1 Introduction

Fuel cell modeling is an inherently multiphysics problem. The aim of this chapter is to present a rigorous mathematical background of the most important physicochemical processes that take place in a fuel cell and must be accounted for in a realistic model. The structure of the chapter reflects the discovery and historical development of the main concepts and phenomena used to describe the fuel cell operation principles.

As any other energy conversion device, a fuel cell must work strictly obeying the laws of thermodynamics. A rigorous analysis of the chemical energy available that can be released by the electrochemical reactions is presented in Section 2.2, leading to the famous *Nernst equation*. Despite the fact that experimental evidences were originally presented by Nernst (1889*a*,*b*), a thermodynamic derivation of this equation will also be presented. Detailed explanations of fundamental thermodynamic concepts can be found in many textbooks (Moran & Shapiro, 2009). Thermodynamics fundamentals of fuel cells are also thoroughly presented in the literature (Barbir, 2005; O'Hayre *et al.*, 2006).

Section 2.3 presents the theoretical framework required to model the electrochemical reaction rates. As for the thermodynamic analysis leading to Nernst equation, the main results in electrochemical kinetics were also obtained experimentally before they could be explained theoretically. The seminal experimental works on chemical and electrochemical reaction kinetics were carried out at the end of 19th century and beginning of the 20th (Arrhenius, 1889; Butler, 1924; Erdey-Gruz & Volmer, 1930; Langmuir, 1918; Tafel, 1905). However, more detailed readings are recommended for a fresher introduction to the basics of electrochemical processes (Atkins & de Paula, 2010; Bard & Faulkner, 2001; Fang & Liu, 2014).

It was not until the 1990s, when fuel cell technology reached its first commercial uses, when the problems of mass and charge transport revealed as crucial for fuel cell development as those derived from thermodynamics or kinetics. Sections 2.4 and 2.5 review the most common models used for the description of mass and charge transport phenomena, respectively.

2.2 Thermodynamic principles of fuel cells

2.2.1 Redox pairs

The most important driving processes that take place in a fuel cell are the electrochemical reactions between the fuel and the oxidant. As implied by the prefix *electro-*[1], these reactions involve the transfer of electric charges, and this fact is achieved through a pair of *redox* (i.e., *re*duction-*ox*idation) reactions. A *redox* reaction is separated into two half-reactions: the oxidation and the reduction reaction. In the oxidation reaction the reactant species losses electrons. By contrast, in the reduction reaction the reactant species gains electrons. In a fuel cell, the oxidation and reduction reactions take place respectively in the anode and cathode electrodes.

In a fuel cell, the redox half-reactions are kept separated by an electrolyte, with the electrodes being electrically connected through an external circuit. The electrolyte is an ionic conductor, while the electrodes and the external circuit are made of good electronic conductors. This configuration makes it possible to separate the ionic and electronic currents, the latter being used to perform electrical work through the external circuit.

The reactants used for the oxidation reactions in PEM fuel cells are hydrogen and alcohols, mostly methanol and ethanol. Protons are the ionic charge carrier in these cells, so the oxidation reaction must generate protons for the operation of the system. For instance, the hydrogen oxidation reaction

$$H_2 \rightarrow 2H^+ + 2e^- \tag{2.1}$$

[1]From Latin electrum, from Ancient Greek élektron, or “amber”, a natural resin, which when rubbed produces static electricity.

generates two protons and two electrons per molecule of hydrogen consumed. This reaction occurs in the anode of low temperature hydrogen PEMFCs, where due to its extreme simplicity the activation losses are very small. In addition to this, the catalyst, typically made of Pt-based particles (Braunchweig *et al.*, 2013; Gasteiger *et al.*, 2004), performs better for simpler reactions such as (2.1). As implied by the above reaction, hydrogen electro-oxidation produces no other products than charge carriers, in this case electrons and protons, hence it is not necessary to evacuate anything else from the anode electrode, except (maybe) the heat evolved by the reaction.

For low-power portable applications, liquid-feed direct alcohol fuel cells (DAFC) may also be used. The most simple alcohol is methanol (CH_3OH). The electro-oxidation of methanol also produces electrons and protons, but generates CO_2 as well and only occurs in the presence of water

$$CH_3OH + H_2O \rightarrow CO_2 + 6H^+ + 6e^- \tag{2.2}$$

which requires the supply of water and the evacuation of CO_2 bubbles. This introduces stronger mass transport limitations in the anode of a DMFC than in hydrogen PEMFCs, motivated in particular by the presence of the bubbles.

The methanol oxidation reaction (MOR) takes place in multiple steps (Braunchweig *et al.*, 2013) some of them leading to the production of undesirable intermediate products, such as CO (Gonzalez & Mota-Lima, 2014; Lamy *et al.*, 2004; Morimoto & Yeager, 1998; Springer *et al.*, 2001; Vigier *et al.*, 2004). Due to the multiple species involved, the reaction is slower and more complex than Reaction (2.1), which leads to significantly lower current densities in direct methanol fuel cells (DMFC) than in hydrogen PEMFCs. As a result, complex and expensive catalyst compositions (Pt-Ru nanoparticles supported on high surface area carbon) must be used to minimize activation losses (Akhairi & Kamarudin, 2016; Antoniassi *et al.*, 2013; Bach Delpeuch *et al.*, 2016; Colmati *et al.*, 2006; Fatih *et al.*, 2010; Kavanagh *et al.*, 2012; Kim *et al.*, 2011; Li *et al.*, 2007; Rousseau *et al.*, 2006; Vigier *et al.*, 2004; Wang & Liu, 2008).

Ethanol is another alcohol used in DAFCs. It is a more complex molecule (CH_3CH_2OH) with a highly stable C–C bond, which makes it even more difficult to react. As will be discussed in Chapter 3, ethanol electro-oxidation may proceed through multiple paths, which includes partial oxidation to acetaldehyde, acetic acid, or methane, as well as complete oxidation to CO_2, according respectively to the following reactions

$$CH_3CH_2OH \rightarrow CH_3COH + 2H^+ + 2e^- \tag{2.3a}$$
$$CH_3CH_2OH + H_2O \rightarrow CH_3COOH + 4H^+ + 4e^- \tag{2.3b}$$
$$CH_3CH_2OH + H_2O \rightarrow CO_2 + CH_4 + 4H^+ + 4e^- \tag{2.3c}$$
$$CH_3CH_2OH + 3H_2O \rightarrow 2CO_2 + 12H^+ + 12e^- \tag{2.3d}$$

While different oxidation reactions may be found in PEM fuel cells depending on the

fuel type, the reduction reaction is common to all of them, namely the oxygen reduction reaction

$$O_2 + 4H^+ + 4e^- \rightarrow 2H_2O \tag{2.4}$$

which combines the electrons and protons produced in the anode with a molecule of oxygen to produce water.

When combining Reactions (2.1), (2.2) or (2.3) with Reaction (2.4), different global reactions can be defined for the cell:

- Hydrogen PEM fuel cells (PEMFC)

$$H_2 + \frac{1}{2}O_2 \rightarrow H_2O \tag{2.5}$$

- Direct methanol fuel cells (DMFC)

$$CH_3OH + \frac{3}{2}O_2 \rightarrow CO_2 + 2H_2O \tag{2.6}$$

- Direct ethanol fuel cells (DEFC)

$$CH_3CH_2OH + \frac{1}{2}O_2 \rightarrow CH_3COH + H_2O \tag{2.7}$$

$$CH_3CH_2OH + O_2 \rightarrow CH_3COOH + H_2O \tag{2.8}$$

$$CH_3CH_2OH + O_2 \rightarrow CO_2 + CH_4 + H_2O \tag{2.9}$$

$$CH_3CH_2OH + 3O_2 \rightarrow 2CO_2 + 3H_2O \tag{2.10}$$

2.2.2 Electric work and Gibbs free energy

The energy released in a fuel cell comes from the chemical energy stored into the fuel and the oxidant, which is released by the electrochemical reactions that take place in the anode and cathode electrodes. The energy released or consumed by a chemical reaction is represented by its *heat of reaction* or *enthalpy of reaction*. This value is the enthalpy change produced in a chemical reaction and it is calculated as the difference in *formation enthalpy* between the reaction products (P) and reactants (R) at a given temperature T

$$\Delta h^0(T) = \sum_{\mathrm{P}} \upsilon_k h_k^0(T) - \sum_{\mathrm{R}} \upsilon_k h_k^0(T) \tag{2.11}$$

In the above expression, υ_k is the stoichiometric coefficient of species k and $h_k^0(T)$ is the molar specific formation enthalpy of species k, which can be evaluated at temperature T

from its reference value at the standard temperature T_0 as follows

$$h_k^0(T) = \Delta_f h_k^0\left(T_0\right) + \left(h_k^0(T) - h_k^0\left(T_0\right)\right) \tag{2.12}$$

This expression shows that the molar enthalpy of a chemical compound is made up by its molar enthalpy of formation at the reference temperature $\Delta_f h_k^0(T_0)$ plus the enthalpy change associated with the state change at fixed composition $h_k^0(T) - h_k^0(T_0)$ (Moran & Shapiro, 2009). An extended data base for these thermodynamic properties, containing data for over 2000 solid, liquid, and gaseous chemical species, is provided by NASA (Mcbride *et al.*, 2002).

During the chemical reactions, entropy also changes. Just like the *enthalpy of reaction* (2.11), the molar *entropy of reaction* at a given temperature T and pressure p is defined as

$$\Delta s(T,p) = \sum_{\mathrm{P}} \upsilon_k s_k(T,p) - \sum_{\mathrm{R}} \upsilon_k s_k(T,p) \tag{2.13}$$

Unlike enthalpy, entropy has no formation contribution. As established by the third law of thermodynamics, the *absolut entropy* is defined as the entropy change between the actual estate and the absolute-zero state. For crystalline substances entropy is zero at the absolute-zero state; whereas non-crystalline substances have a non zero value of the entropy at the absolute-zero state (Moran & Shapiro, 2009). The value of the absolute entropy can also be obtained from the NASA library of thermodynamic data (Mcbride *et al.*, 2002).

It is well known that not all the energy available in a chemical reaction can be converted to useful work. Therefore, in a fuel cell not all the energy released by the electrochemical reactions can be converted to electrical work as a result of entropy production. The Gibbs free energy

$$G = H - TS \tag{2.14}$$

represents the amount of useful energy that can be used as *potential work*. In a given process, the amount of energy that can be released as potential work is the variation of the Gibbs free energy. For an isothermal process, the variation of the molar specific Gibbs free energy reduces to

$$\Delta g = \Delta h - T\Delta s \tag{2.15}$$

The work performed by a fuel cell is completely electrical. In general, electrical work is done when moving a charge Q through a potential difference E. In a fuel cell, the electrical work can be written as

$$W_e = nFE \tag{2.16}$$

where n is the number of moles of electrons transferred in the reaction per mole of fuel consumed and $F = 96485$ C/mole of electrons is Faraday's constant. Since the maximum

amount of electrical work that can be obtained is the reduction of the Gibbs free energy ($W_e = -\Delta g$), the electrical reversible potential (or voltage) obtained from the cell is

$$E = \frac{-\Delta g}{nF} \tag{2.17}$$

The value of the electrical reversible potential at the standard conditions, $T_0 = 298$ K and $p_0 = 100$ kPa, is called the *standard reversible potential of the reaction* E_0

As previously discussed, water is commonly produced in PEM fuel cells. Due to the low temperatures of operation ($T < 100$°C) it can be produced both in liquid and gas phase. However, the enthalpy of formation of both phases is different, the difference being the latent heat of vaporization. As a result, the formation of liquid water yields a significantly higher reaction enthalpy than that of water vapor. To decide which phase should be used for determining the potential work we have to apply the "philosopy" of the *Gibbs free energy* calculation. This accounts for the maximum energy that can be released as work. Since the formation of liquid water releases a larger amount of energy due to the latent heat of vaporization, which is released during condensation, the use of the gas water formation enthalpy implies an incomplete account of the available energy. The value of the reaction enthalpy obtained assuming the formation of liquid water is therefore called the Higher Heating Value (HHV), while that obtained when water vapor is formed is called the Lower Heating Value (LHV).

Another voltage can be defined using the reaction enthalpy (2.11); the *thermoneutral potential* or *enthapy potential* E_{TH} is

$$E_{TH} = \frac{-\Delta h}{nF} \tag{2.18}$$

this potential is useful to evaluate all the available energy contained in the fuel.

The reversible potential E accounts for the decreasing of the the energy due to the entrophy generation of the chemical reactions. In a fuel cell, the actual voltage V established between the electrodes is lower than the reversible voltage E and the enthalpy potential E_{TH} due to the fuel cell irreversibilities. The unused energy is dissipated as heat. Then, the total heat produced by the electrochemical reactions can be simply expressed as

$$Q = I\left(E_{TH} - V\right) \tag{2.19}$$

where I represents the amount of current drawn from the cell. It is interesting to note that when using the LHV to evaluate the enthalpy potential E_{TH} one obtains a lower estimation of the residual heat Q than when using the HHV. The difference comes from the fact that the HHV includes also the heat released during water condensation. However, the global energy balance should remain the same in both cases as long as the latent heat of vaporization is properly accounted for (Weber *et al.*, 2014).

Hydrogen potentials The standard potential of hydrogen PEMFCs is highly dependent

on the phase of water produced. The reversible potential at 25°C is 1.229 V for liquid water and 1.185 V for water vapor (Table 2.1). In both cases the potential decreases with temperature (Figure 2.1). Below 100°C the production of liquid water releases more energy than that of water vapor, so the potential evaluated using the HHV is higher in that range; whereas the potential obtained using the LHV is higher over 100°C. Low temperature PEM fuel cells operate assuming the HHV as maximum expected energy.

Methanol potentials Liquid-feed DMFCs operate at temperatures lower than 100°C, so the HHV is used for calculating their standard potential. At higher temperatures, the phase of methanol also needs to be considered. Figure 2.1 shows the evolution of the standard potential for both liquid and gas methanol and water. The potential predicted assuming both species in liquid phase decreases sightly whit temperature, while that obtained for gas phase is seen to increase with temperature. This fact is the basis to explore the posibility of using DMFCs at temperatures above 100°C (Nacef & Affoune, 2011).

Ethanol potentials The ethanol electrooxidation reaction in DEFCs has very complex kinetics with different products (Antolini, 2007; Antoniassi *et al.*, 2013; Brouzgou *et al.*, 2013; Hitmi *et al.*, 1994; Iwasita & Pastor, 1994; Léger *et al.*, 2005; Li & Pickup, 2006; Meyer *et al.*, 2011; Shao & Adzic, 2005; Wang *et al.*, 2004, 2006). Table 2.1 shows the global reactions considered in this dissertation (Chapter 3). It is seen that the complete oxidation to CO_2 has the higher reversible potential, which decreases monotonically with temperature as shown in Figure 2.1. Although complete oxidation to CO_2 is difficult to achieve, the reversible potential of this reaction is often used as reference for DEFC models.

2.2.3 The Nernst equation

So far, the effect of reactant and product concentrations on reversible cell potential has been ignored. To understand this effect, we must introduce the chemical potential. The chemical potential of species k is defined as

$$\mu_k = \left(\frac{\partial G}{\partial n_k} \right)_{T,p,n_{l \neq k}} \tag{2.20}$$

and represents the change of the Gibbs free energy produced by a change in the number of moles, n_k, of species k. Thermodynamics teaches us that the Gibbs free energy of a mixture can be expressed as the sum of the chemical potentials of all the species composing the mixture

$$G = \sum_k n_k \mu_k \tag{2.21}$$

Table 2.1: —

Global reaction			Standard potential @ $T_0 = 298$ K
$H_2 + \frac{1}{2}O_2$	$\rightarrow$	H_2O (l)	$E_0 = 1.229$V
$H_2 + \frac{1}{2}O_2$	$\rightarrow$	H_2O (g)	$E_0 = 1.185$V
$CH_3OH + \frac{3}{2}O_2$	$\rightarrow$	$CO_2 + 2H_2O$ (l)	$E_0 = 1.213$V
$CH_3CH_2OH + \frac{1}{2}O_2$	$\rightarrow$	$CH_3COH + H_2O$ (l)	$E_0 = 1.049$V
$CH_3CH_2OH + O_2$	$\rightarrow$	$CH_3COOH + H_2O$ (l)	$E_0 = 1.151$V
$CH_3CH_2OH + O_2$	$\rightarrow$	$CO_2 + CH_4 + H_2O$ (l)	$E_0 = 0.889$V
$CH_3CH_2OH + 3O_2$	$\rightarrow$	$2CO_2 + 3H_2O$ (l)	$E_0 = 1.151$V

and that the chemical potential of species k can be expressed as

$$\mu_k = \mu_k^0 + RT \ln a_k \tag{2.22}$$

in terms of the activity of species k, defined as:

$$a_k = \begin{cases} p_k/p_0 & \text{ideal gases} \\ C_k/C_0 \quad \text{for} & \text{ideal dilute solutions} \\ 1 & \text{pure components} \end{cases} \tag{2.23}$$

where $C_0 = 1$ M is the reference concentration.

The variation of the molar specific Gibbs free energy can then be written in terms of the chemical potentials

$$\Delta g = \sum_{\mathrm{P}} \upsilon_k \mu_k^0 - \sum_{\mathrm{R}} \upsilon_k \mu_k^0 + RT \ln \frac{\prod_{\mathrm{P}} a_k^{\upsilon_k}}{\prod_{\mathrm{R}} a_k^{\upsilon_k}} \tag{2.24}$$

where the variation of the chemical potentials in standard conditions can be written as the standard change in the Gibbs free energy Δg^0 for the reaction

$$\Delta g = \Delta g^0 + RT \ln \frac{\prod_{\mathrm{P}} a_k^{\upsilon_k}}{\prod_{\mathrm{R}} a_k^{\upsilon_k}} \tag{2.25}$$

Using this expression to evaluate the reversible potential of the reaction E using Eq. (2.17)

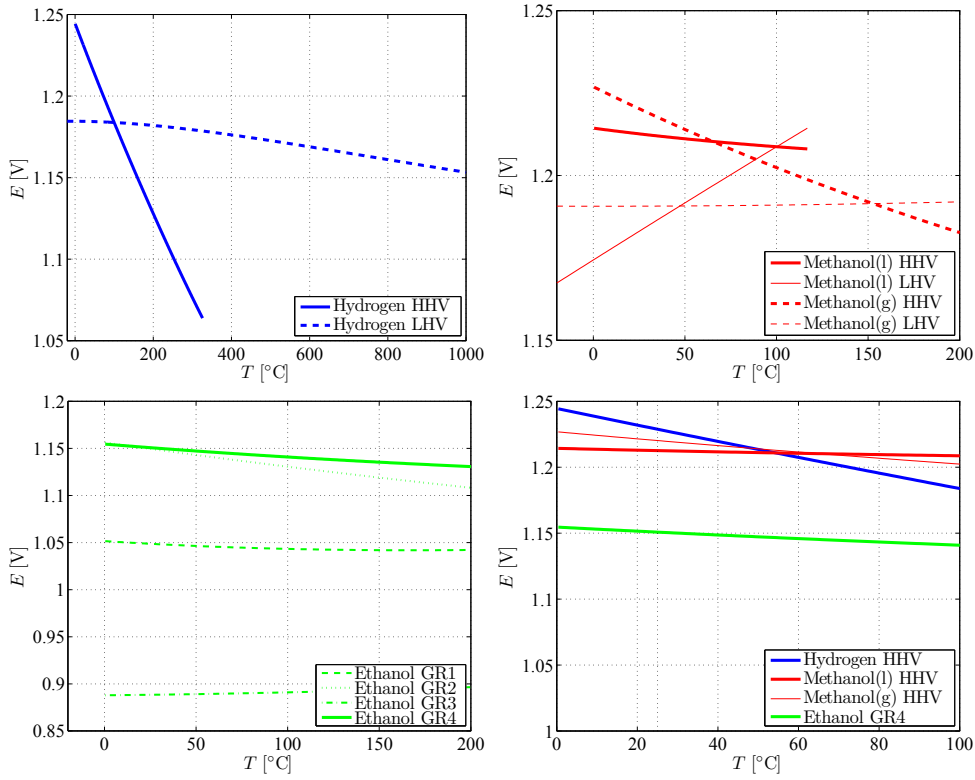

Figure 2.1: Reversible potentials

one obtains the *Nernst equation*

$$E = E^0 - \frac{RT}{nF} \ln \frac{\prod_{\mathrm{P}} a_k^{\upsilon_k}}{\prod_{\mathrm{R}} a_k^{\upsilon_k}} \tag{2.26}$$

which relates the reversible potential E of the electrochemical reaction to the standard reversible potential E^0, temperature, and activities, expressed in terms of concentrations or partial pressures. Equation (2.26) owes its name to the German chemist Walther Nernst[2], who originally obtained it exclusively from experimental work (Nernst, 1889*a*,*b*), although his equation was later deducted from first thermodynamic principles, as has been shown here.

[2]A detailed review of the historical development of Nernst equation can be found in Archer (1989)

2.3 Electrochemical principles of fuel cells

The *key point* to the operation of a fuel cell is that the total reaction is split into two half-reactions that take place separately in the anode and cathode electrodes. The Nernst Equation (2.26) applies to the global reaction, but a deeper understanding requires to study both half-reactions independently. Obviously they are electrochemical reactions as they involve electron transfer. In 1905, Julius Tafel proposed an empirical equation that related the current density j produced by an electrochemical reaction to the so-called overpotential $\eta = E - E^{\star}$, defined as the difference between the applied potential E and the equilibrium potential $E^{\star}$ (Tafel, 1905). This equation is commonly known as the *Tafel equation*, and is customarily written in the form

$$\eta = a + b \log j \quad \text{with} \quad b = \frac{2.3RT}{\alpha F} \tag{2.27}$$

where α is the so-called charge transfer coefficient, whose value must be between 0 and 1, and log indicates decimal logarithm. This equation is widely used in electrochemistry and can be applied in several conditions (Fang & Liu, 2014).

Although Tafel obtained its equation purely by experimental methods, in the 1930s Butler and Volmer (and coworkers) derived it from the Arrhenius equation for the rate constant of a chemical reaction, rewriting the activation energy in terms of the Gibbs free energy of activation and the cell overpotential as will be discussed next.

2.3.1 From Tafel equation to Butler-Volmer equation

In 1889, Arrhenius (1889)[3] proposed that the temperature dependence of the rate constant of a chemical reaction could be expressed as

$$\mathfrak{K} = A \exp\left(\frac{-\Delta_A E}{RT}\right) \tag{2.28}$$

where T is the absolute temperature, A is the frequency factor and $\Delta_A E$ is the activation energy. The frequency factor gives the frequency of collisions between reactant molecules. The activation energy can be defined as the change in internal energy from the reactant state to the *activated complex* state, so it is also called the *internal energy of activation*.

Since all the reactions in a fuel cell can be considered as condensed-phase reactions[4],

[3] A detailed description of the development of Arrhenius equation is presented by Laidler (1984). An English translation of the original paper of Arrhenius can be found in Back & Laidler (2013), first edited in 1967, pp. 31–35.

[4] In general $\Delta H = \Delta E + \Delta(pV)$ but in condensed-phase reactions $\Delta(pV)$ can be neglected, so that $\Delta E \approx \Delta H$ (Bard & Faulkner, 2001)

the *entalphy of activation* is approximately equal to the activation energy, so that

$$\mathfrak{K} \approx A \exp\left(\frac{-\Delta_A H}{RT}\right) \tag{2.29}$$

Rewriting now the parameter A as the product $A' \exp(-\Delta_A S/R)$ allows us to express the reaction constant in terms of the Gibbs free energy of activation $\Delta_A G$

$$\mathfrak{K} = A' \exp\left(\frac{-\Delta_A H - T\Delta_A S}{RT}\right) = A' \exp\left(\frac{-\Delta_A G}{RT}\right) \tag{2.30}$$

Advanced kinetic theories (e.g., transition state theory) have tried to estimate the values of A and $\Delta_A E$ corresponding to a certain electrochemical reaction and to relate them to molecular properties. However, extending our discussion to such complex descriptions is outside the scope of this work. For the interested reader, a deeper discussion of electron transfer kinetics can be found in Bard & Faulkner (2001).

2.3.1.1 Single-step single-electron reactions

To fix ideas, let us consider a generic single-step reversible electrooxidation reaction (similar to the anode half-reaction of a PEMFC) involving the transfer of a single electron

$$\mathrm{R} \rightleftharpoons \mathrm{O} + \mathrm{e}^- \tag{2.31}$$

At this point, it is important to note that the Gibbs free energy of activation at a given condition can be written as the Gibbs free energy of activation at a reference state, usually taken as the equilibrium state, hereafter denoted by the subscript 0, plus an additional term that accounts for the deviation of the potential from its value at the reference state. Thus, for the forward (i.e., oxidation) reaction

$$\Delta_A G_{\mathrm{Ox}} = \Delta_A G^0 - \alpha_{\mathrm{Ox}} F \left(E - E^0\right) \tag{2.32}$$

while for the backward (i.e., reduction) reaction

$$\Delta_A G_{\mathrm{Red}} = \Delta_A G^0 + \alpha_{\mathrm{Red}} F \left(E - E^0\right) \tag{2.33}$$

where α_{Ox} and α_{Red} are the charge transfer coefficients of the oxidation and reduction reactions. The charge transfer coefficients reflect the nature of the electron transfer process in single-step electrochemical reactions (Fang & Liu, 2014). For single electron reactions taking place on metallic surfaces, the value $\alpha_{\mathrm{Ox}} \approx 0.5$ is commonly accepted (Atkins & de Paula, 2010; Barbir, 2005). The value of α_{Ox} is also related to the charge transfer coefficient of the backwards reaction, with the symmetry relation $\alpha_{\mathrm{Red}} = 1 - \alpha_{\mathrm{Ox}}$ being frequently assumed. For a thorough derivation of the above expressions, the reader is referred to Section 3.3.2 of the book of Bard & Faulkner (2001).

According to (2.30), (2.32) and (2.33), the reaction constants for the forward and backward reactions can be written as

$$\begin{aligned}\Re_{\mathrm{Ox}} &= A'_{\mathrm{Ox}} \exp\left(\frac{-\Delta_A G_{\mathrm{Ox}}}{RT}\right) = A'_{\mathrm{Ox}} \exp\left(\frac{-\Delta_A G^0_{\mathrm{Ox}}}{RT}\right) \exp\left(\alpha_{\mathrm{Ox}} \frac{F\left(E-E^0\right)}{RT}\right) \\ \Re_{\mathrm{Red}} &= A'_{\mathrm{Red}} \exp\left(\frac{-\Delta_A G_{\mathrm{Red}}}{RT}\right) = A'_{\mathrm{Red}} \exp\left(\frac{-\Delta_A G^0_{\mathrm{Red}}}{RT}\right) \exp\left(-\alpha_{\mathrm{Red}} \frac{F\left(E-E^0\right)}{RT}\right)\end{aligned} \tag{2.34}$$

When expressed in moles of species R consumed per unit catalyst surface per unit time, the net reaction rate can be written as follows

$$\Gamma = C_{\mathrm{R}} K_{\mathrm{Ox}} \exp\left(\alpha_{\mathrm{Ox}} \frac{F\left(E-E^0\right)}{RT}\right) - C_{\mathrm{O}} K_{\mathrm{Red}} \exp\left(-\alpha_{\mathrm{Red}} \frac{F\left(E-E^0\right)}{RT}\right) \tag{2.35}$$

where the constants K_{Ox} and K_{Red} incorporate all the terms that are independent of the potential

$$K_r = A'_r \exp\left(\frac{-\Delta_A G^0_r}{RT}\right), \quad r = \mathrm{Ox},\ \mathrm{Red} \tag{2.36}$$

In general, the reaction constants K_r appearing in (2.35) depend on the temperature T, the reaction being studied and the type of catalyst where the reaction takes place.

To continue the discussion it is convenient now to consider the equilibrium condition. At equilibrium the net reaction rate Γ is zero, since oxidation and reduction occur at the same rate. At this state the potential reaches an equilibrium value, $E^\star$, and the same happens with the concentrations, $C^\star_{\mathrm{R}}$ and $C^\star_{\mathrm{O}}$. From Equation (2.35), at equilibrium the reaction rate of the oxidation and reduction reactions can be written as

$$\Gamma^\star = C^\star_{\mathrm{R}} K_{\mathrm{Ox}} \exp\left(\frac{\alpha_{\mathrm{Ox}} F\left(E^\star-E^0\right)}{RT}\right) = C^\star_{\mathrm{O}} K_{\mathrm{Red}} \exp\left(-\frac{\alpha_{\mathrm{Red}} F\left(E^\star-E^0\right)}{RT}\right) \tag{2.37}$$

Dividing Equation (2.35) by $\Gamma^\star$ and rearranging yields

$$\frac{\Gamma}{\Gamma^\star} = \frac{C_{\mathrm{R}}}{C^\star_{\mathrm{R}}} \exp\left(\frac{\alpha_{\mathrm{Ox}} F\left(E-E^\star\right)}{RT}\right) - \frac{C_{\mathrm{O}}}{C^\star_{\mathrm{O}}} \exp\left(\frac{-\alpha_{\mathrm{Red}} F\left(E-E^\star\right)}{RT}\right) \tag{2.38}$$

This expression for Γ circumvents the difficulty of referring the potential to the standard potential, as it is much simpler to measure the overpotential experimentally. It was Tafel (1905) the first to write the reaction rate in this form, which can also be expressed as

$$\Gamma = \Gamma^\star \left[\frac{C_{\mathrm{R}}}{C^\star_{\mathrm{R}}} \exp\left(\frac{\alpha_{\mathrm{Ox}} F \eta}{RT}\right) - \frac{C_{\mathrm{O}}}{C^\star_{\mathrm{O}}} \exp\left(\frac{-\alpha_{\mathrm{Red}} F \eta}{RT}\right)\right] \tag{2.39}$$

in terms of the overpotential, $\eta = E - E^\star$. This equation is very often written using the

simpler notation

$$\Gamma = C_{\mathrm{R}} k_{\mathrm{Ox}} \exp\left(\frac{\alpha_{\mathrm{Ox}} F \eta}{RT}\right) - C_{\mathrm{O}} k_{\mathrm{Red}} \exp\left(\frac{-\alpha_{\mathrm{Red}} F \eta}{RT}\right) \tag{2.40}$$

in terms of the oxidation and reduction rate constants

$$k_{\mathrm{Ox}} = \frac{\Gamma^\star}{C_{\mathrm{R}}^\star} \quad \text{and} \quad k_{\mathrm{Red}} = \frac{\Gamma^\star}{C_{\mathrm{O}}^\star} \tag{2.41}$$

The net current density generated by the electrochemical redox reaction, expressed in amperes per unit catalyst surface area, can be obtained by multiplying the net reaction rate Γ given in (2.39) by Faraday's constant, resulting in the well-known *Butler-Volmer equation*

$$j = j_0 \left[\frac{C_{\mathrm{R}}}{C_{\mathrm{R}}^\star} \exp\left(\frac{\alpha_{\mathrm{Ox}} F \eta}{RT}\right) - \frac{C_{\mathrm{O}}}{C_{\mathrm{O}}^\star} \exp\left(\frac{-\alpha_{\mathrm{Red}} F \eta}{RT}\right) \right] \tag{2.42}$$

where $j_0 = \Gamma^\star F$ is the so-called *exchange current density*, a fundamental electrochemical property that represents the rate of the oxidation and reduction reactions at equilibrium expressed in terms of current density. It is interesting to note that Butler (1924) and Volmer (Erdey-Gruz & Volmer, 1930) found this equation separately, so the name honors both. Under conditions where the backward reaction can be neglected, e.g., for sufficiently high overpotentials, Eq. (2.42) reduces to the *Tafel equation*, which is written here in exponential form

$$j = F C_{\mathrm{R}} k_{\mathrm{Ox}} \exp\left(\frac{\alpha_{\mathrm{Ox}} F \eta}{RT}\right) \quad \text{or} \quad \eta = \frac{RT}{\alpha_{\mathrm{Ox}} F} \ln j - \frac{RT}{\alpha_{\mathrm{Ox}} F} \ln\left(F C_{\mathrm{R}} k_{\mathrm{Ox}}\right) \tag{2.43}$$

It should be noted that the original *Tafel equation* was written using the decimal logarithm, which yields the factor 2.3 in (2.27)[5].

The current density j appearing in Eqs. (2.27), (2.42) and (2.43) requires further comment. This current density is expressed in amperes per unit catalyst surface area. In order to convert it to amperes per unit volume, as required for evaluating distributed current sources in three dimensional macro-homogeneous models of fuel cell catalysts layers, the current density j has to be multiplied by a geometric factor representing the catalyst surface area per unit volume of catalyst layer. This conversion factor is the so-called *volume-specific catalyst surface area*, often denoted by the letter a in the literature. Integrating the volumetric current density $a\,j$ over the thickness of the catalyst layer at a certain location one obtains the cell current density, hereafter denoted by i, which represents the current generated by the cell per unit surface area of catalyst layer and coincides with the protonic current density crossing the membrane.

[5] $\ln x = \log x / \log e \approx 2.3 \log x$

2.3.1.2 Multiple-step multiple-electron reactions

Electrochemical reactions in fuel cells usually involve more than a single step and more than a single electron transfer. To deal with multi-step reactions involving the transfer of several electrons it is convenient to assume that there exists an elementary step that is significantly slower than the rest, the so-called *rate-determining step* (RDS) of the global reaction. Some authors (Barbir, 2005; Gileadi, 1993) propose the relation

$$\alpha_{\mathrm{Ox}} + \alpha_{\mathrm{Red}} = \frac{n}{\upsilon} \tag{2.44}$$

where n is the total number of electrons transferred and υ is the number of times that the RDS must occur for the overall reaction to occur. Other authors (Fang & Liu, 2014) propose to write the charge transfer coefficient as a function of the overpotential following *Marcus theory*

$$\alpha_{\mathrm{Ox}} = \frac{1}{2}\left(1 + \frac{F\eta}{\lambda}\right) \tag{2.45}$$

where the parameter λ is referred to as the *reorganization energy*, defined as the energy required to change the nuclear configurations (Marcus, 1956)[6].

Nevertheless, a closer look at the reactions involved in the whole process will give us a better understanding. For a general electrochemical reaction of the form

$$\mathrm{R} \rightleftharpoons \mathrm{O} + \mathrm{ne}^- \tag{2.46}$$

the reaction mechanism could be divided is three parts: the reactions before the RDS

$$\mathrm{R} \rightleftharpoons \mathrm{R}' + n' e^- \tag{2.47}$$

the RDS itself

$$\mathrm{R}' \rightleftharpoons \mathrm{O}' + \quad e^- \tag{2.48}$$

and the reactions after the RDS

$$\mathrm{O}' \rightleftharpoons \mathrm{O} + n'' e^- \tag{2.49}$$

As the RDS acts effectively as a bottle-neck for the multi-step reaction process, the reaction rate of the global reaction will be given in first approximation by that of the RDS. Applying

[6]Rudolph A. Markus received the 1992 Nobel Prize in Chemistry "for his contributions to the theory of electron transfer reactions in chemical systems". A extended review of Markus theory is presented in his review (Marcus, 1964). An extension to organic reactions is presented in Marcus & Sutin (1985).

Equation (2.40) to the RDS, the following expression is obtained

$$\Gamma = C_{\mathrm{R}'} k_{\mathrm{Ox}}^{\mathrm{RDS}} \exp\left(\frac{\alpha_{\mathrm{Ox}}^{\mathrm{RDS}} F\left(E - E^{\star\mathrm{RDS}}\right)}{RT}\right) - C_{\mathrm{O}'} k_{\mathrm{Red}}^{\mathrm{RDS}} \exp\left(\frac{-\alpha_{\mathrm{Red}}^{\mathrm{RDS}} F\left(E - E^{\star\mathrm{RDS}}\right)}{RT}\right) \tag{2.50}$$

Pre- and post-RDS reactions take place significantly faster than the RDS. As a result, the concentration of the intermediate compounds (namely R' and O') can be approximated by the equilibrium values obtained from the pre- and post-RDS reactions, respectively. Combining Equation (2.40) and the equilibrium condition ($\Gamma = 0$) applied to the pre- and post-RDS reactions, expressions for the concentration of the intermediate compounds in terms of the initial and final products (R and O) can be obtained

$$\begin{aligned} C_{\mathrm{R}'} &= C_{\mathrm{R}} \frac{k'_{\mathrm{Ox}}}{k'_{\mathrm{Red}}} \exp\left(\frac{\left(\alpha'_{\mathrm{Ox}} + \alpha'_{\mathrm{Red}}\right) F\left(E - E'^{\star}\right)}{RT}\right) \\ C_{\mathrm{O}'} &= C_{\mathrm{O}} \frac{k''_{\mathrm{Red}}}{k''_{\mathrm{Ox}}} \exp\left(\frac{-\left(\alpha''_{\mathrm{Ox}} + \alpha''_{\mathrm{Red}}\right) F\left(E - E''^{\star}\right)}{RT}\right) \end{aligned} \tag{2.51}$$

Substituting these expressions in Equation (2.50) yields the following expression for the reaction rate of the multi-step electrochemical reaction

$$\begin{aligned} \Gamma = C_{\mathrm{R}} \frac{k_{\mathrm{Ox}}^{\mathrm{RDS}} k'_{\mathrm{Ox}}}{k'_{\mathrm{Red}}} \exp\left(\left[-\left(\alpha'_{\mathrm{Ox}} + \alpha'_{\mathrm{Red}}\right) E'^{\star} + \alpha^{\mathrm{RDS}} E^{\mathrm{RDS}\star}\right] \frac{F}{RT}\right) \\ \times \exp\left(\left(\alpha'_{\mathrm{Ox}} + \alpha'_{\mathrm{Red}} + \alpha_{\mathrm{Ox}}^{\mathrm{RDS}}\right) E \frac{F}{RT}\right) \\ - C_{\mathrm{O}} \frac{k_{\mathrm{Red}}^{\mathrm{RDS}} k''_{\mathrm{Red}}}{k''_{\mathrm{Ox}}} \exp\left(\left[\left(\alpha''_{\mathrm{Ox}} + \alpha''_{\mathrm{Red}}\right) E''^{\star} - \beta^{\mathrm{RDS}} E^{\mathrm{RDS}\star}\right] \frac{F}{RT}\right) \\ \times \exp\left(-\left(\alpha''_{\mathrm{Ox}} + \alpha''_{\mathrm{Red}} + \alpha_{\mathrm{Red}}^{\mathrm{RDS}}\right) E \frac{F}{RT}\right) \end{aligned} \tag{2.52}$$

The above expression involves absolute potentials, which can not be readily measured. In order to express the overall reaction rate Γ in a more convenient way, the first and second terms can be multiplied by the unit factors

$$\exp\left(\left(\alpha'_{\mathrm{Ox}} + \alpha'_{\mathrm{Red}} + \alpha_{\mathrm{Ox}}^{\mathrm{RDS}}\right) \frac{F\left(E^{\star} - E^{\star}\right)}{RT}\right)$$

$$\text{and} \quad \exp\left(\left(\alpha''_{\mathrm{Ox}} + \alpha''_{\mathrm{Red}} + \alpha_{\mathrm{Red}}^{\mathrm{RDS}}\right) \frac{F\left(E^{\star} - E^{\star}\right)}{RT}\right) \tag{2.53}$$

where $E^{\star}$ denotes the equilibrium potential of the complete reaction. This results in the

following expression

$$\Gamma = C_{\mathrm{R}} \overbrace{\frac{k_{\mathrm{Ox}}^{\mathrm{RDS}} k'_{\mathrm{Ox}}}{k'_{\mathrm{Red}}} \exp\left(\left[-\left(\alpha'_{\mathrm{Ox}} + \alpha'_{\mathrm{Red}}\right)\left(E'^{\star} - E^{\star}\right) + \alpha_{\mathrm{Ox}}^{\mathrm{RDS}}\left(E^{\mathrm{RDS}\star} - E^{\star}\right)\right]\frac{F}{RT}\right)}^{k_{\mathrm{Ox}}} \times \exp\left(\overbrace{\left(\alpha'_{\mathrm{Ox}} + \alpha'_{\mathrm{Red}} + \alpha_{\mathrm{Ox}}^{\mathrm{RDS}}\right)}^{\alpha_{\mathrm{Ox}}} \frac{F\left(E - E^{\star}\right)}{RT}\right) - C_{\mathrm{O}} \underbrace{\frac{k_{\mathrm{Red}}^{\mathrm{RDS}} k''_{\mathrm{Red}}}{k''_{\mathrm{Ox}}} \exp\left(\left[\left(\alpha''_{\mathrm{Ox}} + \alpha''_{\mathrm{Red}}\right)\left(E''^{\star} - E^{\star}\right) + \alpha_{\mathrm{Red}}^{\mathrm{RDS}}\left(E^{\mathrm{RDS}\star} - E^{\star}\right)\right]\frac{F}{RT}\right)}_{k_{\mathrm{Red}}} \times \exp\left(-\underbrace{\left(\alpha''_{\mathrm{Ox}} + \alpha''_{\mathrm{Red}} + \alpha_{\mathrm{Red}}^{\mathrm{RDS}}\right)}_{\alpha_{\mathrm{Red}}} \frac{F\left(E - E^{\star}\right)}{RT}\right) \quad (2.54)$$

which can be rewritten as Equation (2.40) by introducing the overpotential η to give

$$\Gamma = C_{\mathrm{R}} k_{\mathrm{Ox}} \exp\left(\frac{\alpha_{\mathrm{Ox}} F \eta}{RT}\right) - C_{\mathrm{O}} k_{\mathrm{Red}} \exp\left(-\frac{\alpha_{\mathrm{Red}} F \eta}{RT}\right) \quad (2.55)$$

The above discussion demonstrates how is it possible to define global charge transfer coefficients, α_{Ox} and α_{Red}, and rate constants, k_{Ox} and k_{Red}, for the overall electrochemical reaction from those of the elementary reaction steps. This technique provides a powerful tool for the analysis of complex electrochemical systems, such as the multi-step ethanol oxidation reaction to be discussed in Chapter 3. As will be seen, the introduction of global kinetic parameters for certain reaction paths will be particularly useful when trying to fit the kinetic constants to the selectivities of the final products.

2.3.2 Coverage factors

The electrochemical reactions that take place in a fuel cell need not only to occur, but also to have a sufficiently high reaction rate. To provide a favourable environment for the reactions, catalysts are always used in fuel cells. A catalyst is a compound that favors the chemical reaction but it is not involved in it. The catalyst acts as substrate for the reaction, in that its surface has *places* where the fuel molecules *take place* to proceed with the reaction. In fuel cells catalyst are pinned up to a porous matrix. The process where the reactive molecules *take place* at the catalyst sites is called adsorption. Once the molecules have been adsorbed they no longer behave as free molecules; they remain attached to the catalyst site. The so-called adsorbates may undergo electrochemical reaction and be desorbed as reaction products or, eventually, be desorbed as unreacted free molecules.

The catalyst act as an anchor to the adsorbed species. The concentration of these species have no physical meaning because they fill spaces where there are catalyst places;

actually they *cover* the catalyst surface. This behavior is equivalent to the adsorption described by Langmuir (1918) for the atomic deposition over glass surfaces. The amount of absorbed specie is thus described by the *surface coverage factor*, Θ, which represents the fraction of the catalyst sites occupied by this specie.

The coverage factor of a given species cannot be larger than unity (full coverage of the catalyst places). And if different species can be adsorbed into the same catalyst type, the sum of their coverage factors cannot exceed unity either

$$\sum_k \Theta_k \leq 1 \tag{2.56}$$

From the definition of the coverage factors, the fraction of free catalyst sites is given by

$$\Theta_F = 1 - \sum_k \Theta_k \tag{2.57}$$

Using these expressions it is possible to evaluate the net adsorption rate of species k. The adsorption rate is proportional to the available catalyst sites, while the desorption rate is proportional to the fraction of occupied sites, so that

$$q_k = \Re_{ads}\Theta_F - \Re_{des}\Theta_k \tag{2.58}$$

where the proporcionality constants $\Re_{ads}$ and $\Re_{des}$ depend on the kind of absorption mechanism. Langmuir (1918) applied this model to the adsorption of a mono atomic layer in a flat surface (e.g., glass); in electrochemical reactions, the absorption/desorption processes often involve reactions with charge transfer. In these cases the adsorbed species is not the same as the free specie, but Equation (2.58) can still be used with the required modifications. The use of coverage factors in kinetic models of catalityc reactions is widely used in fuel cell modeling (Kauranen *et al.*, 1996; Meyer *et al.*, 2011; Nordlund & Lindbergh, 2002; Shivhare *et al.*, 2006, 2007; Sundmacher *et al.*, 2001; Suresh & Jayanti, 2011).

As previously discussed, the reaction rates of the forward and backward reactions are proportional to the molar concentrations of reactants and products, respectively. When an adsorbed species is involved its concentration is equal to the coverage factor of the adsorbate times the concentration C_c of the catalyst

$$C_k = \Theta_k C_c \tag{2.59}$$

where C_c remains unchanged during the reaction. As a result, for adsorption/desorption reactions the catalyst concentration is usually included in the reaction constants, which are also strongly affected by the catalysts type.

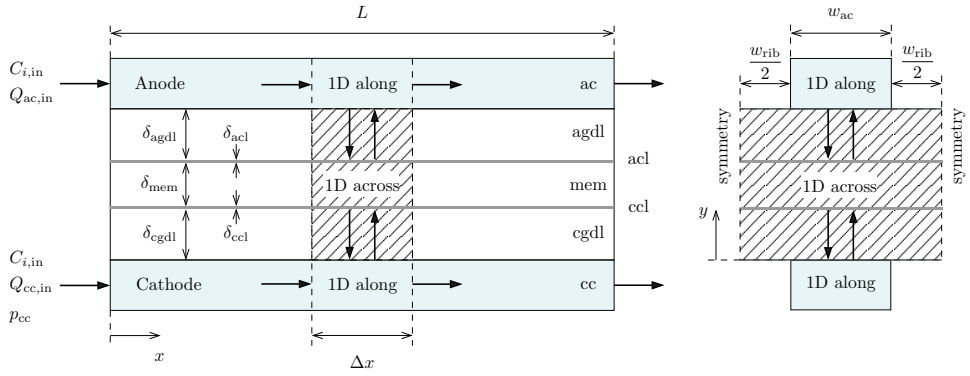

Figure 2.2: Schematic representation showing the different regions of a PEMFC and highlighting the physical domain covered by the across-the-channel and the along-the-channel models. Left: side view; right: cross-sectional view.

2.4 Mass transport in fuel cells

For the continuous operation of a fuel cell, the fuel and the oxidant must be supplied steadily to the electrodes at the same time as the products are removed. The transport phenomena that take place within the cell are of various types due to the heterogeneity of the media composing the flow channels and the MEA. Thus, transport in the channels is dominated by downstream convection and transverse diffusion, while transport in the MEA occurs mainly by Fickian and/or Knudsen diffusion and capillary transport. Figure 2.2 shows an schematic representation of the domains dominated by along-the-channel convection or across-the-channel diffusive and capillary transport.

2.4.1 Flow channels

In the flow channels, the chemical species are transported by a multicomponent (often two-phase) mixture. The mixture is convected downstream under a favorable pressure gradient established by the auxiliary pumping system while interchanging species with the gas diffusion layer across their common interface.

The molar flux of the free species k transferred by convection and diffusion from the bulk fluid to the flow channel/gas diffusion layer interface can be modeled, in first approximation, by means of an overall mass transport coefficient h (Andreadis *et al.*, 2006; Sousa *et al.*, 2008)

$$N_k = -h\left(C_{k,\text{ac}} - C_{k,\text{ac/agdl}}\right) \tag{2.60}$$

where $C_{k,\text{ac}}$ represents the bulk concentration of species k in the anode channel, and $C_{k,\text{ac/agdl}}$ is the concentration of species k at the ac/agdl interface. According to the sign

convention established in Fig. 2.2, the sign of N_k indicates whether the net molar flux of species k is directed in the positive or negative y-direction, with $N_k > 0$ indicating that species k is transported from the catalyst layer to the flow channel, while for $N_k < 0$ it goes from the channel to the gdl.

2.4.2 Porous layers

Different types of porous media are used in the design and construction of PEM fuel cells. It is not only the gas diffusion layers, but also the catalytic layers, as well as the microporous layers added for improved water management. These porous media provide pathways for reactant access and product removal, as well as high electronic and thermal conduction (García-Salaberri *et al.*, 2014). Carbon-based macroporous substrates made of carbon paper or woven cloth are often given hydrophobic treatments using fluorinated polymers such as PTFE to improve water management, while a certain ionomer and catalyst loading must be incorporated to the micro-porous catalyst layer to enable the electrochemical reactions.

As previously discussed, in their flow through the fuel cell the chemical species are mixed with each other. At the cathode side, the oxidant is usually air, so oxygen and nitrogen are introduced into the cell accompanied by water vapor, required for a proper membrane humidification. At the anode side there are two alternatives: hydrogen and liquid-feed direct alcohol fuel cells. In hydrogen fuel cells, a mixture of hydrogen and water vapor is supplied. In liquid-feed DAFCs an alcohol water solution is used. The products species generated are also evacuated in those streams. At the cathode side the only product is water. At the anode side, each kind of fuel cell behaves different. While in hydrogen fuel cells there is no product at the anode reaction, in liquid-feed DAFCs, the electrooxidation of the alcohols produce various carbon compounds that have to be evacuated as dilute species.

Early PEM fuel cell models assumed single-phase flow (Springer *et al.*, 1991). This assumption simplifies the description of mass transport to a large extent and has been widely used both for academic (Barbir, 2005; O'Hayre *et al.*, 2006) and research purposes (Vera, 2007). Multiphase formulations were the natural evolution of PEM fuel cell models (Wang, 2004; Wang & Cheng, 1996). This approach results in significantly more complex formulations and requires a thorough understanding of the processes to be described (García-Salaberri *et al.*, 2015*a*,*b*, 2017; Gostick *et al.*, 2010). The aim of this thesis is to use simplified models to study the multi-step ethanol oxidation reaction in DEFCs and the stability of PEMFC single cell response at different temperatures and relative humidities of the feed streams. As a result, multiphase models are not going to be considered.

In first approximation, the species mass flux in the porous media can be split in a diffusive and a convective flux

$$N_k = \rho v C_k - \rho D_{k,x}^{\text{eff}} \frac{\partial C_k}{\partial y} \tag{2.61}$$

where ρ is the fluid density, v is the y-component of the (superficial) fluid velocity and $D^{\text{eff}}_{k,\text{x}}$ is the effective diffusion coefficient of species k in the porous media. The subscript x indicates the fluid where the diffusive process occur, either air for the cathode electrode or water for the anode in liquid-feed DAFCs. The advective term is usually neglected in single-phase gas models, as when modeling the anode of hydrogen PEMFCs. However, it must be retained in liquid-feed DAFC models due to the water drag effect (Andreadis & Tsiakaras, 2006) produced by water consumption at the catalyst layer and by the crossover flux of water that crosses the membrane.

Diffusive transport in porous media has been widely studied in the literature. The porosity of the porous medium ϵ is known to have a direct impact on the effective diffusion coefficient, with the famous Bruggeman (1935) correction stating that the effective diffusion varies with the porosity to the $3/2$. However, in the last years several studies have shown that the effective diffusivity is strongly affected as well by the nature of the porous structure (e.g., granular vs. fibrous) and by the presence of multiphase flow (García-Salaberri *et al.*, 2015*a*,*b*; Gostick *et al.*, 2006, 2010). Recent modeling studies account also for the anisotropic character of fibrous porous media by incorporating an orthotropic effective diffusivity tensor with different effective diffusivities in the in- and through-plane directions (García-Salaberri & Vera, 2016).

A novel approach to the analysis of multiphase flow in porous media is the pore network method (Blunt, 2001). Although initially applied to geologic porous media such as granular soils or reservoir rocks (Fatt, 1956), these methods have been successfully adapted to the fibrous nature of gas diffusion layers in the last decade (Chapuis *et al.*, 2008; Gostick, 2013; Gostick *et al.*, 2007). Pore network models consider the porous media as a web of pores interconnected by throats with appropriate size distributions. Initially, the network parameters were determined by calibration to experimental gas permeability and drainage capillary pressure data. But more recently the morphology of real porous layers has been incorporated by using pore and throat size distributions and their connectivity obtained from X-ray micro-tomography (Agaesse *et al.*, 2016). The method provides an inhomogeneous liquid water distribution that agrees well with percolation models.

2.4.3 Model dimensions

Fuel cells have an intricate three-dimensional (3D) structure. Therefore, 3D models should be used for an accurate description of these devices. However, the complexity of their implementation and the large computational cost of the numerical integrations have forced researchers to look for simplifications. As previously discussed, in fuel cells two major transport directions appear: (i) transport along the channels and (ii) transport across the channels (i.e., across the MEA), and in some cell geometries those two problems can be readily uncoupled.

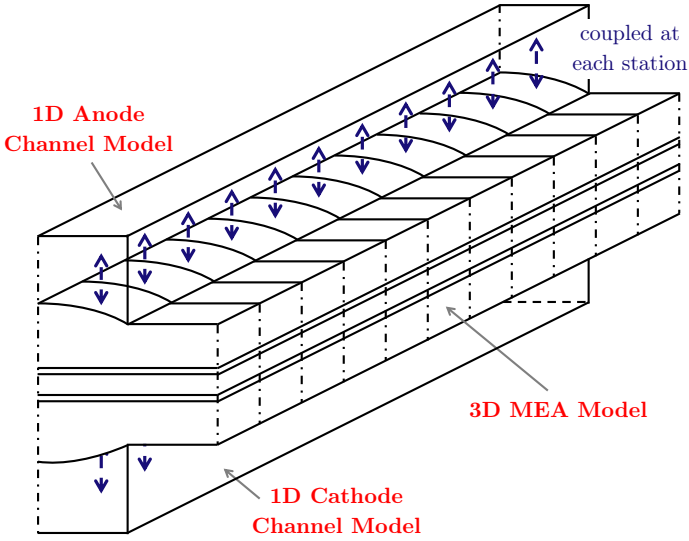

Figure 2.3: Schematic representation of the along-the-channel discretization coupled to across-the-channel slices (García-Salaberri & Vera, 2016)

along the channels Transport processes on the channels are dominated by downstream (liquid or gaseous) advection. As a result of the typically large Peclet numbers of the flow, the variation of the reactant concentrations is significantly smaller in the streamwise direction than in the transverse direction. As a result, in many fuel cell models the channels are divided into elemental channel elements, or *stations*, where the concentrations are assumed to be uniform and, then, the successive stations are connected by a finite volume model (García-Salaberri & Vera, 2016; Wang & Wang, 2003; Yang & Zhao, 2007). This approach requires to solve multiple across-the-channel problems as the flow is evolved downstream. Figure 2.3 shows, for instance, the scheme use by García-Salaberri & Vera (2016). The coupling between anode and cathode can be a challenging task for complicated flow field geometries, such as multi-serpentine co-/counter-flow configurations (Fig. 1.4). In addition, if there is are large pressure differences between contiguous channels, *under rib convection* may play a role (Feser *et al.*, 2006; García-Salaberri & Vera, 2015) that is not easy to take into account.

igure 1.13: Contact pressure distribution at the rib-GDL (top) and membrane-GDL (bottom) inter-ces corresponding to the three simulations shown in Fig. **??**. The inset (a) shows a close-up view of he contact pressure at the membrane-GDL interface in the region below the channel. Note the inverse ertical scale of the lower plot.

across the channels The channel-rib pattern used in conventional fuel cell designs has a direct impact on across-the-channel mass transport processes. Due to the presence of the ribs, the gas diffusion layer interacts with the channels through a significantly narrower surface than with the membrane. Several models use a two-dimensional (2D) approach to retain this effect (García-Salaberri *et al.*, 2014). However, 2D models are still computationally expensive and could still be simplified by means of

quasi-potential transformations based on conformal mapping (Weber & Newman, 2009). Another attempt to incorporate 2D geometry effects in purely 1D models based on the concept of *spatial smoothing* has been recently proposed by Ly *et al.* (2012).

2.5 Transport in the membrane

2.5.1 The membrane water content λ

Charge transport through PEM membranes is based in the water adsorption of the sulfonic groups ($R-S(=O)_2-OH$) which allows the protons H^+ to move freely in the hydrated regions (Jiao, 2011; Jiao & Li, 2011; Kusoglu & Weber, 2017; Weber & Newman, 2004*a*; Zawodzinski *et al.*, 1995). The hydration level of the membrane is characterized by the membrane water content λ, defined as the number of water molecules per sulfonic group

$$\lambda = \frac{\mathrm{EW}_{\mathrm{mem}}}{\rho_{\mathrm{mem}}} C_{\mathrm{W}} \tag{2.62}$$

where ρ_{mem} is the membrane dry (i.e., ionomer) density, and $\mathrm{EW}_{\mathrm{mem}}$ is the so-called membrane equivalent weight, defined as the membrane dry mass divided by the number of sulfonic places (i.e., moles of SO_3^-).

During water absorption the properties of the membrane change appreciably, and in particular the protonic conductivity. Weber & Newman (2004*a*) and Kusoglu & Weber (2017) illustrated it graphically as shown in Fig. 2.4. Under dry conditions, the water molecules are concentrated into the sulfonic sites (a). As water is absorbed by the membrane, water clusters start to grow around the sulfonic sites and cause an increase of the water mobility (b). Nearby clusters connect as the water uptake continues. This effect creates preferential paths and generates a percolation type transport web. When the membrane is highly hydrated a complete network is formed between the clusters (c). When liquid water is in contact with the membrane, it infiltrates and expands the channels, thereby stabilizing the formed paths (d). As the channel network is completely filled with liquid water, water uptake increases without any change in the water chemical potential. This phenomena is the so-called Schroeder paradox (Kusoglu & Weber, 2017; von Schroeder, 1903; Weber & Newman, 2004*a*).

2.5.2 Modeling membrane water transport

Although the transport of water through the membrane is related to inhomogeneous changes in its microscopic structure, macro-homogeneous models have been found to be suitable for the description of these changes at the macroscopic level (Kusoglu & Weber, 2017; Weber & Newman, 2003, 2004*b*,*c*).

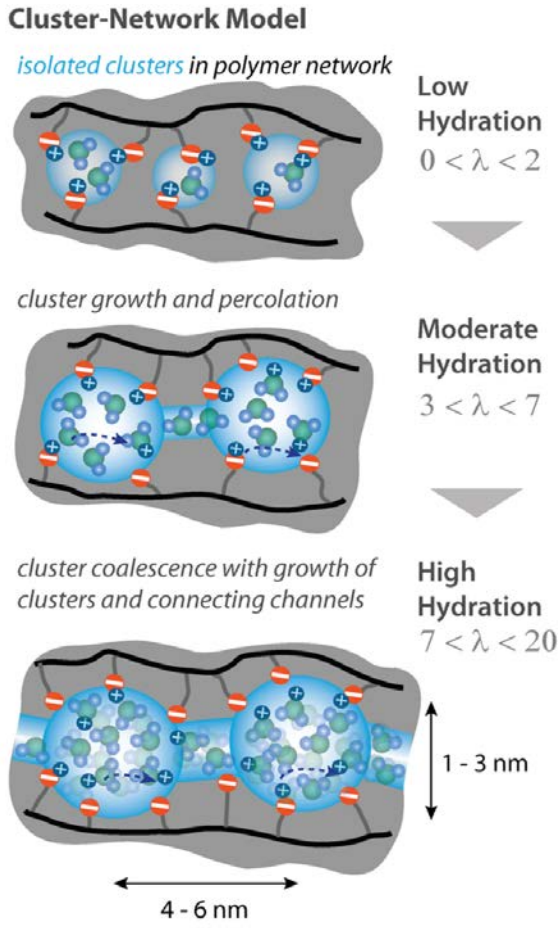

Figure 2.4: Schematic representation of the membrane hydration states due to Kusoglu & Weber (2017). As the membrane water content λ is gradually increased, water clusters grow in size and in connections by saturated channels greatly facilitating H^+ movements through the web.

Water transport through the membrane is due to two main effects, electrooosmotic drag (EOD) and back diffusion. Hydraulic permeation due to pressure gradients can also occur but will not be addressed here because it can typically be neglected due to the small pressure differences between anode and cathode. EOD occurs when the protons drag water molecules in their movement through the membrane. It can be assimilated to a convective transport of water proportional to the proton flux that pulls water from anode to cathode. By contrast, back-diffusion is an ordinary diffusive process that takes water back from cathode to anode due to the fact that water is only generated at the cathode and therefore its concentration is higher there. Mathematically, water transport

can be expressed as

$$N_{\mathrm{w}} = \underbrace{\mathrm{n_d^w}(\lambda, \mathrm{T})\,\mathrm{i}}_{\text{EOD}} \quad \underbrace{- \frac{\rho_{\mathrm{mem}} w_{\mathrm{ion}}}{\mathrm{EW_{mem}}} D_{\mathrm{mem}}^{\mathrm{eff}}(\lambda, T)\frac{\partial \lambda}{\partial y}}_{\text{Back diffusion}} \tag{2.63}$$

The EOD flux is due to the water molecules dragged by the protonic current i. It is calculated with the EOD coefficient $\mathrm{n_d^w}$, which represents the number of water molecules dragged by a proton moving through the membrane. Its value is usually between one, for membranes in contact with water vapor, and 2.5 for membranes in contact with liquid water. It depends both on the membrane water content λ and on the temperature T (Ge *et al.*, 2005; Kulikovsky, 2003; Springer *et al.*, 1991; Weber & Newman, 2003; Zawodzinski *et al.*, 1995, 1993; Zhao *et al.*, 2011). The diffusion term is proportional to the gradient of the water concentration in the membrane and to the non-linear diffusion coefficient $D_{\mathrm{mem}}^{\mathrm{eff}}$, which is also a function of λ and T. Note that the variation of the diffusion coefficient with λ is a result of the microstructural changes that occur during the membrane water uptake process, as previously shown in Fig. 2.4 (Ge *et al.*, 2005; Kulikovsky, 2003; Springer *et al.*, 1991; Zawodzinski *et al.*, 1995, 1993; Zhao *et al.*, 2011). As shown by Eq. (2.63), the EOD flux is proportional to the current density and to the EOD coefficient, so it has to be considered at either at high current densities (high i) or in liquid-feed direct alcohol feed cells (high $\mathrm{n_d^w}$). On the other hand, back diffusion arises when there is a large gradient of λ through the membrane, which is often the case in partially humidified PEMFCs.

2.5.3 Water absorption/desorption

The membrane water uptake occurs at the membrane interface exposed to gas or liquid water. In a fuel cell MEA, this frontier is not a clear surface but a fractal-like structure that expands across the catalyst layers. In these layers there is a coexistence of catalysts particles (Pt, Ru, Sn, etc.), electronic conductor (carbon fibers typically), ionomer (as in the membrane) and void space. This is the required combination that enables the oxidation and reduction reactions, ensuring separated electron and proton fluxes and appropriate fuel supply and product removal (see Fig. 1.1 for details). As a result, water sorption and desorption takes place at the diffuse ionomer interface at a rate given by

$$S_{\mathrm{sd}} = \begin{cases} k_{\mathrm{s}} \dfrac{\rho_{\mathrm{mem}}}{\mathrm{EW_{mem}}} \left(\lambda_{\mathrm{eq}} - \lambda\right) \text{for} & \lambda < \lambda_{\mathrm{eq}} \\ k_{\mathrm{d}} \dfrac{\rho_{\mathrm{mem}}}{\mathrm{EW_{mem}}} \left(\lambda_{\mathrm{eq}} - \lambda\right) \text{for} & \lambda \geq \lambda_{\mathrm{eq}} \end{cases} \tag{2.64}$$

where k_{s} and k_{d} are the sorption and desorption rate constants (Ge *et al.*, 2005) and the driving force is the difference between the equilibrium (λ_{eq}) and actual (λ) membrane

water content; the former given by Springer *et al.* (1991) as

$$\lambda_{\text{eq}} = \begin{cases} 0.04 + 17.81a - 39.85a^2 + 36.0a^3 \text{for} & \text{a} \leq 1 \\ 14 + 1.4(a-1) \text{for} & \text{a} > 1 \end{cases} \tag{2.65}$$

in terms of the water activity

$$a = \frac{p_{\text{H}_2\text{O}}}{p_{\text{H}_2\text{O,sat}}} + 2s \tag{2.66}$$

written here as the sum of two terms, the first one representing the relative humidity of the gas supply and the second one accounting for the presence of liquid water as two times the water saturation s (Jiao & Li, 2011). More recently, Liu *et al.* (2009) proposed a different correlation

$$\lambda_{\text{eq}} = \begin{cases} \left[1 + 0.2a^2\left(\frac{T-303.1}{30}\right)\right]\left(13.4a - 18.9a^2 + 14.2a^3\right) \text{for} & \text{a} \leq 1 \\ \lambda_{\text{eq}}|_{a=1} + 6\,(a + 2s - 1) \text{for} & \text{a} > 1 \end{cases} \tag{2.67}$$

2.6 Conclusions

In this chapter, the operating principles of polymer electrolyte membrane fuel cells have been reviewed, with a focus on electrochemical kinetics, mass transport processes and membrane water content. First, a detailed description of the kinetic modeling of single- and multi-step electrochemical reactions has been presented, as theoretical background for the reaction rate expressions to be used in Chapter 3 for the ethanol electrooxidation reaction. Mass transport in fuel cells involves a bunch of intertwined physical mechanism whose precise description requires exceedingly complex numerical models. Nonetheless, under some conditions, several simplifications can be adopted to clear up models when transport is not the dominant phenomena, e.g., direct alcohol fuel cells; where the alcohol electrooxidation reactions leads the cell performances. Membrane properties are directly related to the membrane water contain. Absorption/desorption process is determined not only by the relative humidity of the inlet supplies but also by the current density.

Nomenclature

Symbols

a_k	activity of specie k
C_k	molar concentration of specie k[mol m^{-3}]
$D_{k,\text{x}}$	molecular diffusivity of species k in media x [m^2 s^{-1}]
E	electric potential [V]
EW	equivalent weight [kg mol^{-1}]

F	Faraday constant $F = 96480$ C
h	molar enthalpy [J mol^{-1}]
H	enthalpy [J]
g	molar Gibbs free energy [J mol^{-1}]
G	Gibbs free energy [J]
I	electric current [I]
i	electric current density [I m^{-2}]
j	electric current density per catalyst surface [I m^{-2}]
n	number electrons transferred
N_k	molar flux of specie k [mol m^{-2} s^{-1}]
p_k	pressure of specie k [Pa]
Q	heat [W]
s	molar entropy [J K^{-1}mol^{-}1]
S	entropy [J K^{-1}]
T	temperature [K]
V	electric voltage [V]
v	fluid velocity [m s^{-1}]
w_{ion}	ionomer fraction
W_e	Electric work [W]

Greek letters

α	charge transfer coefficient
Γ	volumetric molar rate of reaction [mol m^{3}s^{-1}]
η	overpotential $\eta = E - E^\star$ [V]
Θ_k	coverage factor of specie k
λ	membrane water content
μ_k	chemical potential of specie k
ρ	density [kg m^3]
υ_k	stoichiometric coefficient specie k[0.35cm] ***Subscripts***
ac	anode channel
ac/agdl	anode channel/gdl interface
agdl	anode gas diffusion layer
cc	cathode channel
cc/cgdl	cathode channel/gdl interface
cgdl	cathode gas diffusion layer
e	electric
eff	effective property
ion	ionomer
f	formation
k	specie
Ox	oxidation reaction
mem	membrane

r	reaction
Red	reduction reaction
x	media x
w	water

Superscripts

0	reference state conditions
$\star$	equilibrium state conditions

References

AGAESSE, T., LAMIBRAC, A., BÜCHI, F. N., PAUCHET, J. & PRAT, M. 2016 Validation of pore network simulations of ex-situ water distributions in a gas diffusion layer of proton exchange membrane fuel cells with X-ray tomographic images. *J. Power Sources* **331**, 462–474.

AKHAIRI, M. A. F. & KAMARUDIN, S. K. 2016 Catalysts in direct ethanol fuel cell (DEFC): An overview. *Int. J. Hydrogen Energy* **41** (7), 4214–4228.

ANDREADIS, G. M., SONG, S. & TSIAKARAS, P. E. 2006 Direct ethanol fuel cell anode simulation model. *J. Power Sources* **157** (2), 657–665.

ANDREADIS, G. M. & TSIAKARAS, P. E. 2006 Ethanol crossover and direct ethanol PEM fuel cell performance modeling and experimental validation. *Chem. Eng. Sci.* **61** (22), 7497–7508.

ANTOLINI, E. 2007 Catalysts for direct ethanol fuel cells. *J. Power Sources* **170** (1), 1–12.

ANTONIASSI, R. M., OLIVEIRA NETO, A., LINARDI, M. & SPINACÉ, E. V. 2013 The effect of acetaldehyde and acetic acid on the direct ethanol fuel cell performance using PtSnO2/C electrocatalysts. *Int. J. Hydrogen Energy* **38** (27), 12069–12077.

ARCHER, M. D. 1989 Genesis of the Nernst Equation. *Electrochem. Past Present* (1883), 115–126.

ARRHENIUS, S. 1889 Über die Dissociationswärme und den Einfluss der Temperatur auf den Dissociationsgrad der Elektrolyte. *Zeitschrift für Phys. Chemie* **4** (1).

ATKINS, P. & DE PAULA, J. 2010 *Atkins' Physical Chemistry*, 9th edn. Oxford University Press.

BACH DELPEUCH, A., MAILLARD, F., CHATENET, M., SOUDANT, P. & CREMERS, C. 2016 Ethanol oxidation reaction (EOR) investigation on Pt/C, Rh/C, and Pt-based bi- and tri-metallic electrocatalysts: A DEMS and in situ FTIR study. *Appl. Catal. B Environ.* **181**, 672–680.

BACK, M. H. & LAIDLER, K. J. 2013 *Selected readings in chemical kinetics*. Elsevier.

BARBIR, F. 2005 *PEM Fuel Cells: Theory and practice*. Elsevier Academic.

BARD, A. J. & FAULKNER, L. R. 2001 *Electrochemical methods: fundamentals and applications*. Wiley.

BLUNT, MARTIN J. 2001 Flow in porous media — pore-network models and multiphase flow. *Curr. Opin. Colloid Interface Sci.* **6** (3), 197–207.

BRAUNCHWEIG, B., HIBBITTS, D., NEUROCK, M. & WIECKOWSKI, A. 2013 Electrocatalysis: A direct alcohol fuel cell and surface science perspective. *Catal. Today* **202** (1), 197–209.

BROUZGOU, A., PODIAS, A. K. M. & TSIAKARAS, P. 2013 PEMFCs and AEMFCs directly fed with ethanol: A current status comparative review. *J. Appl. Electrochem.* **43** (2), 119–136.

BRUGGEMAN, D. A. G. 1935 Berechnung verschiedener physikalischer Konstanten von heterogenen Substanzen. I. Dielektrizitätskonstanten und Leitfähigkeiten der Mischkörper aus isotropen Substanzen. *Ann. Phys.* **416** (7), 636–664.

BUTLER, J. A. V. 1924 Studies in heterogeneous equilibria. Part II.—The kinetic interpretation of the nernst theory of electromotive force. *Trans. Faraday Soc.* **19** (March), 729–733.

CHAPUIS, O., PRAT, M., QUINTARD, M., CHANE-KANE, E., GUILLOT, O. & MAYER, N. 2008 Two-phase flow and evaporation in model fibrous media. *J. Power Sources* **178** (1), 258–268.

COLMATI, F., ANTOLINI, E. & GONZALEZ, E. R. 2006 Effect of temperature on the mechanism of ethanol oxidation on carbon supported Pt, PtRu and Pt$_3$Sn electrocatalysts. *J. Power Sources* **157** (1), 98–103.

ERDEY-GRUZ, T. & VOLMER, M. 1930 Zur theorie der wasserstoff{ü}berspannung. *Z. Phys. Chem.* **150**, 203.

FANG, Y.-H. & LIU, Z.-P. 2014 Tafel Kinetics of Electrocatalytic Reactions: From Experiment to First-Principles. *ACS Catal.* **4** (12), 4364–4376.

FATIH, K., NEBURCHILOV, V., ALZATE, V., NEAGU, R. & WANG, H. 2010 Synthesis and characterization of quaternary PtRuIrSn/C electrocatalysts for direct ethanol fuel cells. *J. Power Sources* **195** (21), 7168–7175.

FATT, I. 1956 The Network Model of Porous Media. *Pet. Trans. AIME* **207**, 144–181.

FESER, J.P., PRASAD, A.K. & ADVANI, S.G. 2006 On the relative influence of convection in serpentine flow fields of PEM fuel cells. *J. Power Sources* **161** (1), 404–412.

GARCÍA-SALABERRI, P. A., GOSTICK, J. T., HWANG, G., WEBER, A. Z. & VERA, M. 2015*a* Effective diffusivity in partially-saturated carbon-fiber gas diffusion layers: Effect of local saturation and application to macroscopic continuum models. *J. Power Sources* **296**, 440–453.

GARCÍA-SALABERRI, P. A., HWANG, G., VERA, M., WEBER, A. Z. & GOSTICK, J. T. 2015*b* Effective diffusivity in partially-saturated carbon-fiber gas diffusion layers: Effect of through-plane saturation distribution. *Int. J. Heat Mass Transf.* **86**, 319–333.

GARCÍA-SALABERRI, P. A., SÁNCHEZ, D. G., BOILLAT, P., VERA, M. & FRIEDRICH, K. A. 2017 Hydration and dehydration cycles in polymer electrolyte fuel cells operated with wet anode and dry cathode feed: A neutron imaging and modeling study. *J. Power Sources* **359**, 634–655.

GARCÍA-SALABERRI, P. A. & VERA, M. 2015 On the effects of assembly compression on the performance of liquid-feed DMFCs under methanol-limiting conditions: A 2D numerical study. *J. Power Sources* **285**, 543–558.

GARCÍA-SALABERRI, P. A. & VERA, M. 2016 On the effect of operating conditions in liquid-feed direct methanol fuel cells: A multiphysics modeling approach. *Energy* **113**, 1265–1287.

GARCÍA-SALABERRI, P. A., VERA, M. & IGLESIAS, I. 2014 Modeling of the anode of a liquid-feed DMFC: Inhomogeneous compression effects and two-phase transport phenomena. *J. Power Sources* **246**, 239–252.

GASTEIGER, H. A., PANELS, J. E. & YAN, S. G. 2004 Dependence of PEM fuel cell performance on catalyst loading. *J. Power Sources* **127** (1-2), 162–171.

GE, S., LI, X., YI, B. & HSING, I.-M. 2005 Absorption, Desorption, and Transport of Water in Polymer Electrolyte Membranes for Fuel Cells. *J. Electrochem. Soc.* **152** (6), A1149.

GILEADI, ELIEZER 1993 *Electrode kinetics for chemists, chemical engineers, and materials scientists*. New York: VCH Publishers.

GONZALEZ, E. R. & MOTA-LIMA, A. 2014 Catalysts for Methanol Oxidation. In *Direct Alcohol Fuel Cells*, pp. 33–62. Dordrecht: Springer Netherlands.

GOSTICK, J. T. 2013 Random Pore Network Modeling of Fibrous PEMFC Gas Diffusion Media Using Voronoi and Delaunay Tessellations. *J. Electrochem. Soc.* **160** (8), F731–F743.

GOSTICK, J. T., FOWLER, M. W., IOANNIDIS, M. A., PRITZKER, M. D., VOLFKOVICH, Y. M. & SAKARS, A. 2006 Capillary pressure and hydrophilic porosity in gas diffusion layers for polymer electrolyte fuel cells. *J. Power Sources* **156** (2), 375–387.

GOSTICK, J. T., IOANNIDIS, M. A., FOWLER, M. W. & PRITZKER, M. D. 2007 Pore network modeling of fibrous gas diffusion layers for polymer electrolyte membrane fuel cells. *J. Power Sources* **173** (1), 277–290.

GOSTICK, J. T., IOANNIDIS, M. A., PRITZKER, M. D. & FOWLER, M. W. 2010 Impact of Liquid Water on Reactant Mass Transfer in PEM Fuel Cell Electrodes. *J. Electrochem. Soc.* **157** (4), B563.

HITMI, H., BELGSIR, E. M., LÉGER, J.-M., LAMY, C. & LEZNA, R. O. 1994 A kinetic analysis of the electro-oxidation of ethanol at a platinum electrode in acid medium. *Electrochim. Acta* **39** (3), 407–415.

IWASITA, T. & PASTOR, E. 1994 A dems and FTir spectroscopic investigation of adsorbed ethanol on polycrystalline platinum. *Electrochim. Acta* **39** (4), 531–537.

JIAO, K. 2011 Experimental and Modelling Studies of Cold Start Processes in Proton Exchange Membrane Fuel Cells .

JIAO, K. & LI, X. 2011 Water transport in polymer electrolyte membrane fuel cells. *Prog. Energy Combust. Sci.* **37** (3), 221–291.

KAURANEN, P. S., SKOU, E. & MUNK, J. 1996 Kinetics of methanol oxidation on carbon-supported Pt and Pt + Ru catalysts. *J. Electroanal. Chem.* **404** (1), 1–13.

KAVANAGH, R., CAO, X. M., LIN, W. F., HARDACRE, C. & HU, P. 2012 Origin of low CO$_2$ selectivity on platinum in the direct ethanol fuel cell. *Angew. Chem. Int. Ed. Engl.* **51** (7), 1572–5.

KIM, I., HAN, O. H., CHAE, S. A., PAIK, Y., KWON, S.-H., LEE, K.-S., SUNG, Y.-E. & KIM, H. 2011 Catalytic reactions in direct ethanol fuel cells. *Angew. Chem. Int. Ed. Engl.* **50** (10), 2270–4.

KULIKOVSKY, A. A. 2003 Quasi-3D Modeling of Water Transport in Polymer Electrolyte Fuel Cells. *J. Electrochem. Soc.* **150** (11), A1432.

KUSOGLU, A. & WEBER, A. Z. 2017 New Insights into Perfluorinated Sulfonic-Acid Ionomers. *Chem. Rev.* **117** (3), 987–1104.

LAIDLER, K. J. 1984 The development of the Arrhenius equation. *J. Chem. Educ.* **61** (6), 494.

LAMY, C., ROUSSEAU, S., BELGSIR, E. M., COUTANCEAU, C. & LÉGER, J.-M. 2004 Recent progress in the direct ethanol fuel cell: development of new platinum–tin electrocatalysts. *Electrochim. Acta* **49** (22-23), 3901–3908.

LANGMUIR, I. 1918 The adsorption of gases on plane surfaces of glass, mica and platinum. *J. Am. Chem. Soc.* **40** (9), 1361–1403.

LÉGER, J.-M., ROUSSEAU, S., COUTANCEAU, C., HAHN, F. & LAMY, C. 2005 How bimetallic electrocatalysts does work for reactions involved in fuel cells?: Example of ethanol oxidation and comparison to methanol. *Electrochim. Acta* **50** (25), 5118–5125.

LI, G. & PICKUP, P. G. 2006 Analysis of performance losses of direct ethanol fuel cells with the aid of a reference electrode. *J. Power Sources* **161** (1), 256–263.

LI, H., SUN, G., CAO, L., JIANG, L. & XIN, Q. 2007 Comparison of different promotion effect of PtRu/C and PtSn/C electrocatalysts for ethanol electro-oxidation. *Electrochim. Acta* **52** (24), 6622–6629.

LIU, Y., MURPHY, M. W., BAKER, D. R., GU, W., JI, C., JORNE, J. & GASTEIGER, H. A. 2009 Proton Conduction and Oxygen Reduction Kinetics in PEM Fuel Cell Cathodes: Effects of Ionomer-to-Carbon Ratio and Relative Humidity. *J. Electrochem. Soc.* **156** (8), B970.

LY, H., BIRGERSSON, E. & VYNNYCKY, M. 2012 Fuel cell model reduction through the spatial smoothing of flow channels. *Int. J. Hydrogen Energy* **37** (9), 7779–7795.

MARCUS, R. A. 1956 On the Theory of OxidationReduction Reactions Involving Electron Transfer. I. *J. Chem. Phys.* **24** (5), 966–978.

MARCUS, R. A. 1964 Chemical and Electrochemical Electron-Transfer Theory. *Annu. Rev. Phys. Chem.* **15** (1), 155–196.

MARCUS, R. A. & SUTIN, N. 1985 Electron transfers in chemistry and biology. *Biochim. Biophys. Acta - Rev. Bioenerg.* **811** (3), 265–322.

MCBRIDE, B. J, ZEHE, M. J. & GORDON, S. 2002 NASA Glenn Coefficients for Calculating Thermodynamic Properties of Individual Species. *Tech. Rep.*.

MEYER, M., MELKE, J. & GERTEISEN, D. 2011 Modelling and simulation of a direct ethanol fuel cell considering multistep electrochemical reactions, transport processes and mixed potentials. *Electrochim. Acta* **56** (11), 4299–4307.

MORAN, M. J. & SHAPIRO, H. N. 2009 *Fundamentals of engineering thermodynamics*, 6th edn. John Wiley and Sons Inc., New York, NY.

MORIMOTO, Y. & YEAGER, E.. B. 1998 CO oxidation on smooth and high area Pt, Pt-Ru and Pt-Sn electrodes. *J. Electroanal. Chem.* **441** (1-2), 77–81.

NACEF, M. & AFFOUNE, A.M. 2011 Comparison between direct small molecular weight alcohols fuel cells' and hydrogen fuel cell's parameters at low and high temperature. Thermodynamic study. *Int. J. Hydrogen Energy* **36** (6), 4208–4219.

NERNST, W. 1889*a* Die elektromotorische Wirksamkeit der Jonen. *Zeitschrift für Phys. Chemie* **4** (1), 129–181.

NERNST, W. 1889*b* Zur Theorie umkehrbarer galvanischer Elemente. (vorgelegt von Hrn. von Helmholtz am 17. Januar). *Sitzungsberichte der Preuss. Akad. der Wissenschaften zu Berlin* **1889** (1), 83–85.

NORDLUND, J. & LINDBERGH, G. 2002 A Model for the Porous Direct Methanol Fuel Cells Anode. *J. Electrochem. Soc.* **149** (9), A1107.

O'HAYRE, R., CHA, S.-W., COLELLA, W. & PRINZ, F. B. 2006 *Fuel Cell Fundamentals*. Hoboken, NJ, USA: John Wiley \& Sons, Inc.

ROUSSEAU, S., COUTANCEAU, C., LAMY, C. & LÉGER, J.-M. 2006 Direct ethanol fuel cell (DEFC): Electrical performances and reaction products distribution under operating conditions with different platinum-based anodes. *J. Power Sources* **158** (1), 18–24.

VON SCHROEDER, P. L. 1903 Uber Erstarrungs–und Quellungserscheinungen von Gelatine. *Z. Phys. Chem.* **45**, 57.

SHAO, M. H. & ADZIC, R. R. 2005 Electrooxidation of ethanol on a Pt electrode in acid solutions: in situ ATR-SEIRAS study. *Electrochim. Acta* **50** (12), 2415–2422.

SHIVHARE, M. R., ALLEN, R. G., SCOTT, K., MORRIS, A. J. & MARTIN, E. B. 2006 A kinetic model for the direct methanol fuel cell anode based on surface coverage. *J. Electroanal. Chem.* **595** (2), 145–151.

SHIVHARE, M. R., JACKSON, C. L., SCOTT, K. & MARTIN, E. B. 2007 Simplified model for the direct methanol fuel cell anode. *J. Power Sources* **173** (1), 240–248.

SOUSA, R., DOS ANJOS, D. M., TREMILIOSI-FILHO, G., GONZALEZ, E. R., COUTANCEAU, C., SIBERT, E., LÉGER, J.-M. & KOKOH, K. B. 2008 Modeling and simulation of the anode in direct ethanol fuels cells. *J. Power Sources* **180** (1), 283–293.

SPRINGER, T. E., ROCKWARD, T., ZAWODZINSKI, T. A. & GOTTESFELD, S. 2001 Model for Polymer Electrolyte Fuel Cell Operation on Reformate Feed: Effects of CO, H[sub 2] Dilution, and High Fuel Utilization. *J. Electrochem. Soc.* **148** (1), A11.

SPRINGER, T. E., ZAWODZINSKI, T. A. & GOTTESFELD, S. 1991 Polymer Electrolyte Fuel Cell Model. *J. Electrochem. Soc.* **138** (8), 2334.

SUNDMACHER, K., SCHULTZ, T., ZHOU, S., SCOTT, K., GINKEL, M. & GILLES, E. D. 2001 Dynamics of the direct methanol fuel cell (DMFC): experiments and model-based analysis. *Chem. Eng. Sci.* **56** (2), 333–341.

SURESH, N.S. & JAYANTI, S. 2011 Cross-over and performance modeling of liquid-feed Polymer Electrolyte Membrane Direct Ethanol Fuel Cells. *Int. J. Hydrogen Energy* **36** (22), 14648–14658.

TAFEL, J. 1905 Über die Polarisation bei kathodischer Wasserstoffentwicklung. *Z. Phys. Chem.* **50A**, 641–712.

VERA, M. 2007 A single-phase model for liquid-feed DMFCs with non-Tafel kinetics. *J. Power Sources* **171** (2), 763–777.

VIGIER, F., COUTANCEAU, C., HAHN, F., BELGSIR, E. M. & LAMY, C. 2004 On the mechanism of ethanol electro-oxidation on Pt and PtSn catalysts: electrochemical and in situ IR reflectance spectroscopy studies. *J. Electroanal. Chem.* **563** (1), 81–89.

WANG, C.-Y. 2004 Fundamental Models for Fuel Cell Engineering. *Chem. Rev.* **104** (10), 4727–4765.

WANG, C. Y. & CHENG, P. 1996 A multiphase mixture model for multiphase, multicomponent transport in capillary porous media—I. Model development. *Int. J. Heat Mass Transf.* **39** (17), 3607–3618.

WANG, H., JUSYS, Z. & BEHM, R. J. 2004 Ethanol Electrooxidation on a Carbon-Supported Pt Catalyst: Reaction Kinetics and Product Yields. *J. Phys. Chem. B* **108** (50), 19413–19424.

WANG, H., JUSYS, Z. & BEHM, R.J. J. 2006 Ethanol electro-oxidation on carbon-supported Pt, PtRu and Pt3Sn catalysts: A quantitative DEMS study. *J. Power Sources* **154** (2), 351–359.

WANG, H.-F. & LIU, Z.-P. 2008 Comprehensive mechanism and structure-sensitivity of ethanol oxidation on platinum: new transition-state searching method for resolving the complex reaction network. *J. Am. Chem. Soc.* **130** (33), 10996–1004.

WANG, Z. H. & WANG, C. Y. 2003 Mathematical Modeling of Liquid-Feed Direct Methanol Fuel Cells. *J. Electrochem. Soc.* **150** (4), A508.

WEBER, A. Z., BORUP, R. L., DARLING, R. M., DAS, P. K., DURSCH, T. J., GU, W., HARVEY, D., KUSOGLU, A., LITSTER, S., MENCH, M. M., MUKUNDAN, R., OWEJAN, J. P., PHAROAH, J. G., SECANELL, M. & ZENYUK, I. V. 2014 A Critical Review of Modeling Transport Phenomena in Polymer-Electrolyte Fuel Cells. *J. Electrochem. Soc.* **161** (12), F1254–F1299.

WEBER, A. Z. & NEWMAN, J. 2003 Transport in Polymer-Electrolyte Membranes: I. Physical Model. *J. Electrochem. Soc.* **150** (7), A1008.

WEBER, A. Z. & NEWMAN, J. 2004*a* Modeling Transport in Polymer-Electrolyte Fuel Cells. *Chem. Rev.* **104** (10), 4679–4726.

WEBER, A. Z. & NEWMAN, J. 2004*b* Transport in Polymer-Electrolyte Membranes: II. Mathematical Model. *J. Electrochem. Soc.* **151** (2), A311.

WEBER, A. Z. & NEWMAN, J. 2004*c* Transport in Polymer-Electrolyte Membranes: III. Model Validation in a Simple Fuel-Cell Model. *J. Electrochem. Soc.* **151** (2), A326.

WEBER, A. Z. & NEWMAN, J. 2009 Using a Quasi-Potential Transformation for Modeling Diffusion Media in Polymer-Electrolyte Fuel Cells. *SIAM J. Appl. Math.* **70** (2), 488–509.

YANG, W. W. & ZHAO, T. S. 2007 A two-dimensional, two-phase mass transport model for liquid-feed DMFCs. *Electrochim. Acta* **52**, 6125–6140.

ZAWODZINSKI, T. A., DAVEY, J., VALERIO, J. & GOTTESFELD, S. 1995 The water content dependence of electro-osmotic drag in proton-conducting polymer electrolytes. *Electrochim. Acta* **40** (3), 297–302.

ZAWODZINSKI, T. A., SPRINGER, T. E., DAVEY, J., JESTEL, R., LOPEZ, C., VALERIO, J. & GOTTESFELD, S. 1993 A Comparative Study of Water Uptake By and Transport Through Ionomeric Fuel Cell Membranes. *J. Electrochem. Soc.* **140** (7), 1981.

ZHAO, Q., MAJSZTRIK, P. & BENZIGER, J. 2011 Diffusion and Interfacial Transport of Water in Nafion. *J. Phys. Chem. B* **115** (12), 2717–2727.

Part I

Electrochemical model for Direct Ethanol Fuel Cells

CHAPTER

THREE

A genetically optimized kinetic model for ethanol electro-oxidation on Pt-based binary catalysts used in Direct Ethanol PEM Fuel Cells

Contents

3.1 Introduction

Direct Alcohol Fuel Cells (DAFC) represent a potential alternative to the archetypical hydrogen-fed Polymer Exchange Membrane Fuel Cell (PEMFC) for two main reasons: the ease of production, storage, and delivery of liquid alcohols (e.g., methanol, ethanol, ethylene glycol, n–propanol, etc.), and their higher volumetric energy density compared to hydrogen (Lamy *et al.*, 2002). This makes them suitable power sources for portable electronic devices such as cell phones, laptop computers, or military equipment, as well as for transportation applications. In contrast, DAFCs have two major drawbacks: the sluggish kinetics of the alcohol electro-oxidation reaction and the crossover of alcohol and water from anode to cathode through the polymeric membrane (Brouzgou *et al.*, 2013; Friedl & Stimming, 2013; Kamarudin *et al.*, 2013; Song & Tsiakaras, 2006).

Among various alcohols, methanol is the most used due to its high energy density and relatively fast electro-oxidation kinetics. However, it has several drawbacks: it is easily flammable, highly volatile (boiling point 65°C), and relatively toxic, which may lead to environmental problems due to its large miscibility with water. Moreover, it is not fully renewable, as it is typically produced from gaseous hydrocarbons or synthesis gas (i.e., $H_2 + CO$) obtained by the partial oxidation of a hydrocarbonaceous feed. Ethanol offers an interesting alternative because it can be readily produced by fermentation of biomass, including agricultural raw materials, and is much less toxic (Kamarudin *et al.*, 2013; Wang *et al.*, 1995). Furthermore, it has a lower crossover rate than methanol, which together with its slower electrochemical oxidation kinetics produces a lesser effect on the cathode performance (Ekdharmasuit *et al.*, 2013; Song *et al.*, 2005*b*). On top of that, its mass energy density is about 30% larger than that of methanol, and it is already the major renewable biofuel. For instance, countries like Brazil have already deployed a strong ethanol distribution network in petrol stations (Goldemberg *et al.*, 2004).

Nevertheless, the Ethanol Oxidation Reaction (EOR) is slower and significantly more complex than the MOR. The EOR proceeds through a multi-step reaction process that involves adsorbed species like acetyl (CH_3CO_{ads}) and carbon monoxide (CO_{ads}), and leads to a variety of oxidation products such as acetaldehyde (CH_3CHO), acetic acid (CH_3COOH), carbon dioxide (CO_2), and methane (CH_4) (Antolini, 2007; Antoniassi *et al.*, 2013; Brouzgou *et al.*, 2013; Hitmi *et al.*, 1994; Iwasita & Pastor, 1994; Léger *et al.*, 2005; Li & Pickup, 2006; Meyer *et al.*, 2011; Shao & Adzic, 2005; Wang *et al.*, 2004, 2006); but also minor products such as ethyl acetate, ethane, ethane-1,1-diol ethoxyhydroxymethane and formic acid (Jablonski *et al.*, 2011; Kim *et al.*, 2011; Taneda & Yamazaki, 2006; Wang *et al.*, 2006). The major oxidation products of ethanol on Pt electrodes are indeed acetaldehyde and acetic acid, not carbon dioxide (Rightmire *et al.*, 1964), making the incomplete oxidation of ethanol one of the main unresolved problems in Direct Ethanol Fuel Cells (DEFC). It has been found that the main reason for the low CO_2 selectivity is related to the C–C bond cleavage due to the blocking effect of the surface oxidant (Kavanagh *et al.*, 2012; Wang & Liu, 2008) and that the sp^2 bond is less susceptible to react (Akhairi & Kamarudin, 2016; Kavanagh *et al.*, 2012). Binary catalysts, such as Pt–Sn and Pt–Ru, exhibit a larger activity for the EOR compared to pure Pt electrodes (Akhairi & Kamarudin, 2016; Antoniassi *et al.*, 2013; Bach Delpeuch *et al.*, 2016; Colmati *et al.*, 2006; Fatih *et al.*, 2010; Kavanagh *et al.*, 2012; Kim *et al.*, 2011; Li *et al.*, 2007; Rousseau *et al.*, 2006; Vigier *et al.*, 2004*a*; Wang & Liu, 2008). In this case, the blockage of active sites is partially mitigated via a bifunctional mechanism (Vigier *et al.*, 2004*b*, 2006; Watanabe & Motoo, 1975) that allows the absorption of hydroxyl groups at lower potentials on the secondary metal, thus favoring further oxidation of Pt-adsorbates blocking active catalyst sites.

Another problem that hinders DEFC operation is the permeation of ethanol from anode to cathode, which leads to the parasitic electro-oxidation of ethanol at the cathode catalyst. The negative effects of ethanol crossover include cathode depolarization,

poisoning of the cathode catalyst by the permeated ethanol and its intermediate oxidation products, and reduced fuel utilization (James & Pickup, 2010; Li & Pickup, 2006; Song *et al.*, 2005*a*; Zakaria *et al.*, 2016). These phenomena result in a reduction of the overall system efficiency, which is particularly pronounced at low current densities and high ethanol concentrations.

Regarding the modeling activity on DEFCs, most early models assumed the complete oxidation of ethanol to CO_2 with the transfer of 12 electrons Andreadis *et al.* (2006); Andreadis & Tsiakaras (2006). Other models considered the oxidation of ethanol to acetic acid with the transfer of only 4 electrons (Andreadis *et al.*, 2008, 2009; Lin Ee & Birgersson, 2011). It was not until recently that DEFC models started to account for the complex multi-step kinetics of the EOR (Meyer *et al.*, 2011; Pramanik & Basu, 2010; Sousa *et al.*, 2008), including the effect of intermediate species such as acetic acid and acetaldehyde Hitmi *et al.* (1994). These models typically involve the calculation of the coverage factors of the intermediate species adsorbed on the catalyst layers (CL) (Kauranen *et al.*, 1996), an approach also used in Direct Methanol Fuel Cell (DMFC) modeling (Shivhare *et al.*, 2006, 2007; Sundmacher *et al.*, 2001; Suresh & Jayanti, 2011). Recent work of Meyer *et al.* (2011) proposed a branched reaction mechanism that involved different electron transfers depending on the pathway. Despite the good agreement in terms of polarization curves, the composition of the products predicted with this model is far from satisfactory, as recently discussed by the authors (Sanchez-Monreal *et al.*, 2016). Sousa *et al.* (2008) considered two pathways that produced 2 and 4 electrons, and Pramanik & Basu (2010) used only one pathway producing 4 electrons.

Due to the importance of crossover in DEFC performance, most models have included this effect (Andreadis *et al.*, 2008, 2009, 2006; Andreadis & Tsiakaras, 2006; Lin Ee & Birgersson, 2011; Meyer *et al.*, 2011; Pramanik & Basu, 2010; Suresh & Jayanti, 2011; Zakaria *et al.*, 2016). Since the molecular structures of ethanol and methanol are very similar, all crossover models for ethanol are based on those previously developed for methanol (Vera, 2007), with the crossover flux driven by molecular diffusion and electro-osmotic drag. By contrast, the crossover of free intermediate species such as acetaldehyde or acetic acid has not been fully addressed except by Meyer *et al.* (2011). Interestingly enough, even when ethanol crossover is considered, only a few models account for the mixed potential at the cathode due the parasitic electro-oxidation of ethanol. The crossover of oxygen from cathode to anode, with the associated mixed potential at the anode, represents another source of potential losses in DEFCs which has also been addressed recently (Brouzgou *et al.*, 2013; Jablonski *et al.*, 2011).

The aim of this paper is to develop a one-dimensional (1D) across-the-channel model for the anode of a DEFC accounting for the complex multi-step character of the EOR. The reaction mechanism, which considers free and adsorbed intermediate species on a Pt-based binary catalyst, represents an extension of the mechanism recently proposed by Meyer *et al.* (2011). As main novelty, the improved mechanism incorporates acetaldehyde among the adsorbed intermediates, and a genetic algorithm is used to select the reaction

constants so as to enhance the predictive capabilities (including both anode overpotential and product selectivity) at the full current density range.

The structure of the paper is as follows. The mathematical model is presented first; including the description of the model assumptions, the physical domain, and of full set of equations. These include the multi-step description of the EOR at the anode catalyst, the mass transport of the free species at the anode gas diffusion layer, and ethanol and acetaldehyde crossover. Illustrative numerical results are presented next, with special emphasis on the validation of the model against experimental results and a discussion of the agreements and disagreements. The concluding remarks are presented in the last section.

3.2 Model assumptions

In the development of the mathematical model, a number of simplifying assumptions have been made: *i*) the cell operates in steady-state; *ii*) the cell temperature (T) is uniform *iii*) the concentrations of ethanol (E), acetaldehyde (A), and acetic acid (AA) are sufficiently small for the liquid phase to be considered a diluted aqueous solution; *iv*) the membrane (assumed to be Nafion® 117) is fully hydrated and is impermeable to gases; *v*) the ohmic losses in the catalyst layers, gas diffusion layers, and bipolar plates are considered negligible compared to ohmic losses in the membrane; *vi*) the overpotentials, coverage factors, and free species concentrations are constant across the catalyst layers; *vii*) the catalyst layer consists of a Pt-based binary catalysts that allows the absorption of hydroxyl groups at lower potentials on the secondary metal according to the bifunctional mechanism described in (Vigier *et al.*, 2004*b*, 2006; Watanabe & Motoo, 1975). Although some of this assumptions could be easily revised to incorporate additional effects in future work, they will be maintained here for simplicity.

3.3 Physical domain

Figure 3.1 shows a schematic representation of a DEFC. The cell is divided into seven regions: anode channel (ac); anode gas diffusion layer (agdl); anode catalyst layer (acl); polymeric membrane (mem); cathode catalyst layer (ccl); cathode gas diffusion layer (cgdl); and cathode channel (cc). In the 1D across-the-channel anode model presented in this work only the anode gas diffusion layer (agdl), the anode catalyst layer (acl), and the membrane (mem) are included. The figure also shows the notation used for the concentrations of the free species at the anode/cathode channels, and for the thickness of the different layers of the MEA.

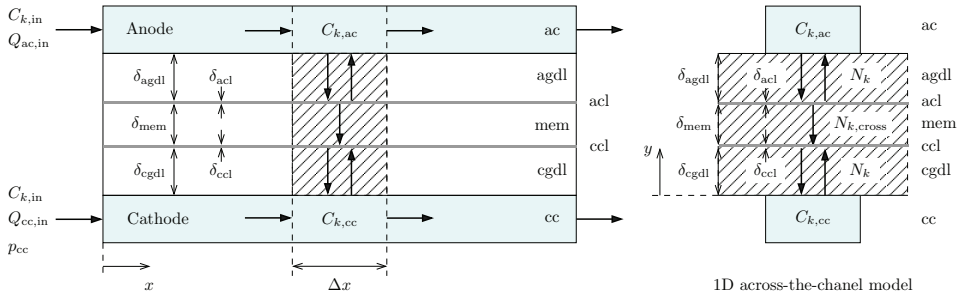

Figure 3.1: Schematic representation showing the different regions of a DEFC and highlighting the physical domain covered by the 1D across-the-channel model. The figure summarizes the notation used for the channel concentrations, $C_{k,\mathrm{ac/cc}}$, the molar fluxes across the porous layers, N_k, and the membrane crossover flux, $N_{k,\mathrm{cross}}$, of free species, k, as well as the thickness of the different layers of the MEA (δ_ℓ, ℓ = agdl, acl, mem, ccl, cgdl). Left: side view; right: cross-sectional view.

3.4 Anode one-dimensional model

3.4.1 Anode catalyst layer

Different reaction mechanisms have been proposed in the literature for the EOR (Abd-El-Latif *et al.*, 2010; Kavanagh *et al.*, 2012; Kim *et al.*, 2011; Kutz *et al.*, 2011; Wang & Liu, 2008). Due to the large amount of intermediate species, both free and adsorbed, and of potential elementary reactions, mathematical models exhibit different levels of complexity in the description of the EOR multi-step reaction (Meyer *et al.*, 2011; Pramanik & Basu, 2010; Sousa *et al.*, 2008). Figure 3.2 shows the kinetic model proposed in this work. The different elementary reactions considered are listed in Table 3.1. The mechanism involves five adsorbed species, four of them attached to the Pt-sites (CH_3CHOH_{ads}, CH_3CO_{ads}, CO_{ads} and $CH_{3\,ads}$), and the fifth (OH_{ads}) to the secondary metal, according to the bimetallic catalyst assumption. Following previous work, there are two pathways leading to the production of adsorbed acetyl (Abd-El-Latif *et al.*, 2010; Giz & Camara, 2009; Kavanagh *et al.*, 2012; Kim *et al.*, 2011; Kutz *et al.*, 2011): one through acetaldehyde production (Reactions 1 and 2) and other through the successive dehydrogenation of the carbon attached to the alcohol group (Reactions I and II). Ignoring the second pathway, as done by Meyer *et al.* (2011), results in a reaction mechanism that is unable to predict product selectivities at low current densities (Sanchez-Monreal *et al.*, 2016). For this reason the second pathway is also considered in this work, to enable the generation of acetic acid even at low acetaldehyde production (Li & Pickup, 2006). Following Meyer *et al.* (2011), the two reaction pathways that emerge from adsorbed acetyl lead to the formation of either acetic acid (Reaction 4) or of CO_{ads} and $CH_{3\,ads}$ through the C–C bond breaking step (Reaction 5).

The hypothesis that the membrane is impermeable to gases implies that oxygen

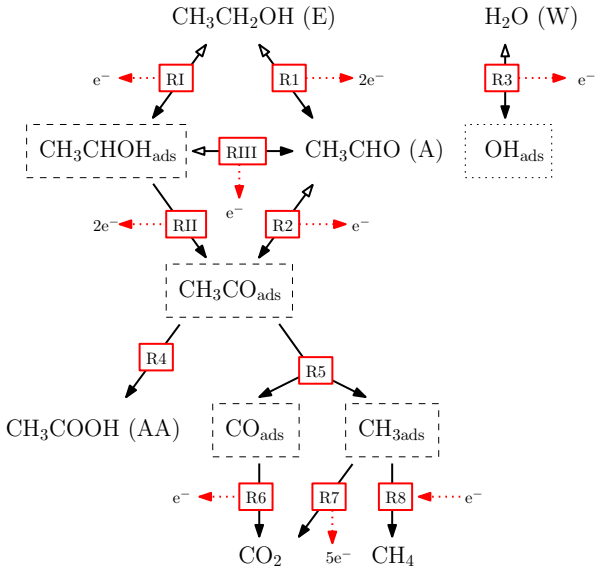

Figure 3.2: Reaction mechanism for the Electron Oxidation Reaction (EOR) on binary Pt-based catalysts proposed in this work. Pt-site adsorbed species are indicated by a dashed box; OH_{ads} is boxed using dotted lines to indicate that it is adsorbed at the secondary metal sites. Reactions 4, 6 and 7 use the adsorbed hydroxyl groups to proceed. The exact stoichiometries are shown in Table 3.1.

crossover should be ignored. Jablonski *et al.* (2011) detected the presence of acetaldehyde and acetic acid in the anode outlet stream under open circuit conditions, which was attributed to the parasitic electro-oxidation of ethanol at the anode electrode with the oxygen crossing the membrane from cathode to anode. Their experiments were carried out with pure oxygen feed at 200 kPa cathode pressure, which could have accentuated the oxygen crossover rate. This effect, however, is anticipated to be less important for fuel cells operated with air at nearly atmospheric pressure. Unlike Jablonski *et al.* (2011), James & Pickup (2010) attributed the presence of acetaldehyde and acetic acid in the anode outlet to the parasitic electrooxidation of ethanol at the cathode side followed by the back diffusion of those two products to the anode side, from where they were evacuated by the anode liquid stream. The lack of agreement found in the literature and the small quantitative effect of oxygen crossover justify in any case ignoring the crossover of oxygen in the analysis.

In the proposed kinetic mechanism, Reaction I represents the adsorption of ethanol to

Table 3.1: The 11-step reaction mechanism proposed in this work.

Reaction			n_α
I. $CH_3CH_2OH \rightleftharpoons CH_3CHOH_{ads} + H^+ + e^-$	k_{If}	α_I	1
	k_{Ib}		1
II. $CH_3CHOH_{ads} \rightarrow CH_3CO_{ads} + 2H^+ + 2e^-$	k_{IIf}	α_{II}	2
	k_{IIb}		2
III. $CH_3CHOH_{ads} \rightleftharpoons CH_3CHO + H^+ + e^-$	k_{IIIf}	α_{III}	1
	k_{IIIb}		1
1. $CH_3CH_2OH \rightleftharpoons CH_3CHO + 2H^+ + 2e^-$	k_{1f}	α_1	2
	k_{1b}		2
2. $CH_3CHO \rightleftharpoons CH_3CO_{ads} + H^+ + e^-$	k_{2f}	α_2	1
	k_{2b}		1
3. $H_2O \rightleftharpoons OH_{ads} + H^+ + e^-$	k_{3f}	α_3	1
	k_{3b}		1
4. $CH_3CO_{ads} + OH_{ads} \longrightarrow CH_3COOH$	k_4		
5. $CH_3CO_{ads} \longrightarrow CO_{ads} + CH_{3\,ads}$	k_5		
6. $CO_{ads} + OH_{ads} \longrightarrow CO_2 + H^+ + e^-$	k_6	α_6	1
7. $CH_{3\,ads} + 2OH_{ads} \longrightarrow CO_2 + 5H^+ + 5e^-$	k_7	α_7	5
8. $CH_{3\,ads} + H^+ + e^- \longrightarrow CH_4$	k_8	α_8	1

CH_3CHOH_{ads}. The net ethanol adsorption rate is given by the Butler-Volmer equation

$$q_I = \left(1 - \Theta_{CH_3CHOH_{ads}} - \Theta_{CH_3CO_{ads}} - \Theta_{CO_{ads}} - \Theta_{CH_{3\,ads}}\right) C_{E,acl} k_{If} \exp\left(\frac{\alpha_I F}{RT}\eta_a\right) - \Theta_{CH_3CHOH_{ads}} k_{Ib} \exp\left(-\frac{(1-\alpha_I)F}{RT}\eta_a\right) \quad (3.1)$$

where the factor between brackets in the forward reaction rate, which accounts for the blocking of active Pt-sites, does not include the adsorbed OH groups because in binary catalysts they are preferably attached to the secondary metal.

Reaction II describes the oxidation of CH_3CHOH_{ads} to CH_3CO_{ads}, whose reaction rate is given by

$$q_{II} = \Theta_{CH_3CHOH_{ads}} k_{II} \exp\left(\frac{\alpha_{II} 2F}{RT}\eta_a\right) \quad (3.2)$$

Note that this reaction is considered to occur in a single step, as possible intermediates are assumed to produce no other species (Kavanagh *et al.*, 2012; Kim *et al.*, 2011; Wang & Liu, 2008). Like other reactions between adsorbates, Reaction II is considered to be irreversible, hence the reaction rate given in Equation (3.2) accounts only for the forward reaction.

CH_3CHOH_{ads} can also be desorbed to give acetaldehyde through Reaction III. The net

reaction rate is given by

$$q_{\mathrm{III}} = \Theta_{\mathrm{CH_3CHOH_{ads}}} k_{\mathrm{IIIf}} \exp\left(\frac{\alpha_{\mathrm{III}} F}{RT}\eta_a\right) - \left(1 - \Theta_{\mathrm{CH_3CHOH_{ads}}} - \Theta_{\mathrm{CH_3CO_{ads}}} - \Theta_{\mathrm{CO_{ads}}} - \Theta_{\mathrm{CH_{3\,ads}}}\right) C_{\mathrm{A,acl}} k_{\mathrm{IIIb}} \exp\left(-\frac{(1-\alpha_{\mathrm{III}})2F}{RT}\eta_a\right) \tag{3.3}$$

In our extended reaction model, Reaction III is considered to be reversible, with acetaldehyde being also produced from ethanol by Reaction 1 and oxidized to CH_3CO_{ads} through Reaction 2 Kavanagh *et al.* (2012); Kim *et al.* (2011); Wang & Liu (2008). In this case, the backward reaction rate is proportional to the concentration of acetaldehyde and to the available Pt-sites.

Reaction 1 represents the redox reaction between ethanol and acetaldehyde. Under the bimetallic catalyst assumption, the net reaction rate is given by

$$q_1 = \left(1 - \Theta_{\mathrm{CH_3CHOH_{ads}}} - \Theta_{\mathrm{CH_3CO_{ads}}} - \Theta_{\mathrm{CO_{ads}}} - \Theta_{\mathrm{CH_{3\,ads}}}\right)\left[C_{\mathrm{E,acl}} k_{1\mathrm{f}} \exp\left(\frac{\alpha_1 2F}{RT}\eta_a\right) - C_{\mathrm{A,acl}} k_{1\mathrm{b}} \exp\left(-\frac{(1-\alpha_1)2F}{RT}\eta_a\right)\right] \tag{3.4}$$

As discussed above, the oxidation of acetaldehyde to CH_3CO_{ads} is described by Reaction 2, with the net reaction rate given by

$$q_2 = \left(1 - \Theta_{\mathrm{CH_3CO_{ads}}} - \Theta_{\mathrm{CO_{ads}}} - \Theta_{\mathrm{CH_{3\,ads}}}\right) C_{\mathrm{A,acl}} k_{2\mathrm{f}} \exp\left(\frac{\alpha_2 F}{RT}\eta_a\right) - \Theta_{\mathrm{CH_3CO_{ads}}} k_{2\mathrm{b}} \exp\left(-\frac{(1-\alpha_2)F}{RT}\eta_a\right) \tag{3.5}$$

The dissociative adsorption of water to yield adsorbed hydroxyl groups is represented by Reaction 3. The water activation rate, which in binary Pt-based catalysts occurs on the secondary metal, is given by

$$q_3 = k_{3\mathrm{f}}\left(1 - \Theta_{\mathrm{OH_{ads}}}\right)\exp\left(\frac{\alpha_3 F}{RT}\eta_a\right) - k_{3\mathrm{b}}\Theta_{\mathrm{OH_{ads}}}\exp\left(-\frac{(1-\alpha_3)F}{RT}\eta_a\right) \tag{3.6}$$

Reaction 4 describes the formation of acetic acid from adsorbed acetyl and hydroxyl groups. Since this reaction does not involve charge transfer it is independent of the anode overpotential, and its rate can be written as

$$q_4 = k_4 \Theta_{\mathrm{CH_3CO_{ads}}} \Theta_{\mathrm{OH_{ads}}} \tag{3.7}$$

An alternative pathway for the subsequent oxidation of acetyl starts with the breaking of the C–C bond to give CO_{ads} and CH_{3ads}. The rate of the C–C bond breaking step, represented by Reaction 5, does not involve charge transfer either, so it is simply proportional to the acetyl coverage factor

$$q_5 = k_5 \Theta_{CH_3CO_{ads}} \tag{3.8}$$

The CO_{ads} produced in Reaction 5 can be further oxidized to CO_2 using an adsorbed hydroxyl group following Reaction 6. The corresponding rate of CO_2 production from CO_{ads} is given by

$$q_6 = k_6 \Theta_{CO_{ads}} \Theta_{OH_{ads}} \exp\left(\frac{\alpha_6 F}{RT}\eta_a\right) \tag{3.9}$$

Although the final fate of the adsorbed CH_3-fragment is not clear, (Meyer *et al.*, 2011) presumed that it was either oxidized to CO_2 with the help of two OH-groups through Reaction 7, or reduced at low potentials to CH_4 following Reaction 8. The corresponding rates of CH_{3ads} oxidation and reduction to carbon dioxide and methane are respectively given by

$$q_7 = k_7 \Theta_{CH_{3\,ads}} \Theta^2_{OH_{ads}} \exp\left(\frac{\alpha_7 5F}{RT}\eta_a\right) \tag{3.10}$$

and

$$q_8 = k_8 \Theta_{CH_{3\,ads}} \exp\left(-\frac{\alpha_8 F}{RT}\eta_a\right) \tag{3.11}$$

To determine the coverage factors of the five adsorbed species (CH_3CHOH_{ads}, CH_3CO_{ads}, CO_{ads}, $CH_{3\,ads}$, and OH_{ads}) the steady-state approximation (SSA) is applied to all of them, which yields the following set of equations

$$\text{SSA } CH_3CHOH_{ads}: \quad q_{\text{I}} - q_{\text{II}} - q_{\text{III}} = 0 \tag{3.12}$$

$$\text{SSA } CH_3CO_{ads}: \quad q_2 + q_{\text{II}} - q_5 - q_4 = 0 \tag{3.13}$$

$$\text{SSA } OH_{ads}: \quad q_3 - q_4 - q_6 - 2q_7 = 0 \tag{3.14}$$

$$\text{SSA } CO_{ads}: \quad q_5 - q_6 = 0 \tag{3.15}$$

$$\text{SSA } CH_{3\,ads}: \quad q_5 - q_8 - q_7 = 0 \tag{3.16}$$

As shown in Appendix 3.A, upon substitution of expressions (3.1)–(3.11) for the net reaction rates q_r into Eqs. (3.12)–(3.16), a system of five non-linear algebraic equations is obtained for the five coverage factors Θ_k. After some algebraic manipulations, the system can be reduced to a fifth-order polynomial equation for $\Theta_{OH_{ads}}$, which can be shown to have a real root between 0 and 1. This root can be obtained numerically for specified values of the ethanol and acetaldehyde concentrations at the anode catalyst layer, $C_{E,acl}$ and $C_{A,acl}$, and of the anode overpotential, η_a, readily yielding the remaining coverage factors from algebraic expressions. The cell temperature, T, and the set of kinetic parameters

(including the rate constants, k_k, and transfer coefficients, α_k) must also be specified, and will be kept constant throughout the iterative solution process.

It is worth noting that, unlike previous models (Meyer *et al.*, 2011; Sanchez-Monreal *et al.*, 2016), here the coverage factors depends explicitly on the concentration of ethanol at the anode catalyst layer, $C_{\mathrm{E,acl}}$, through the net reaction rate q_{I}. The reason is that our reaction mechanism includes, as previously stated, the production of CH_3CHOH_{ads} through Reaction I as a possible pathway for the oxidation of ethanol to CH_3CO_{ads}, which has not been explicitly considered in previous studies.

Once the coverage factors are known, the area specific net production (or consumption) rates of the free species, expressed in moles produced (or consumed) per unit time and per unit surface area of anode catalyst layer, can be written as

$$\omega_{\mathrm{E}} = -\left(q_{\mathrm{I}} + q_1\right)\delta_{\mathrm{acl}} \tag{3.17}$$

$$\omega_{\mathrm{A}} = \left(q_1 + q_{\mathrm{III}} - q_2\right)\delta_{\mathrm{acl}} \tag{3.18}$$

$$\omega_{\mathrm{AA}} = q_4\delta_{\mathrm{acl}} \tag{3.19}$$

$$\omega_{\mathrm{CO_2}} = \left(q_6 + q_7\right)\delta_{\mathrm{acl}} \tag{3.20}$$

$$\omega_{\mathrm{CH_4}} = q_8\delta_{\mathrm{acl}} \tag{3.21}$$

$$\omega_{\mathrm{W}} = -q_3\delta_{\mathrm{acl}} \tag{3.22}$$

where the subscript W denotes water. With this notation, positive (or negative) values of ω_k indicate net production (or consumption) of species k. Multiplying the area specific reaction rates, $q_r\delta_{\mathrm{acl}}$, by the number of electrons transferred in each reaction, n_r, adding the resulting electron generation rates all together and multiplying by Faraday's constant provides the current density generated at the anode catalyst layer

$$i = F\left(q_{\mathrm{I}} + 2q_{\mathrm{II}} + q_{\mathrm{III}} + 2q_1 + q_2 + q_3 + q_6 + 5q_7 - q_8\right)\delta_{\mathrm{acl}} \tag{3.23}$$

Note in particular the relevant role of Reaction 7, which releases 5 electrons and therefore may have a significant impact on the total current density generation even for moderately low values of q_7.

3.4.2 Anode gas diffusion layer

The net molar flux of the free reacting species, transported by convection and diffusion from the bulk fluid in the anode channel (ac) to the anode channel/gas diffusion layer interface (agdl/ac), is modeled using an overall mass transport coefficient h (Andreadis *et al.*, 2006; Sousa *et al.*, 2008), which allows to write

$$N_k = -h\left(C_{k,\mathrm{ac}} - C_{k,\mathrm{ac/agdl}}\right) \qquad k = \mathrm{E,A} \tag{3.24}$$

where $C_{k,\mathrm{ac}}$ represents the bulk concentration of species k in the anode channel, and $C_{k,\mathrm{ac/agdl}}$ is the concentration of species k at the ac/agdl interface. Note that the sign of N_k indicates whether the net molar flux of species k is directed in the positive or negative y-direction, with $N_k > 0$ indicating that the net molar flux of species k goes from the catalyst layer to the flow channel, while for $N_k < 0$ it goes from the channel to the catalyst layer.

The mass transport of free species across the gas diffusion layer is driven by Fickian diffusion and by the convective drag of water flowing through the gas diffusion layer

$$N_k = -D^{\mathrm{eff}}_{k,\mathrm{agdl}} \frac{\partial C_k}{\partial y} + v_{\mathrm{W}} C_k \qquad k = \mathrm{E}, \mathrm{A} \tag{3.25}$$

where $D^{\mathrm{eff}}_{k,\mathrm{agdl}} = \epsilon^{3/2} D_{k,\mathrm{W}}$ is the effective diffusivity of species k in the porous media, expressed using Bruggeman correction in terms of the porosity ϵ of the gas diffusion layer and of the bulk diffusivity $D_{k,\mathrm{W}}$ of species k in water. Although this correction is known to overestimate the effective diffusivity (García-Salaberri *et al.*, 2015*a*,*b*), it is also the most extended assumption for the description of diffusive transport in DEFC (Andreadis *et al.*, 2006; Meyer *et al.*, 2011; Sundmacher *et al.*, 2001; Suresh & Jayanti, 2011) and therefore will be adopted here for simplicity. The values of the bulk diffusivity and gdl porosity used in this work are shown in Table 3.4.

A more realistic description of diffusive transport in the gas diffusion layer would have required accounting for two-dimensional effects coming from the rib-channel pattern, porosity variations (García-Salaberri *et al.*, 2011) across the porous layer, or the use of a 3.5 exponent for the through-plane effective diffusivity (García-Salaberri *et al.*, 2015*b*). However, the lack of agreement in the values of the diffusion coefficients reported in the literature, with values from 1/3 (Meyer *et al.*, 2011) to 3 (Andreadis *et al.*, 2009, 2006; Hitmi *et al.*, 1994) times the one considered here, makes it meaningless to consider a more complex model.

Equation (3.25) involves the average velocity of water across the gas diffusion layer

$$v_{\mathrm{W}} = \frac{W_{\mathrm{W}}}{\rho_{\mathrm{W}}} \left(\omega_{\mathrm{W}} - n_d^{\mathrm{W}} \frac{i}{F} \right) \tag{3.26}$$

which is induced by the water consumption rate ω_{W} (< 0) at the anodic reaction and the electro-osmotic flux of water crossing the membrane, to be addressed below. Note that with the transverse y-coordinate pointing from cathode to anode (see Figure 3.1), the water velocity v_w must be negative, since water always moves from anode to cathode.

Integrating Equation (3.25) across the gas diffusion layer, with boundary conditions $C_k = C_{k,\mathrm{ac/agdl}}$ at the ac/agdl interface and $C_k = C_{k,\mathrm{acl}}$ at the acl, and making use of (3.24) to eliminate $C_{k,\mathrm{ac/agdl}}$ from the resulting expression, the molar flux of species k can be

written as (Andreadis & Tsiakaras, 2006)

$$N_k\left(C_{k,\mathrm{ac}}; C_{\mathrm{E,acl}}, C_{\mathrm{A,acl}}, \eta_a\right) = -\frac{C_{k,\mathrm{ac}} e^{v_{\mathrm{W}}/k_{k,\mathrm{gdl}}} - C_{k,\mathrm{acl}}}{e^{v_{\mathrm{W}}/k_{k,\mathrm{gdl}}}\left(1 + v_{\mathrm{W}}/h\right) - 1}\, v_{\mathrm{W}} \qquad k = \mathrm{E,A} \tag{3.27}$$

where $k_{k,\mathrm{agdl}} = D^{\mathrm{eff}}_{k,\mathrm{agdl}}/\delta_{\mathrm{acl}}$ denotes the diffusive mass transfer coefficient of the gas diffusion layer.

It should be noted that the molar fluxes given in Equation (3.27) are a function of $C_{\mathrm{E,acl}}$, $C_{\mathrm{A,acl}}$, and η_a, because the water velocity v_{W} given in (3.26) depends both on ω_{W} and i, which in turn depend on $C_{\mathrm{E,acl}}$, $C_{\mathrm{A,acl}}$, and η_a. As will be shown below, the values of $C_{\mathrm{E,acl}}$ and $C_{\mathrm{A,acl}}$ must be determined iteratively from the solution of the full mass transport problem, which includes the effect of ethanol and acetaldehyde crossover.

3.4.3 Ethanol and acetaldehyde crossover

The permeation of ethanol and other reactive species, such as acetaldehyde, through the polymeric membrane constitutes a severe problem in DEFCs. The reactive species that cross the membrane are prone to react electrochemically with oxygen at the cathode catalyst, which results in a parasitic current that increases the cathode overpotential. But this is not the only effect of crossover, which is also noticeable at the anode electrode, where a fraction of the fuel that reaches the active region of the cell leaks across the membrane due to the crossover flux. This reduces the amount of fuel that is available to produce current at the anode catalyst layer, thereby increasing the so-called concentration overpotential.

In our model, we shall consider only the effect of ethanol and acetaldehyde crossover, since in low-temperature DEFCs they are the only reacting free species that generate electrons in the EOR. Just like the crossover flux of methanol in DMFCs (Vera, 2007), the crossover flux of ethanol and acetaldehyde are driven by Fickian diffusion and electro-osmotic drag

$$N_{k,\mathrm{cross}}\left(C_{\mathrm{E,acl}}, C_{\mathrm{A,acl}}, \eta_a\right) = -D^{\mathrm{eff}}_{k,\mathrm{mem}} \frac{\partial C_{k,\mathrm{acl}}}{\partial y} + n_d^k \frac{i}{F} \qquad k = \mathrm{E,A} \tag{3.28}$$

where $D^{\mathrm{eff}}_{k,\mathrm{mem}}$ is the effective diffusivity of species k in the membrane and n_d^k is the electro-osmotic drag coefficient of species k, defined as the number of molecules of species k dragged by a proton crossing the membrane. For low species concentrations, this coefficient can be expressed in terms of the electro-osmotic drag coefficient of water, n_d^{W}, as

$$n_d^k = \frac{W_{\mathrm{W}}}{\rho_{\mathrm{W}}} n_d^{\mathrm{W}} C_{k,\mathrm{acl}} \tag{3.29}$$

where W_{W} is the molecular weight of water, ρ_{W} is the density of water, and n_d^{W} is given

in terms of temperature by Guo & Ma (2004)

$$n_d^w = 2.9 \exp\left[1029\left(\frac{1}{333} - \frac{1}{T}\right)\right] \tag{3.30}$$

Assuming that the electro-oxidation of both ethanol and acetaldehyde in the cathode electrode is fast enough for the resulting concentrations of both species at the cathode catalyst layer to be much smaller than those at the anode catalyst layer, the crossover fluxes can be written in first approximation as

$$N_{k,\text{cross}}\left(C_{\text{E,acl}}, C_{\text{A,acl}}, \eta_a\right) = -\left[\frac{D_{k,\text{mem}}^{\text{eff}}}{\delta_{\text{mem}}} + \frac{W_{\text{W}}}{\rho_w} n_d^{\text{W}} \frac{i}{F}\right] C_{k,\text{acl}} \qquad k = \text{E, A} \tag{3.31}$$

3.4.4 Determination of the free species concentrations

The concentrations of ethanol and acetaldehyde at the anode catalyst layer are determined from the local mass balance of ethanol and acetaldehyde at this layer. Imposing that the molar flux of ethanol (acetaldehyde) that reaches the acl by convection and diffusion from the anode backing must be equal to the rate of ethanol (acetaldehyde) consumption at the anode catalyst layer, plus the flux of ethanol (acetaldehyde) that crosses the membrane, yields the two equations

$$N_{\text{E}}\left(C_{\text{E,ac}}; C_{\text{E,acl}}, C_{\text{A,acl}}, \eta_a\right) = \omega_{\text{E}}\left(C_{\text{E,acl}}, C_{\text{A,acl}}, \eta_a\right) - N_{\text{E,cross}}\left(C_{\text{E,acl}}, C_{\text{A,acl}}, \eta_a\right) \tag{3.32}$$

$$N_{\text{A}}\left(C_{\text{A,ac}}; C_{\text{E,acl}}, C_{\text{A,acl}}, \eta_a\right) = \omega_{\text{A}}\left(C_{\text{E,acl}}, C_{\text{A,acl}}, \eta_a\right) - N_{\text{A,cross}}\left(C_{\text{E,acl}}, C_{\text{A,acl}}, \eta_a\right) \tag{3.33}$$

where the molar fluxes N_k reaching the acl are given by (3.27), the electrochemical consumption rates ω_k by (3.17) and (3.18), and the crossover fluxes $N_{k,\text{cross}}$ by (3.31). Note that Equations (3.32) and (3.33) do not show the explicit dependence of the different terms on the cell temperature T and the reaction constants, which are assumed to remain unchanged during the iterative solution process.

Given the channel concentrations, $C_{\text{E,ac}}$ and $C_{\text{A,ac}}$, and the anode overpotential, η_a, equations (3.32) and (3.33) represent a system of two non-linear algebraic equations for the two unknowns $C_{\text{E,acl}}$ and $C_{\text{A,acl}}$ that must be solved numerically. To this end, we used the *fsolve* routine from the MATLAB optimization toolbox, specifying sufficiently small values for the concentrations of ethanol and acetaldehyde (e.g., $C_{\text{E,acl}}^0 = C_{\text{E,acl}}^0 = 0.05$ M) as suitable initial guesses to avoid reaching negative spurious solutions during the iterative process. The concentration of the remaining non-adsorbed species (i.e., acetic acid, CO_2, and CH_4) at the acl, which do not influence the electro-oxidation rate of ethanol and acetaldehyde, could be obtained *a posteriori* from the corresponding mass balances.

3.4.5 Product selectivity

As widely seen in the literature, a handy index to analyze the product distribution in DEFCs is the product selectivity (Andreadis *et al.*, 2010; Antoniassi *et al.*, 2013; Li & Pickup, 2006), defined as the fractional amount of the overall molar production rate corresponding to a given species k. In DEFCs, the product selectivity of species k can be calculated as follows

$$s_k\,[\%] = \frac{\omega_k}{\omega_{\mathrm{A}} + \omega_{\mathrm{AA}} + \omega_{\mathrm{CO_2}} + \omega_{\mathrm{CH_4}}} \qquad k = \mathrm{E, A, CO_2, CH_4} \tag{3.34}$$

in terms of the molar production rates of the different products generated by the EOR. The product selectivities can also be expressed in terms of the net reaction rates q_r as follows

$$\begin{aligned} s_{\mathrm{A}} &= \frac{q_1 + q_{\mathrm{III}} - q_2}{q_1 + q_{\mathrm{III}} - q_2 + q_4 + q_6 + q_7 + q_8} \\ s_{\mathrm{AA}} &= \frac{q_4}{q_1 + q_{\mathrm{III}} - q_2 + q_4 + q_6 + q_7 + q_8} \\ s_{\mathrm{CH_4}} &= \frac{q_8}{q_1 + q_{\mathrm{III}} - q_2 + q_4 + q_6 + q_7 + q_8} \\ s_{\mathrm{CO_2}} &= \frac{q_6 + q_7}{q_1 + q_{\mathrm{III}} - q_2 + q_4 + q_6 + q_7 + q_8} \end{aligned} \tag{3.35}$$

expressions obtained by substituting the ω_k given in (3.17)–(3.22) into Equation (3.34).

3.4.6 Model fitting procedure

A simulation campaign was carried out to fit the predictive capabilities of the model using experimental data reported in the literature. The output data used for comparison was limited to the polarization curve of the anode electrode, and to the selectivity index s_k of the main products, k = acetaldehyde (A), acetic acid (AA), carbon dioxide (CO_2), and methane (CH_4). As part of the model set-up process, a set of reaction constants was calculated to fit the model to the available experimental results of selectivity and anode overpotential (Li & Pickup, 2006), the latter obtained with the aid of a *dynamic hydrogen electrode* (DHE). An optimization procedure was used to obtain the set of reaction constants. As in previous work (Sanchez-Monreal *et al.*, 2016), the built-in *gamultiobj* multiobjective genetic algorithm solver, available in MATLAB, was used to optimize an objective function. The objective function used was the quadratic norm of the relative errors for the current density, acetaldehyde, acetic acid, an CO_2 selectivities for the pair of anode overpotentials 0.3375 V and 0.4009 V

$$err = \sqrt{\sum_i \left(\frac{x_{i,\mathrm{LP}} - x_i}{x_{i,\mathrm{LP}}} \right)^2} \tag{3.36}$$

Table 3.2: Experimentally measured product selectivity data reported by Li & Pickup (2006).

η_a [V]	0.3375	0.4009
i [A m^{-2}]	300	600
s_{A}	0.165	0.377
s_{AA}	0.768	0.556
$s_{\mathrm{CO_2}}$	0.067	0.067

where $x_{i,\mathrm{LP}}$ denote the current density and product selectivities reported by Li & Pickup (2006), which are summarized in Table 3.2, and x_i is the corresponding value computed with the present model. The set of reaction constants and transfer coefficients obtained in Sanchez-Monreal *et al.* (2016) was used as initial population for Reactions 1 to 8. For Reactions I to III the initial population was obtained adopting the reaction constants of similar reactions found in the original mechanism of Meyer *et al.* (2011). For instance, Reactions I and III are adsorption/desorption reactions, just like Reaction 2; whereas Reaction II is a reaction between adsorbed species, just like Reaction 5. The set of reaction constants and transfer coefficients obtained from the optimization process is shown in Table 3.3. The reaction constants and transfer coefficients reported in previous works are also included for comparative purposes.

3.4.7 Effective electron generation number

Each ethanol molecule consumed in the EOR may follow one of the three main chemical paths represented in Figure 3.2: acetaldehyde production, acetic acid production or C–C bond breaking. The first path produces one molecule of acetaldehyde for each molecule of ethanol consumed and releases 2 electrons. The second path produces one molecule of acetic acid for each molecule of ethanol, releasing 4 electrons instead. The third path proceeds through the C–C bond breaking step, and therefore produces two single carbon molecules for each molecule of ethanol consumed. These two molecules may be either a CO_2 and a CH_4 molecule (produced by Reactions 6 and 8 releasing 4 electrons) or two CO_2 molecules (produced by Reactions 6 and 7 releasing 12 electrons) depending on the final fate of the adsorbed methyl group. While the carbonyl group is always oxidized to CO_2 through Reaction 6, the methyl group can be either oxidized to CO_2 through Reaction 7 or reduced to CH_4 through reaction 8. As a result, the generation of a CO_2 molecule by Reaction 6 is always accompanied either by the production of another CO_2 molecule by Reaction 7 or by the production of a CH_4 molecule by Reaction 8. As a result, the molar production rate of CO_2 by Reaction 6 must be equal to the sum of the molar production rates of CO_2 and CH_4 by Reactions 7 and 8

$$q_6 = q_7 + q_8 \tag{3.37}$$

Table 3.3: Sets of reactions constants and charge transfer coefficients originally reported by Meyer *et al.* (2011), and genetically optimized to fit Li & Pickup (2006) overpotential and product selectivity data using Meyer et al.'s mechanism and the extended mechanism proposed in this work.

Constant	Meyer *et al.* (2011)	Meyer *et al.* (2011) Fitted to Li & Pickup (2006)	Extended mechanism Fitted to Li & Pickup (2006)
k_{If} $\left[s^{-1}\right]$	–	–	0.3306
k_{Ib} $\left[mol\ m^{-3}\ s^{-1}\right]$	–	–	1.8×10^{-3}
k_{II} $\left[mol\ m^{-3}\ s^{-1}\right]$	–	–	1.34×10^{2}
k_{IIIf} $\left[mol\ m^{-3}\ s^{-1}\right]$	–	–	1.01×10^{3}
k_{IIIb} $\left[s^{-1}\right]$	–	–	22.67
k_{1f} $\left[s^{-1}\right]$	2.8×10^{-6}	1.5×10^{-5}	3.49×10^{-5}
k_{1b} $\left[s^{-1}\right]$	2.21×10^{-2}	1.86×10^{-2}	13.784
k_{2f} $\left[s^{-1}\right]$	6.22×10^{-5}	8.92×10^{-4}	6.4×10^{-2}
k_{2b} $\left[mol\ m^{-3}\ s^{-1}\right]$	10^{-8}	5.54×10^{-9}	10^{-4}
k_{3f} $\left[mol\ m^{-3}\ s^{-1}\right]$	7.4×10^{-3}	3.5×10^{-3}	0.9619
k_{3b} $\left[mol\ m^{-3}\ s^{-1}\right]$	1.8×10^{3}	1.8×10^{3}	1.01×10^{2}
k_4 $\left[mol\ m^{-3}\ s^{-1}\right]$	2×10^{4}	3.4×10^{6}	2.77×10^{2}
k_5 $\left[mol\ m^{-3}\ s^{-1}\right]$	10^{-7}	3.15×10^{4}	5.67
k_6 $\left[mol\ m^{-3}\ s^{-1}\right]$	1.15×10^{-2}	9.53×10^{-1}	0.1391
k_7 $\left[mol\ m^{-3}\ s^{-1}\right]$	10^{-14}	6.78×10^{9}	9.2
k_8 $\left[mol\ m^{-3}\ s^{-1}\right]$	2.9×10^{-4}	7.42×10^{-4}	45.04
α_I	–	–	0.325
α_{II}	–	–	0.473
α_{III}	–	–	0.362
α_1	0.5	0.495	0.499
α_2	0.5	0.329	0.359
α_3	0.5	0.346	0.355
α_6	0.5	0.38	0.319
α_7	0.5	0.488	0.427
α_8	0.5	0.447	0.423

a result that follows mathematically from Equations (3.15) and (3.16).

To investigate the origin of the different species produced by the EOR, and in particular the chemical pathways leading to CO_2 formation, let us consider the following set of global reactions

$$CH_3CH_2OH \longrightarrow CH_3CHO + 2H^+ + 2e^- \quad \text{(GR1)}$$

$$CH_3CH_2OH + H_2O \longrightarrow CH_3COOH + 4H^+ + 4e^- \quad \text{(GR2)}$$

$$CH_3CH_2OH + H_2O \longrightarrow CO_2 + CH_4 + 4H^+ + 4e^- \quad \text{(GR3)}$$

$$CH_3CH_2OH + 3H_2O \longrightarrow 2CO_2 + 12H^+ + 12e^- \quad \text{(GR4)}$$

which represent, respectively, the overall processes leading to the generation of (GR1) acetaldehyde, (GR2) acetic acid, (GR3) CO_2 and CH_4 through Reactions 6 and 8, and (GR4) $2CO_2$ through Reactions 6 and 7, indicating the number of electrons released in each case. Hereafter the fraction of ethanol consumed by the different global reactions shall be denoted as the path selectivity, $s^{\mathrm{GR}j}$, $j = \{1,2,3,4\}$, such that $\sum_{j=1}^{4} s^{\mathrm{GR}j} = 1$. It is also convenient to introduce the effective electron generation number, n^{eff}, defined as the average number of electrons produced by each ethanol molecule consumed at the anode catalyst layer. This number, which gives us an idea about the overall effectiveness of the EOR in terms of current production, can be calculated from the path selectivities as

$$n^{\mathrm{eff}} = 2s^{\mathrm{GR1}} + 4s^{\mathrm{GR2}} + 4s^{\mathrm{GR3}} + 12s^{\mathrm{GR4}} \tag{3.38}$$

Note that this expression distinguishes the fractions of CO_2 produced by Reaction 6 that correspond either to (GR3) or (GR4).

The path selectivity of the four global reactions can be computed from the model results as

$$s^{\mathrm{GR1}} = \frac{q_1 + q_{\mathrm{III}} - q_2}{|q_1 + q_{\mathrm{I}}|}, \quad s^{\mathrm{GR2}} = \frac{q_4}{|q_1 + q_{\mathrm{I}}|}, \quad s^{\mathrm{GR3}} = \frac{q_8}{|q_1 + q_{\mathrm{I}}|}, \quad s^{\mathrm{GR4}} = \frac{q_7}{|q_1 + q_{\mathrm{I}}|} \tag{3.39}$$

where the denominator $|q_1 + q_{\mathrm{I}}|$ represents the ethanol consumption rate. The numerator of each path selectivity represents the rate of each global reaction according to the present model. Unlike the product selectivity, the path selectivity accounts for the fraction of ethanol that is consumed through each global reaction. A relationship between path and product selectivities is thus needed if we want to calculate the effective electron generation number from (3.38) using experimental data, which only provide product selectivities. To this end, the product selectivities are first expressed in terms of the path selectivities as

$$\begin{aligned}
s_{\mathrm{A}} &= \frac{s^{\mathrm{GR1}}}{s^{\mathrm{GR1}} + s^{\mathrm{GR2}} + 2\left(s^{\mathrm{GR3}} + s^{\mathrm{GR4}}\right)} \\
s_{\mathrm{AA}} &= \frac{s^{\mathrm{GR2}}}{s^{\mathrm{GR1}} + s^{\mathrm{GR2}} + 2\left(s^{\mathrm{GR3}} + s^{\mathrm{GR4}}\right)} \\
s_{\mathrm{CH_4}} &= \frac{s^{\mathrm{GR3}}}{s^{\mathrm{GR1}} + s^{\mathrm{GR2}} + 2\left(s^{\mathrm{GR3}} + s^{\mathrm{GR4}}\right)} \\
s_{\mathrm{CO_2}} &= \frac{s^{\mathrm{GR3}} + 2s^{\mathrm{GR4}}}{s^{\mathrm{GR1}} + s^{\mathrm{GR2}} + 2\left(s^{\mathrm{GR3}} + s^{\mathrm{GR4}}\right)}
\end{aligned} \tag{3.40}$$

where it has been taken into account that, according to their global stoichiometries, (GR3) and (GR4) yield two molecules of reaction products for each molecule of ethanol consumed. The above expressions are not linearly independent because the sum of the product selectivities is equal to unity by definition. Using three of them together with the linear relation $\sum_{j=1}^{4} s^{\mathrm{GR}j} = 1$, one obtains a system of four linear equations for the four

path selectivities, which can be readily inverted to give

$$
\begin{aligned}
s^{\mathrm{GR1}} &= \frac{s_{\mathrm{A}}}{s_{\mathrm{A}} + s_{\mathrm{AA}} + \frac{1}{2}\left(s_{\mathrm{CO_2}} + s_{\mathrm{CH_4}}\right)} \\
s^{\mathrm{GR2}} &= \frac{s_{\mathrm{AA}}}{s_{\mathrm{A}} + s_{\mathrm{AA}} + \frac{1}{2}\left(s_{\mathrm{CO_2}} + s_{\mathrm{CH_4}}\right)} \\
s^{\mathrm{GR3}} &= \frac{s_{\mathrm{CH_4}}}{s_{\mathrm{A}} + s_{\mathrm{AA}} + \frac{1}{2}\left(s_{\mathrm{CO_2}} + s_{\mathrm{CH_4}}\right)} \\
s^{\mathrm{GR4}} &= \frac{\frac{1}{2}\left(s_{\mathrm{CO_2}} - s_{\mathrm{CH_4}}\right)}{s_{\mathrm{A}} + s_{\mathrm{AA}} + \frac{1}{2}\left(s_{\mathrm{CO_2}} + s_{\mathrm{CH_4}}\right)}
\end{aligned}
\tag{3.41}
$$

Using these expressions in Equation (3.38), the effective electron generation number can alternatively be written as

$$
n^{\mathrm{eff}} = \frac{2s_{\mathrm{A}} + 4s_{\mathrm{AA}} + 6s_{\mathrm{CO_2}} - 2s_{\mathrm{CH_4}}}{s_{\mathrm{A}} + s_{\mathrm{AA}} + \frac{1}{2}\left(s_{\mathrm{CO_2}} + s_{\mathrm{CH_4}}\right)} = \frac{2s_{\mathrm{A}} + 4s_{\mathrm{AA}} + 6s_{\mathrm{CO_2}} - 2s_{\mathrm{CH_4}}}{1 - \frac{1}{2}\left(s_{\mathrm{CO_2}} + s_{\mathrm{CH_4}}\right)} \tag{3.42}
$$

thereby enabling its evaluation either from experimental data or numerical/modeling results.

3.5 Results and discussion

All the results presented below were obtained using the fixed set of physical constants, mass transport properties and design parameters presented in Table 3.4. This includes, in particular, a constant ethanol feed concentration of 1 M, and a cell operating temperature of 80°C, values adopted from the available experimental data used to optimize the kinetic constants.

Figure 3.3 shows the anode polarization curve predicted by the present model compared against the experimental data of Li & Pickup (2006). As can be seen, the model, optimized genetically to fit both the polarization and product selectivity data, correctly reproduces the anode overpotential in the whole current density range. For comparative purposes, the figure also shows the anode polarization curve reported by Meyer *et al.* (2011). When using the reaction mechanism and kinetic parameters suggested by Meyer *et al.* (2011), the polarization curve predicted by our model also agrees well with the experimental data, although the range of power densities under study is significantly narrower in this case.

Figures 3.4a, 3.4b and 3.4c show the variation of the product selectivities with the current density predicted by the present model compared with the experimental data reported by Li & Pickup (2006). It is seen that acetaldehyde (A), acetic acid

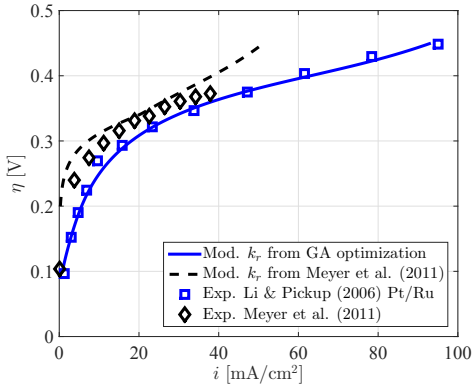

Figure 3.3: Anode overpotential measured experimentally by Meyer *et al.* (2011) and Li & Pickup (2006) and computed with the present model optimized to fit Li & Pickup's Li & Pickup (2006) overpotential and product selectivity data (solid line), and using the set of reaction constants proposed by Meyer *et al.* (2011) (dashed line).

(AA), and CO_2 selectivities are correctly reproduced at both high and low currents. The experimental data used to optimize the kinetic parameters of Table 3.2 precludes the production of methane at the current densities under study. However, the model predicts a slight methane yield ($s_{CH_4} \sim 0.05$) at very low currents (< 3 mA/cm^2), although no experimental data is available to confirm this result. Summarizing, the experimental results show that acetaldehyde selectivity increases with current density, while acetic acid decreases and CO_2 remains unchanged. These trends are correctly predicted by the optimized kinetic model. However, when using the mechanism of Meyer *et al.* (2011) the predicted selectivity of acetaldehyde remains above 90% up to 50 mA/cm^2, in contrast with the much lower values measured by Li & Pickup (2006) and captured by the new model. Interestingly enough, the new reaction mechanism yields much better agreement in terms of product selectivities also when the mechanism by Meyer *et al.* (2011) is supplied with a genetically optimized set of reaction constants, as has been recently shown by the authors elsewhere (Sanchez-Monreal *et al.*, 2016).

The improved performance of the extended model, particularly in terms of product selectivity, stems from the fact that it is not biased towards the formation of acetaldehyde like the mechanism originally proposed by Meyer *et al.* (2011), which hinders the production of acetic acid at low current densities due to the acetaldehyde bottleneck effect (Sanchez-Monreal *et al.*, 2016). By contrast, the new model is able to predict high acetic acid selectivities at low currents thanks to the new chemical pathway involving adsorbed species (Reactions I, II and III). The improvement is also observed in the predicted effective electron generation number. As seen in Figure 3.4d, the new model predicts values of $n^{\text{eff}} \simeq 4$ for all current densities in agreement with the experimental data reported in (Andreadis *et al.*, 2010; Li & Pickup, 2006). The agreement disappears

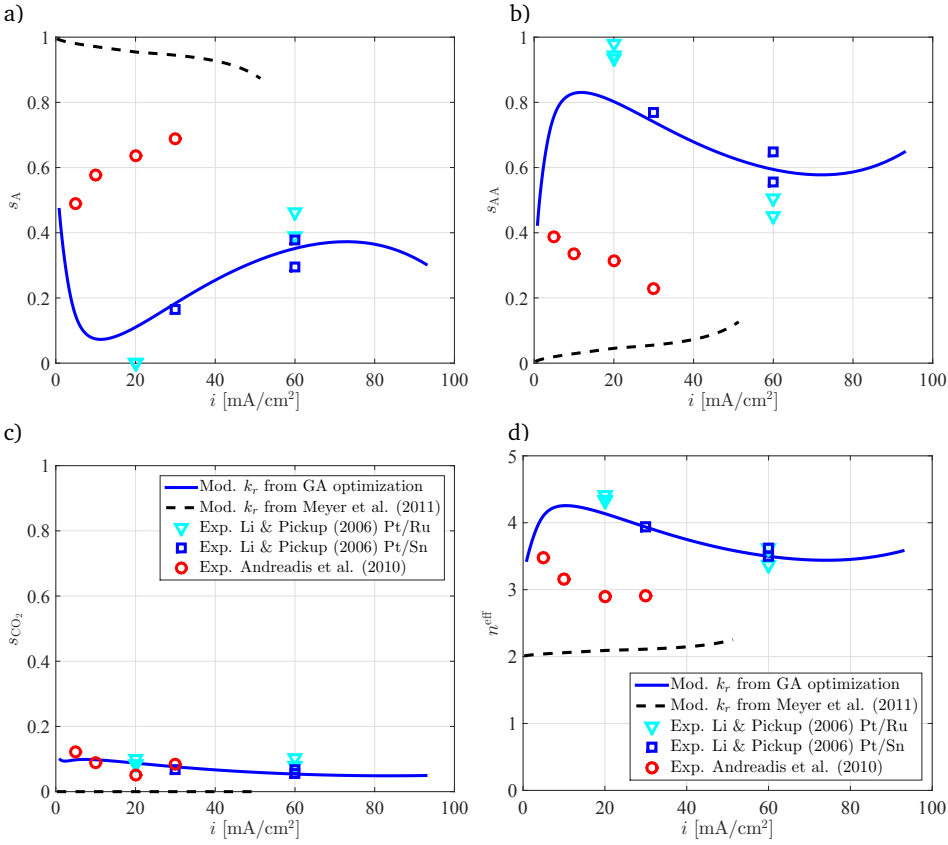

Figure 3.4: Variation of a) acetaldehyde, b) acetic acid, and c) CO_2 selectivity, and d) the effective electron generation number with the current density as obtained with the present model optimized to fit Li & Pickup (2006) overpotential and product selectivity data (solid line), and using the set of reaction constants proposed by Meyer *et al.* (2011) (dashed line).

when using the reaction mechanism of Meyer *et al.* (2011), which result in values of $n^{\text{eff}} \simeq 2$ much lower than those observed experimentally.

As previously discussed, the proposed model exhibits two paths leading to the production of adsorbed acetyl: one through acetaldehyde production (Reactions 1 and 2) and other through CH_3CHOH_{ads} (Reactions I and II). The numerical results show that this dual path fits perfectly in the full current density range. Figures 3.5 and 3.6 show, respectively, the net reaction rate of all the elementary reactions involved in the new mechanism and the area specific molar production (A, AA ans CO_2) and consumption (E and W) rates of the free species. Ethanol is consumed by two reactions, Reactions 1 and I, with a net consumption rate given by Equation (3.17). At low currents ethanol consumption proceeds mainly through Reaction I, while at high currents Reaction 1 takes over and becomes dominant although Reaction I still contributes significantly.

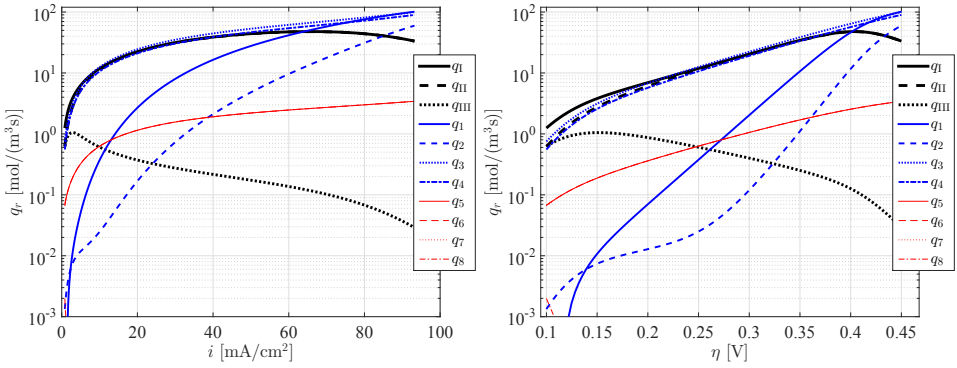

Figure 3.5: Net reaction rate of all the reactions involved in the model plotted as a function of current density (top) and anode overpotential (bottom). Calculation performed with the set of reactions constants optimized to fit Li & Pickup (2006) overpotential and product selectivity data. Note that since $q_5 = q_6 = q_7 + q_8$, with $q_8 \ll q_7$, the curves for q_5, q_6 and q_7 are indistinguishable.

Acetaldehyde is the only free intermediate species and therefore plays a crucial role in the EOR. It is produced by Reactions 1 and III and consumed by Reaction 2, with a net production rate given by Equation (3.18). As can be see, at low current densities acetaldehyde production occurs mainly through Reaction III. The rate of this reaction decreases steadily and is soon surpassed by that of Reaction 1, which constitutes the main path for acetaldehyde production at high currents. Acetaldehyde consumption becomes also significant at high currents, when the rate of Reaction 2 approaches that of Reaction 1. At this point, net acetaldehyde production starts to decline due to the effect of mass transport losses, since ethanol starvation forces the cell to draw current from acetaldehyde consumption. Note also that at low-to-medium currents the net production rate of acetaldehyde is relatively small compared to other species, particularly acetic acid, leading to the low acetaldehyde selectivity shown in Figure 3.4a in agreement with the experimental data reported in literature Andreadis *et al.* (2010); Li & Pickup (2006). By way of contrast, a significantly higher acetaldehyde selectivity is predicted at very low currents due to production through Reaction III, although no experimental data is available to validate this results.

Figure 3.7 shows the coverage factors of the five adsorbed species plotted as a function of the anode overpotential. The numerical results exhibit high CO_{ads} occupation at low-to-medium overpotentials, with representative values $\Theta_{CO_{ads}} = \{0.95, 0.9, 0.85, 0.8\}$ occurring for $\eta = \{0.167, 0.233, 0.273, 0.303\}$. At higher overpotentials, the Pt-sites left free by the carbonyl groups are occupied by adsorbed acetyl molecules, which promotes the production of acetic acid and the C–C bond breaking step. Figure 3.5 shows that the former (q_4) is significantly faster than the latter (q_5), with a ratio between both reaction rates of order 20 for all current densities. As a result, low CO_2 selectivity is observed at low and high overpotentials. Kavanagh *et al.* (2012) attributed the low CO_2 selectivity at

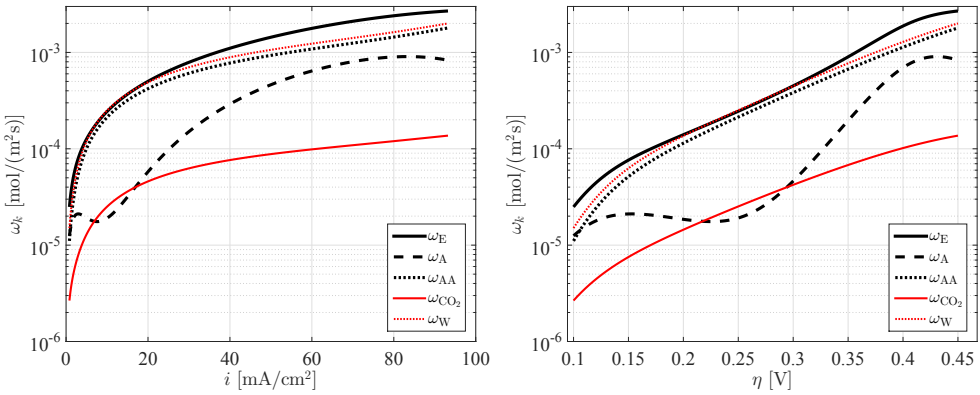

Figure 3.6: Net production and consumption rates of the five free species involved in the model plotted as a function of current density (top) and anode overpotential (bottom). Calculation performed with the set of reactions constants optimized to fit Li & Pickup (2006) overpotential and product selectivity data.

low overpotentials to the unavailability of oxidants, which inhibits the electro-oxidation of CO_{ads} to CO_2, the former effectively acting as a poisoning species. This is compatible with the high CO_{ads} occupation observed in Figure 3.7 at low-to-medium overpotentials. They also attributed the low CO_2 selectivity at higher potentials in Pt catalysts to the fact that C–C bond cleavage is inhibited by the presence of surface oxidants. This effect can not be observed in our model, where the hydroxyl groups are mainly attached to the secondary metal sites, since water activation into the Pt-sites does not occur at the overpotential range considered here (Vigier *et al.*, 2004*b*, 2006; Watanabe & Motoo, 1975).

Water activation is required, in particular, for Reactions 4, 6 and 7. As seen in Figure 3.6, the water consumption rate is lower than the ethanol consumption rate both at low and high current densities, the ranges where acetaldehyde selectivity is higher. There is only a narrow gap in the middle, with the lowest acetaldehyde selectivities, where water consumption is sightly higher than ethanol consumption. As indicated by the stoichiometry of the global reactions, water consumption is required for the production of acetic acid, CO_2 and CH_4 through reactions (GR2), (GR3) and (GR4), but not for the production of acetaldehyde through reaction (GR1), which explains the relation between water consumption and acetaldehyde selectivity.

Figures 3.8 show the percentage of the total current density generated by the elementary reactions involving electron transfer. It is seen that the reactions that lead to the formation of adsorbed acetyl (Reactions I, II, III, 1 and 2) generate between 70% and 75% of the total current density. The new path considered in this work (Reactions I, II and III) dominates at low current densities while the original path proposed by Meyer *et al.* (2011) (Reactions 1 and 2) dominates at higher currents. This is compatible with

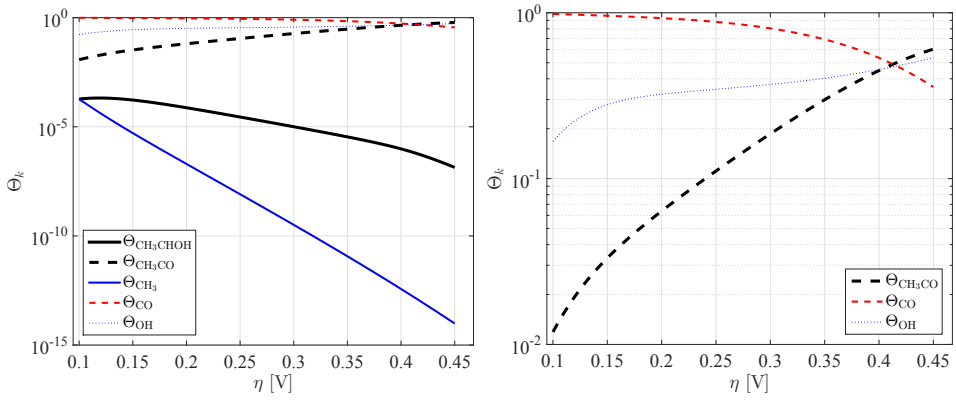

Figure 3.7: Coverage factors of the five adsorbed species involved in the model plotted as a function of anode overpotential (top) and detail representing only the three largest coverage factors (bottom). Calculation performed with the set of reactions constants optimized to fit Li & Pickup (2006) overpotential and product selectivity data.

the low acetaldehyde selectivities observed at low-to-medium current densities. Reaction 3 plays also a key role, since it generates about 20% of the total current and produces the adsorbed hydroxyl groups required for Reactions 4, 6 and 7 to proceed. The rest of the current is generated by Reactions 6 and 7, which have nearly the same reaction rate (see Figure 3.5), although the latter generates five times more current because it involves the transfer of five electrons instead of one. Note that Reaction 8 does not contribute to current generation. This is because the model predicts a negligible methane production ($q_8 \ll q_7$) following the lack of methane selectivity reported in the literature (Andreadis *et al.*, 2010; Antoniassi *et al.*, 2013; Li & Pickup, 2006). According to Equations (3.15) and (3.37), the same reaction rates are then obtained for Reactions 5, 6 and 7.

To finish the discussion of results, Figures 3.9 show the selectivity of the four global reactions GRj. Due to the negligible methane production predicted by the model, the selectivity of the global reactions is very similar to that of their corresponding product species. The largest selectivity of the second global reaction, leading to the production of acetic acid, agrees well with the effective electron generation number n^{eff}, which is always close to 4.

3.6 Conclusions

A detailed reaction mechanism has been proposed to describe ethanol electro-oxidation on binary Pt-based catalysts used in Direct Ethanol PEM Fuel Cells. The kinetic model involves five adsorbates (CH_3CHOH_{ads}, CH_3CO_{ads}, CO_{ads}, $CH_{3\,ads}$, and OH) and six free species, including two reactants (water and ethanol) and four product species

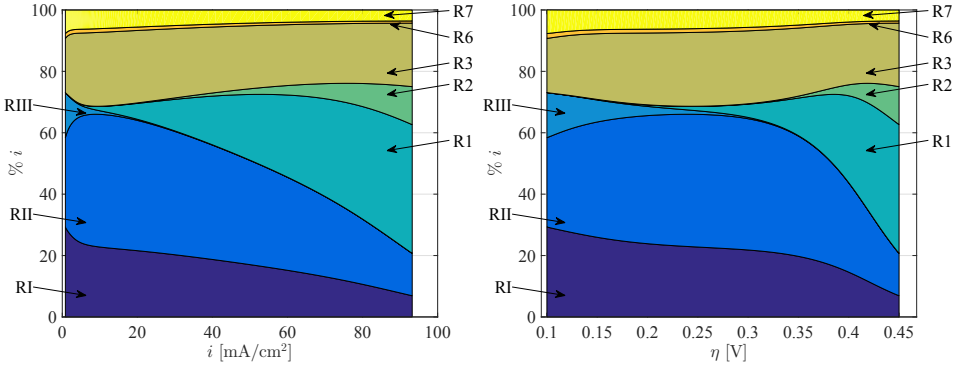

Figure 3.8: Percentage of the total current density generated by the elementary reactions involving electrons transfer plotted as a function of current density and anode overpotential. Calculation performed with the set of reactions constants optimized to fit Li & Pickup (2006) overpotential and product selectivity data.

(acetaldehyde, acetic acid, carbon dioxide, and methane). The model has been coupled to a 1D across-the-channel description of the mass transport processes that take place in the anode of a DEFC. The resulting mathematical problem yields the coverage factors of the adsorbates, the rates of the elementary reactions, the production/consumption rates of the free species, the cell current density, the product and global reaction selectivities, and the effective electron generation number for given values of the concentrations of ethanol and acetaldehyde at the anode channel, the anode overpotential, the cell temperature, and a particular set of kinetic constants. A new methodology based on the use of a multi-objective genetic algorithm has been used to optimize the set of kinetic constants that better fits selected results taken from the literature. As a result, the genetically optimized model is able to reproduce experimental anode polarization and product selectivity data for all the current densities under study.

Among the chemical species included in the reaction mechanisms, the main species involved in current generation are ethanol and acetaldehyde, and the main non-reactive products are acetic acid and CO_2, the concentration of secondary species such as methane being negligibly small. The computation of the global reaction selectivities and the effective electron generation number n^{eff}, introduced for the first time in this work, showed that the EOR produces roughly 4 electrons in the binary Pt-based catalyst compositions used in state-of-the-art DEFCs. This explains why previous EOR models with acetic acid as unique final product yielded good results in terms of polarization curves. However, they were unable to predict product selectivity.

The proposed 1D across-the-channel model could be extended to account for the remaining layers of the MEA, namely the cathode catalyst layer (ccl) and the cathode gas diffusion layer (cgdl). The resulting full MEA model (including the agdl, acl,

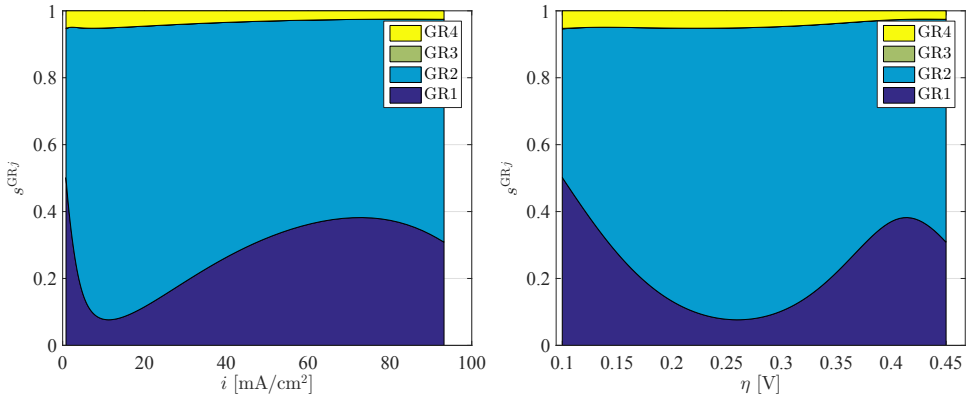

Figure 3.9: Selectivity of the global reactions GRj, $j = 1,\ldots,4$, plotted as a function of current density and anode overpotential. Calculation performed with the set of reactions constants optimized to fit Li & Pickup (2006) overpotential and product selectivity data.

mem, ccl, and cgdl, where mass/charge fluxes are dominated by transverse gradients in the through-plane direction) could be coupled to a 1D along-the-channel model (including the anode and cathode channels, where mass transport fluxes are dominated by downstream convection) to yield a fully predictive 1D+1D operational model for DEFCs. However, introducing such complexity at this early stage of development was considered counterproductive for our main goal of optimizing the multi-step EOR mechanism. As a result, such extensions are left for future work.

The influence of mass transport also warrants further work. The fibrous nature of the GDL combined with the cell assembly process are known to modify the effective mass transport properties. Effective diffusivities derived from detailed studies of fibrous porous layers (García-Salaberri *et al.*, 2015*a*,*b*) may be used to improve the values of the kinetic constants reported herein. The methodology described in this work could also be used to investigate the kinetics of the EOR on different catalyst layers, provided overpotential and product selectivity data were available.

References

ABD-EL-LATIF, A. A., MOSTAFA, E., HUXTER, S., ATTARD, G. & BALTRUSCHAT, H. 2010 Electrooxidation of ethanol at polycrystalline and platinum stepped single crystals: A study by differential electrochemical mass spectrometry. *Electrochim. Acta* **55** (27), 7951–7960.

AKHAIRI, M. A. F. & KAMARUDIN, S. K. 2016 Catalysts in direct ethanol fuel cell (DEFC): An overview. *Int. J. Hydrogen Energy* **41** (7), 4214–4228.

Table 3.4: Physical constants, mass transport coefficients and design parameters used in the 1D across-the-channel model.

Property	Value	Reference
Molecular diffusivity of ethanol in water, $D_{E,W}$	10^{-9} m^{2}s^{-1}	Lide (1990)
Molecular diffusivity of acetaldehyde in water, $D_{A,W}$	10^{-9} m^{2}s^{-1}	Lide (1990)
Molecular diffusivity of ethanol in membrane, $D_{E,mem}$	10^{-9} m^{2}s^{-1}	Andreadis *et al.* (2006)
Molecular diffusivity of acetaldehyde in membrane, $D_{A,mem}$	10^{-9} m^{2}s^{-1}	Andreadis *et al.* (2006)
GDL porosity, ϵ	0.78	Meyer *et al.* (2011)
Mass transfer coefficient ac/agdl, h	10^{-6} m s^{-1}	Assumed
Anode gdl thickness, δ_{agdl}	280 μm	Meyer *et al.* (2011)
Anode cl thickness, δ_{acl}	20 μm	Meyer *et al.* (2011)
Membrane thickness, δ_{mem}	178 μm	Meyer *et al.* (2011)
Ethanol feed concentration, $C_{E,ac}$	1 M	Assumed
Temperature, T	80	Assumed

ANDREADIS, G. M., PODIAS, A. K. M. & TSIAKARAS, P. E. 2008 The effect of the parasitic current on the Direct Ethanol PEM Fuel Cell Operation. *J. Power Sources* **181** (2), 214–227.

ANDREADIS, G. M., PODIAS, A. K. M. & TSIAKARAS, P. E. 2009 A model-based parametric analysis of a direct ethanol polymer electrolyte membrane fuel cell performance. *J. Power Sources* **194** (1), 397–407.

ANDREADIS, G. M., SONG, S. & TSIAKARAS, P. E. 2006 Direct ethanol fuel cell anode simulation model. *J. Power Sources* **157** (2), 657–665.

ANDREADIS, G. M., STERGIOPOULOS, V., SONG, S. & TSIAKARAS, P. E. 2010 Direct ethanol fuel cells: The effect of the cell discharge current on the products distribution. *Appl. Catal. B Environ.* **100** (1-2), 157–164.

ANDREADIS, G. M. & TSIAKARAS, P. E. 2006 Ethanol crossover and direct ethanol PEM fuel cell performance modeling and experimental validation. *Chem. Eng. Sci.* **61** (22), 7497–7508.

ANTOLINI, E. 2007 Catalysts for direct ethanol fuel cells. *J. Power Sources* **170** (1), 1–12.

ANTONIASSI, R. M., OLIVEIRA NETO, A., LINARDI, M. & SPINACÉ, E. V. 2013 The effect of acetaldehyde and acetic acid on the direct ethanol fuel cell performance using PtSnO2/C electrocatalysts. *Int. J. Hydrogen Energy* **38** (27), 12069–12077.

BACH DELPEUCH, A., MAILLARD, F., CHATENET, M., SOUDANT, P. & CREMERS, C. 2016 Ethanol oxidation reaction (EOR) investigation on Pt/C, Rh/C, and Pt-based bi- and tri-metallic electrocatalysts: A DEMS and in situ FTIR study. *Appl. Catal. B Environ.* **181**, 672–680.

BROUZGOU, A., PODIAS, A. K. M. & TSIAKARAS, P. 2013 PEMFCs and AEMFCs directly fed with ethanol: A current status comparative review. *J. Appl. Electrochem.* **43** (2), 119–136.

COLMATI, F., ANTOLINI, E. & GONZALEZ, E. R. 2006 Effect of temperature on the mechanism of ethanol oxidation on carbon supported Pt, PtRu and Pt$_3$Sn electrocatalysts. *J. Power Sources* **157** (1), 98–103.

EKDHARMASUIT, P., THERDTHIANWONG, A. & THERDTHIANWONG, S. 2013 Anode structure design for generating high stable power output for direct ethanol fuel cells. *Fuel* **113**, 69–76.

FATIH, K., NEBURCHILOV, V., ALZATE, V., NEAGU, R. & WANG, H. 2010 Synthesis and characterization of quaternary PtRuIrSn/C electrocatalysts for direct ethanol fuel cells. *J. Power Sources* **195** (21), 7168–7175.

FRIEDL, J. & STIMMING, U. 2013 Model catalyst studies on hydrogen and ethanol oxidation for fuel cells. *Electrochim. Acta* **101**, 41–58.

GARCÍA-SALABERRI, P. A., GOSTICK, J. T., HWANG, G., WEBER, A. Z. & VERA, M. 2015*a* Effective diffusivity in partially-saturated carbon-fiber gas diffusion layers: Effect of local saturation and application to macroscopic continuum models. *J. Power Sources* **296**, 440–453.

GARCÍA-SALABERRI, P. A., HWANG, G., VERA, M., WEBER, A. Z. & GOSTICK, J. T. 2015*b* Effective diffusivity in partially-saturated carbon-fiber gas diffusion layers: Effect of through-plane saturation distribution. *Int. J. Heat Mass Transf.* **86**, 319–333.

GARCÍA-SALABERRI, P. A., VERA, M. & ZAERA, R. 2011 Nonlinear orthotropic model of the inhomogeneous assembly compression of PEM fuel cell gas diffusion layers. *Int. J. Hydrogen Energy* **36** (18), 11856–11870.

GIZ, M. J. & CAMARA, G. A. 2009 The ethanol electrooxidation reaction at Pt (111): The effect of ethanol concentration. *J. Electroanal. Chem.* **625** (2), 117–122.

GOLDEMBERG, J., COELHO, S. T., NASTARI, P. M. & LUCON, O. 2004 Ethanol learning curve—the Brazilian experience. *Biomass and Bioenergy* **26** (3), 301–304.

GUO, H. & MA, C.-F. 2004 2D analytical model of a direct methanol fuel cell. *Electrochem. commun.* **6** (3), 306–312.

HITMI, H., BELGSIR, E. M., LÉGER, J.-M., LAMY, C. & LEZNA, R. O. 1994 A kinetic analysis of the electro-oxidation of ethanol at a platinum electrode in acid medium. *Electrochim. Acta* **39** (3), 407–415.

IWASITA, T. & PASTOR, E. 1994 A dems and FTir spectroscopic investigation of adsorbed ethanol on polycrystalline platinum. *Electrochim. Acta* **39** (4), 531–537.

JABLONSKI, A., KULESZA, P. J. & LEWERA, A. 2011 Oxygen permeation through Nafion 117 membrane and its impact on efficiency of polymer membrane ethanol fuel cell. *J. Power Sources* **196** (10), 4714–4718.

JAMES, D. D. & PICKUP, P. G. 2010 Effects of crossover on product yields measured for direct ethanol fuel cells. *Electrochim. Acta* **55** (11), 3824–3829.

KAMARUDIN, M. Z. F., KAMARUDIN, S. K., MASDAR, M. S. & DAUD, W. R. W. 2013 Review: Direct ethanol fuel cells. *Int. J. Hydrogen Energy* **38** (22), 9438–9453.

KAURANEN, P. S., SKOU, E. & MUNK, J. 1996 Kinetics of methanol oxidation on carbon-supported Pt and Pt + Ru catalysts. *J. Electroanal. Chem.* **404** (1), 1–13.

KAVANAGH, R., CAO, X. M., LIN, W. F., HARDACRE, C. & HU, P. 2012 Origin of low CO$_2$ selectivity on platinum in the direct ethanol fuel cell. *Angew. Chem. Int. Ed. Engl.* **51** (7), 1572–5.

KIM, I., HAN, O. H., CHAE, S. A., PAIK, Y., KWON, S.-H., LEE, K.-S., SUNG, Y.-E. & KIM, H. 2011 Catalytic reactions in direct ethanol fuel cells. *Angew. Chem. Int. Ed. Engl.* **50** (10), 2270–4.

KUTZ, R. B., BRAUNSCHWEIG, B., MUKHERJEE, P., BEHRENS, R. L., DLOTT, D. D. & WIECKOWSKI, A. 2011 Reaction pathways of ethanol electrooxidation on polycrystalline platinum catalysts in acidic electrolytes. *J. Catal.* **278** (2), 181–188.

LAMY, C., LIMA, A., LERHUN, V., DELIME, F., COUTANCEAU, C. & LÉGER, J.-M. 2002 Recent advances in the development of direct alcohol fuel cells (DAFC). *J. Power Sources* **105** (2), 283–296.

LÉGER, J.-M., ROUSSEAU, S., COUTANCEAU, C., HAHN, F. & LAMY, C. 2005 How bimetallic electrocatalysts does work for reactions involved in fuel cells?: Example of ethanol oxidation and comparison to methanol. *Electrochim. Acta* **50** (25), 5118–5125.

LI, G. & PICKUP, P. G. 2006 Analysis of performance losses of direct ethanol fuel cells with the aid of a reference electrode. *J. Power Sources* **161** (1), 256–263.

LI, H., SUN, G., CAO, L., JIANG, L. & XIN, Q. 2007 Comparison of different promotion effect of PtRu/C and PtSn/C electrocatalysts for ethanol electro-oxidation. *Electrochim. Acta* **52** (24), 6622–6629.

LIDE, D. R. 1990 *Handbook of Chemistry and Physics*. Boca Raton: CRC Press.

LIN EE, S. & BIRGERSSON, E. 2011 Two-Dimensional Approximate Analytical Solutions for the Direct Liquid Fuel Cell. *J. Electrochem. Soc.* **158** (10), B1224.

MEYER, M., MELKE, J. & GERTEISEN, D. 2011 Modelling and simulation of a direct ethanol fuel cell considering multistep electrochemical reactions, transport processes and mixed potentials. *Electrochim. Acta* **56** (11), 4299–4307.

PRAMANIK, H. & BASU, S. 2010 Modeling and experimental validation of overpotentials of a direct ethanol fuel cell. *Chem. Eng. Process. Process Intensif.* **49** (7), 635–642.

RIGHTMIRE, R. A., ROWLAND, R. L., BOOS, D. L. & BEALS, D. L. 1964 Ethyl Alcohol Oxidation at Platinum Electrodes. *J. Electrochem. Soc.* **111** (2), 242.

ROUSSEAU, S., COUTANCEAU, C., LAMY, C. & LÉGER, J.-M. 2006 Direct ethanol fuel cell (DEFC): Electrical performances and reaction products distribution under operating conditions with different platinum-based anodes. *J. Power Sources* **158** (1), 18–24.

SANCHEZ-MONREAL, J., GARCÍA-SALABERRI, P. A. & VERA, M. 2016 Mathematical Modeling of Direct Ethanol Fuel Cells Using a Multi-Step Chemical Kinetic Mechanism. *ECS Trans.* **72** (25), 1–16.

SHAO, M. H. & ADZIC, R. R. 2005 Electrooxidation of ethanol on a Pt electrode in acid solutions: in situ ATR-SEIRAS study. *Electrochim. Acta* **50** (12), 2415–2422.

SHIVHARE, M. R., ALLEN, R. G., SCOTT, K., MORRIS, A. J. & MARTIN, E. B. 2006 A kinetic model for the direct methanol fuel cell anode based on surface coverage. *J. Electroanal. Chem.* **595** (2), 145–151.

SHIVHARE, M. R., JACKSON, C. L., SCOTT, K. & MARTIN, E. B. 2007 Simplified model for the direct methanol fuel cell anode. *J. Power Sources* **173** (1), 240–248.

SONG, S. & TSIAKARAS, P. 2006 Recent progress in direct ethanol proton exchange membrane fuel cells (DE-PEMFCs). *Appl. Catal. B Environ.* **63** (3), 187–193.

SONG, S., WANG, G., ZHOU, W., ZHAO, X., SUN, G., XIN, Q., KONTOU, S. & TSIAKARAS, P. 2005*a* The effect of the MEA preparation procedure on both ethanol crossover and DEFC performance. *J. Power Sources* **140** (1), 103–110.

SONG, S., ZHOU, W., LIANG, Z., CAI, R., SUN, G., XIN, Q., STERGIOPOULOS, V. & TSIAKARAS, P. 2005*b* The effect of methanol and ethanol cross-over on the performance of PtRu/C-based anode DAFCs. *Appl. Catal. B Environ.* **55** (1), 65–72.

SOUSA, R., DOS ANJOS, D. M., TREMILIOSI-FILHO, G., GONZALEZ, E. R., COUTANCEAU, C., SIBERT, E., LÉGER, J.-M. & KOKOH, K. B. 2008 Modeling and simulation of the anode in direct ethanol fuels cells. *J. Power Sources* **180** (1), 283–293.

SUNDMACHER, K., SCHULTZ, T., ZHOU, S., SCOTT, K., GINKEL, M. & GILLES, E. D. 2001 Dynamics of the direct methanol fuel cell (DMFC): experiments and model-based analysis. *Chem. Eng. Sci.* **56** (2), 333–341.

SURESH, N.S. & JAYANTI, S. 2011 Cross-over and performance modeling of liquid-feed Polymer Electrolyte Membrane Direct Ethanol Fuel Cells. *Int. J. Hydrogen Energy* **36** (22), 14648–14658.

TANEDA, K. & YAMAZAKI, Y. 2006 Study of direct type ethanol fuel cells. *Electrochim. Acta* **52** (4), 1627–1631.

VERA, M. 2007 A single-phase model for liquid-feed DMFCs with non-Tafel kinetics. *J. Power Sources* **171** (2), 763–777.

VIGIER, F., COUTANCEAU, C., HAHN, F., BELGSIR, E. M. & LAMY, C. 2004*a* On the mechanism of ethanol electro-oxidation on Pt and PtSn catalysts: electrochemical and in situ IR reflectance spectroscopy studies. *J. Electroanal. Chem.* **563** (1), 81–89.

VIGIER, F., COUTANCEAU, C., PERRARD, A., BELGSIR, E. M. & LAMY, C. 2004*b* Development of anode catalysts for a direct ethanol fuel cell. *J. Appl. Electrochem.* **34** (4), 439–446.

VIGIER, F., ROUSSEAU, S., COUTANCEAU, C., LEGER, J.-M. & LAMY, C. 2006 Electrocatalysis for the direct alcohol fuel cell. *Top. Catal.* **40** (1-4), 111–121.

WANG, H., JUSYS, Z. & BEHM, R. J. 2004 Ethanol Electrooxidation on a Carbon-Supported Pt Catalyst: Reaction Kinetics and Product Yields. *J. Phys. Chem. B* **108** (50), 19413–19424.

WANG, H., JUSYS, Z. & BEHM, R.J. J. 2006 Ethanol electro-oxidation on carbon-supported Pt, PtRu and Pt3Sn catalysts: A quantitative DEMS study. *J. Power Sources* **154** (2), 351–359.

WANG, H.-F. & LIU, Z.-P. 2008 Comprehensive mechanism and structure-sensitivity of ethanol oxidation on platinum: new transition-state searching method for resolving the complex reaction network. *J. Am. Chem. Soc.* **130** (33), 10996–1004.

WANG, J., WASMUS, S. & SAVINELL, R. F. 1995 Evaluation of Ethanol, 1-Propanol, and 2-Propanol in a Direct Oxidation Polymer-Electrolyte Fuel Cell. *J. Electrochem. Soc.* **142** (12), 4218.

WATANABE, M. & MOTOO, S. 1975 Electrocatalysis by ad-atoms. *J. Electroanal. Chem. Interfacial Electrochem.* **60** (3), 275–283.

ZAKARIA, Z., KAMARUDIN, S. K. & TIMMIATI, S. N. 2016 Membranes for direct ethanol fuel cells: An overview. *Appl. Energy* **163**, 334–342.

Appendix 3.A Solution for the coverage factors

The coverage factors of the absorbed species (CH_3CHOH_{ads}, CH_3CO_{ads}, CO_{ads}, $CH_{3\,ads}$, and OH_{ads}) are determined by the system of non-linear algebraic equations (3.12)–(3.16)

$$\Theta_{CH_3CHOH}: \quad q_I - q_{II} - q_{III} = 0 \tag{3.12}$$

$$\Theta_{CH_3CO}: \quad q_2 + q_{II} - q_5 - q_4 = 0 \tag{3.13}$$

$$\Theta_{OH}: \quad q_3 - q_4 - q_6 - 2q_7 = 0 \tag{3.14}$$

$$\Theta_{CO}: \quad q_5 - q_6 = 0 \tag{3.15}$$

$$\Theta_{CH_3}: \quad q_5 - q_8 - q_7 = 0 \tag{3.16}$$

This non-linear system can not be solved analytically, and may have multiple solutions, including complex ones. To avoid non-physical solutions, the system can be reduced to a fifth-order polynomial equation for $\Theta_{OH_{ads}}$, which can be shown to have at least one real root between 0 and 1.

In order to simplify the algebraic expressions, the following notation will be used for the rate constants of the reactions involving electrons transfer

$$\mathfrak{K}_{rf} = k_{rf} \exp\left(\frac{\alpha_r nF}{RT}\eta_a\right) \quad \mathfrak{K}_{rb} = k_{rb} \exp\left(-\frac{(1-\alpha_r)nF}{RT}\eta_a\right) \tag{3.43}$$

Introducing expressions (3.1)–(3.11) for the reaction rates in Eqs. (3.12)–(3.16) yields the following set of equations for the coverage factors

$$\begin{aligned}\left(1-\Theta_{CH_3CHOH}-\Theta_{CH_3CO}-\Theta_{CO}-\Theta_{CH_3}\right)C_{E,acl}\mathfrak{K}_{If}\\ -\Theta_{CH_3CHOH}\mathfrak{K}_{Ib}-\Theta_{CH_3CHOH}\mathfrak{K}_{IIf}+\Theta_{CH_3CO}\mathfrak{K}_{IIb}-\Theta_{CH_3CHOH}\mathfrak{K}_{IIIf}\\ +\left(1-\Theta_{CH_3CHOH}-\Theta_{CH_3CO}-\Theta_{CO}-\Theta_{CH_3}\right)C_{A,acl}\mathfrak{K}_{IIIb}=0\end{aligned} \tag{3.12'}$$

$$\begin{aligned}\left(1-\Theta_{CH_3CHOH}-\Theta_{CH_3CO}-\Theta_{CO}-\Theta_{CH_3}\right)C_{A,acl}\mathfrak{K}_{2f}-\Theta_{CH_3CO}\mathfrak{K}_{2b}\\ +\Theta_{CH_3CHOH}\mathfrak{K}_{IIf}-\Theta_{CH_3CO}\mathfrak{K}_{IIb}-\Theta_{CH_3CO}\Theta_{OH}k_4-\Theta_{CH_3CO}k_5=0\end{aligned} \tag{3.13'}$$

$$\left(1-\Theta_{OH}\right)\mathfrak{K}_{3f}-\Theta_{OH}\mathfrak{K}_{3b}-\Theta_{CH_3CO}\Theta_{OH}k_4-\Theta_{CO}\Theta_{OH}\mathfrak{K}_6-2\Theta_{CH_3}\Theta_{OH}^2\mathfrak{K}_7=0 \tag{3.14'}$$

$$\Theta_{CH_3CO}k_5-\Theta_{CH_3}\Theta_{OH}^2\mathfrak{K}_7-\Theta_{CH_3}\mathfrak{K}_8=0 \tag{3.15'}$$

$$\Theta_{CH_3CO}k_5-\Theta_{CO}\Theta_{OH}\mathfrak{K}_6=0 \tag{3.16'}$$

To convert this system of equations into a single equation for $\Theta_{OH_{ads}}$, a series of algebraic

transformations are needed. First, from Eq. (3.15') we get

$$\Theta_{CH_3CO} = \frac{\Theta_{CH_3}\left(\Re_7\Theta_{OH}^2 + \Re_8\right)}{k_5} \tag{3.44}$$

Substituting this expression in Eq. (3.16') leads to

$$\Theta_{CO} = \frac{\Theta_{CH_3}\left(\Re_7\Theta_{OH}^2 + \Re_8\right)}{\Re_6\Theta_{OH}} \tag{3.45}$$

And using (3.44) and (3.45) in Eq. (3.12') yields

$$\Theta_{CH_3CHOH} = \left(1 - \frac{\Theta_{CH_3}\left(\Re_7\Theta_{OH}^2 + \Re_8\right)}{\Re_6\Theta_{OH}} - \Theta_{CH_3}\right)\chi_1 - \left(\frac{\Theta_{CH_3}\left(\Re_7\Theta_{OH}^2 + \Re_8\right)}{k_5}\right)\chi_2 \tag{3.46}$$

with

$$\chi_1 = \frac{C_{E,acl}\Re_{If} + C_{A,acl}\Re_{IIIb}}{C_{E,acl}\Re_{If} + C_{A,acl}\Re_{IIIb} + \Re_{Ib} + \Re_{IIf} + \Re_{IIIf}} \tag{3.47}$$

$$\chi_2 = \frac{C_{E,acl}\Re_{If} + C_{A,acl}\Re_{IIIb} - \Re_{IIb}}{C_{E,acl}\Re_{If} + C_{A,acl}\Re_{IIIb} + \Re_{Ib} + \Re_{IIf} + \Re_{IIIf}} \tag{3.48}$$

Substituting now (3.44), (3.45) and (3.46) in Eq. (3.13') provides the following expression

$$\Theta_{CH_3} = \frac{C_{A,acl}\Re_{2f} + \left(\Re_{IIf} - C_{A,acl}\Re_{2f}\right)\chi_1}{\beta_{-1}\Theta_{OH}^{-1} + \beta_0 + \beta_1\Theta_{OH} + \beta_2\Theta_{OH}^2 + \beta_3\Theta_{OH}^3} \tag{3.49}$$

with

$$\beta_{-1} = C_{A,acl}\Re_{2f}\frac{\Re_8}{\Re_6} + \left(\Re_{IIf} - C_{A,acl}\Re_{2f}\right)\chi_1\frac{\Re_8}{\Re_6} \tag{3.50}$$

$$\begin{aligned}\beta_0 &= -C_{A,acl}\Re_{2f} - \left(C_{A,acl}\Re_{2f} + \Re_{2b} + k_5\right)\frac{\Re_8}{k_5} \\ &\quad + \left(C_{A,acl}\Re_{2f} - \Re_{IIf}\right)\left(\chi_1 + \chi_2\frac{\Re_8}{k_5}\right) - \Re_{IIb}\frac{\Re_8}{k_5}\end{aligned} \tag{3.51}$$

$$\beta_1 = \frac{C_{A,acl}\Re_{2f}\Re_7}{k_5} + \frac{k_4\Re_8}{k_5} + \chi_1\frac{\Re_7}{\Re_6}\left(\Re_{IIf} - C_{A,acl}\Re_{2f}\right) \tag{3.52}$$

$$\beta_2 = \left(C_{A,acl}\Re_{2f} + \Re_{2b} + k_5\right)\frac{\Re_7}{k_5} + \left(\Re_{IIb} + \chi_2\left(\Re_{IIf} - C_{A,acl}\Re_{2f}\right)\right)\frac{\Re_7}{k_5} \tag{3.53}$$

$$\beta_3 = \frac{k_4\Re_7}{k_5} \tag{3.54}$$

On the other hand, with the aid of (3.44) and (3.45), Eq. (3.14') can be written exclusively

in terms of Θ_{OH} and Θ_{CH_3}, such that

$$1-\varphi\Theta_{OH}-\left(\eta_0+\eta_1\Theta_{OH}+\eta_2\Theta_{OH}^2+\eta_3\Theta_{OH}^3\right)\Theta_{CH_3}=0 \tag{3.55}$$

where

$$\varphi=1+\frac{\mathfrak{K}_{3b}}{\mathfrak{K}_{3f}},\quad \eta_0=\frac{\mathfrak{K}_8}{\mathfrak{K}_{3f}},\quad \eta_1=\frac{k_4\mathfrak{K}_8}{k_5\mathfrak{K}_{3f}},\quad \eta_2=3\frac{\mathfrak{K}_7}{\mathfrak{K}_{3f}},\quad \eta_3=\frac{k_4\mathfrak{K}_7}{k_5\mathfrak{K}_{3f}} \tag{3.56}$$

Combining Eqs. (3.49) and (3.55), the following equation for $\Theta_{OH_{ads}}$ is obtained

$$\begin{aligned}
&(\quad +\varphi\beta_3 \quad\quad)\Theta_{OH}^5\\
&+(B\eta_3+\varphi\beta_2\ -\beta_3\ )\Theta_{OH}^4\\
&+(B\eta_2+\varphi\beta_1\ -\beta_2\ )\Theta_{OH}^3\\
&+(B\eta_1+\varphi\beta_0\ -\beta_1\ )\Theta_{OH}^2\\
&+(B\eta_0+\varphi\beta_{-1}-\beta_0\ )\Theta_{OH}\\
&+(\quad\quad\quad\quad -\beta_{-1})\quad\quad =0
\end{aligned} \tag{3.57}$$

The fact that this is a fifth-order polynomial equation guarantees that there is at least one real root of (3.57). Moreover, the positive and negative values of the highest order coefficient ($\varphi\beta_3$) and the independent term ($-\beta_{-1}$) make sure that this root is positive. In fact, in order to be physically meaningful, the value of Θ_{OH} thus obtained must lie between 0 and 1.

CHAPTER

FOUR

A 1D+1D model for direct ethanol fuel cells based on detailed ethanol electro-oxidation kinetics

Contents

4.1 Introduction

This chapter presents an isothermal, single-phase, 1D+1D model for direct ethanol fuel cells (DEFC) involving free and adsorbed intermediate species. The detailed reaction mechanism for the ethanol oxidation reaction (EOR) developed in Chapter 3 is coupled to a one-dimensional description of diffusive transport across the cathode gas diffusion layer (García-Salaberri *et al.*, 2014; Vera, 2007). In addition, a simple advection model is proposed to describe the spatial variation of the concentrations of the different species as well as the local and parasitic current densities along the flow channels. The combined 1D+1D model is optimized using a genetic algorithm to fit published experimental data. The resulting DEFC model is used to investigate the effects of production, accumulation and consumption of ethanol and other free species along the flow channels. A parametric study of the cell performance for varying operating conditions, including different ethanol dilutions and feed flow rates, is finally presented.

The first DEFC models considered that the EOR was much slower than the oxygen reduction reaction (ORR). As a result, the activation overpotential of the cathodic reaction

was often neglected (Andreadis *et al.*, 2006; Andreadis & Tsiakaras, 2006). Later work modeled the ORR as a single Tafel reaction (Andreadis *et al.*, 2008, 2009; Lin Ee & Birgersson, 2011; Pramanik & Basu, 2010; Suresh & Jayanti, 2011), while, more recently, the inverse reaction has also been included making use of Butler-Volmer kinetics (Meyer *et al.*, 2011). The combined effect of multi-component gaseous diffusion in the cathode compartment and hydraulic permeation through the membrane has been considered as well (Suresh & Jayanti, 2011).

A common feature of most DEFC models published so far is that they are limited to one-dimensional (1D) across-the-channel formulations (Andreadis *et al.*, 2008, 2009, 2006; Andreadis & Tsiakaras, 2006; Meyer *et al.*, 2011; Pramanik & Basu, 2010; Suresh & Jayanti, 2011). In this case, species transport across the MEA is induced by molecular diffusion (Meyer *et al.*, 2011) or the combined action of molecular diffusion and water drag (Andreadis *et al.*, 2008, 2009, 2006; Andreadis & Tsiakaras, 2006; Pramanik & Basu, 2010; Suresh & Jayanti, 2011). Due to the key role played by the electrochemical reactions, the catalyst layers are often represented as porous media of finite thickness with non-uniform species concentrations (Andreadis *et al.*, 2008, 2009, 2006; Andreadis & Tsiakaras, 2006; Meyer *et al.*, 2011; Pramanik & Basu, 2010; Suresh & Jayanti, 2011). Two-dimensional (2D) along-the-channel models are more scarce (Lin Ee & Birgersson, 2011; Sousa *et al.*, 2008), and in this case the electrochemical reactions at the catalyst layers are typically introduced as boundary, or jump, conditions.

4.2 Model assumptions and physical domain

The assumptions adopted in the development of the mathematical model are very similar to those considered in Chapter 3 (Sec. 3.2): *i*) the cell operates in steady-state; *ii*) the cell temperature (T) is uniform *iii*) the concentrations of ethanol (E), acetaldehyde (A), and acetic acid (AA) are sufficiently small for the liquid phase to be considered a diluted aqueous solution; *iv*) the membrane (assumed to be Nafion® 117) is fully hydrated and is impermeable to gases; *v*) the overpotentials, coverage factors, and free species concentrations are constant across the catalyst layers; *vi*) the anode catalyst layer consists of a Pt-based binary catalyst that allows the absorption of hydroxyl groups at lower potentials on the secondary metal according to the bifunctional mechanism described in (Vigier *et al.*, 2004, 2006; Watanabe & Motoo, 1975). The only difference is that, in addition to the protonic resistance of the membrane, the full 1D+1D model includes as fitting parameter an effective electronic/contact resistance R_{con} that contributes to the overall ohmic resistance of the cell.

Regarding the physical domain, shown in Figure 4.1, the cell is divided into seven regions: anode channel (ac); anode gas diffusion layer (agdl); anode catalyst layer (acl); polymeric membrane (mem); cathode catalyst layer (ccl); cathode gas diffusion layer (cgdl); and cathode channel (cc). The figure also shows the domains covered by the

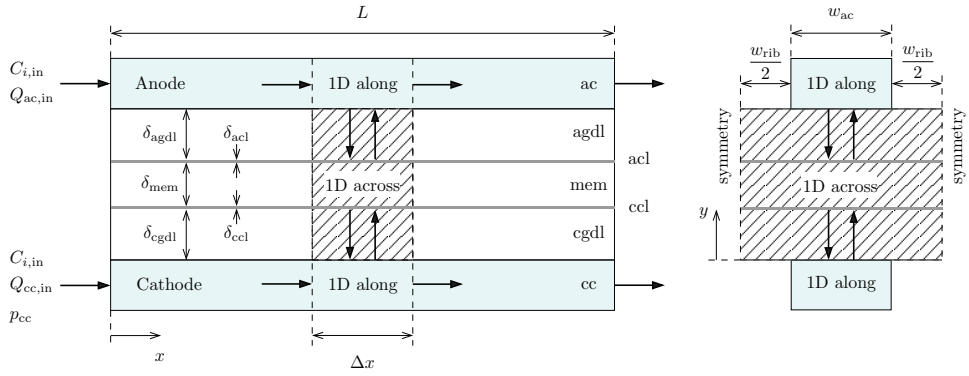

Figure 4.1: Schematic representation of the physical domains covered by the one-dimensional across- and along-the-channel models, showing the inlet conditions, the channel and rib dimensions (length, L, channel width, w_{ac}, and rib width, w_{rib}), and the thickness of the different layers of the MEA (δ_ℓ, ℓ = agdl, acl, mem, ccl, cgdl). Left: side view; right: cross-sectional view.

1D across-the-channel model (the MEA: agdl, acl, mem, ccl, and cgdl, dominated by transverse diffusive fluxes in the y-direction) and the 1D along-the-channel model (the flow channels: ac and cc, dominated by longitudinal convective fluxes in the x-direction). It also shows the notation for the inlet conditions at the anode and cathode channels, and the thickness of the different layers of the MEA.

4.3 1D across-the-channel model

The 1D across-the-channel model presented in this chapter is based on the anode model developed in Chapter 3 (Sec. 3.4), extended to cover also the cathode gas diffusion layer.

4.3.1 Anode electrode

The anode electrode is described using the optimized model presented in Chapter 3. As previously discussed, this model accounts for a detailed kinetic description of the EOR that is able to predict anode polarization and product selectivity data taken from the literature. It also incorporates the parasitic current generated at the cathode electrode by the crossover fluxes of ethanol and acetaldehyde and the associated mixed potential.

4.3.2 Cathode electrode

The cathode side of the MEA is described in a much simpler way. The ORR is modeled as a single reversible reaction with Butler-Volmer kinetics, whereas species mass transport

across the cathode gas diffusion layer is assumed to take place purely by diffusion. For the sake of simplicity, no attempt has been made to include multiphase flow effects, as DEFC performance is known to be limited mainly by the sluggish kinetics of the EOR. The impact of multiphase flow effects, such as cathode flooding, are limited in DEFC due to the low current densities reached in these cells.

4.3.2.1 Cathode catalyst layer (ccl)

Unlike the detailed EOR model considered in the anode, in the cathode the OOR will be modeled adopting a more simplistic approach, based on a single reversible reaction of the form

$$O_2 + 4H^+ + 4e^- \rightleftharpoons 2H_2O \tag{4.1}$$

with the corresponding oxygen consumption rate given by the Butler-Volmer equation

$$q_{O_2} = \frac{(aj_0)_c}{4F} \frac{C_{O_2,ccl}}{C_{O_2,ref}} \left[\exp\left(\frac{2\alpha F \eta_c}{RT} \right) - \exp\left(-\frac{2(1-\alpha)F\eta_c}{RT} \right) \right] \tag{4.2}$$

where $C_{O_2,ref}$ is the reference molar concentration of oxygen in air at standard conditions, a is the effective catalyst surface area per unit volume, and j_0 is the exchange current density of the cathodic reaction. Note that the net reaction rate q_{O_2} represents the number of moles of oxygen consumed by the ORR per unit volume per unit time.

Although a reduction of the active catalyst surface area should be expected in (4.2) due to the presence of adsorbed species generated by the parasitic electrooxidation of ethanol (e.g., CO poisoning), and to the occupation of the active catalyst sites by the OH-groups adsorbed at high cathode overpotentials, this effect will be ignored, as it is known to introduce corrections below 10% in practical applications (Meyer *et al.*, 2011). According to the global stoichiometry of reaction (4.1), the net current density generated by the ORR is

$$i_c = 4F\delta_{ccl} q_{O_2} \tag{4.3}$$

which must be equal to the sum of the current produced at the anodic reaction, i, plus the parasitic current density, i_p, generated by the electro-oxidation of the free species that cross the membrane from anode to cathode

$$i_c = i + i_p \tag{4.4}$$

It is important to note that in Eq. (4.3) the factor δ_{ccl} represents the thickness of the cathode catalyst layer, where according to assumption *v*) the reaction rate q_{O_2} is assumed to be spatially uniform.

In the following discussion the transfer coefficient appearing in (4.2) will be assumed to be $\alpha = 0.5$, which facilitates the obtention of an analytical equation for the activation polarization in terms of the current density. Specifically, in this case the Butler-Volmer

equation (4.2) can be rewritten as

$$q_{O_2} = \frac{(ai_0)_c}{2F} \frac{C_{O_2,ccl}}{C_{O_2,ref}} \sinh\left(\frac{F\eta_c}{RT}\right) \tag{4.5}$$

which, together with Eqs. (4.3) and (4.4), leads to the following closed-form analytical expression for the cathode overpotential

$$\eta_c = \frac{RT}{F} \sinh^{-1}\left(\frac{1}{2\delta_{ccl}} \frac{i_c}{(aj_0)_c} \frac{C_{O_2,ref}}{C_{O_2,ccl}}\right) \tag{4.6}$$

in terms of the cathode current density, i_c, and the concentration of oxygen at the cathode catalyst layer, $C_{O_2,ccl}$.

4.3.2.2 Cathode gas diffusion layer (cgdl)

The molar flux of species k, transported by convection and diffusion from the bulk fluid in the cathode channel (cc) to the cathode channel/gas diffusion layer interface, and from there by diffusion to the cathode catalyst layer (ccl), is computed using an overall mass transport coefficient $\mathfrak{h}_c$ such that

$$N_k = \mathfrak{h}_c\left(C_{k,cc} - C_{k,ccl}\right) \qquad k = O_2, W, AA \tag{4.7}$$

where $C_{k,cc}$ is the bulk concentration of species k in the cathode channel, and $C_{k,ccl}$ is the effective concentration of species k at the cathode catalyst layer. Like in Chapter 3, the sign of N_k indicates whether the molar flux of species k is directed in the positive or negative y-direction. However, due to the opposite relative positions of the cathode channel and catalyst layer along the y-axis, shown in Figure 4.1, in this case $N_k > 0$ means that the net flux of species k goes from the channel to the catalyst layer, while $N_k < 0$ means that goes in the opposite direction.

The effect of convective drag in the cathode gas diffusion layer is expected to be small, just like in the anode, so it will be neglected. Thus, if mass transport in the cathode is dominated by molecular diffusion, the global transport coefficient can be written as

$$\mathfrak{h}_c = \left(\frac{1}{h} + \frac{\delta_{cgdl}}{D^{eff}_{k,cgdl}}\right)^{-1} \tag{4.8}$$

which combines the effects of convective/diffusive transport at the cathode flow channel through the convective coefficient h, and Fickian diffusion at the cathode gas diffusion layer (cgdl) through the diffusive transport coefficient $D^{eff}_{k,cgdl}/\delta_{cgdl}$. Like in the anode model presented in Chapter 3, the Bruggeman correction is used to calculate the effective diffusivity, $D^{eff}_{k,cgdl} = \epsilon^{3/2} D_{k,air}$, in terms of the porosity ϵ of the cathode gas diffusion layer

and of the bulk diffusivity $D_{k,\text{air}}$ of the transported species in air.

The molar flux of oxygen that reaches the cathode catalyst layer from the cathode flow channel must equal the rate of oxygen consumption by electrochemical reactions

$$N_{\text{O}_2} = \frac{i_\text{c}}{4F} \tag{4.9}$$

Combining Eqs. (4.7) and (4.9) leads to the following expression for the concentration of oxygen at the cathode catalyst layer

$$C_{\text{O}_2,\text{ccl}} = C_{\text{O}_2,\text{cc}} - \frac{1}{\mathfrak{h}_\text{c}} \frac{i_\text{c}}{4F} \tag{4.10}$$

which can be used in (4.6) to determine the cathode overpotential η_c for given values of $C_{\text{O}_2,\text{cc}}$ and i_c.

The water molecules produced by the ORR and desorbed from the catalyst surface, as well as the water that permeates the membrane by crossover, must be evacuated through the cathode gas diffusion layer to the cathode channel. Assuming that all water is transported in the form of water vapor, the total flux of water (W) that emerges from the cathode catalyst layer towards the cathode gas diffusion layer can be written as

$$N_\text{W} = N_{\text{W,cross}} - \left(\frac{i}{2F} + n_d^\text{W} \frac{i}{F} \right) \tag{4.11}$$

where the first term represents the molar flux of water generated by the oxidation of the crossover species, to be evaluated next, the second term is the water produced by the OOR with the protons conducted by the membrane from anode to cathode, i.e., the cell current density, and the the last term is the electroosmotic drag of water that crosses the membrane.

4.3.3 Species crossover

As already discussed, the permeation of ethanol and other species through the polymeric membrane constitutes a severe problem for DEFC performance, particularly at low current densities. The reason is that the reactive species that cross the membrane are prone to react electrochemically with oxygen at the cathode catalyst layer, which results in a parasitic current that increases the cathode overpotential.

For the sake of simplicity, the present model will only consider the effects of ethanol and acetaldehyde crossover, as in low-temperature DEFCs they represent the two major reacting species generating electrons during the electro-oxidation process. Additionally, because the cathode potential is always higher than the anode potential, the overpotential $\eta = E - E^\star$ of the cathodic parasitic reactions is higher than that of the anodic oxidation reactions. Thus, the parasitic oxidation of ethanol and acetaldehyde will be assumed to

proceed to completion, yielding acetic acid through the overall reactions

$$CH_3CH_2OH + O_2 \rightarrow CH_3COOH + H_2O \tag{4.12}$$

$$CH_3CHO + \frac{1}{2}O_2 \rightarrow CH_3COOH \tag{4.13}$$

involving respectively the transfer of 4 and 2 electrons.

Reaction (4.12) is obtained as the sum of the global reaction (GR2) and the forward reaction (4.1)

$$\begin{array}{lll} CH_3CH_2OH + H_2O \rightarrow CH_3COOH + 4H^+ + 4e^- & & \text{(GR2)} \\ O_2 + 4H^+ + 4e^- \rightarrow 2H_2O & & \text{(4.1)} \\ \hline CH_3CH_2OH + O_2 \rightarrow CH_3COOH + H_2O & & \text{(4.12)} \end{array}$$

while reaction (4.13) stems from a combination of Reactions 2, 3 and 4 from Table 3.1 and one half of the forward reaction (4.1)

$$\begin{array}{lll} CH_3CHO \rightarrow CH_3CO_{ads} + H^+ + e^- & & \text{Reaction 2} \\ H_2O \rightarrow OH_{ads} + H^+ + e^- & & \text{Reaction 3} \\ CH_3CO_{ads} + OH_{ads} \rightarrow CH_3COOH & & \text{Reaction 4} \\ \frac{1}{2}O_2 + 2H^+ + 2e^- \rightarrow H_2O & & (4.1)\times\frac{1}{2} \\ \hline CH_3CHO + \frac{1}{2}O_2 \rightarrow CH_3COOH & & \text{(4.13)} \end{array}$$

The parasitic current density induced at the cathode catalyst layer by crossover can be obtained as the sum of the ethanol and acetaldehyde parasitic current densities

$$i_p = i_{E,p} + i_{A,p} \tag{4.14}$$

According to the global stoichiometries of reactions (4.12) and (4.13), the ethanol and acetaldehyde parasitic current densities can be expressed as

$$i_{E,p} = -4FN_{E,\text{cross}} \quad \text{and} \quad i_{A,p} = -2FN_{A,\text{cross}} \tag{4.15}$$

in terms of the respective crossover fluxes, given by (3.31). The assumption that both ethanol and acetaldehyde are completely oxidized to acetic acid agrees well with the values of the EOR effective electron generation number given in Chapter 3 (see Fig. 3.4), always close to $n^{\text{eff}} = 4$. Note that with the orientation of the coordinate system shown in Figure 4.1 the crossover fluxes $N_{E,\text{cross}}$ and $N_{A,\text{cross}}$ are always negative, since ethanol and acetaldehyde cross the membrane in the negative y-direction, which is the reason why the minus signs must be used in (4.15).

According to reaction (4.12), the electrooxidation of ethanol to acetic acid produces one mole of acetic acid and one mole of water per mole of ethanol. In consequence, the

molar production rates of acetic acid and water vapor induced by the parasitic oxidation of ethanol (E) at the cathode catalyst are given by

$$\omega_{\mathrm{W,c}}^{(\mathrm{E})} = \omega_{\mathrm{AA,c}}^{(\mathrm{E})} = N_{\mathrm{E,cross}} = -\frac{i_{\mathrm{E},p}}{4F} \tag{4.16}$$

By contrast, the electrooxidation of acetaldehyde to acetic acid following reaction (4.13) does not produce water. In this case, the molar production rate of acetic acid due to the parasitic oxidation of acetaldehyde (A) at the cathode catalyst layer is given by

$$\omega_{\mathrm{AA,c}}^{(\mathrm{A})} = N_{\mathrm{A,cross}} = -\frac{i_{\mathrm{A},p}}{2F} \tag{4.17}$$

The molar flux of water induced by the electrooxidation of the crossover species at the cathode catalyst layer is thus limited to the contribution of the parasitic oxidation of ethanol

$$N_{\mathrm{W,cross}} = \omega_{\mathrm{W,c}}^{(\mathrm{E})} = -\frac{i_{\mathrm{E},p}}{4F} \tag{4.18}$$

Substituting the last expression in Eq. (4.11), the net molar flux of water leaving the cathode catalyst layer can be written as

$$N_{\mathrm{W}} = -\left(\frac{i_{\mathrm{E},p}}{4F} + \frac{i}{2F} + n_d^{\mathrm{W}}\frac{i}{F}\right) \tag{4.19}$$

in terms of the parasitic current density induced by ethanol crossover, $i_{\mathrm{E},p}$, and the net current density, i, generated by the cell. Similarly, the net molar production rate of acetic acid at the cathode catalyst layer is obtained adding the contributions due to ethanol and acetaldehyde crossover

$$\omega_{\mathrm{AA,c}} = \omega_{\mathrm{AA,c}}^{(\mathrm{E})} + \omega_{\mathrm{AA,c}}^{(\mathrm{A})} \tag{4.20}$$

4.3.4 Solution procedure

This section summarizes the procedure used to solve the mathematical problem stated in the previous sections. The cornerstone that allows closing the problem is the equation for the cell voltage, V, which is here expressed as

$$V = E_{\mathrm{cell}} - \eta_{\mathrm{a}} - \eta_{\mathrm{c}} - \eta_{\mathrm{ohm}} \tag{4.21}$$

in terms of the cell reversible potential, E_{cell}, the anode overpotential, η_{a}, the cathode overpotential, η_{c}, and the ohmic overpotentital

$$\eta_{\mathrm{ohm}} = i\,(R_{\mathrm{mem}} + R_{\mathrm{con}}) \tag{4.22}$$

written here in terms of the protonic resistance of the membrane, R_{mem}, and an effective electronic/contact resistance, R_{con}, used to simulate ohmic voltage losses coming from cell elements other than the membrane.

Let us consider that, at a particular channel section, we are given the concentrations of ethanol and acetaldehyde at the anode channel, $C_{\text{E,ac}}$ and $C_{\text{A,ac}}$, and the concentration of oxygen at the cathode channel, $C_{\text{O}_2,\text{cc}}$. Then, for a fixed cell voltage, V, Eq. (4.21) can be rewritten as follows

$$f\left(\eta_{\text{a}}; C_{\text{E,ac}}, C_{\text{A,ac}}, C_{\text{O}_2,\text{cc}}, V\right) \equiv E_{\text{cell}} - V - \eta_{\text{a}} - \eta_{\text{c}}\left(C_{\text{O}_2,\text{cc}}, i_{\text{c}}\left(C_{\text{E,ac}}, C_{\text{A,ac}}, \eta_{\text{a}}\right)\right) - i\left(C_{\text{E,ac}}, C_{\text{A,ac}}, \eta_{\text{a}}\right)\left(R_{\text{mem}} + R_{\text{con}}\right) = 0 \quad (4.23)$$

where the dependence of the cathode overpotential on $C_{\text{O}_2,\text{cc}}$ and i_{c} is given analytically by Eq. (4.6), whereas the dependence of the current densities i and i_{c} on $C_{\text{E,ac}}$, $C_{\text{A,ac}}$ and η_{a} results from their dependence on $C_{\text{E,acl}}$, $C_{\text{A,acl}}$ and η_{a} established in Chapter 3, and the implicit dependence of the concentrations of ethanol and acetaldehyde at the anode catalyst layer, $C_{\text{E,acl}}$ and $C_{\text{A,acl}}$, on $C_{\text{E,ac}}$, $C_{\text{A,ac}}$ and η_{a} resulting from the mass balances (3.32) and (3.33).

For fixed values of $C_{\text{E,ac}}$, $C_{\text{A,ac}}$, $C_{\text{O}_2,\text{cc}}$ and V, the nonlinear algebraic equation (4.23) can be solved for the anode overpotential η_{a} using, for instance, a Newton-Raphson method. This method requires to evaluate in each iteration the derivative of f with respect to η_{a}, which can be written using the chain rule as

$$\frac{\text{d}f}{\text{d}\eta_{\text{a}}} = -1 - \frac{\text{d}\eta_{\text{c}}}{\text{d}i_{\text{c}}}\frac{\text{d}i_{\text{c}}}{\text{d}\eta_{\text{a}}} - \frac{\text{d}i}{\text{d}\eta_{\text{a}}}\left(R_{\text{mem}} + R_{\text{con}}\right) \quad (4.24)$$

From Eq. (4.6), the derivative of η_{c} with respect to i_{c} can be written analytically as

$$\frac{\text{d}\eta_{\text{c}}}{\text{d}i_{\text{c}}} = \frac{\left(RT/F\right)}{2\delta_{\text{ccl}}}\frac{C_{\text{O}_2,\text{ref}}}{(ai_0)_{\text{c}}}\left\{1 + \left[\frac{1}{2\delta_{\text{ccl}}}\frac{i_{\text{c}}}{(ai_0)_{\text{c}}}\frac{C_{\text{O}_2,\text{ref}}}{C_{\text{O}_2,\text{ccl}}}\right]^2\right\}^{-1/2}\left[\frac{C_{\text{O}_2,\text{ccl}} + i_{\text{c}}/\left(4F\mathfrak{h}_{\text{c}}\right)}{C_{\text{O}_2,\text{ccl}}^2}\right] \quad (4.25)$$

whereas the derivatives of the current densities i and i_{c} with respect to η_{a} have to be evaluated numerically by solving the anode problem stated in Chapter 3 for two neighboring values of η_{a} and applying the definition of partial derivative, i.e.,

$$\frac{\text{d}i}{\text{d}\eta_{\text{a}}} \approx \frac{i\left(C_{\text{E,ac}}, C_{\text{A,ac}}, \eta_{\text{a}} + \Delta\eta_{\text{a}}\right) - i\left(C_{\text{E,ac}}, C_{\text{A,ac}}, \eta_{\text{a}}\right)}{\Delta\eta_{\text{a}}} \quad \text{with} \quad \Delta\eta_{\text{a}} \ll \eta_{\text{a}} \quad (4.26)$$

4.4 1D-along the channel model

The electrochemical consumption and production of free species, combined with the redistribution effect of water and species crossover, makes the bulk fluid velocities and

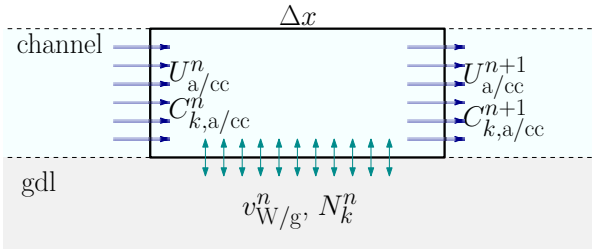

Figure 4.2: Schematic representation of the continuity equation and mass conservation equation of species k applied to the n-th channel element. The water velocity v^n_{W} must be used at the anode and the gas velocity v^n_{g} at the cathode.

species concentrations to vary along the flow channels. Such spatial variations can be determined, in first approximation, using a simple one-dimensional advection model. The model is based on the discretization of the flow channels in a large number of elements, $N \gg 1$, such that the length of a single channel element, $\Delta x = L/N$, is much smaller than the full channel length, L. As will be shown below, the analysis of the flow and species mass transport in the n-th channel element, $x \in (x_n, x_{n+1})$, $x_n = (n-1)\Delta x$, can be used to determine the recursive laws that govern the variation of the flow velocities and species concentrations along the flow channels.

4.4.1 Anode flow channels

The 1D along-the-channel model is based on the application of the continuity equation and the mass conservation equation of species k to the discrete n-th channel element. Assuming that the fluid in the anode channel is a diluted aqueous solution that flows at sufficiently large Peclet numbers, streamwise diffusion can be neglected. This is a fair approximation in DEFCs, where for typical operating conditions the Peclet number in the anode channels is between 10^4 and 10^5, and about 10^2 in the cathode channels.

Under these conditions, and assuming steady state operation, the discretized form of the continuity and species conservation equations takes the form

$$U^n_{\mathrm{ac}} h_{\mathrm{c}} + v^n_{\mathrm{W}} \Delta x = \quad U^{n+1}_{\mathrm{ac}} h_{\mathrm{c}} \tag{4.27}$$

$$C^n_{k,\mathrm{ac}} U^n_{\mathrm{ac}} h_{\mathrm{c}} + N^n_k \Delta x = C^{n+1}_{k,\mathrm{ac}} U^{n+1}_{\mathrm{ac}} h_{\mathrm{c}} \tag{4.28}$$

where U_{ac} is the average water velocity, $C_{k,\mathrm{ac}}$ is the bulk molar concentration of species k, h_{c} is the channel height, v_{W} is the transverse water velocity, and N_k is the molar flux of species k. The last two values, evaluated at the channel/gas diffusion layer interface, mus be obtained from the solution of the 1D across-the-channel model presented in Section 4.3.4. Note that the superscript n appearing in the convective terms, involving

U^n_{ac} and $C^n_{k,\mathrm{ac}}$, denotes that the corresponding magnitud is evaluated at $x = x_n$, while that appearing in the transverse transport terms, involving v^n_{W} and N^n_k, denotes the average value at the n-th channel element/gas diffusion layer interface.

Given the local concentrations of ethanol, acetaldehyde and oxygen at $x = x_n$, $C^n_{\mathrm{E,ac}}$, $C^n_{\mathrm{AA,ac}}$ and $C^n_{\mathrm{O_2,ac}}$, along with the cell voltage, V, the procedure outlined in Sec. 4.3.4 should provide the local anode overpotential η^n_{a}. Applying appropriate mass balances to the anode catalyst layer results in expressions similar to those derived in Chapter 3 for the ethanol and acetaldehyde, (3.32) and (3.33), for the transverse molar fluxes of the remaining species, N^n_k, k = E, A, AA and CO_2, as a function of known quantities. Note that the effect of methane production can be safely omitted here due to the exceedingly small quantities predicted by the analysis of the EOR presented in the previous chapter.

Under the assumption of convectively dominated transport along the flow channels leading to (4.27) and (4.28), the discrete channel elements can be solved successively from channel inlet to channel outlet. First, from Eq. (4.27) the average fluid velocity at $x = x_{n+1}$ can be expressed as

$$U^{n+1}_{\mathrm{ac}} = U^n_{\mathrm{ac}} + \frac{\Delta x}{h_{\mathrm{c}}} v^n_{\mathrm{W}} \tag{4.29}$$

in terms of the fluid velocity at the previous channel section, U^n_{ac}, and the transverse velocity of the fluid at the n-th channel element, v^n_{W}. Substitution of this expression into (4.28) finally provides the concentration of species k at $x = x_{n+1}$ as follows

$$C^{n+1}_{k,\mathrm{ac}} = \left(C^n_{k,\mathrm{ac}} + \frac{\Delta x}{h_{\mathrm{c}}} \frac{N^n_k}{U^n_{\mathrm{ac}}} \right) \left(1 + \frac{\Delta x}{h_{\mathrm{c}}} \frac{v^n_{\mathrm{W}}}{U^n_{\mathrm{ac}}} \right)^{-1} \tag{4.30}$$

in terms of the concentration at $x = x_n$, $C^n_{k,\mathrm{ac}}$, and the average transverse molar flux of species k at the n-th channel element, N^n_k.

4.4.2 Cathode flow channels

The flow channels can be treated in a similar way, except that in this case the working fluid must be treated as a mixture of ideal gases. Assuming that oxygen, water vapor and acetic acid are the only active (i.e., electrochemically consumed or produced) species in the cathode catalyst layer, the recursive laws that provide the flow velocity and species concentrations at $x = x_{n+1}$ from those at $x = x_n$ can be written as

$$U^{n+1}_{\mathrm{cc}} = U^n_{\mathrm{cc}} - \frac{\Delta x}{h_{\mathrm{c}}} v^n_{\mathrm{g}} \tag{4.31}$$

and

$$C^{n+1}_{k,\mathrm{cc}} = \left(C^n_{k,\mathrm{cc}} - \frac{\Delta x}{h_{\mathrm{c}}} \frac{N^n_k}{U^n_{\mathrm{cc}}} \right) \left(1 - \frac{\Delta x}{h_{\mathrm{c}}} \frac{v^n_g}{U^n_{\mathrm{cc}}} \right)^{-1} \tag{4.32}$$

where the role of the water flux velocity v_{W} at the anode gas diffusion layer is now played by the gas velocity at the cathode gas diffusion layer

$$\begin{aligned} v_{\mathrm{g}} &= \frac{RT}{p_{\mathrm{c}}}\left(N_{\mathrm{O_2}} + N_{\mathrm{W}} + N_{\mathrm{AA}}\right) \\ &= \frac{RT}{p_{\mathrm{c}}}\left[\frac{i_{\mathrm{c}}}{4F} - \left(\frac{i_{\mathrm{E},p}}{4F} + \frac{i}{2F} + n_d^{\mathrm{W}}\frac{i}{F}\right) - \left(\frac{i_{\mathrm{E},p}}{4F} + \frac{i_{\mathrm{A},p}}{2F}\right)\right] \\ &= -\frac{RT}{p_{\mathrm{c}}}\left(\frac{i + i_{\mathrm{E},p} + i_{\mathrm{A},p}}{4F} + n_d^{\mathrm{W}}\frac{i}{F}\right) \end{aligned} \tag{4.33}$$

which has been written here using Eqs. (4.9), (4.14), (4.19) and (4.20) to express the molar fluxes of oxygen, water vapor, and acetic acid in terms of i, $i_{\mathrm{E},p}$ and $i_{\mathrm{A},p}$.

It is important to note that the transverse gas velocity v_{g} is always negative, meaning that it always contributes to increasing the gas velocity along the cathode channel. This is true even under open circuit conditions ($i = 0$), when there is a net source of gas due to the production of water and acetic acid by the parasitic electrooxidation of ethanol and acetaldehyde. The gases generated at the cathode catalyst layer have to be evacuated through the cathode gas diffusion layer in the negative y-direction, thereby resulting in a negative gas velocity. Note that due to the high water permeation rates typical of fully humidified Nafion membranes ($n_{\mathrm{w}} \sim 2.5 - 3$), the water crossover term becomes dominant for non-zero current densities, and a significant gas production rate is expected along the cathode channels.

Table 4.1: Physical constants, convective mass transport coefficient and geometrical parameters used in the 1D across-the-channel model. The fitted parameters $(aj_0)_{\mathrm{c}}$ and R_{con} provided by the optimization algorithm are also shown for completeness.

Property	Value	Reference
α	0.50	Assumed
$C_{\mathrm{O_2,ref}}$	8.73 mol/m^3	Assumed
$D_{\mathrm{O_2,air}}$	$2.5 \times 10^{-5}\left(\frac{T}{298}\right)^{3/2}\left(\frac{p_{amb}}{p}\right)$ m^{2}s^{-1}	Lide (1990)
h	10^{-2} m s^{-1}	Assumed
ϵ	0.78	Meyer *et al.* (2011)
δ_{agdl}	280 μm	Meyer *et al.* (2011)
δ_{acl}	20 μm	Meyer *et al.* (2011)
δ_{mem}	178 μm	Meyer *et al.* (2011)
$(aj_0)_{\mathrm{c}}$	6.816 A/m^3	Fitted
R_{con}	1.5056×10^{-4} Ωm^2	Fitted

Table 4.2: Geometrical and operational parameters used in the 1D along-the-channel model.

Property	Value
Rib width, w_{rib}	1 mm
Channel width, w_{ch}	1 mm
Channel height, h_{c}	0.7 mm
Cell surface area, S	5 cm^2
Effective channel length, L	$S/(w_{\text{rib}} + w_{\text{ch}})$ =0.25 m
Anode volume flow rate, $Q_{\text{ac,in}}$	5 ml min^{-1}
Cathode volume flow rate, $Q_{\text{cc,in}}$	60 ml min^{-1}
Ethanol feed concentration, $C_{\text{E,in}}$	1 M
Oxygen feed concentration, $C_{\text{O}_2\text{,in}}$	10.22 mol/m^3
Cathode pressure, p_{c}	1.5 bar
Cell Temperature, T	80°C

4.4.3 Model fitting procedure

As in Chapter 3, a simulation campaign was carried out to improve the predictive power of the model by using experimental data reported in the literature. To be consistent with the optimization of the anode reaction mechanism, the cell polarization curve measured by Li & Pickup (2006) was used here as target data. All the simulations were carried out with a fixed set of physical constants, mass transport properties and design parameters, as shown in Tables 4.1 and 4.2.

A genetic optimization algorithm was used to determine the cathode exchange current density $(aj_0)_{\text{c}}$ and the electronic/contact resistance R_{con}. The objective function used was the root-mean-square error of the computed current density corresponding to a set of cell voltages reported experimentally

$$\text{err} = \sqrt{\sum_i \left(\frac{x_{i,\text{LP}} - x_i}{x_{i,\text{LP}}} \right)^2} \tag{4.34}$$

where $x_{i,\text{LP}}$ denotes the experimental current density measurements of Li & Pickup (2006). To avoid spurious results, only the data corresponding to cell voltages equal or smaller than 0.4 V were considered in the model fitting process. The values of $(aj_0)_{\text{c}}$ and R_{con} thus obtained are shown in Table 4.1.

Figure 4.3 shows the polarization curve, along with the anode overpotential and cathode potential vs. current density curves, computed at different sections along the flow channels using the optimized 1D+1D model and measured experimentally by Li & Pickup (2006). The corresponding power density curves are also shown for comparison. The model results show that with the operational conditions considered by Li & Pickup (2006) the variation of performance along the flow channels is almost negligible. As can be seen,

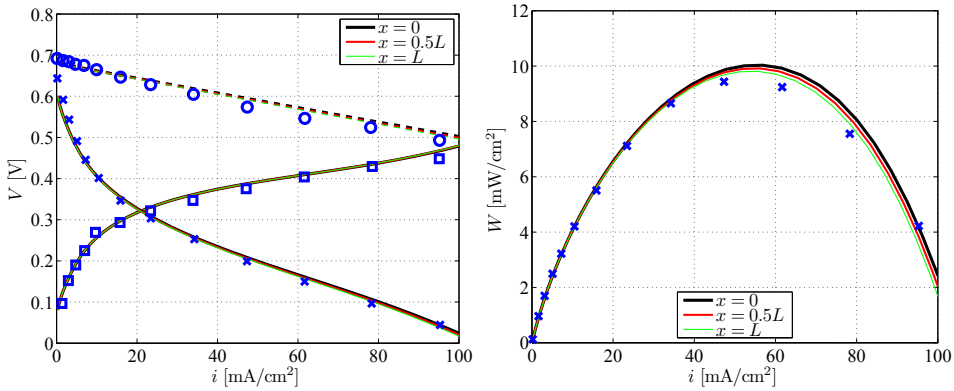

Figure 4.3: Left: cell voltage (×), cathode potential (○) and anode overpotential (□) reported by Li & Pickup (2006) and computed with the present model (solid, dashed and dash-dotted lines, respectively) at different sections along the flow channels as indicated in the legends. Right: computed (solid lines) and experimental (×) power density curves corresponding to the polarization data shown on the left.

the model correctly predicts the cell current density in the whole range of cell voltages. There is also a satisfactory agreement of the anode and cathode overpotential. The anode overpotential was already optimized in Chapter 3, hence its good agreement was to be expected. The optimization of the cathode exchange current density $(a\,j_0)_c$ and the overall electronic/contact resistance R_{con} of the cell carried out in this chapter yields an excellent agreement also in the cathode potential and cell polarization curves. Considering a reference value of the exchange current density per catalyst surface of $j_0 = 0.0422$ A/m^2 (García-Salaberri & Vera, 2015; Vera, 2007; Yang & Zhao, 2007*a*,*b*), the value obtained for the *volume-specific catalyst surface area* of the cathode yields $a_c \approx 165$ m^{-1} which is small compared with the values expected circa 10^4–10^5 m^{-1}. Such a reduced active area could be attributed to a high occupation of the cathode catalyst sites by intermediate adsorbates implied in the parasitic oxidation ethanol and acetaldehyde at the cathode catalyst layer. The negative impact of crossover has therefore two different aspects, as it not only creates a parasitic current density that raises the cathode overpotential, but also reduces the cathode active area for the ORR, which raises the overpotential even further.

4.5 Results and discussion

Once the model has been optimized to fit the experimental results, a parametric study will be carried out to asses the effect of the main operational parameters influencing cell performance: the anode flow rate and the ethanol feed concentration. If either of them decreases appreciably the cell performance start to be affected by ethanol depletion, an

effect that becomes more serious along the flow channels at low cell voltages. As ethanol becomes scarce, the cell starts using the acetaldehyde produced upstream, which results in an interesting evolution of species concentrations to be addressed next.

4.5.1 Downstream evolution along the flow channel

In order to accentuate the effect of ethanol depletion, a cell with larger active surface area and lower anode feed flow rate will be considered. Table 4.3 summarizes the modified design and operational parameters considered in the present study, the remaining parameters being maintained as in Tables 4.1 and 4.2. Comparing with the initial values used in the previous section there is a fivefold increase in the cell surface area, which in turn results in a fivefold growth in the effective channel length (under the assumption of a single serpentine geometry). In addition, the anode feed flow rate is reduced by a factor $5/0.3 = 16.7$. The significantly lower anode stoichiometry results in a much faster reduction of the ethanol concentration along the flow channels, which will be accompanied by nontrivial evolutions of the concentrations of other species, such as acetaldehyde or acetic acid, but also of the cell and parasitic current densities.

Figure 4.4 shows the polarization curve, along with the anode overpotential and cathode potential vs. current density curves, computed at different sections along the flow channels. The differences between the channel inlet and channel outlet become significant at mid-to-low voltages (i.e., mid-to-high currents), when ethanol consumption becomes significant. At 0.1 V the current density drops about 17 mA/cm^2 from channel inlet to channel outlet. The maximum power density is obtained at the channel inlet and a cell voltage of 0.19 V.

Figure 4.5 shows the evolution of the cell current density along the flow channels. It can be observed that at low cell potentials the decrease at the end of the channel is sharper. The blue marks indicate the channel section that generates the average current density. At cell voltages lower than 0.1 V its position is sightly displaced downstream the mid point of the channel. Figure 4.5 shows also the ratio between the current density and the average current density for different cell voltages. The relative variation is between circa 10% for high cell voltages (including the voltage at maximum power density) to over 20% at lower cell voltages. For instance, at 0.05 V the current density at the channel inlet is 19% larger than the average current density, while at the channel exit it is 26%

Table 4.3: Design and operation parameters used in the 1D along-the-channel model.

Property	Value	Li & Pickup (2006)
Cell surface area, S	25 cm^2	5 cm^2
Effective channel length, L	$S/(w_{\text{rib}} + w_{\text{ch}})$ =1.25 m	0.25 m
Anode volume flow rate	0.3 ml min^{-1}	5 ml min^{-1}

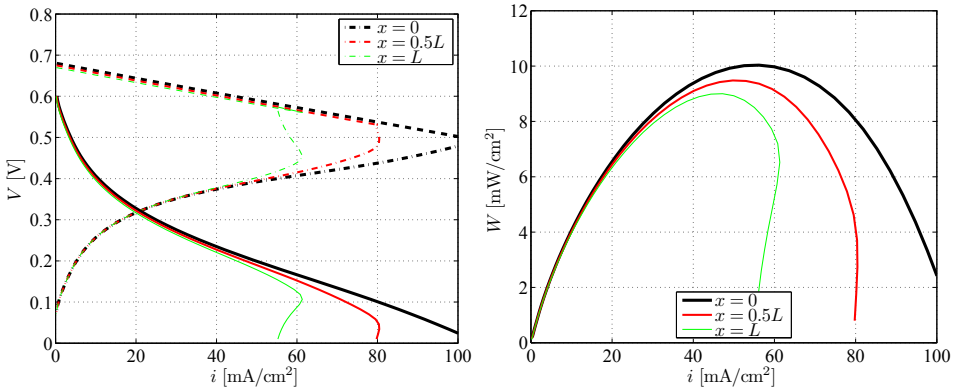

Figure 4.4: Polarization and power density curves for the 25 cm^2 simulated cell. Left: cell voltage (solid lines), cathode potential (dashed lines) and anode overpotential (dash-dotted lines) computed with the present model at different sections along the flow channels. Right: power density curves corresponding to the polarization curves shown on the left panel.

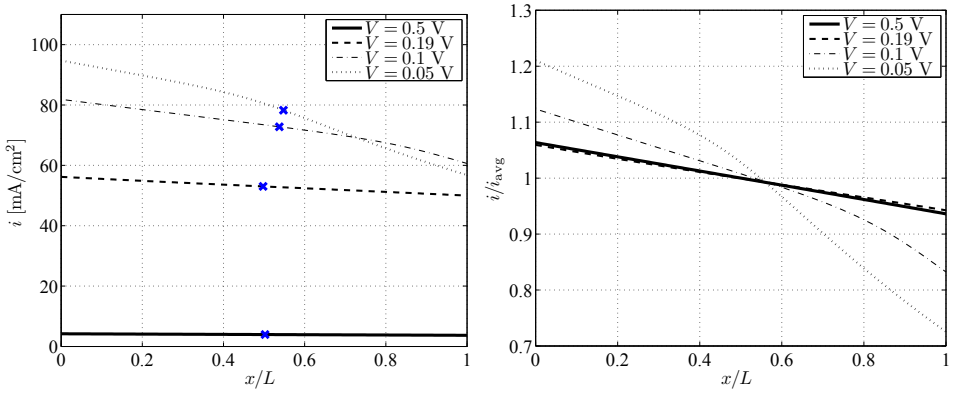

Figure 4.5: Evolution of the cell current density along the flow channels for different cell voltages. The blue marks indicate the average value of the current density at each cell voltage and the position where it is obtained along the cell. Left: current density. Right: current density measured with the average current density, i_{avg}.

lower than te average value.

Figure 4.6 shows the variation of the parasitic current density along the flow channel for different cell voltages. As can be seen, the parasitic current decays along the channel due to the reduction of ethanol crossover as ethanol is consumed. The variation is steeper at low cell voltages, when reactant consumption is larger. As can be seen, the parasitic current is drastically reduced at very low cell voltages due to reactant starvation. The right panel of Fig. 4.6 shows the variation of the parasitic current density with the cell

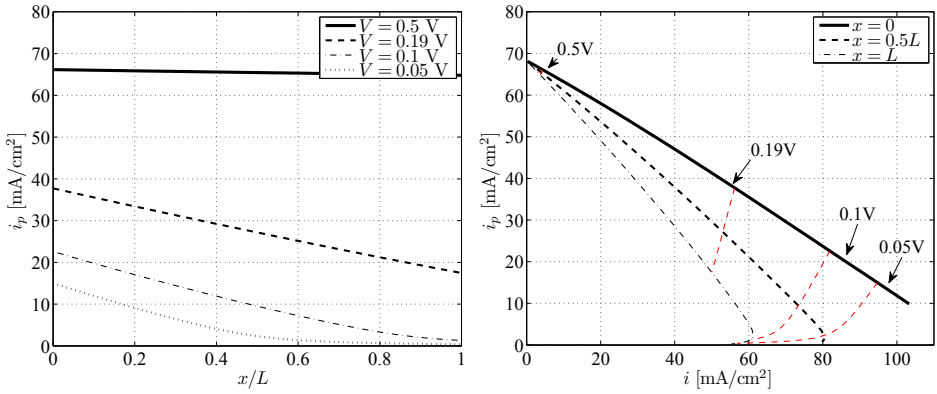

Figure 4.6: Evolution of the parasitic current density along the flow channels for different cell voltages (left) and variation of the parasitic current density with the cell current density at different sections along the flow channels (right). The dashed lines labeled by arrows correspond to each of the cell voltages represented on the left panel.

current density at different sections along the flow channel. The figure shows that the parasitic current decreases almost linearly with the cell current density, with a slope that becomes more and more negative towards the end of the cell.

In a direct alcohol fuel cell, the *fuel utilization* is defined as the ratio of the amount of fuel consumed at the anode and converted to useful current to the total amount of fuel consumed by the cell, which includes the fuel that reacts at the cathode electrode due to crossover. The fuel utilization is thus given by

$$\text{FU}\,[\%] = \frac{i}{i + i_p} \tag{4.35}$$

Figure 4.7 shows the variation of the FU along the channel for different cell voltages. It can be seen that the FU grows along the cell as a result of the reduction of the parasitic current shown in Fig. 4.6. The right panel of Fig. 4.7 shows the variation of the FU with the cell current density at different sections along the flow channel. It is seen that the FU grows almost linearly from 0% at open circuit conditions to almost 100% at the highest current densities reached at each channel station. Note that at maximum power density conditions (channel inlet at 0.19 V) the fuel utilization reaches only a moderate 60%.

The variation of the cell current density along the flow channel induces changes in the net molar production and consumption rates of the different species involved. Figure 4.8 shows the spatial evolution of the molar production rates of ethanol, acetaldehyde, acetic acid and carbon dioxide for different cell voltages. As the primary reacting species, ethanol is consumed along the whole channel length, although its consumption rate is seen to decrease due to the reduction of its concentration along the channel. Acetaldehyde

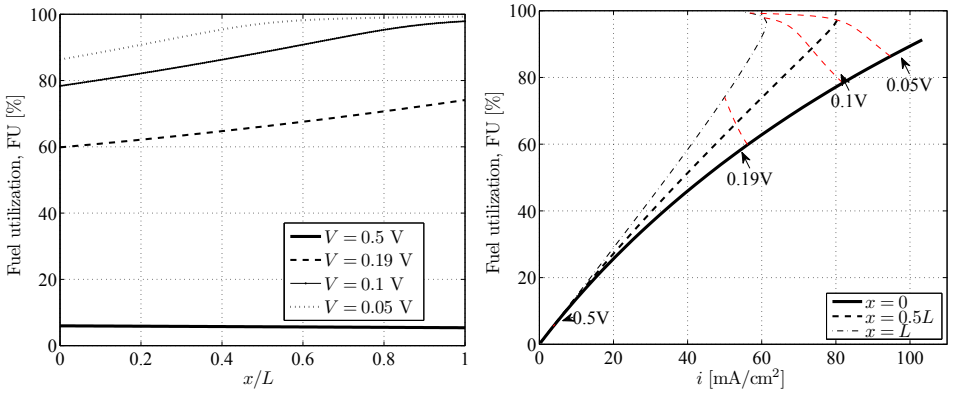

Figure 4.7: Evolution of the fuel utilization along the flow channels for different cell voltages (left) and variation of the fuel utilization with the cell current density at different sections along the flow channel (right). The dashed lines labeled by arrows correspond to each of the cell voltages represented on the left panel.

is the only other free reacting species considered in the EOR model, which can be either produced or consumed depending on the local flow conditions. For medium-to-high voltages (about 0.15 V or higher) there is net acetaldehyde production along the whole channel. However, at lower voltages acetaldehyde is first produced and then consumed, with the higher consumption rates reached near the channel exit. Under these conditions the cell consumes acetaldehyde as a means to compensate the low ethanol concentrations found at the channel exit as the current density becomes higher and higher. By contrast, the production of acetic acid and CO_2 remains almost constant along the flow channel. Only at very low voltages ($V \sim 0.1-0.05$ V) there is a noticeable reduction of their molar production rates associated with the reduction of ethanol consumption, which can not be fully compensated by acetaldehyde conversion.

Figure 4.9 shows the variation of ethanol concentration at the anode channel and at the anode catalyst layer. For the operating conditions under study, corresponding to moderately low anode stoichiometries, a significant reduction is observed both at the channel and the catalyst layer except perhaps at the highest voltages, when the cell hardly consumes any ethanol. At maximum power density (channel inlet at $V = 0.19$ V) almost 35% of the inlet ethanol is consumed. At the catalyst layer, ethanol starvation is observed at low cell voltages ($V < 0.1$ V) coinciding with the conditions leading to the consumption of acetaldehyde.

At the cathode electrode, the concentration of oxygen at the catalyst layer and at the flow channel does not differ more than 0.05 mol/m^3, which indicates that mass transport looses are negligibly small. Figure 4.10 shows the variation of the oxygen consumption of O_2 along the cathode channel. Note that at the cathode side a positive molar flux of oxygen (i.e., pointing in the positive y-direction) represents consumption. It is worth

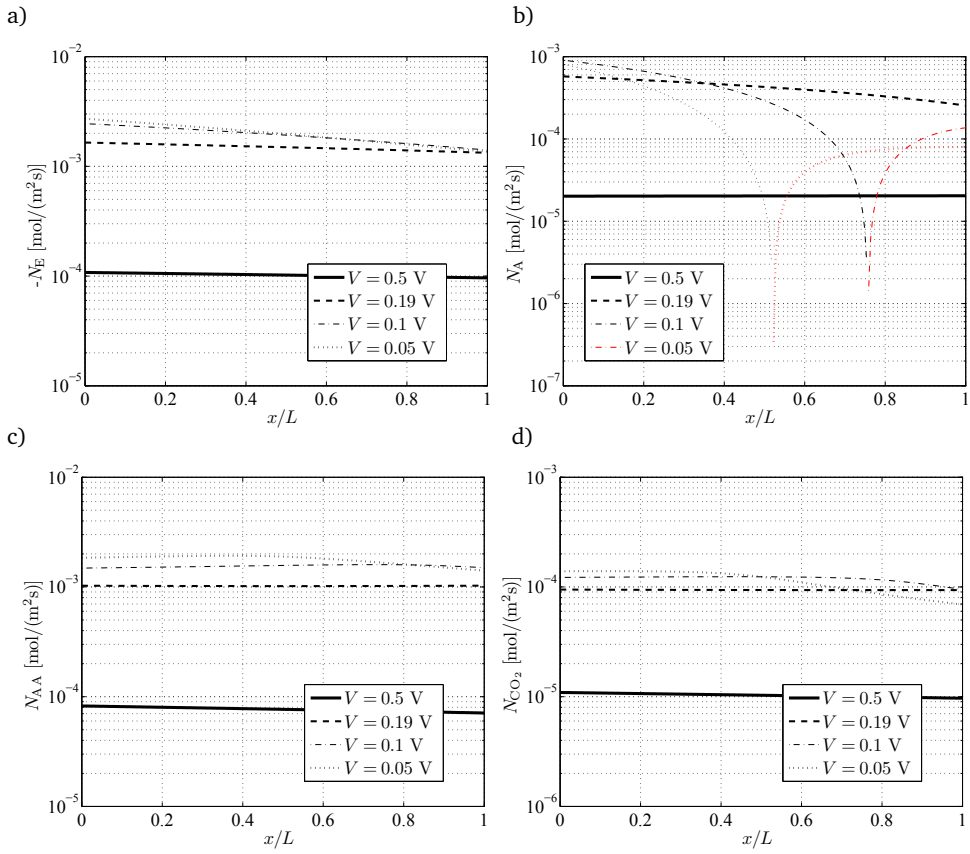

Figure 4.8: Evolution of the molar production and consumption rates of free species along the anode channel for different cell voltages: a) ethanol (consumption), b) acetaldehyde (production in black and consumption in red), c) acetic acid (production) and d) CO_2 (production).

noting that the oxygen consumption rate varies only slightly in the whole cell voltage range, due to the contribution of the parasitic current at high voltages. As a result, the evolution of the oxygen concentration along the anode channel, shown on the right panel, differs less for high and low voltages than that of ethanol shown in Fig. 4.9. Note that for the conditions under study the concentration of oxygen at the channel exit decreases to, roughly, half of its initial value for cell voltages below 0.19 V.

The main products of the EOR at the anode electrode are acetaldehyde, acetic acid and CO_2. The concentration of these species along the channel and catalyst layer is shown in Figure 4.11. As already discussed, acetaldehyde is not strictly a final product, because at the same time as it is produced it is also consumed to generate further products. As a result, at cell voltages lower than 0.19 V the concentration of acetaldehyde first increases, then reaches a maximum, and finally decreases due to the net consumption rates induced

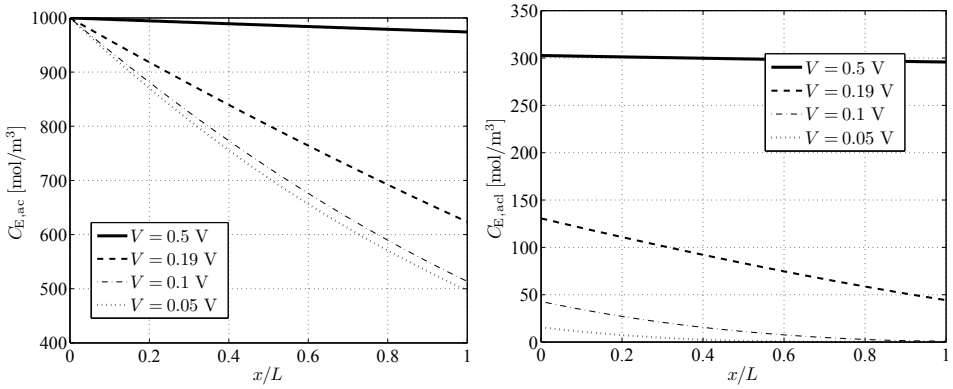

Figure 4.9: Evolution of the molar concentration of ethanol along the anode channel (left) and at the catalyst layer (right)

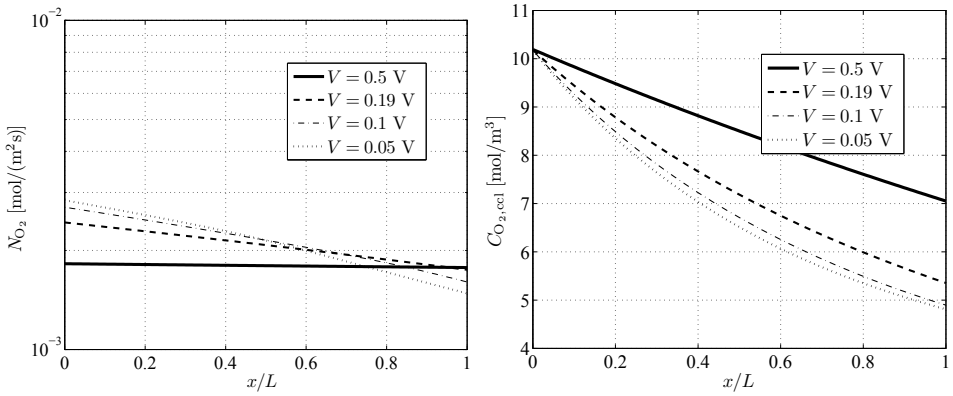

Figure 4.10: Evolution of the molar consumption rate of O_2 along the cathode channel (left) and of the molar concentration of O_2 at the catalyst layer (right).

by ethanol starvation at the channel exit (see Fig. 4.8b). However, the consumption of acetaldehyde cannot fully compensate the lack of ethanol, particularly at very low voltages, when acetaldehyde is also starved at the very end of the channel. This, in turn, has a negative impact on CO_2 production, whose concentration at the catalyst layer is also reduced, as can be seen in Fig. 4.11c.

The evolution of the product selectivities along the channel is presented in Fig. 4.12. Selectivities behave similarly to those presented in Chapter 3 (Fig. 3.4). It is interesting to note that the consumption of acetaldehyde at low cell voltages reduces acetaldehyde selectivity in favor of acetic acid near the channel exit. CO_2 selectivity remains close to 10% in the whole cell voltage range, being approximately constant along the channel.

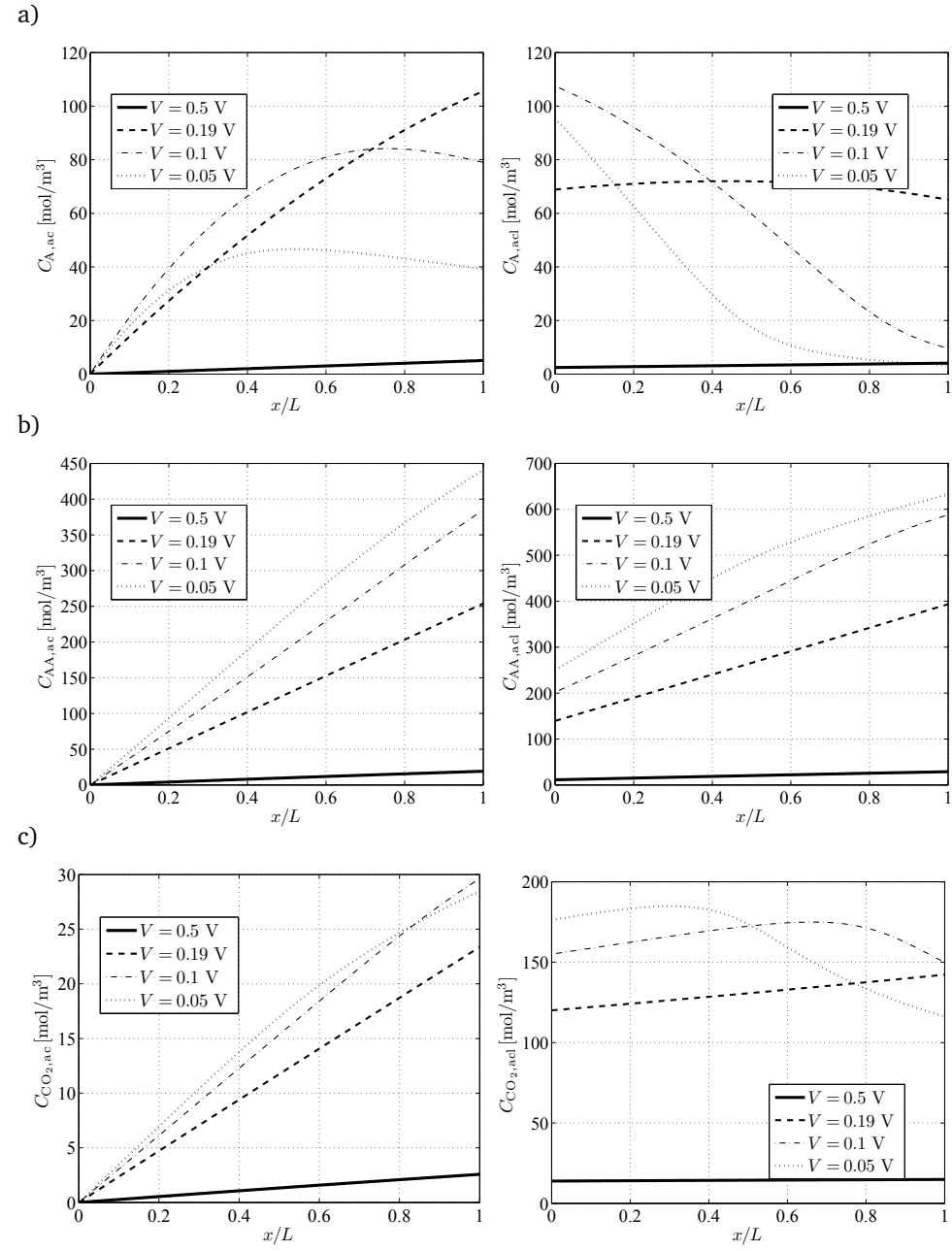

Figure 4.11: Evolution of the molar concentration along the anode channel at the channel (left) and at the catalyst layer (right) for different cell voltages of: a) acetaldehyde, b) acetic acid and c) CO_2.

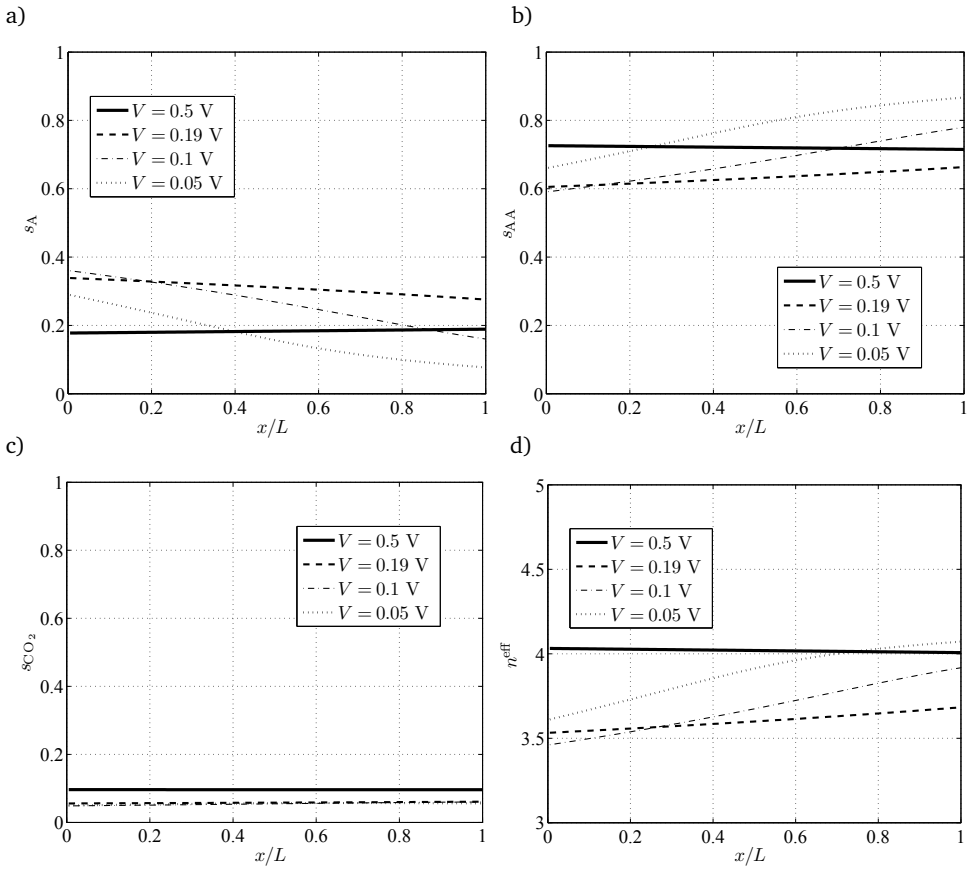

Figure 4.12: Evolution of the product selectivities of the anode products species along the channel for different cell voltages: a) acetaldehyde, b) acetic acid and c) CO_2. d) shows the evolution of the effective electron generation number.

The effective electron generation number, n^{eff}, is also shown in Figure 4.12, with values ranging between 3.5 an 4, in agreement with those reported in the previous chapter. Note that, despite the reduction of the availability of ethanol along the flow channel, the effective electron generation number is seen to grow as a result of the increased selectivity of acetic acid under ethanol starvation conditions.

4.5.2 Effect of anode flow rate and ethanol feed concentration

This section presents a parametric study aimed to assess the effect of both anode flow rate and ethanol feed concentration on overall DEFC performance. This includes cell voltage, power density, parasitic current and fuel utilization vs. current density curves. The same

25 cm^2 cell of the previous section was simulated here for different anode flow rates $Q_{ac,in} = (5, 1, 0.5, 0.1)$ ml/min and ethanol feed concentrations $C_{E,in} = (2, 1, 0.5, 0.2)$ M. Tables 4.3 and 4.2 summarize the remaining design and operational parameters, which were kept unchanged in this study.

Figure 4.13 shows cell voltage, power density, parasitic current and fuel utilization vs. current density curves for the whole range of parameters under study. High ethanol feed concentrations induce increased crossover rates and therefore higher parasitic current densities. As a result, a 2M ethanol feed concentration barely reaches the 50% of fuel utilization. This effect significantly reduces the cell performance in the whole operational range, even though it reduces ethanol starvation at low cell potentials. Maximum power density is obtained with 0.5M ethanol feed concentration, but 1M shows almost the same peak but exhibits a much larger limiting current density, thus ensuring a more stable cell operation. It is also seen that low ethanol feed concentrations lead to fuel utilizations near 100% due to the reduced crossover rates.

The outlet concentrations of ethanol, acetaldehyde, acetic acid and CO_2 are shown in Figure 4.14. The reduction in ethanol concentration with the cell current density is almost linear, and is steeper for low anode flow rates as should be expected. Acetaldehyde concentration increases with current density until ethanol starvation is reached, then the amount of acetaldehyde at the outlet starts to decline. For low ethanol feed molarity (below, say, 0.5M) the concentration of acetaldehyde at the outlet vanishes at low cell potentials, meaning that it is completely depleted before leaving the cell. Figure 4.15 shows this same effect in terms of the average molar production rates. It is clear that acetaldehyde production peaks, and ethanol consumption reduces its growth rate with increasing current density, when ethanol starvation starts to affect the EOR at the anode catalyst layer.

In the case of acetic acid, both the outlet concentration (Fig. 4.14c) and the molar production rate (Fig. 4.15c) increase steadily with the current density, with a sharper growth rate at the final ethanol starvation regime. The outlet concentration of CO_2 grows with the current density but it remains significantly lower than those of acetaldehyde and acetic acid, in agreement with its significantly lower selectivity (Fig. 3.4). Figures 4.14 and 4.15 also show that at low ethanol feeds (below 0.5M), when ethanol starvation starts to be important, the outlet concentration and net production rate of CO_2 are sharply reduced. This is a result of the enhanced production of acetic acid discussed before. The reduction of CO_2 production in this regime is due to the presence of oxidants such OH_{ads} (Kavanagh *et al.*, 2012) which favor the production of acetic acid instead of the C-C bond breaking steps (Reactions 4 and 5, respectively, in Table 3.1). A closer analysis of the values of the reaction constants obtained in the previous chapter (Table 3.3) reveals that k_4 is almost two orders of magnitude larger than k_5. Thus, as soon as the coverage factor of the adsorbed hydroxyl groups becomes significant (which occurs at high anode overpotentials, as illustrated by Fig. 3.7), Reaction 4 becomes dominant, significantly reducing the further production of CO_2.

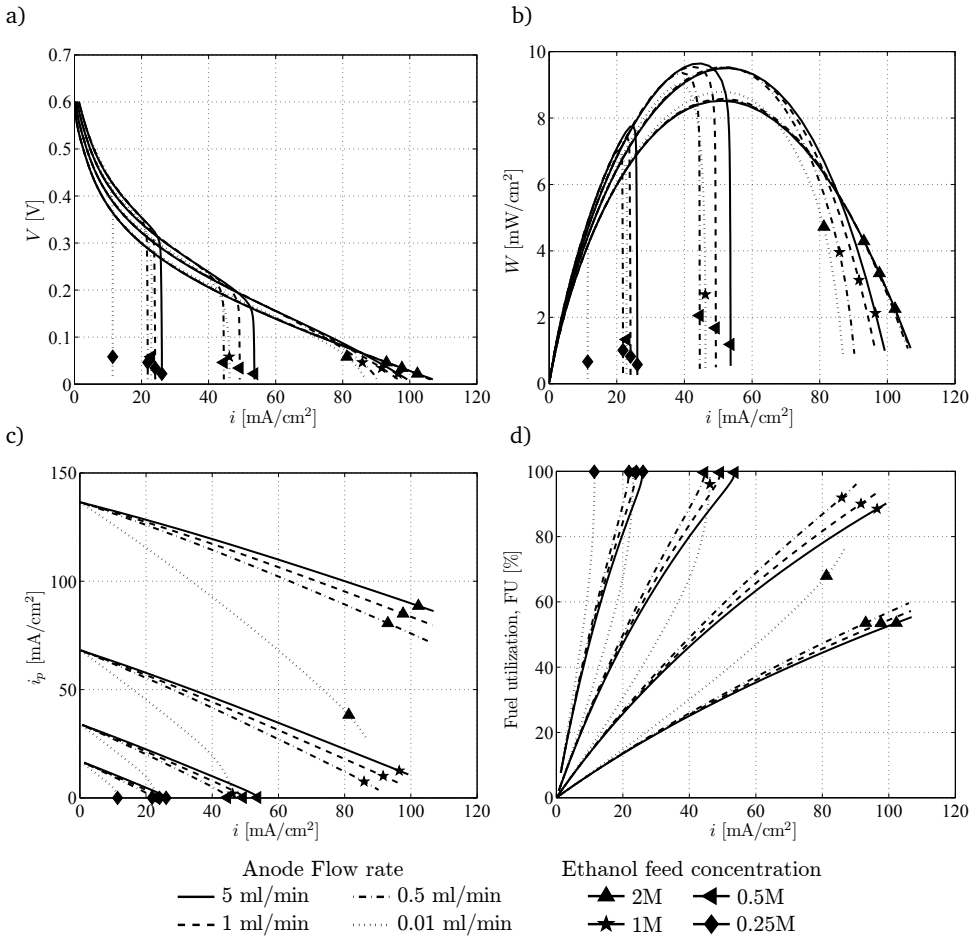

Figure 4.13: Overall cell performance computed with the present model for the different anode flow rates and ethanol feed concentrations indicated in the legend: a) cell voltage, b) power density, c) average parasitic current density and d) average fuel utilization as a function of the average cell current density. Other design and operational parameters as specified in Tables 4.3 and 4.2.

Figure 4.16 shows the product selectivities at the anode channel outlet as a function of the average current density. The overall behavior resembles that discussed in Chapter 3 (Fig. 3.4), but appropriately rescaled with the limiting current density, which depends both on the anode flow rate and the ethanol feed concentration. Acetaldehyde selectivity decreases as the limiting current decreases, eventually vanishing under severe starvation conditions. Under these conditions, acetic acid selectivity grows sharply beyond 0.8, reaching 0.95 for the lowest ethanol molarities. Simultaneously, CO_2 selectivity decreases to roughly 0.05. The drop of acetaldehyde selectivity increases the effective electron generation number, which grows beyond 4 under severe starvation conditions due to

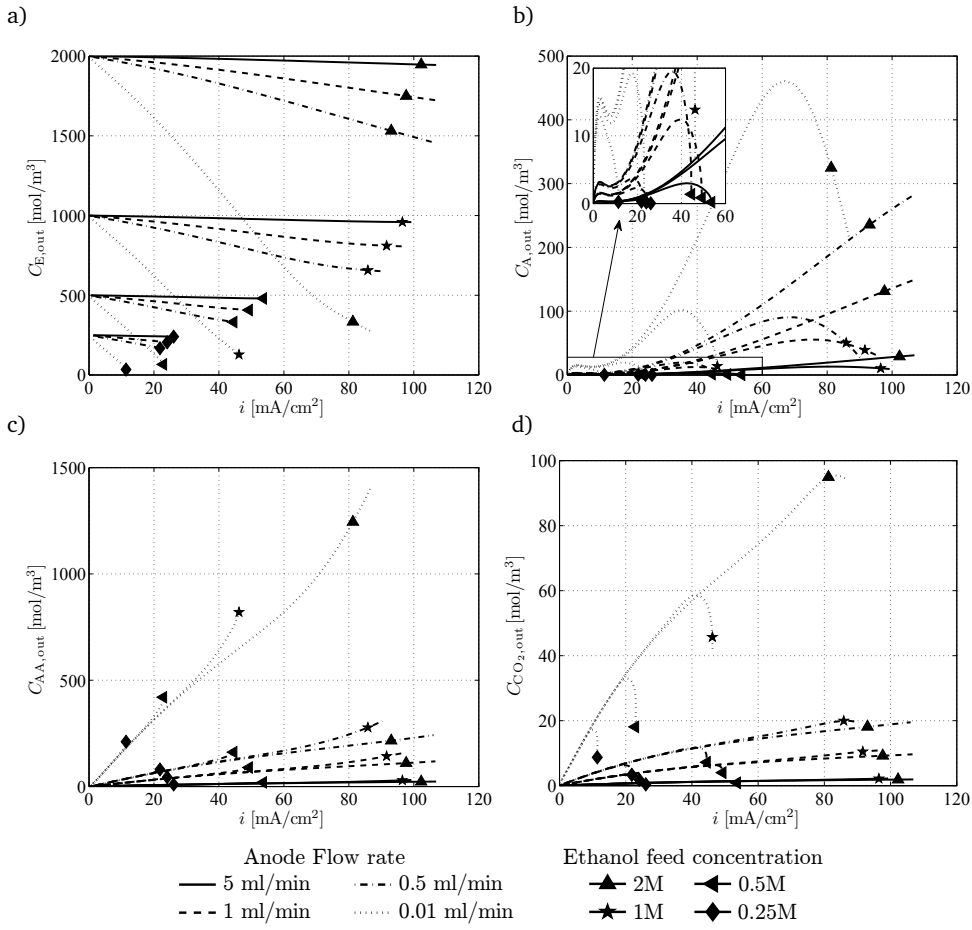

Figure 4.14: Species concentrations at the anode channel outlet for the different anode flow rates and ethanol feed concentrations indicated in the legend: a) ethanol, b) acetaldehyde, c) acetic acid and d) CO_2obtained with the model presented in this thesis. Other design and operational parameters as specified in Tables 4.3 and 4.2.

the importance of acetic acid production. Note again that the highest values of n^{eff} are reached for the lowest acetaldehyde selectivities, indicating a better utilization of the ethanol consumed. Thus, for 1M ethanol feed the value of n^{eff} is about 0.5 larger than for 2M at high current densities (> 70 mA/cm^2), implying a more efficient cell operation.

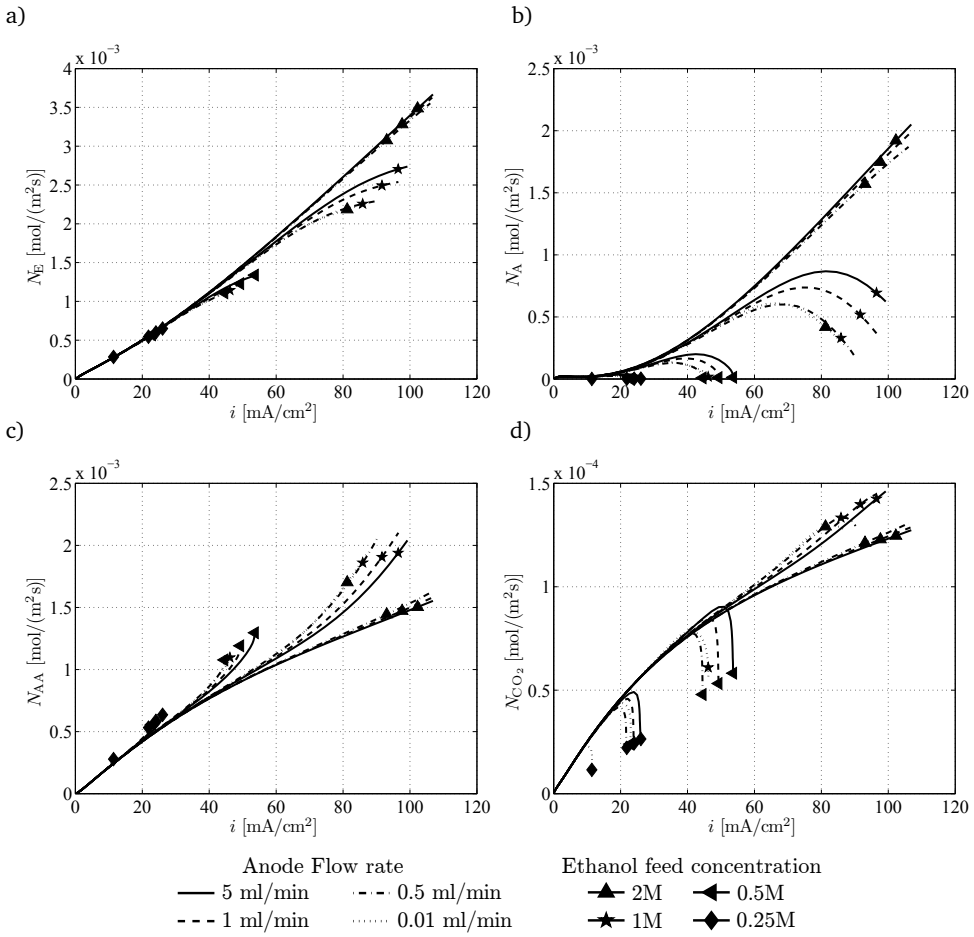

Figure 4.15: Average molar consumptions/production rates at the anode for the different flow rates and ethanol feed concentrations indicated in the legend: a) ethanol (consumption), b) acetaldehyde (production), c) acetic acid (production) and d) CO_2(production). Other design and operational parameters as specified in Tables 4.3 and 4.2.

4.6 Conclusions

A detailed reaction mechanism for the ethanol oxidation reaction on binary Pt-based catalysts has been used to develop a 1D+1D model for direct ethanol PEM fuel cells. A 1D diffusive model with simple oxygen reduction kinetics has been used to describe the cathode electrode. The effective electron generation number has been used to calculate the parasitic current density due to ethanol and acetaldehyde crossover. The resulting 1D across-the-channel model has been coupled to a simple 1D along-the-channel advection model to describe the evolution of the different variables of interest along the flow

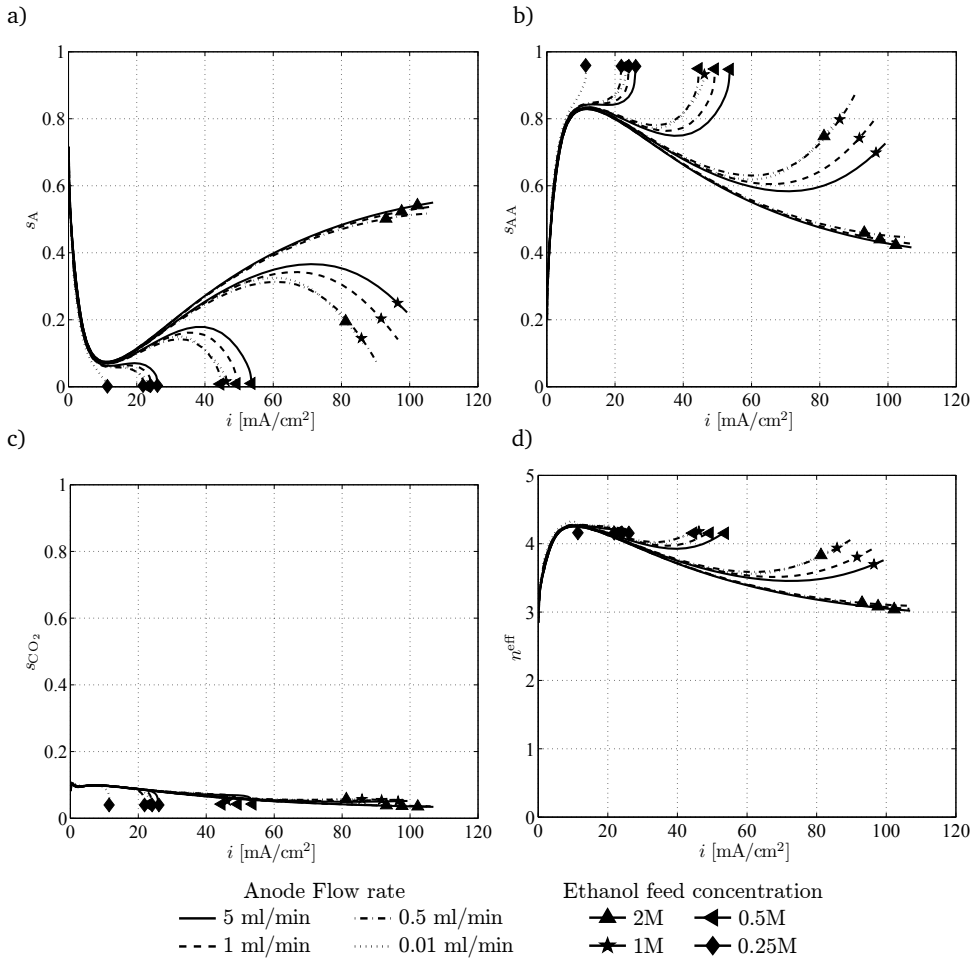

Figure 4.16: Variation with the current density of a) acetaldehyde, b) acetic acid, and c) CO_2 selectivity, and d) the effective electron generation number for the different flow rates and ethanol feed concentrations indicated in the legend. Other design and operational parameters as specified in Tables 4.3 and 4.2.

channels, including reactant concentrations at the channels and catalyst layers, molar consumption/production rates, overpotentials and cell and parasitic current densities. A genetic optimization algorithm has been used to determine the cathodic exchange current density and the electronic/contact resistance of the cell that enabled a better fit to the experimental results taken from the literature. The volume-specific catalyst surface area obtained from the experimental fit is small compared with the values reported in the literature for PEMFCs. Nevertheless, the correct agreement with the experimental results indicates that another effect is likely blocking the catalyst sites at the cathode,

thus reducing the active area available for the ORR. A detailed kinetic mechanism for the cathode electrode may shed further light on this interesting topic.

Ethanol and acetaldehyde emerge as the main species involved in generating current in the anode kinetic model. The evolution of their concentrations along the anode channel significantly affects the EOR by imposing varying local conditions at each channel section. The role of acetaldehyde as free intermediate species is particularly remarkable. The acetaldehyde produced in the upstream sections of the cell is transported to the channel by diffusion and then it is convected downstream, which gradually increases its concentration along the channel. This acetaldehyde may be consumed downstream under ethanol starvation conditions, leading to the existence of a peak acetaldehyde concentration inside the cell that may not be detected at the outlet. Indeed, numerical simulations have shown that under extreme starvation conditions acetaldehyde may be completely consumed before leaving the cell. The consumption of all the acetaldehyde produced upstream implies a high electrical efficiency for the ethanol conversion process, i.e., high n_{eff}, although it would still be preferable to produce more CO_2, which would boost the cell efficiency even further.

After analyzing the downstream evolution along the cell, a parametric study was carried out to asses the effect of different ethanol feed concentrations and anode flow rates on the overall cell performance. For the conditions under study, the results show the existence of an optimum ethanol feed concentration around 1M for various reasons: 1M exhibits a high maximum power density, a much larger limiting current density that 0.5M, a fuel utilization circa 80% for high current densities and an effective electron generation number approaching 4.

References

ANDREADIS, G. M., PODIAS, A. K. M. & TSIAKARAS, P. E. 2008 The effect of the parasitic current on the Direct Ethanol PEM Fuel Cell Operation. *J. Power Sources* **181** (2), 214–227.

ANDREADIS, G. M., PODIAS, A. K. M. & TSIAKARAS, P. E. 2009 A model-based parametric analysis of a direct ethanol polymer electrolyte membrane fuel cell performance. *J. Power Sources* **194** (1), 397–407.

ANDREADIS, G. M., SONG, S. & TSIAKARAS, P. E. 2006 Direct ethanol fuel cell anode simulation model. *J. Power Sources* **157** (2), 657–665.

ANDREADIS, G. M. & TSIAKARAS, P. E. 2006 Ethanol crossover and direct ethanol PEM fuel cell performance modeling and experimental validation. *Chem. Eng. Sci.* **61** (22), 7497–7508.

GARCÍA-SALABERRI, P. A. & VERA, M. 2015 On the effects of assembly compression on the performance of liquid-feed DMFCs under methanol-limiting conditions: A 2D numerical study. *J. Power Sources* **285**, 543–558.

GARCÍA-SALABERRI, P. A., VERA, M. & IGLESIAS, I. 2014 Modeling of the anode of a liquid-feed DMFC: Inhomogeneous compression effects and two-phase transport phenomena. *J. Power Sources* **246**, 239–252.

KAVANAGH, R., CAO, X. M., LIN, W. F., HARDACRE, C. & HU, P. 2012 Origin of low CO$_2$ selectivity on platinum in the direct ethanol fuel cell. *Angew. Chem. Int. Ed. Engl.* **51** (7), 1572–5.

LI, G. & PICKUP, P. G. 2006 Analysis of performance losses of direct ethanol fuel cells with the aid of a reference electrode. *J. Power Sources* **161** (1), 256–263.

LIDE, D. R. 1990 *Handbook of Chemistry and Physics*. Boca Raton: CRC Press.

LIN EE, S. & BIRGERSSON, E. 2011 Two-Dimensional Approximate Analytical Solutions for the Direct Liquid Fuel Cell. *J. Electrochem. Soc.* **158** (10), B1224.

MEYER, M., MELKE, J. & GERTEISEN, D. 2011 Modelling and simulation of a direct ethanol fuel cell considering multistep electrochemical reactions, transport processes and mixed potentials. *Electrochim. Acta* **56** (11), 4299–4307.

PRAMANIK, H. & BASU, S. 2010 Modeling and experimental validation of overpotentials of a direct ethanol fuel cell. *Chem. Eng. Process. Process Intensif.* **49** (7), 635–642.

SOUSA, R., DOS ANJOS, D. M., TREMILIOSI-FILHO, G., GONZALEZ, E. R., COUTANCEAU, C., SIBERT, E., LÉGER, J.-M. & KOKOH, K. B. 2008 Modeling and simulation of the anode in direct ethanol fuels cells. *J. Power Sources* **180** (1), 283–293.

SURESH, N.S. & JAYANTI, S. 2011 Cross-over and performance modeling of liquid-feed Polymer Electrolyte Membrane Direct Ethanol Fuel Cells. *Int. J. Hydrogen Energy* **36** (22), 14648–14658.

VERA, M. 2007 A single-phase model for liquid-feed DMFCs with non-Tafel kinetics. *J. Power Sources* **171** (2), 763–777.

VIGIER, F., COUTANCEAU, C., PERRARD, A., BELGSIR, E. M. & LAMY, C. 2004 Development of anode catalysts for a direct ethanol fuel cell. *J. Appl. Electrochem.* **34** (4), 439–446.

VIGIER, F., ROUSSEAU, S., COUTANCEAU, C., LEGER, J.-M. & LAMY, C. 2006 Electrocatalysis for the direct alcohol fuel cell. *Top. Catal.* **40** (1-4), 111–121.

WATANABE, M. & MOTOO, S. 1975 Electrocatalysis by ad-atoms. *J. Electroanal. Chem. Interfacial Electrochem.* **60** (3), 275–283.

YANG, W.W. & ZHAO, T.S. 2007*a* A two-dimensional, two-phase mass transport model for liquid-feed DMFCs. *Electrochim. Acta* **52** (20), 6125–6140.

YANG, W W & ZHAO, T S 2007*b* Two-phase, mass-transport model for direct methanol fuel cells with effect of non-equilibrium evaporation and condensation. *J. Power Sources* **174**, 136–147.

Nomenclature DEFC

Symbols

a_c	effective cathodic catalyst surface [m^{-1}]
$C_{k,\ell}$	molar concentration of species k in layer ℓ [$mol\,m^{-3}$]
$D_{k,\ell}$	molecular diffusivity of species k in layer ℓ [$m^2\ s^{-1}$]
F	Faraday's constant, F =96487 C
FU	Fuel utilization
h	mass transport coefficient c/gdl [$m\,s^{-1}$]
$\mathfrak{h}$	overall mass transport coefficient c/gdl [$m\,s^{-1}$]
h_{ac}	anode channel height [m]
h_{cc}	cathode channel height [m]
i	current density [$A\,m^{-2}$]
j	current density per catalyst surface [$A\,m^{-2}$]
k_r	rate constant of Reaction r [$mol\,m^{-3}\,s^{-1}$] or [s^{-1}]
n^{eff}	effective electron generation number
n_d^k	electroosmotic drag coefficient of species k
N_k	molar flux of species k [$mol\,m^{-2}\,s^{-1}$]
p	pressure [Pa]
q_r	net reaction rate of Reaction r [$mol\,m^{-3}\,s^{-1}$]
R	ideal-gas constant, 8.3143 [$J\,mol^{-1}\,K^{-1}$]
R_{mem}	membrane ohmic resistance Ωm^2
S	cell surface [m^2]
s_k	selectivity of the product species k
s^{GRj}	selectivity of the global reaction GRj
T	Temperature [K]
U_c	channel velocity [$m\ s^{-1}$]
v_W	drag velocity of water [m s—1]
W	molar mass [$kg\,mol^{-1}$]
w_{rib}	rib width [m]
w_{ch}	channel width [m]
x	coordinate along the channel
y	coordinate across the membrane

Greek letters

α_r	charge transfer coefficient of Reaction r [-]

δ_ℓ	thickness of layer ℓ [μm]
ϵ	gdl porosity [-]
η	overpotential [V]
Θ_k	coverage factor of adsorbed species k [-]
ρ	fluid density [$\mathrm{kg\,m^{-3}}$]
ω_k	net molar production rate of free species k [$\mathrm{mol\,m^{-2}\,s^{-1}}$]

Subscripts

a	anode
ac	anode channel
acl	anode catalyst layer
agdl	anode gas diffusion layer
ads	adsorbed
A	acetaldehyde (CH_3CHO)
AA	acetic acid (CH_3COOH)
c	cathode
cc	cathode channel
ccl	cathode catalyst layer
cgdl	cathode gas diffusion layer
con	contact property
cross	crossover flux
E	ethanol (CH_3CH_2OH)
k	species k
ℓ	generic layer
p	parasitic
r	reaction r
W	water (H_2O)

Superscripts

eff	effective property
n	channel section n

Part II

Water Management in Hydrogen Polymer Exchange Membrane Fuel Cells

CHAPTER

FIVE

Experimental analysis of the influence of temperature and gas humidity on the performance stability of polymer electrolyte membrane fuel cells

This chapter describes the experimental results obtained by Sanchez *et al.* (2016) in the Department of Electrochemical Energy Technology at the German Aerospace Center (DLR) in Stuttgart, in which the author collaborated actively during two short stays during the falls of 2013 and 2014. The author greatly appreciates the hospitality of Prof. Dr. *rer. nat.* K. Andreas Friedrich, and the helpful guide of Dr. Daniel G. Sánchez.

Contents

5.1 Introduction

As previously discussed, one of the main requirements that PEM fuel cell membranes must meet is to have a high proton conductivity. Current membranes, e.g., Nafion™, use highly hydrophilic sulfonic groups attached to a hydrophobic backbone (usually Teflon) to achieve this purpose (Jiao, 2011; Jiao & Li, 2011). The absorption of water on the sulfonic groups enables proton mobility in the hydrated regions, which behave as dilute acids. Sulfonic groups are highly attached to the Teflon structure so that an adequate amount of water is necessary to connect all the membrane water clusters and create an homogeneous

proton conducting network. As a result, the membrane must contain enough water to ensure a high membrane conductivity and thus guarantee a stable cell performance. However, excess inlet gas humidification as well as condensation processes within the cell are likely to produce the accumulation of liquid water in the porous electrodes and gas diffusion media, an effect known as flooding, thereby blocking the access of reactants to the catalyst layers and decreasing cell performance. Adequate *water management* thus emerges as one of the main challenges in the design and operation of PEM fuel cells.

Water is usually supplied to cell by the humidification of the gas feed streams. This process requires energy, so a proper strategy to optimize the addition of water is needed to increase the overall efficiency of the fuel cell as power source (Atkins *et al.*, 2004; Colinart *et al.*, 2009; Hsuen & Yin, 2012; Kim *et al.*, 2009; Lee *et al.*, 2009; Sanchez & Garcia-Ybarra, 2012; Vengatesan *et al.*, 2006). Since water is produced in the cell cathode, operation of PEMFC under dry gases supply has also been studied (Buchi & Srinivasan, 1997; Zhang *et al.*, 2007).

An adequate water management strategy must ensure an homogeneous distribution of the cell current density. A disruption of the homogeneous water distribution leads to membrane regions with lower proton conductivity and therefore a reduction of the current density in those regions. But an inhomogeneous distribution of the current density during PEM operation is often accompanied by unstable cell behaviors and a significant reduction of membrane life (Barbir *et al.*, 2005; Collier *et al.*, 2006; Knights *et al.*, 2004; Li *et al.*, 2008; Sanchez *et al.*, 2017; Tüber *et al.*, 2003; Wu *et al.*, 2008; Yousfi-Steiner *et al.*, 2008).

As the measurement of the total current density generated by the cell does not give any information about its spatial distribution, other experimental techniques must be considered to address this issue. As a particular example, the segmented cell approach developed at DLR provides local measurements of the cell current density (Schulze *et al.*, 2007). To achieve this goal, a segmented printed circuit board (PCB) is used as anode bipolar plate (Fig. 5.1). The printed board also features integrated temperature sensors. The plate is divided into a large matrix of individual segments that provide local current density measurements. Using this procedure, deactivated zones of the membrane can be easily identified. Segmented cells have been widely used to analyze current density distribution in PEM fuel cells (Büchi *et al.*, 2005; Hwnag *et al.*, 2008; Sanchez & Garcia-Ybarra, 2012; Sanchez *et al.*, 2010; Schneider *et al.*, 2007; Tang *et al.*, 2013; Weng *et al.*, 2008; Yoon *et al.*, 2003).

Several investigations have focused on how the relative humidity of the inlet gases affects the cell performance stability (Owejan *et al.*, 2007*a*,*b*; Reshetenko *et al.*, 2011, 2012; Schulze *et al.*, 2007). An homogeneous water distribution has been addressed as an improving performances factor (Owejan *et al.*, 2007*b*). Water maldistribution and accumulation has been directly related with oscillatory behaviors (Benziger *et al.*, 2005; Hanke-Rauschenbach *et al.*, 2011; Nazarov & Promislow, 2006; Sanchez & Garcia-Ybarra, 2012; Sanchez *et al.*, 2010). The oscillations have been found to correspond to transitions between hydrated and dehydrated membrane states (Benziger *et al.*, 2005;

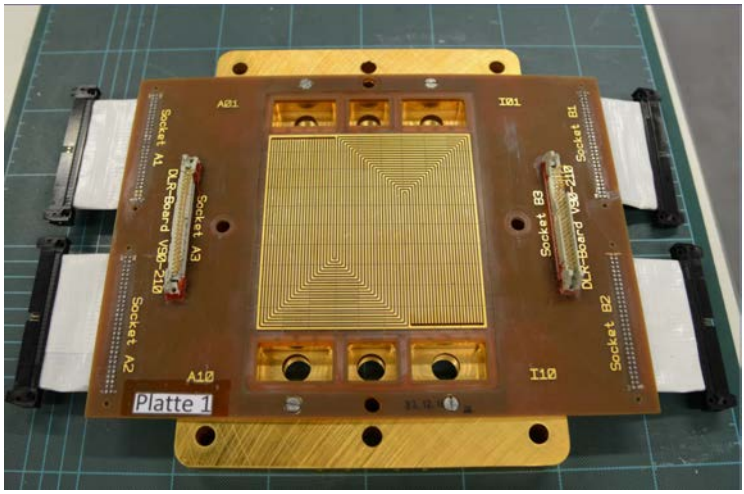

Figure 5.1: Segmented board detail

García-Salaberri *et al.*, 2017; Nazarov & Promislow, 2006) . Oscillatory behaviors have also been found under low cathode humidification conditions (Atkins *et al.*, 2004; Sanchez *et al.*, 2010). All these studies show the relevance of water management in the optimization of fuel cell output performance.

With the aim of clarifying the influence of temperature and gas humidity on the performance stability of PEM Fuel Cells, a wide experimental campaign was performed at DLR-Stuttgart to correlate the relative humidity of the anode an cathode gas feed streams to the stability and performance of the cell. A single fuel cell operated in galvanostatic mode ($0.7 Am^{-2}$) and equipped with a segmented board was used for this purpose. From the reference conditions (50% RH in anode and cathode) the humidification conditions where changed to look for the lowest values of the anode and cathode humidifications compatible with stable cell behavior, the flooding regimes and the drying conditions. Two different operating temperatures were selected (60°C and 80°C), in order to compare the influence of the different water uptake rates of the gaseous streams at both temperatures.

5.2 Experimental set-up

To study the cell response at different humidification levels, a single cell with an electrode area of 142 cm^2 was used. The cell was developed in-house to be used in stack testing at the German Aerospace Center (DLR). The test bench is equipped with programmable logic controllers (PLCs) and commercial electronic loads. It allows automatic control of the operating cell conditions, such as cell pressure, cell temperature, gas flow rates, and humidity of the reactants. The relative humidity (RH) of the inlet gases is controlled by mass evaporator mixers and the cell temperature is kept constant at 60°C or 80°C using a

Table 5.1: Set up parameters

Experimental Conditions	
Temperature	60°C / 80°C
Hydrogen / Air flow	840 / 3320 ml min^{-1}, 1.5 bar
Stoichiometry	Anode 1.2 / Cathode 2.0
Current	100 A
Surface	142 cm^2
Membrane	Nafion© XL
Catalist Layer	0.3 mgPt cm^2 (Ion Power Inc)
Gas Diffusion Layer	Sigracet 25 BC (SGL Group)

thermostat. The electronic load may be operated in galvanostatic (i.e., constant current) or potentiostatic (i.e., constant voltage) modes.

The operating conditions are summarized in Table 5.1. Performance stability was investigated by recording the voltage in galvanostatic conditions for at least 50 min. If the voltage decay was smaller than twice the usual degradation rate, the performance was considered stable. Normal fluctuations in the voltage signal during this time were observed to be less than 50 mV. Cell responses not fulfilling these conditions were classified as either semi-stable, if only a slight drop ($< 20\%$) of performance was observed, or unstable, if a drastic drop ($> 20\%$) of performance was detected.

For the sake of clarity, it should be pointed out that although in some parts of the text the dry gases supply is referred to as 0% RH when the gas humidification is inactive, the actual relative humidity is in this case about 2%.

The membrane electrode assembly (MEA) used in the present work consists of a commercial Nafion XL membrane, with an anode and cathode platinum loading of 0.3 mgPt cm^{-2} on each side (Ion Power Inc). For the GDL, SGL Group Sigracet 25 BC was used for all measurements.

In order to visualize the effects of different gas relative humidity levels on the homogeneity of the current density distribution, locally resolved current density measurements Oberholzer & Boillat (2013); Sanchez *et al.* (2010) were performed. For that purpose, the DLR patented printed circuit board (PCB) for current density measurements was adapted for the use in a multi-serpentine segmented bipolar plate with a 142 cm^2 MEA, allowing for a maximum working temperature of 210°C. The PCB is divided into 90 segments, with 25 integrated temperature sensors, and was used as anode bipolar plate. The coupling of the anode and cathode current density distributions on DLR PCB is described by Lin *et al.* (2011).

The bipolar plate of a fuel cell generally conducts current in three dimensions. To measure the current density distribution in cells with plane MEAs, in-plane current spreading within the plates has to be avoided. For this reason the bipolar plate of the

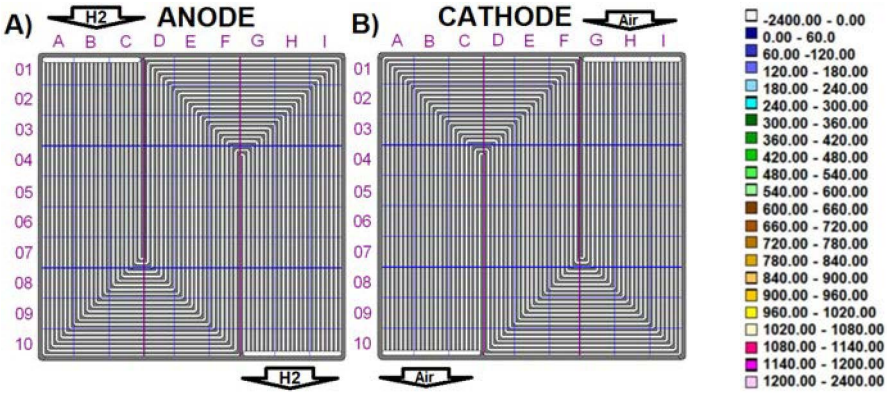

Figure 5.2: Multi-serpentine segmented cell design; a) anode side flow field showing the location of the cell segments and H2 inlet and outlet, b) cathode side flow field showing the location of the cell segments and air inlet and outlet and color code used for the current density distributions presented in Figures 5.3-5.8

cell is replaced by a current density measurement board which conducts current in only one dimension, i.e., only in the through-plane direction. This is achieved by using a plate made of non-conducting material which is covered with conducting layers. The top and back layer of the board are connected which each other by conducting wires and the layer which is in contact with the MEA (segmented surface) is divided into segments to avoid lateral (i.e. in-plane) conduction. This setup forces the current between the segmented surface and the collector surface (back layer) on discrete pathways which connect every segment surface with the collector surface. The current flow in each of the pathways can then be easily measured by integrating calibrated resistors in each path and measuring the voltage drop across each resistor via sense wires connected to a data acquisition unit.

Figure 5.2 shows the multi-serpentine segmented bipolar plate design used in the present experiments, indicating the location of the cell segments in anode side and cathode side flow fields, as well as the color code used in this work. This color code will allow easy identification of changes in the homogeneity of the current density distributions at the different operating conditions considered in Figures 5.3-5.8.For clarity in the evaluation of the cell performance stability, all the plots showing the time evolution of the cell voltage (Figs. 5.3-5.8) include the average (Avg) value and the standard deviation (STD) from the average cell voltage.

All the experiments were performed under the conditions shown in Table 5.1. Under such conditions (pressure, cell current, flow rates, relative humidities), the capacity of the gases to absorb water varies significantly with temperature. The water uptake rate is also referred in the following as water advection capacity (since both the flow rate and the thermodynamic properties of the inlet and outlet streams determine uptake rates). For the particular conditions considered in this work, the (negative, i.e., drying) advection

capacity of the cathode stream at 50%RH inlet relative humidity is roughly 30% of its value at 80°C at the same humidification level. This notable difference can justify the dissimilar behavior observed at low values of RH at the two temperatures under study, which are to be described below.

5.3 Cell temperature 80°C

With the initial aim of finding humidity conditions that allow cell operation without significant performance loss, the cell was first tested at 100%RH on both anode and cathode sides. The measured evolution of the cell voltage is plotted in Figure 5.3a (Avg = 645 mV, STD = 5.38 mV), along with two very similar current density distributions taken with a time lapse of about an hour.

The cell was then tested with partially humidified gases, concluding that values of 50%RH on anode and cathode did not reduce the performance compared to fully humidified gases (Avg = 645 mV, STD = 4.93 mV); such conditions even improved the cell stability (smaller STD) due to the lack of liquid water inside the cell, maintaining the highly stable and homogeneous current density distribution shown in Figure 5.3b. For this reason, reference humidification conditions were defined at 50%RH on both sides.

In order to reduce influences between consecutive experiments, and to ensure the same initial cell conditions before measuring at different RH levels, the cell was always returned to the reference conditions (i.e., 50% RH on both sides) after each experiment. These conditions were maintained until the reference cell output voltage and current density distributions shown in Figure 5.3b were recovered.

To study the influence of reducing the relative humidity of the feed streams from their reference level, RH was reduced to 20%RH first on the anode, and then on the cathode. Figures 5.3c and 5.3d show the voltage responses and current density distributions after the corresponding RH reduction was performed.

Figure 5.3c shows that decreasing the RH to 20%RH on the anode side does not produce any important changes in the stability and current density homogeneity, the cell power output being reduced by less than 1.6% compared with the reference conditions of Figs. 5.3a and 5.3b. Conversely, Figure 5.3d shows that the same percentage reduction in the RH on the cathode side produces the deactivation of large areas of the MEA, which shows very low current densities in the region dominated by the cathode inlet (Fig. 5.2, columns G, H, and I). As the deactivated area increases with time, the voltage response is no longer stable, and a drastic voltage decline eventually occurs, as previously reported by Sanchez & Garcia-Ybarra (2012). It is worth noting that in the experimental conditions considered here the mass flow rate of the cathode stream is about four times larger than that of the anode (see Table 5.1), which justifies the much larger influence of cathode RH on cell performance stability.

As demonstrated in the experiments reported in Figures 5.3c and 5.3d (whose purpose

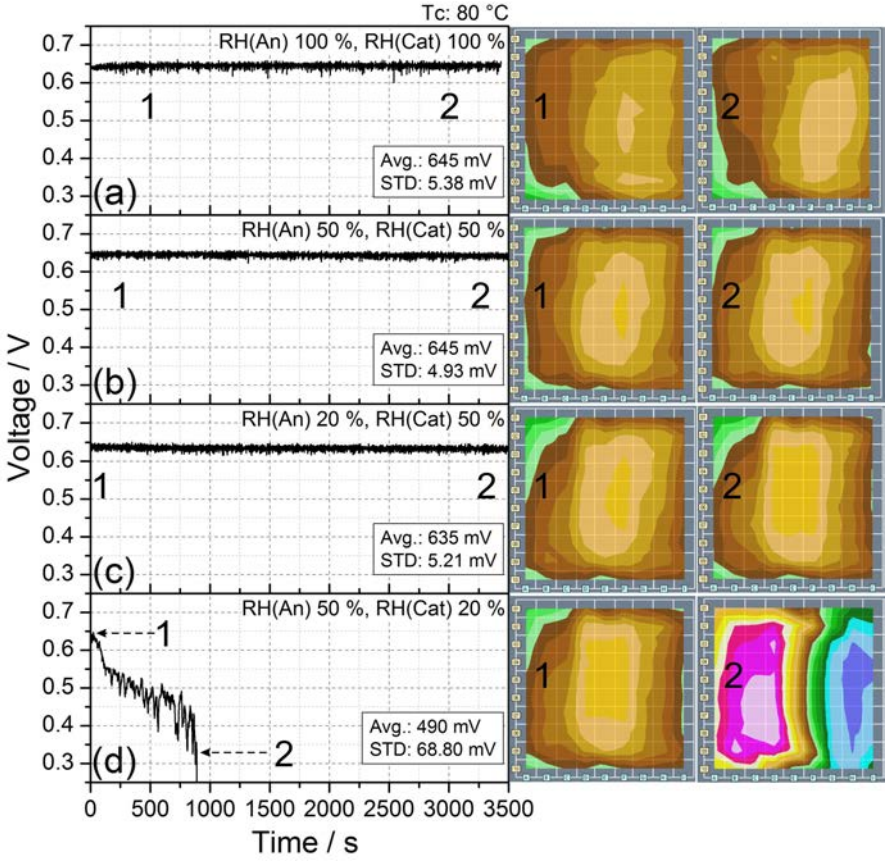

Figure 5.3: Examples of stability of the cell response at relative humidity levels of a) 100% and b) 50% on both anode and cathode sides, c) RH(An) 20% and RH(Cat) 50%, and d) RH(An) 50% and RH(Cat) 20%. The plots show the average value and the standard deviation of the cell voltage, as well as two current densities mappings at different instants of time (see Figure 5.2 to correlate segment positions and current scale). The condition shown in plot b) (i.e., 50% RH on both sides) was chosen as reference condition. The experiments were performed under the conditions reported in Table 5.1 at Tc 80°C. The plots only report a portion of the whole duration of the experiment.

was to find the lowest values of humidification compatible with stable cell behavior), the reduction of the relative humidity in the anode side does not lead to a drastic loss of cell performances and stability. Therefore, the cell was then operated with dry gas supply at the anode side, while successively reducing the relative humidity of the cathode side. Figure 5.4 shows the measured cell responses for a) 100%, b) 70%, c) 50%, and d) 20% RH cathode feed (i.e., air supply).

At cathode RH between 100% and 50%, a stable cell response without significant performance losses is observed. Furthermore, the current density distribution is quite homogeneous and similar to the reference conditions reported in Figures 5.3a and 5.3b.

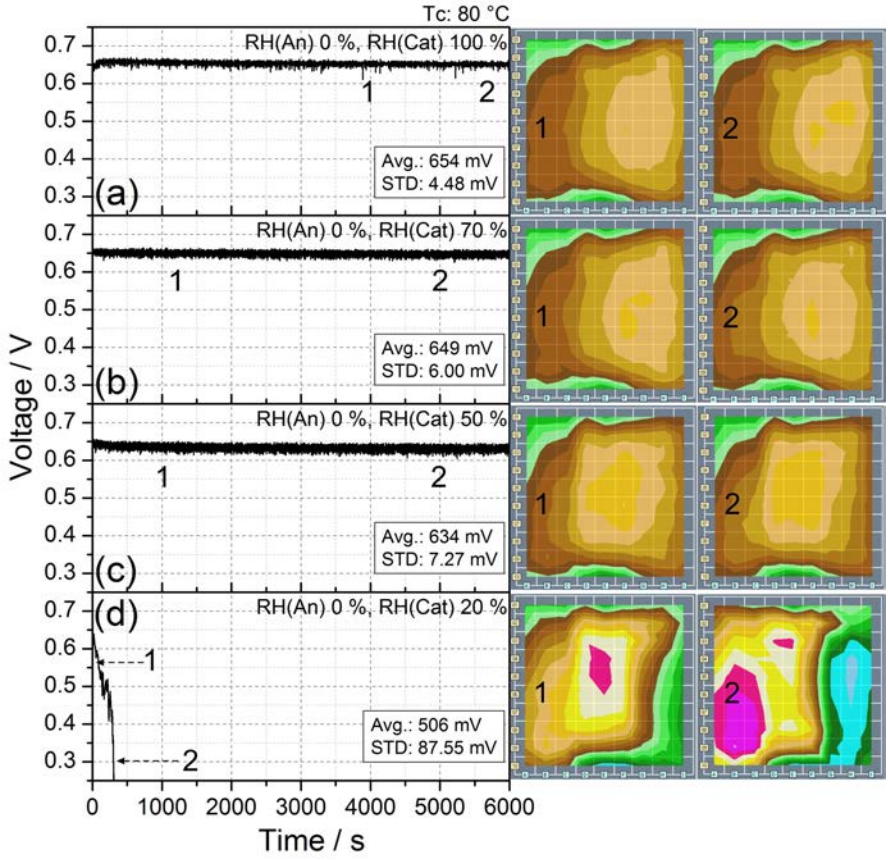

Figure 5.4: Transient cell response at Tc 80°C under dry anode supply and different RH values at the cathode inlet: RH (Cat) a) 100%, b) 70%, c) 50%, and d) 20%. Other experimental conditions are reported in Table 5.1. The numbers represent the times corresponding to the relative current density distribution maps shown on the right.

In contrast, Figure 5.4d shows that 20%RH on the cathode produces an unstable behavior, accompanied by current density deactivations and a drastic voltage drop. This behavior can be correlated to the observation in Figure 5.3d. Note that the voltage drop is faster in Figure 5.4d than in Figure 5.3d as a result of the lower RH at the anode side.

The experiments reported in Figure 5.4 showed the possibility of running the cell under low anode humidification, whereas cathode humidity levels below 20%RH where seen to produce a high decline in cell voltage. Thus, new tests were carried out to study the cell response and performance stability under low cathode and increasing anode humidification levels.

Figure 5.5 shows the consequence of raising the humidification in the anode side under low cathode humidification, particularly with 20% RH at the cathode side. Values

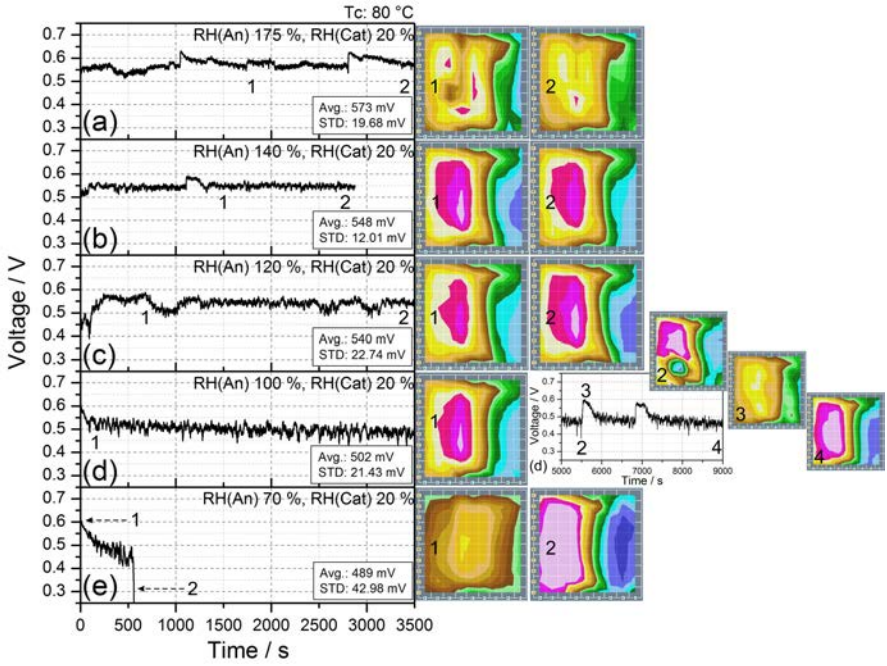

Figure 5.5: Transient cell response at Tc 80°C under different values of anode RH, with 20% RH on the cathode side and under the experimental conditions reported in Table 5.1. The numbers represent the times corresponding to the relative current density distribution maps shown on the right.

of 70%RH on the anode, Figure 5.5e, cannot counteract the low cathode humidification, producing current density deactivations and consequently a drastic voltage drop, as previously observed in Figs. 5.3 and 5.4.

Figure 5.5d shows how increasing anode RH from 70% to 100% prevents the voltage drop, creating a stable state with a significantly lower cell voltage (about 22% less) than in the reference conditions. This was previously reported in the studies by Sanchez at al. 18,38 Sanchez *et al.* (2010, 2013) investigating oscillatory cell behavior under low cathode humidification. Such characteristic voltage oscillations can also be observed in Figure 5.5d, points 2 and 3. Under such conditions, the drying process in the cathode side dominates the cell behavior, producing the current deactivation in areas dominated by the cathode inlet (Fig. 5.2, columns G, H, and I), as a consequence of the low humidification at the air supply.

Figures 5.5a, 5.5b and 5.5c show how raising the relative humidity at the anode side up to values of RH 175% can produce improved voltages with less current density deactivations. Supplying the anode side with over saturated gas produces, however, the erratic accumulation of liquid water on some specific areas of the flow field (see, e.g., segment C7 in Fig. 5.2a, where the flow channel changes direction). Excess liquid water

(i.e., flooding) results in the partial blockage of some channels,which leads to a current reduction on these areas as a result of oxygen starvation, an effect that can be observed in diagram 1 of Figure 5.5a.

Once the possibility of working under low cathode humidification (20% RH, Figs. 5.5a and 5.5b) has been ascertained, the question that remains is whether it could be possible to operate the cell under dry air supply at 80°C. With this aim, new experiments were performed, successively increasing the RH in the anode side while keeping the cathode side under dry gas supply. Stable cell operation was obtained with high performance at sufficiently high values of anode RH; in particular, a quite good response (around 600 mV average voltage) was observed at 250% anode RH, meaning strong water condensation at the anode. In contrast to that observed in Figure 5.5a with 175% RH at the anode and 20% RH at the cathode, the use of dry cathode supply with the same anode RH of 175% leads to an unstable behavior with a drastic voltage drop.

The experiments carried out with low cathode humidification are consistent with previous results obtained with the differential cell technology (Oberholzer & Boillat, 2013)and show how the instable cell behavior, occurring as a result of low cathode humidification, could be compensated using very high relative humidities at the anode (Fig. 5.5).

5.4 Cell temperature 60°C

After illustrating in the previous section the influence that low relative humidities of the feed streams have on the response stability and in the current distribution homogeneity at a cell temperature of 80°C, similar experiments were performed at a cell temperature of 60°C. The aim is to understand the effect of the different advection capacities of the feed streams at different temperatures on the cell performance and stability.

Figure 5.6 displays that similar voltage evolutions and current density distribution are obtained when operating the cell at RH values of 100% (Avg = 611 mV, STD = 6.14 mV) and 50% (Avg = 615 mV, STD = 3.15 mV) on both sides under a cell temperature of 60°C. The same behavior previously observed at 80°C, see Figures 5.3a and 5.3b. In both cases (80°C and 60°C) the cell response was more stable at 50% RH due to the reduction of the flow perturbations induced by the absence of liquid water in the cathode flow field.

As previously observed at 80°C (Fig. 5.4), reducing the relative humidity of the anode feed has a negligible influence on cell stability and performance also at 60°C. Figure 5.7 shows the stable operation obtainable under dry anode supply, for a) 100%, b) 70%, c) 50%, and d) 20% RH cathode feed. Only a slight decrease of 5% in cell performance was observed during the test at 20% RH on the cathode side (Fig. 5.7d), accompanied by a minor local current decrement in the segments of columns H and I corresponding to the cathode inlet 02-03 (Fig. 5.2). Comparison of Figs. 5.5d and 5.7d shows that the drastic voltage drop and current losses observed at 80°C under low humidity conditions does not

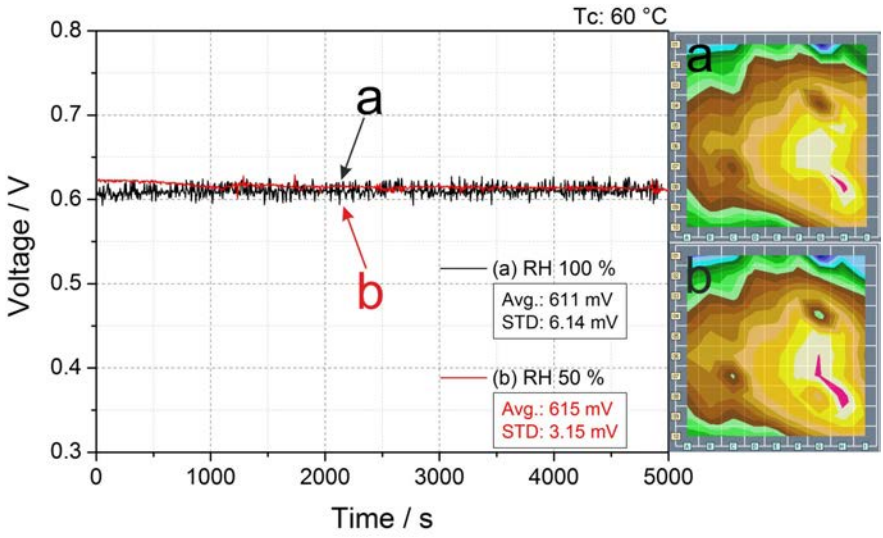

Figure 5.6: Comparison of cell response between relative humidity levels (same on anode and cathode) of 100% (black) and 50% (red), measured at Tc 60°C under the operating conditions reported in Table 5.1. The labels a and b represent the conditions corresponding to the relative current density distribution maps shown on the right.

occur at 60°C. The calculations presented in the next section indicate that the (negative, i.e., drying) advection capacity of the gases at the cathode side at 60°C is much smaller than at 80°C with the same RH cathode feed. This could explain why at a cell temperature of 60°C, under low levels of cathode RH, such as 20%, the deactivation of the cathode inlet segments is not so drastic, and is compatible with a stable cell response, as shown in Figure 5.7d.

The experiments reported in Figure 5.7 show the possibility to operate the cell under low anode humidification even when cathode humidification levels are as low as 20%. Thus new tests were carried out to study the cell response and stability when working under low (20% RH) and dry (0% RH) cathode humidification. Figure reffig:60-3 illustrates how a reduction on cathode relative humidity from 50% (reference condition, Figure 5.3b) to 20% (Fig. 5.8, curve a) and later to 0% (Fig. 5.8, curve b) does not produce a significant effect in the voltage, even when the cell is supplied with dry air. Only a small decrease in cell performance was measured (approximately 3% and 11% less than in the reference condition for 20% and 0% RH cathode feed, respectively), and the cell reached always a stable behavior after several minutes of operation, a markedly different behavior compared to the drastic voltage drop observed at 80°C at the same RH conditions (see, e.g., Figure 5.3d for 50% RH anode and 20% RH cathode).

Thus, stable working conditions can be achieved even when the cell is supplied with dry air at a cell temperature of 60°C. The current density plots included in Figure 5.8 show

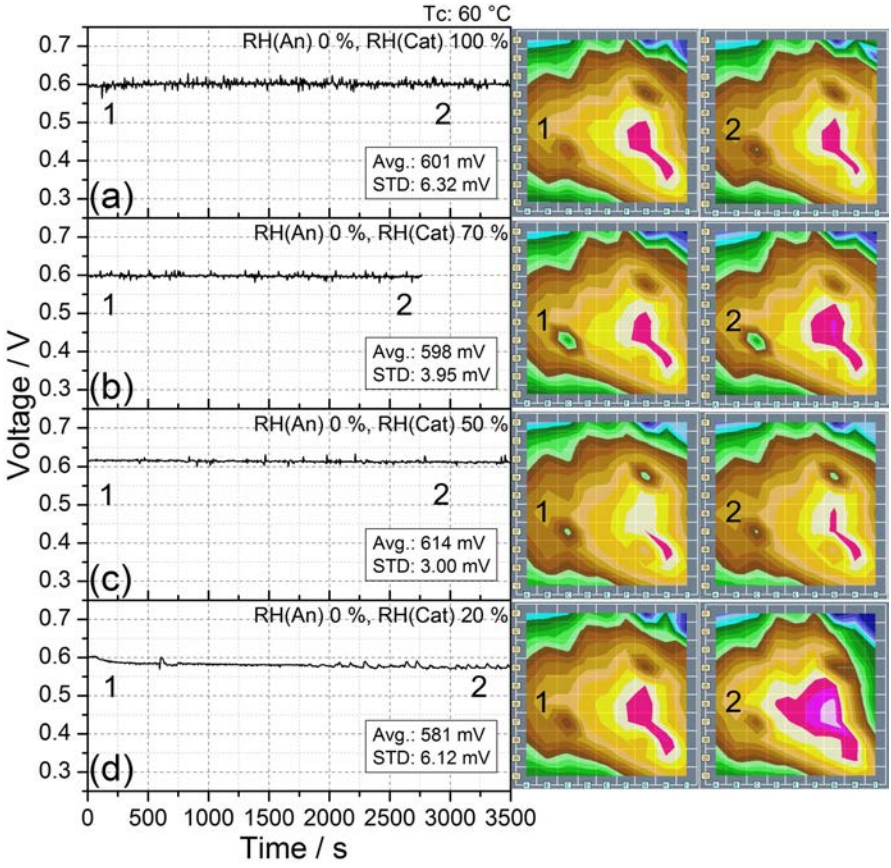

Figure 5.7: Transient cell performance at Tc 60°C under dry anode supply and different RH values at cathode inlet: a) 100%, b) 70%, c) 50% and d) 20%. The other experimental conditions are reported in Table 5.1. The numbers represent the times corresponding to the relative current density distribution maps shown on the right.

the evolution of the current density distribution from the beginning of the experiment (a), and after some minutes of running the cell with dry air supply (b). A reduction of the current on the segments dominated by the cathode inlet (Fig. 5.2, columns G, H, and I) can be observed. This decrease was more pronounced at 0% RH (Fig. 5.8b) than at 20% RH (Fig. 5.8c) as a result of the lower (negative, i.e., drying) advection capacity of the cathode stream at 20% RH than at 0% RH. Indeed, it has already been claimed that this could be the reason for the voltage drop (Sanchez & Garcia-Ybarra, 2012) Anyway, this slight voltage decline is regarded as acceptable (which is not the case at 80°C, see Figure 5.3d), and it does not compromise the stability of the cell response, as observed in Figure 5.8.

The experiment illustrated in Figure 5.8c shows the interesting possibility of operating

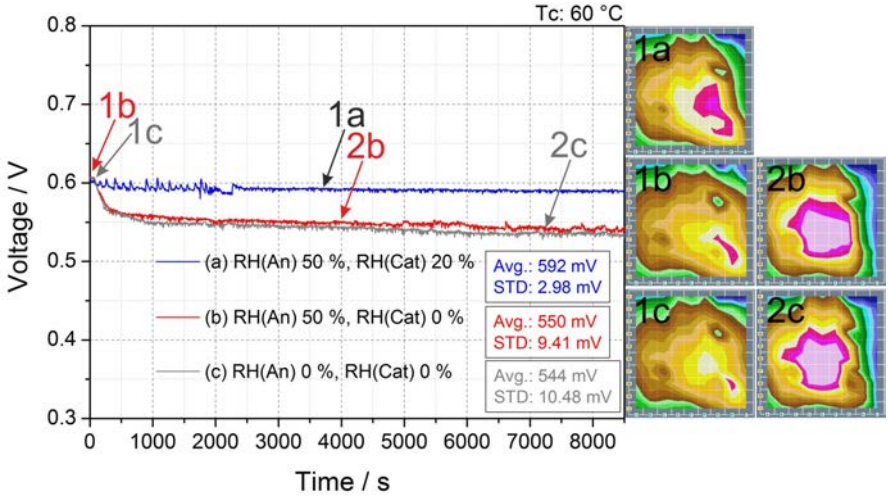

Figure 5.8: Effect on cell response of the reduction of cathode RH from the reference conditions of 50% RH on both sides at Tc 60°C to a) (blue) 50% anode, 20% cathode, b) (red) 50% anode, 0% cathode and c) (grey) 0% anode, 0% cathode. Current density distribution maps recorded at the beginning of the test and after 1 or 2 h are shown.

the cell at 60°C with dry gas supply on both anode and cathode. The plot of the voltage evolution displays how in the first 1000 s the voltage decreases by 50 mV, accompanied by a simultaneous current decrement in the segments of columns H and I located at the cathode inlet. However, after the first 1000 s a stable behavior was established, with no further changes in the current density distribution, thus demonstrating the possibility of operating the cell with dry gases.

5.5 Conclusions

Taking into account all the experiments performed at 60°C and 80 C, a stability map was generated summarizing the observed cell behavior. Figure 5.9 provides an intuitive mapping of the cell stability achievable at different RH of the anode and cathode feed streams. Colors are correlated with performance stability, and boundaries were defined using the experimental results reported in the previous sections, which are represented by hollow squares in the diagram. Looking at this chart, it is clearly seen that the relative humidity of the cathode is the main parameter controlling the performance stability: in fact, RH values on cathode side between 50% and 20% are critical to obtain a relatively stable behavior, while minimizing the level of RH. Table 5.2 summarizes the average and standard deviation values of the cell voltage corresponding to the most substantial experiments presented so far.

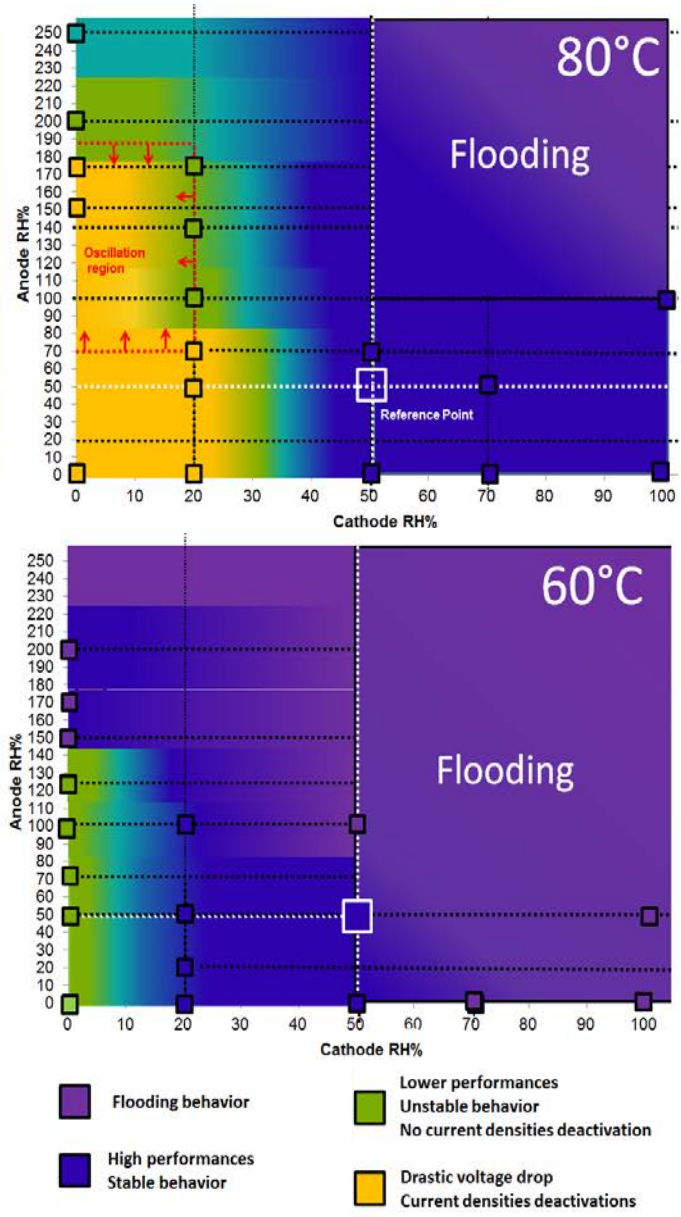

Figure 5.9: Relation between RH and cell performance stability. Squares represent the combination of RH conditions at anode and cathode adopted during the different experiments. Purple is used for flooding behavior, blue for high performances at stable condition, green for slight loss of performances with stable behavior, and orange for unstable behavior with deactivation.

References

ATKINS, J. R., SAVETT, S. C. & CREAGER, S. E. 2004 Large-scale current fluctuations in PEM

Table 5.2: Summary of voltage average (Avg) and standard deviation (STD) values from Figures 5.3, 5.4, 5.5, 5.6, 5.7 and 5.8; (D) indicates drastic voltage drop.

		80°C		
Anode RH	Cathode RH	Avg (mV)	STD(mV)	Figure
100	100	645	5.38	5.3 a
50	50	645	4.93	5.3 b
20	50	645	5.21	5.3 c
50	20	409	68.8(D)	5.3 d
50	0	–	–	
0	100	654	4.48	5.4 a
0	70	649	6.00	5.4 b
0	50	634	7.27	5.4 c
0	20	506	85.55(D)	5.4 d
0	0	–	–	
175	20	573	19.68	5.5 a
140	20	548	12.01	5.5 b
120	20	540	22.74	5.5 c
100	20	502	21.43	5.5 d
70	20	489	42.98(D)	5.5 e
		60°C		
Anode RH	Cathode RH	Avg (mV)	STD(mV)	Figure
100	100	611	6.14	5.6 a
50	50	615	3.15	5.6 b
20	50	–	–	
50	20	592	2.18	5.8 a
50	0	550	9.41	5.8 b
0	100	601	6.32	5.7 a
0	70	598	3.95	5.7 b
0	50	614	3.00	5.7 c
0	20	581	6.12	5.7 d
0	0	544	10.48	5.8 c

fuel cells operating with reduced feed stream humidification. *J. Power Sources* **128** (2), 201–207.

BARBIR, F., GORGUN, H. & WANG, X. 2005 Relationship between pressure drop and cell resistance as a diagnostic tool for PEM fuel cells. *J. Power Sources* **141** (1), 96–101.

BENZIGER, J., CHIA, E., MOXLEY, J. F. & KEVREKIDIS, I. G. 2005 The dynamic response of PEM fuel cells to changes in load. *Chem. Eng. Sci.* **60** (6), 1743–1759.

BÜCHI, F. N., GEIGER, A. B. & NETO, R. P. 2005 Dependence of current distribution on water management in PEFC of technical size. *J. Power Sources* **145** (1), 62–67.

BUCHI, F. N. & SRINIVASAN, S. 1997 Operating Proton Exchange Membrane Fuel Cells Without External Humidification of the Reactant Gases. *J. Electrochem. Soc.* **144** (8), 2767.

COLINART, T., CHENU, A., DIDIERJEAN, S., LOTTIN, O. & BESSE, S. 2009 Experimental study on water transport coefficient in Proton Exchange Membrane Fuel Cell. *J. Power Sources* **190** (2), 230–240.

COLLIER, A., WANG, H., ZI YUAN, X., ZHANG, J. & WILKINSON, D. P. 2006 Degradation of polymer electrolyte membranes. *Int. J. Hydrogen Energy* **31** (13), 1838–1854.

GARCÍA-SALABERRI, P.A., SÁNCHEZ, D.G., BOILLAT, P., VERA, M. & FRIEDRICH, K.A. 2017 Hydration and dehydration cycles in polymer electrolyte fuel cells operated with wet anode and dry cathode feed: A neutron imaging and modeling study. *J. Power Sources* **359**, 634–655.

HANKE-RAUSCHENBACH, R., MANGOLD, M. & SUNDMACHER, K. 2011 Nonlinear dynamics of fuel cells: a review. *Rev Chem Eng* **27**, 23–52.

HSUEN, H.-K. & YIN, K.-M. 2012 Performance equations of proton exchange membrane fuel cells with feeds of varying degrees of humidification. *Electrochim. Acta* **62**, 447–460.

HWNAG, J. J., CHANG, W. R., PENG, R. G., CHEN, P. Y. & SU, A. 2008 Experimental and numerical studies of local current mapping on a PEM fuel cell. *Int. J. Hydrogen Energy* **33** (20), 5718–5727.

JIAO, K. 2011 Experimental and Modelling Studies of Cold Start Processes in Proton Exchange Membrane Fuel Cells .

JIAO, K. & LI, X. 2011 Water transport in polymer electrolyte membrane fuel cells. *Prog. Energy Combust. Sci.* **37** (3), 221–291.

KIM, H.-T., SONG, K.-Y., RESHETENKO, T. V., HAN, S.-I., KIM, T.-Y., CHO, S.-Y., MIN, M.-K., CHAI, G.-S. & SHIN, S.-C. 2009 Electrochemical analysis of polymer electrolyte membrane fuel cell operated with dry-air feed. *J. Power Sources* **193** (2), 515–522.

KNIGHTS, S. D., COLBOW, K. M., ST-PIERRE, J. & WILKINSON, D. P. 2004 Aging mechanisms and lifetime of PEFC and DMFC. *J. Power Sources* **127** (1), 127–134.

LEE, Y., KIM, B. & KIM, Y. 2009 An experimental study on water transport through the membrane of a PEFC operating in the dead-end mode. *Int. J. Hydrogen Energy* **34** (18), 7768–7779.

LI, H., TANG, Y., WANG, Z., SHI, Z., WU, S., SONG, D., ZHANG, J., FATIH, K., ZHANG, J., WANG, H., LIU, Z., ABOUATALLAH, R. & MAZZA, A. 2008 A review of water flooding issues in the proton exchange membrane fuel cell. *J. Power Sources* **178** (1), 103–117.

LIN, R., GULZOW, E., SCHULZE, M. & FRIEDRICH, K. A. 2011 Investigation of Membrane Pinhole Effects in Polymer Electrolyte Fuel Cells by Locally Resolved Current Density. *J. Electrochem. Soc.* **158** (1), B11.

NAZAROV, I. & PROMISLOW, K. 2006 Ignition waves in a stirred PEM fuel cell. *Chem. Eng. Sci.* **61** (10), 3198–3209.

OBERHOLZER, P. & BOILLAT, P. 2013 Local Characterization of PEFCs by Differential Cells: Systematic Variations of Current and Asymmetric Relative Humidity. *J. Electrochem. Soc.* **161** (1), F139–F152.

OWEJAN, J. P., TRABOLD, T. A., GAGLIARDO, J. J., JACOBSON, D. L., CARTER, R. N., HUSSEY, D. S. & ARIF, M. 2007*a* Voltage instability in a simulated fuel cell stack correlated to cathode water accumulation. *J. Power Sources* **171** (2), 626–633.

OWEJAN, J. P., TRABOLD, T. A., JACOBSON, D. L., ARIF, M. & KANDLIKAR, S. G. 2007*b* Effects of flow field and diffusion layer properties on water accumulation in a PEM fuel cell. *Int. J. Hydrogen Energy* **32**, 4489–4502.

RESHETENKO, T. V., BENDER, G., BETHUNE, K. & ROCHELEAU, R. 2011 Systematic study of back pressure and anode stoichiometry effects on spatial PEMFC performance distribution. *Electrochim. Acta* **56** (24), 8700–8710.

RESHETENKO, T. V., BENDER, G., BETHUNE, K. & ROCHELEAU, R. 2012 Systematic studies of the gas humidification effects on spatial PEMFC performance distributions. *Electrochim. Acta* **69**, 220–229.

SANCHEZ, D. G. & GARCIA-YBARRA, P. L. 2012 PEMFC operation failure under severe dehydration. *Int. J. Hydrogen Energy* **37** (8), 7279–7288.

SANCHEZ, D. G., GUINEA DIAZ, D., HIESGEN, R., WEHL, I. & FRIEDRICH, K. A. 2010 Oscillations of PEM fuel cells at low cathode humidification. *J. Electroanal. Chem.* **649** (1-2), 219–231.

SANCHEZ, D. G., ORTIZ, A. & FRIEDRICH, K. A. 2013 Oscillation of PEFC under Low Cathode Humidification: Effect of Gravitation and Bipolar Plate Design. *J. Electrochem. Soc.* **160** (6), F636–F644.

SANCHEZ, D. G., RUIU, T., BISWAS, I., SCHULZE, M., HELMLY, S. & FRIEDRICH, K. A. 2017 Local impact of humidification on degradation in polymer electrolyte fuel cells .

SANCHEZ, D. G., RUIU, T., FRIEDRICH, K. A., SANCHEZ-MONREAL, J. & VERA, M. 2016 Analysis of the Influence of Temperature and Gas Humidity on the Performance Stability of Polymer Electrolyte Membrane Fuel Cells. *J. Electrochem. Soc.* **163** (3), F150–F159.

SCHNEIDER, I. A., FREUNBERGER, S. A., KRAMER, D., WOKAUN, A. & SCHERER, G. G. 2007 Oscillations in Gas Channels. *J. Electrochem. Soc.* **154** (4), B383.

SCHULZE, M., GÜLZOW, E., SCHÖNBAUER, S., KNÖRI, T. & REISSNER, R. 2007 Segmented cells as tool for development of fuel cells and error prevention/prediagnostic in fuel cell stacks. *J. Power Sources* **173** (1), 19–27.

TANG, W., LIN, R., WENG, Y., ZHANG, J. & MA, J. 2013 The effects of operating temperature on current density distribution and impedance spectroscopy by segmented fuel cell. *Int. J. Hydrogen Energy* **38** (25), 10985–10991.

TÜBER, KLAUS, PÓCZA, DAVID & HEBLING, CHRISTOPHER 2003 Visualization of water buildup in the cathode of a transparent PEM fuel cell. *J. Power Sources* **124** (2), 403–414.

VENGATESAN, S., KIM, H.-J., CHO, E. A., JEONG, S. U., HA, H. Y., OH, I.-H., HONG, S.-A. & LIM, T.-H. 2006 Operation of a proton-exchange membrane fuel cell under non-humidified conditions using thin cast Nafion membranes with different gas-diffusion media.

WENG, F.-B., JOU, B.-S., LI, C.-W., SU, A. & CHAN, S.-H. 2008 The effect of low humidity on the uniformity and stability of segmented PEM fuel cells. *J. Power Sources* **181** (2), 251–258.

WU, J., YUAN, X. Z., MARTIN, J. J., WANG, H., ZHANG, J., SHEN, J., WU, S. & MERIDA, W. 2008 A review of PEM fuel cell durability: Degradation mechanisms and mitigation strategies. *J. Power Sources* **184** (1), 104–119.

YOON, Y.-G., LEE, W.-Y., YANG, T.-H., PARK, G.-G. & KIM, C.-S. 2003 Current distribution in a single cell of PEMFC. *J. Power Sources* **118** (1), 193–199.

YOUSFI-STEINER, N., MOÇOTÉGUY, PH., CANDUSSO, D., HISSEL, D., HERNANDEZ, A. & ASLANIDES, A. 2008 A review on PEM voltage degradation associated with water management: Impacts, influent factors and characterization. *J. Power Sources* **183** (1), 260–274.

ZHANG, J. J., TANG, Y., SONG, C., CHENG, X., ZHANG, J. J. & WANG, H. 2007 PEM fuel cells operated at 0\% relative humidity in the temperature range of 23–120°C. *Electrochim. Acta* **52** (15), 5095–5101.

CHAPTER

SIX

Global balance of water model: analysis of the influence of temperature and gas humidity on the performance stability of polymer electrolyte membrane fuel cells

Contents

6.1 Introduction

This chapter presents a zero-dimensional balance of water (BOW) model that can be used to investigate theoretically the influence of temperature and gas humidity on the performance stability of polymer exchange membrane fuel cells (PEMFCs). The model accounts for the water flow rates coming into and out of the anode and cathode channels, as well as the water production rate due to the oxygen reduction reaction. The resulting expression for the rate of water accumulation in the cell provides a clear-cut frontier between overall hydration and dehydration conditions for different cell temperatures and anode and cathode relative humidities, to be compared with the experimentally observed performance stability maps obtained in the previous chapter. Accounting for the thermal energy of the different streams coming into and out of the cell, as well as the heat released by the electrochemical reactions, a global energy balance allows to compare the heat required for humidification of the feed streams with the heat available in the cell under

the conditions tested in the experiments. After particularizing the global balances to the experimental set-up considered in Chapter 5, a detailed analysis of the water advection capacities of the anode and cathode streams leads to a dimensionless interpretation of the BOW model that uses the water production rate by the oxygen reduction reaction (ORR) as the appropriate scaling factor. The dimensionless BOW model thus obtained enables to draw general conclusions on the performance stability of PEMFCs that go beyond the particular experimental setup considered previously.

Several models have studied water transport in fuel cells (Jiao & Li, 2011; Nazarov & Promislow, 2006; Nguyen & White, 1993; Sanchez & Garcia-Ybarra, 2012; Weber *et al.*, 2014; Weber & Newman, 2004). The main focus of these models was generally membrane hydration and the processes of water absorption from saturated vapor and water desorption into dry or humidified gases. These models deepened into the water absorption from gas phase and from liquid phase, including the Schroeder paradox (von Schroeder, 1903). Unlike these works, the present model addresses the problem from a global perspective, considering the cell as a *black-box* like system. The model accounts for the gas inlets and outlets as well as the water production rate in order to provide a global balance of water.

A similar analysis was previously presented by Barbir (2005), who applied a global mass balance separately to the anode and cathode electrodes assuming a constant water transfer rate from anode to cathode across the membrane. The Barbir model was used to estimate the amount of water needed by each side for fixed operating conditions and assuming complete water saturation of the outlet gases. Instead, in this work the global balance of water will be used as a qualitative index to correlate the fuel cell performance stability.

6.2 Global balance of water (BOW)

In order to gain further insight into the experimental results reported in Chapter 5, a global balance of water for operating PEMFCs can be used. The net amount of water added to, or removed from, the cell is closely related to the volume flow rate and the water content of the inlet and outlet gases, and to the water production rate due to electrochemical reactions. An integral mass balance for the cell water content applied to the control volume shown in Fig. 6.1 yields

$$\mathrm{BOW} \equiv \frac{\mathrm{d}m_{\mathrm{W,cell}}}{\mathrm{d}t} = \left(\dot{m}_{\mathrm{W,a,in}} - \dot{m}_{\mathrm{W,a,out}}\right) + \left(\dot{m}_{\mathrm{W,c,in}} - \dot{m}_{\mathrm{W,c,out}}\right) + \dot{m}_{\mathrm{W,P}} \qquad (6.1)$$

stating that the net mass of water that accumulates in the cell per unit time, hereafter denoted as BOW, is equal to the water flow rates provided by the anode, $\dot{m}_{\mathrm{W,a,in}}$, and cathode, $\dot{m}_{\mathrm{W,c,in}}$, feed streams, minus the water flow rates removed from the cell by the anode, $\dot{m}_{\mathrm{W,a,out}}$, and cathode, $\dot{m}_{\mathrm{W,c,out}}$, outlet gases, plus the water production rate due

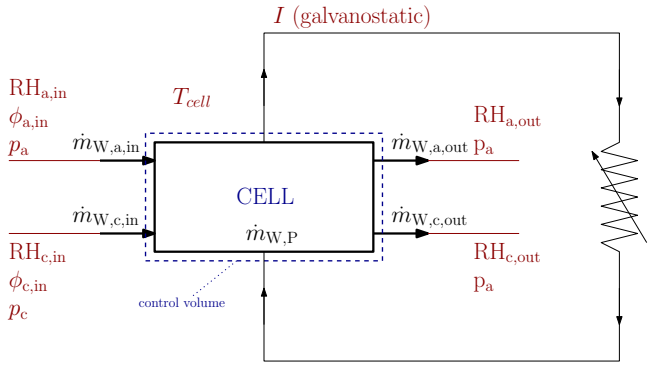

Figure 6.1: Schematic representation of the control volume considered to evaluate the global balance of water in the cell.

to the oxygen reduction reaction, $\dot{m}_{\mathrm{W,P}}$. Note that, with this deffinition, a negative BOW implies global cell dehydration, whereas a positive BOW indicates cell hydration.

Consider a hydrogen PEM fuel cell operating in galvanostatic mode at temperature T_{cell} and anode and cathode back pressures p_{a} and p_{c}. If the total current produced by the cell is denoted by I, the hydrogen and air volume flow rates in the feed streams can be expressed in terms of the anode and cathode stoichiometries, ϕ_{a} and ϕ_{c}, as

$$Q_{\mathrm{H_2}} = \phi_{\mathrm{a}} \frac{I}{2F} V_{\mathrm{m}}^{\mathrm{sc}} \quad \text{and} \quad Q_{\mathrm{air}} = \phi_{\mathrm{c}} \frac{I}{4F} V_{\mathrm{m}}^{\mathrm{sc}} \frac{1}{X_{\mathrm{O_2}}^{\mathrm{air}}} \tag{6.2}$$

where $V_{\mathrm{m}}^{\mathrm{sc}} = 22.4$ l/mol is the standard molar volume, i.e., the volume occupied by one mole of ideal gas at standard temperature and pressure (273 K and 1 atm), and $X_{\mathrm{O_2}}^{\mathrm{air}} = 0.21$ is the molar fraction of oxygen in dry air. Note that these expressions provide the feed flow rates in standard volume units per unit time (usually standard liters per minute, or standard cubic centimeters per minute, sccm). Multiplying by the standard densities of hydrogen and air provides the corresponding feed mass flow rates

$$\dot{m}_{\mathrm{H_2,a,in}} = \rho_{\mathrm{H_2}}^{\mathrm{sc}} Q_{\mathrm{H_2}} = \phi_{\mathrm{a}} \frac{I}{2F} M_{\mathrm{H_2}} \quad \text{and} \quad \dot{m}_{\mathrm{air,c,in}} = \rho_{\mathrm{air}}^{\mathrm{sc}} Q_{\mathrm{air}} = \phi_{\mathrm{c}} \frac{I}{4F} M_{\mathrm{air}} \frac{1}{X_{\mathrm{O_2}}^{\mathrm{air}}} \tag{6.3}$$

where $M_{\mathrm{H_2}} = 2.016$ g/mol and $M_{\mathrm{air}} = 28.97$ g/mol are the molar masses of hydrogen and air, respectively.

As previously discussed, to maintain a proper water management the reactant gases are humidified so as to reach the desired relative humidities, $\mathrm{RH_{a,in}}$ and $\mathrm{RH_{c,in}}$, prior to enter the cell. To evaluate the global balance of water, the net amount of gases feed to or removed from the cell (i.e., the inlet and outlet mass flow rates of hydrogen and water at the anode, and of air and water at the cathode) have to be determined at the specified operating conditions. To this end, the mass flow rates of the feed streams are calculated

assuming ideal gas flows at the inflow conditions given in Table 5.1. The anode feed is thus considered a partially humidified hydrogen stream (at the specified $RH_{a,in}$) and the cathode feed a partially humidified air stream (at the specified $RH_{c,in}$). The outlet streams could be assumed to be fully humidified (Barbir, 2005), but a more general discussion results when considering arbitrary humidifications, $RH_{a,out}$ and $RH_{c,out}$. It is important to note that their mass flow rates differ from those of the inlet streams due to the consumption of reactants and the generation of products by the electrochemical reactions. For instance, in our experiments, at the anode side ($\phi_a = 1.2$) the outlet stream carries only $(\phi_a - 1)/\phi_a = 16.7\%$ of the initial hydrogen flow, whereas at the cathode side ($\phi_c = 2.0$) the outlet stream carries only $(\phi_c - 1)/\phi_c = 50\%$ of the initial oxygen flow. As a result, the outlet streams are able to carry less water than the corresponding inlet streams at the same RH, something that has a definite impact on the global water management, as will be shown below.

6.2.1 Water production rate

During PEMFC operation, water is generated at the cathode by the ORR. Therefore, a net water source exists at the cathode catalyst layer, with a water production rate that, in the absence of crossover, is directly proportional to the cell current

$$\dot{m}_{W,P} = \frac{I}{2F} M_W \tag{6.4}$$

where $M_W = 18.015$ g/mol is the molar mass of water and the factor 2 in the denominator stems from the global stoichiometry of the ORR

$$O_2 + 4H^+ + 4e^- \rightarrow 2H_2O \tag{2.4}$$

which requires two protons and two electrons to produce a single water molecule. In the experimental study presented in Chapter 5 all the tests were carried out in galvanostatic mode with $I = 100$ A, hence the water production rate given by (6.4) remained constant at 9.34×10^{-6} kg/s $= 33.6$ g/h in all cases.

6.2.2 Water content in the anode streams

As previously discussed, the anode supply gases are hydrated to a given relative humidity $RH_{a,in}$, which corresponds to a certain water mass flow rate $\dot{m}_{W,a,in}$ being fed to the cell. At the anode outlet, due to consumption of hydrogen by the electrochemical reactions, only a fraction $(\phi_a - 1)/\phi_a$ of the hydrogen fed comes out from the channel outlet. The reduction on the mass flow rate implies also a reduction of the water removal capacity, $\dot{m}_{W,a,out}$, which depends also on the relative humidity of the outlet gases, $RH_{a,out}$.

6.2.2.1 Anode inlet

For a given relative humidity $\mathrm{RH}_{\mathrm{a,in}}$ of the anode gas feed, the partial pressure of water $p_{\mathrm{W,a,in}}$ is only a function of the cell temperature

$$p_{\mathrm{W,a,in}} = \left(\frac{\mathrm{RH}_{\mathrm{a,in}}}{100}\right) p_{\mathrm{sat}}\left(T_{\mathrm{cell}}\right) \tag{6.5}$$

where the saturation vapor pressure of water is given by (Springer *et al.*, 1991)

$$\log_{10} p_{\mathrm{sat}} = -2.1794 + 0.02953 T_{\mathrm{cell}} - 9.1837 \times 10^{-5} T_{\mathrm{cell}}^2 + 1.4454 \times 10^{-7} T_{\mathrm{cell}}^3 \tag{6.6}$$

with p_{sat} in atm and T_{cell} in degrees Celsius. Dividing the water vapor pressure by the total anode pressure yields the molar fraction of water at the anode inlet

$$X_{\mathrm{W,a,in}} = \frac{p_{\mathrm{W,a,in}}}{p_{\mathrm{a}}} \tag{6.7}$$

To obtain the mass flow of water that enters the cell with the anode gas feed, $\dot{m}_{\mathrm{W,a,in}}$, first the molar fraction of water must be expressed in terms of the mass fractions of hydrogen and water as

$$X_{\mathrm{W,a,in}} = \frac{\dfrac{Y_{\mathrm{W,in}}}{M_{\mathrm{W}}}}{\dfrac{Y_{\mathrm{W,in}}}{M_{\mathrm{W}}} + \dfrac{Y_{\mathrm{H_2,in}}}{M_{\mathrm{H_2}}}} = \frac{\dfrac{\dot{m}_{\mathrm{W,a,in}}}{M_{\mathrm{W}}}}{\dfrac{\dot{m}_{\mathrm{W,a,in}}}{M_{\mathrm{W}}} + \dfrac{\dot{m}_{\mathrm{H_2,a,in}}}{M_{\mathrm{H_2}}}} \tag{6.8}$$

where the mass fractions have been written for convenience in terms of the respective mass flow rates

$$Y_k = \frac{\dot{m}_k}{\dot{m}_{\mathrm{H_2,a,in}} + \dot{m}_{\mathrm{W,a,in}}} \quad \text{with} \quad k = \mathrm{H_2}, \mathrm{W} \tag{6.9}$$

Solving now (6.8) for $\dot{m}_{\mathrm{W,a,in}}$ yields

$$\dot{m}_{\mathrm{W,a,in}} = \frac{X_{\mathrm{W,a,in}}}{1 - X_{\mathrm{W,a,in}}} \left(\frac{M_{\mathrm{W}}}{M_{\mathrm{H_2}}}\right) \dot{m}_{\mathrm{H_2,a,in}} \tag{6.10}$$

where the hydrogen mass flow rate, $\dot{m}_{\mathrm{H_2,a,in}}$, can be expressed in terms of the cell current density as in (6.3). Using this expression in (6.10) results in the desired expression for the mass flow rate of water coming into the cell through the anode inlet

$$\dot{m}_{\mathrm{W,a,in}} = \frac{X_{\mathrm{W,a,in}}}{1 - X_{\mathrm{W,a,in}}} \phi_{\mathrm{a}} \frac{I}{2F} M_{\mathrm{W}} \tag{6.11}$$

6.2.2.2 Anode outlet

At the anode outlet, hydrogen has been partially consumed and the water content depends on the relative humidity of the anode outlet gases, $\mathrm{RH}_{\mathrm{a,out}}$. The hydrogen mass flow rate at the outlet, $\dot{m}_{\mathrm{H_2,a,out}}$, is obtained as the unconsumed fraction of the inlet mass flow rate

$$\dot{m}_{\mathrm{H_2,a,out}} = \frac{\phi_{\mathrm{a}} - 1}{\phi_{\mathrm{a}}} \dot{m}_{\mathrm{H_2,a,in}} = (\phi_a - 1) \frac{I}{2F} M_{\mathrm{H_2}} \tag{6.12}$$

The water vapor pressure and molar fraction of water at the outlet are obtained as

$$p_{\mathrm{W,a,out}} = \left(\frac{\mathrm{RH}_{\mathrm{a,out}}}{100} \right) p_{\mathrm{sat}} \left(T_{\mathrm{cell}} \right) \quad \text{and} \quad X_{\mathrm{W,a,out}} = \frac{p_{\mathrm{W,a,out}}}{p_{\mathrm{a}}} \tag{6.13}$$

Proceeding as in the anode inlet, i.e., expressing the molar fraction of water in terms of the mass fractions of hydrogen and water at the anode outlet, yields the mass flow of water coming out of the cell through the anode outlet

$$\dot{m}_{\mathrm{W,a,out}} = \frac{X_{\mathrm{W,a,out}}}{1 - X_{\mathrm{W,a,out}}} \left(\frac{M_{\mathrm{W}}}{M_{\mathrm{H_2}}} \right) \dot{m}_{\mathrm{H_2,a,out}} = \frac{X_{\mathrm{W,a,out}}}{1 - X_{\mathrm{W,a,out}}} \left(\phi_{\mathrm{a}} - 1 \right) \frac{I}{2F} M_{\mathrm{W}} \tag{6.14}$$

where Eq. (6.12) has been used to write the second equality. As can be seen, the above expression is very similar to (6.11), except for the fact that the factor $(\phi_{\mathrm{a}} - 1)$, which takes into account the consumption of hydrogen at the anode electrode, appears here instead of ϕ_{a}. It is interesting to note that in the limit $\phi_{\mathrm{a}} \to 1$ both $\dot{m}_{\mathrm{H_2,a,out}}$ and $\dot{m}_{\mathrm{W,a,out}}$ tend to zero, as they are proportional to $\phi_{\mathrm{a}} - 1$. This particular limit corresponds to the so-called *dead-end* operation mode, where no gas is allowed to flow out the anode channel.

6.2.3 Water content in the cathode streams

As in the anode compartment, the cathode air flow is hydrated to a given relative humidity $\mathrm{RH}_{\mathrm{c,in}}$ before entering the cell, which implies a certain water mass flow rate $\dot{m}_{\mathrm{W,c,in}}$ being fed to the cell. At the cathode outlet, due to consumption of oxygen by the electrochemical reactions, only a fraction $(\phi_{\mathrm{c}} - 1)/\phi_{\mathrm{c}}$ of the initial oxygen comes out from the cell. However, the large amount of nitrogen present in the air stream remains virtually unreacted, which introduces certain differences with respect to the anode stream. In particular, the water removal capacity of the cathode outlet gases, $\dot{m}_{\mathrm{W,c,out}}$, turns out to be much larger than that of the anode.

6.2.3.1 Cathode inlet

For a given relative humidity $\mathrm{RH}_{\mathrm{c,in}}$ of the air feed stream, the partial pressure of water and the water molar fraction at the cathode inlet are given by

$$p_{\mathrm{W,c,in}} = \left(\frac{\mathrm{RH}_{\mathrm{c,in}}}{100}\right) p_{\mathrm{sat}}\left(T_{\mathrm{cell}}\right) \quad \text{and} \quad X_{\mathrm{W,c,in}} = \frac{p_{\mathrm{W,c,in}}}{p_{\mathrm{c}}} \tag{6.15}$$

Dry air is composed mainly by nitrogen (78%), oxygen (about 21%), argon (almost 1%) and many other species, which are present in very small quantities. For simplicity in the presentation, in the following discussion air will be assumed to be composed only of oxygen and nitrogen, with molar fractions $X^{\mathrm{air}}_{\mathrm{O}_2} = 0.21$ and $X^{\mathrm{air}}_{\mathrm{N}_2} = 0.79$.

After being humidified with water vapor, the new molar fractions of nitrogen and oxygen in the humid air stream are

$$X_{\mathrm{N}_2,\mathrm{c,in}} = (1 - X_{\mathrm{W,c,in}}) X^{\mathrm{air}}_{\mathrm{N}_2} \quad \text{and} \quad X_{\mathrm{O}_2,\mathrm{c,in}} = (1 - X_{\mathrm{W,c,in}}) X^{\mathrm{air}}_{\mathrm{O}_2} \tag{6.16}$$

As in the anode side, to obtain the water mass flow rate injected to the cell, the molar fraction of water $X_{\mathrm{W,c,in}}$ must be expressed in terms of the mass fractions of oxygen, nitrogen and water at the cathode inlet

$$X_{\mathrm{W,c,in}} = \frac{\dfrac{Y_{\mathrm{W,c,in}}}{M_{\mathrm{W}}}}{\dfrac{Y_{\mathrm{W,c,in}}}{M_{\mathrm{W}}} + \dfrac{Y_{\mathrm{O}_2,\mathrm{c,in}}}{M_{\mathrm{O}_2}} + \dfrac{Y_{\mathrm{N}_2,\mathrm{c,in}}}{M_{\mathrm{N}_2}}} = \frac{\dfrac{\dot{m}_{\mathrm{W,c,in}}}{M_{\mathrm{W}}}}{\dfrac{\dot{m}_{\mathrm{W,c,in}}}{M_{\mathrm{W}}} + \dfrac{\dot{m}_{\mathrm{O}_2,\mathrm{c,in}}}{M_{\mathrm{O}_2}} + \dfrac{\dot{m}_{\mathrm{N}_2,\mathrm{c,in}}}{M_{\mathrm{N}_2}}} \tag{6.17}$$

which, solving for $\dot{m}_{\mathrm{W,c,in}}$, yields

$$\dot{m}_{\mathrm{W,c,in}} = \frac{X_{\mathrm{W,c,in}}}{1 - X_{\mathrm{W,c,in}}} \left(\frac{M_{\mathrm{W}}}{M_{\mathrm{O}_2}} \dot{m}_{\mathrm{O}_2,\mathrm{c,in}} + \frac{M_{\mathrm{W}}}{M_{\mathrm{N}_2}} \dot{m}_{\mathrm{N}_2,\mathrm{c,in}}\right) \tag{6.18}$$

The oxygen and nitrogen mass flow rates appearing in (6.18) are given by

$$\dot{m}_{\mathrm{O}_2,\mathrm{c,in}} = \rho^{\mathrm{sc}}_{\mathrm{O}_2} X^{\mathrm{air}}_{\mathrm{O}_2} Q_{\mathrm{air}} = \phi_{\mathrm{c}} \frac{I}{4F} M_{\mathrm{O}_2} \tag{6.19}$$

$$\dot{m}_{\mathrm{N}_2,\mathrm{c,in}} = \rho^{\mathrm{sc}}_{\mathrm{N}_2} X^{\mathrm{air}}_{\mathrm{N}_2} Q_{\mathrm{air}} = \frac{X^{\mathrm{air}}_{\mathrm{N}_2}}{X^{\mathrm{air}}_{\mathrm{O}_2}} \phi_{\mathrm{c}} \frac{I}{4F} M_{\mathrm{N}_2} \tag{6.20}$$

where the last equalities emerge when using (6.2) to write for Q_{air} in terms of the cell current. Using the above expressions in (6.18) gives the following expression for the mass

flow rate of water coming into the cell through the cathode inlet

$$\dot{m}_{\mathrm{W,c,in}} = \frac{X_{\mathrm{W,c,in}}}{1-X_{\mathrm{W,c,in}}}\left(\phi_{\mathrm{c}} + \frac{X^{\mathrm{air}}_{\mathrm{N_2}}}{X^{\mathrm{air}}_{\mathrm{O_2}}}\phi_{\mathrm{c}}\right)\frac{I}{4F}M_{\mathrm{W}} \tag{6.21}$$

6.2.3.2 Cathode outlet

At the cathode outlet, oxygen has been partially consumed but nitrogen remains the same, as it does not undergo any chemical reaction. Therefore, the corresponding mass flow rates can be written as

$$\dot{m}_{\mathrm{O_2,a,out}} = \frac{\phi_{\mathrm{c}}-1}{\phi_{\mathrm{c}}}\dot{m}_{\mathrm{O_2,a,in}} \quad \text{and} \quad \dot{m}_{\mathrm{N_2,a,out}} = \dot{m}_{\mathrm{N_2,a,in}} \tag{6.22}$$

The water content depends on the relative humidity at the outlet. Typically, saturated conditions could be considered, but a more general discussion results by considering an arbitrary value of $\mathrm{RH_{c,out}}$. The partial pressure and molar fraction of water at the cathode outlet are related to the relative humidity considered as discussed before

$$p_{\mathrm{W,c,out}} = \left(\frac{\mathrm{RH_{c,out}}}{100}\right)p_{\mathrm{sat}}\left(T_{\mathrm{cell}}\right) \quad \text{and} \quad X_{\mathrm{W,c,out}} = \frac{p_{\mathrm{W,c,out}}}{p_{\mathrm{c}}} \tag{6.23}$$

And again, from the expression of the molar fraction of water written in terms of the mass fractions of oxygen, nitrogen and water, the following expression results for the water mass flow rate exiting the cell at the cathode outlet

$$\begin{aligned}\dot{m}_{\mathrm{W,c,out}} &= \frac{X_{\mathrm{W,c,out}}}{1-X_{\mathrm{W,c,out}}}\left(\frac{\dot{m}_{\mathrm{O_2,c,out}}}{M_{\mathrm{O_2}}} + \frac{\dot{m}_{\mathrm{N_2,c,out}}}{M_{\mathrm{N_2}}}\right)M_{\mathrm{W}} \\ &= \frac{X_{\mathrm{W,c,out}}}{1-X_{\mathrm{W,c,out}}}\left(\phi_{\mathrm{c}} - 1 + \frac{X^{\mathrm{air}}_{\mathrm{N_2}}}{X^{\mathrm{air}}_{\mathrm{O_2}}}\phi_{\mathrm{c}}\right)\frac{I}{4F}M_{\mathrm{W}}\end{aligned} \tag{6.24}$$

For illustrative purposes, assuming fully humidified outlet gases and equal pressures at the anode and the cathode, the ratio of the water mass flow rates removed by both gas streams can be written as

$$\frac{\dot{m}_{\mathrm{W,c,out}}}{\dot{m}_{\mathrm{W,a,out}}} = \frac{\phi_{\mathrm{c}} - 1 + \left(X^{\mathrm{air}}_{\mathrm{N_2}}/X^{\mathrm{air}}_{\mathrm{O_2}}\right)\phi_{\mathrm{c}}}{2\left(\phi_{\mathrm{a}}-1\right)} = \frac{4.76\phi_{\mathrm{c}}-1}{2\left(\phi_{\mathrm{a}}-1\right)} \tag{6.25}$$

which for the anode and cathode stoichiometries considered in the experiments, $\phi_{\mathrm{a}} = 1.2$ and $\phi_{\mathrm{c}} = 2$, results in a ratio $\dot{m}_{\mathrm{W,c,out}}/\dot{m}_{\mathrm{W,a,out}} \simeq 21.3 \gg 1$. As can be seen, the presence of nitrogen in the cathode gases enables a much larger water removal capacity than in the anode. This fact is mainly due to the third term $(X^{\mathrm{air}}_{\mathrm{N_2}}/X^{\mathrm{air}}_{\mathrm{O_2}})\phi_{\mathrm{c}} = 3.76\phi_c$ appearing in the bracketed factor of (6.24).

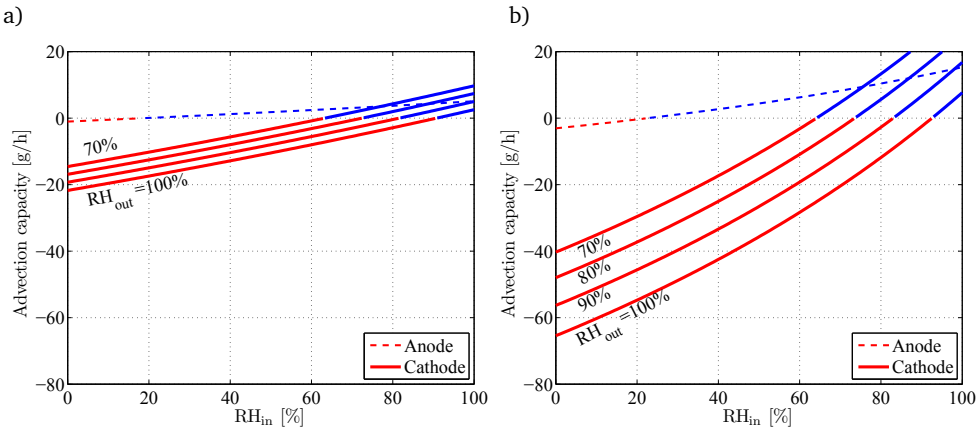

Figure 6.2: Advection capacities of anode and cathode streams at a) 60°C and b) 80°C.

6.2.4 Advection capacities and global balance of water

To begin the discussion of results, let us first consider the advection capacities of the anode (A) and cathode (C) streams, defined as the net mass of water that they supply or remove from the cell per unit time

$$\mathrm{A} = \dot{m}_{\mathrm{W,a,in}} - \dot{m}_{\mathrm{W,a,out}} \tag{6.26}$$

$$\mathrm{C} = \dot{m}_{\mathrm{W,c,in}} - \dot{m}_{\mathrm{W,c,out}} \tag{6.27}$$

The advection capacities are obtained as the mass flow rates of water supplied by the inlet (i.e., feed) stream minus those removed by the outlet streams, provided by Eqs. (6.10), (6.14), (6.18) and (6.24). A negative advection capacity indicates that the corresponding stream is drying (i.e., removing water from) its side of the cell, whereas a positive advection capacity means the stream is hydrating it.

Figure 6.2 shows the variation of the anode and cathode advection capacities with the relative humidity of the anode and cathode feed streams for the cell operating at 60°C (Fig. 6.2a) and 80°C (Fig. 6.2b) and with fully saturated outlet streams. These results do not include any electrochemical water production rate, but are very illustrative for the following discussion of the global balance of water, which does include this effect. As can be seen, the advection capacity of the anode stream is typically positive (except close to dry conditions, $\mathrm{RH_{a,in}} \lesssim 20\%$), whereas that of the cathode stream is typically negative and large (except at very high inlet humidification levels, $\mathrm{RH_{c,in}} \gtrsim 90\%$). This is due to the much higher reactant consumption relative to the reactant inflow rate in the anode side. As a result, even a fully humidified anode outlet stream carries a very small amount of water, which would reduce to zero in the limit of a dead-end configuration.

For reference purposes, Figure 6.2 also shows the variation of the advection capacity

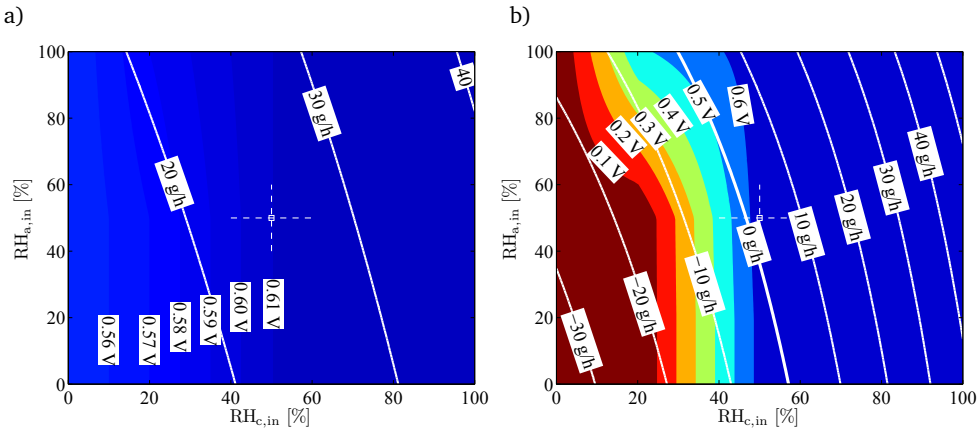

Figure 6.3: White lines represent BOW isocontours in g/h for a) 60°C and b) 80°C, and the underlying color map shows the cell voltages obtained experimentally, expressed in Volts. The color scale uses blue for stable conditions and red for severe deactivation. The reference conditions (50% RH at both anode and cathode) are indicated by a white cross. As can be seen, negative values of BOW are clearly correlated with the deactivation of the cell, as shown in the experiments at 80°C.

of the cathode stream with the RH of the air supply for cases where the outlet gases are not fully humidified. As can be observed, since the outlet stream removes less water when it is only partially humidified, the advection capacity becomes less negative, reaching positive values for humidification levels of the air supply below 90% RH. At 80°C there is a reduction of the cathode advection capacity close to 1 g/h per 1% RH reduction, whereas at 60°C the reduction is about 0.2 g/h per 1% RH reduction. The effect of reducing the humidification of the outlet gases on the anode side is negligible compared to that of the cathode and is not shown in the figure.

When written in terms of the anode and cathode advection capacities, the global balance of water given in Eq. (6.1) takes the simple form

$$\mathrm{BOW} = \mathrm{A} + \mathrm{C} + \dot{m}_{\mathrm{W,P}} \tag{6.28}$$

Figure 6.3 shows isocontours of BOW computed for different relative humidities of the anode and cathode feed streams, superimposed onto the experimentally measured cell voltages, shown as the background color map. The calculations are limited to fully saturated outlet conditions. It is observed that in most cases a positive BOW implies stable cell behavior (voltage $\gtrsim$ 0.6 V). At 80°C (Fig. 6.3b) the experimental results show severe deactivation for cathode RH conditions below 50%. At such low water contents, the calculated BOW indicates cell dehydration regardless of the anode RH condition. Note that, due to the significantly lower mass flow rate of the anode stream compared with that of the cathode, even a fully saturated anode stream can only partially compensate the cell

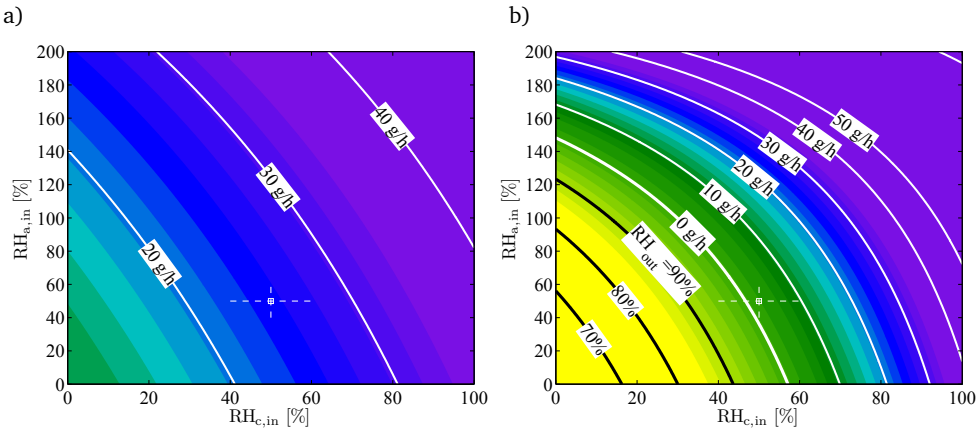

Figure 6.4: Estimation of the global balance of water (BOW) in g/h at a) 60°C and b) 80°C. The reference conditions (50% RH at both anode and cathode) are indicated by white dashed lines. The color scale represents the qualitative cell behavior. Blue is used for high performances at stable condition, purple for flooding behavior, green for slight loose of performances with stable behavior and yellow for unstable behavior with deactivation. As shown, BOW at 60°C is always positive and the cell behavior remains always stable. In contrast, at 80°C BOW is negative for low cathode RH conditions which evidences unstable cell performances. Negative BOW levels have been substituted by lines that indicate the relative humidity of the outlet streams that gives zero BOW.

drying induced by the highly negative cathode advection capacity resulting at low cathode humidification (see Fig. 6.2). At 60°C (Fig. 6.3a) only slight voltage losses are observed at low humidity conditions due to local deactivation at the gases inlets, but no global dehydration of the cell is observed, in agreement with the positive BOW obtained for all anode and cathode RH conditions.

It is interesting to note that non-zero values of BOW are incompatible with the steady operation of the cell under the assumptions stated above. Particularly, the assumption of fully humidified outlet gases must be revised for both positive and negative BOWs. On one hand, if the cell is operated with a positive BOW water will be accumulated in the system. Provided it is not too large, the excess water could be easily removed by small condensate water droplets expelled intermittently from the cathode outlet, leading to a new stable regime. On the other hand, a negative BOW produces a continuous drying of the cell. In this case the outlet streams may not reach full humidification. For slightly negative BOWs a new stable condition could also be reached with a new equilibrium relative humidity of the outlet gases slightly below 100%. For instance, the experiment at 80°C with dry anode and 50% RH cathode feed is stable even with a small negative BOW, roughly -5 g/h. The new stable conditions attained with small positive or negative BOW could not be sustained either with large positive BOW, which lead to flooding, or large negative BOW, which lead to membrane dehydration, both cases being incompatible with stable cell behavior.

Figure 6.4 shows isocontorus of BOW for a range of inlet relative humidities similar to that considered in the experimental campaign, including, in particular, supersaturated anode feed with inlet $RH_{a,in}$ reaching up to 200%, leading to strong water condensation at the anode inlet. The color scale has been chosen so as to reproduce the qualitative behavior of the cell represented in Fig. 5.9. As can be seen, Figs. 5.9 and 6.4 show a very similar aspect, with all stable conditions being correlated with positive values of BOW. For illustrative purposes, in Figure 6.4b the negative BOW isocontours have been substituted by isocontours of the relative humidity of the outlet gas streams (assumed equal for anode and cathode) that gives zero BOW.

6.3 Energy analysis

During cell operation, the anode and cathode feed streams must be conveniently heated and humidified. The amount of energy required for the conditioning process will be computed in this section in all the conditions tested in the experiments and compared with the residual heat available in the cell. Several models have been proposed in the literature for the evaluation of the energy required for the cell humidification (Amphlett *et al.*, 1996; Johnson *et al.*, 2001; O'Hayre *et al.*, 2006; Picot *et al.*, 1998; Wang, 2004; Weber *et al.*, 2014; Weber & Newman, 2004; Yu *et al.*, 2005). These models are based on a series of assumptions that are commonly adopted for the calculations: i) the cell is assumed to operate in steady state; ii) cathode and anode inflow and outflow streams are considered mixtures of ideal gases; iii) the temperature of the cell is assumed uniform due to its high thermal conductivity; and, finally, iv) product water is assumed to be either in liquid or gaseous phase. In this work, the water produced by the oxygen reduction reaction will be assumed to be in liquid phase, so that the enthalpy of reaction to be used is the higher heating value (Weber *et al.*, 2014). In this case, the latent heat of evaporation required to vaporize the liquid product water must be included in the energy balance, since, as previously discussed, the anode and cathode outlet streams are assumed to be fully gaseous. This assumption may not be correct for the flooding conditions, but those cases are out of the scope of this work, devoted to the study of cell performance stability under low humidification conditions.

The sensible heat used to heat the feed streams, Q_{SEN}, must include all the species entering the anode and cathode sides. The anode feed contains hydrogen and water, whereas the cathode feed contains oxygen, nitrogen, and water, so that

$$\begin{aligned} Q_{SEN} = {} & \dot{m}_{H_2,a,in} c_{p,H_2} \left(T_{CELL} - T_0\right) + \dot{m}_{O_2,c,in} c_{p,O_2} \left(T_{CELL} - T_0\right) \\ & + \dot{m}_{N_2,c,in} c_{p,N_2} \left(T_{CELL} - T_0\right) + \left(\dot{m}_{W,a,in} + \dot{m}_{W,c,in}\right) c_{p,W} \left(T_{CELL} - T_0\right) \end{aligned} \quad (6.29)$$

where $c_{p,k}$ is the specific heat at constant pressure of species k, $T_0 = 15°C$ is the temperature of the gaseous supply line, and T_{CELL} is the operating temperature of the

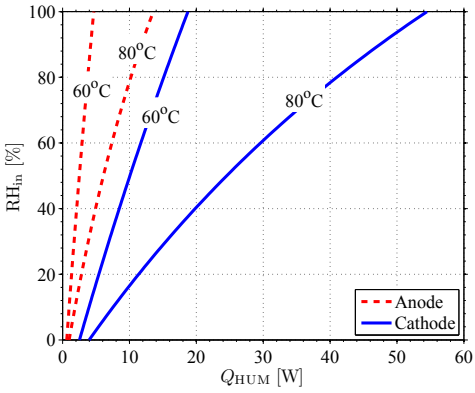

Figure 6.5: Condition heat Q_{HUM} for the anode and cathode streams at different cell temperatures. The condition heat is nearly 4 times higher for the cathode than for the anode due to the larger mass flow rate involved, whereas it is nearly 2.5 larger at 80°C than at 60°C for both electrodes.

cell.

The latent heat, Q_{LAT}, measures the amount of energy required to vaporize the water employed to humidify the anode and cathode streams

$$Q_{\mathrm{LAT}} = \left(\dot{m}_{\mathrm{W,a,in}} + \dot{m}_{\mathrm{W,c,in}}\right) H_{lv} \tag{6.30}$$

where $H_{lv} = 2257$ kJ/kg is the enthalpy (or latent heat) of the liquid vapor phase change.

The total heat used to condition the feed streams, Q_{HUM}, is given by the sum of the sensible and latent heats

$$Q_{\mathrm{HUM}} = Q_{\mathrm{SEN}} + Q_{\mathrm{LAT}} \tag{6.31}$$

Figure 6.5 shows the condition heat, Q_{HUM}, separately for the anode and cathode streams for the two cell temperatures under study. It should be noted that the cathode side requires substantially more power due to its significantly higher mass flow rate. In addition, the required thermal power for 80°C is between 2.5 and 3 times larger that for 60°C due to the larger amount of water that must be vaporized to reach the same RH[1].

The heat required to evaporate the liquid product water, Q_{P}, is estimated as H_{lv} times the liquid water production rate $\dot{m}_{\mathrm{W,P}}$ provided by Eq. (6.4)

$$Q_{\mathrm{P}} = \dot{m}_{\mathrm{W,P}} H_{lv} \tag{6.32}$$

As previously discussed, for the conditions tested in the experiments, i.e., cell operating in galvanostatic mode at a constant current of $I = 100$ A, the water production rate was $\dot{m}_{\mathrm{W,P}} = 33.6$ g/h, which results in a heat of evaporation of $Q_{\mathrm{P}} = 21.1$ W.

[1] $p_{\mathrm{sat}}(80°\mathrm{C}) / p_{\mathrm{sat}}(60°\mathrm{C}) \simeq 2.38$

As discussed in Chapter 2, see Sec. 2.2.2, the electrochemical reaction releases a certain amount of heat, Q_{RES}, which must also be accounted for in the energy balance. Following Eq. (2.19), this heat can be evaluated as the difference between the theoretical energy that can be produced by the electrochemical reaction, $Q_{\mathrm{TH}} = IE_{TH}$, and the electrical power actually produced by the cell, $W_{\mathrm{ELEC}} = IV$, i.e.,

$$Q_{\mathrm{RES}} = Q_{\mathrm{TH}} - W_{\mathrm{ELEC}} = I(E_{TH} - V) = \left(1 - \frac{V}{E_{TH}}\right) IE_{TH} = (1-\varepsilon)\, IE_{TH} \tag{6.33}$$

where E_{TH} denotes the electrical thermoneutral potential (or voltage) obtained from the cell, and V is the actual voltage established between the electrodes. Since water is assumed to be produced in liquid phase, the higher heating value must be used in the evaluation of $E_{TH} = -\Delta h^{HHV}/2F$ (Amphlett *et al.*, 1996; Johnson *et al.*, 2001; O'Hayre *et al.*, 2006; Picot *et al.*, 1998; Wang, 2004; Weber *et al.*, 2014; Weber & Newman, 2004; Yu *et al.*, 2005). The ratio between the electrical power output and the theoretical energy of reaction, $\varepsilon = W_{\mathrm{ELEC}}/Q_{\mathrm{TH}}$, equal to the ratio between the cell voltage and the electrical reversible potential appearing in Eq. (6.33), is the so-called voltage efficiency of the cell.

Summarizing, the net heat available during cell operation is the difference between the residual heat generated by the electrochemical reactions, Q_{RES}, minus the amount of heat required to evaporate water produced at the cell, Q_{P}, that is

$$Q_{\mathrm{AVAILABLE}} = Q_{\mathrm{RES}} - Q_{\mathrm{P}} \tag{6.34}$$

Figure 6.6 compares the available heat, $Q_{\mathrm{AVAILABLE}}$, evaluated from Eqs. (6.32)–(6.34), with the total heat required to condition the anode and cathode streams, Q_{HUM}, given by Eqs. (6.29)–(6.31). As can be seen, at both temperatures 60°C and 80°C the estimated condition heat is always lower than the available heat, even for fully humidified gases. As a result, in our particular experimental setup the condition heat could always be provided by the available residual heat regardless of the anode and cathode RH conditions.

If the outlet streams were not fully gaseous, as was assumed here, but contained a certain amount of condensed water as expected for conditions with positive BOW (e.g., flooding), the latent heat required to evaporate only the gaseous fraction of the product water would be smaller than Q_{P}, and therefore the available heat would be larger than $Q_{\mathrm{AVAILABLE}}$. As a result, the hypothesis of fully gaseous outlet streams does not invalidate the main result of the energy analysis, i.e., that the available heat is always higher than the condition heat required to heat and humidify the inlet streams.

As an illustrative example, with the cell operating at 80°C, decreasing the relative humidity of both streams from 100% to 50% and then to 20% reduces the power used for humidification respectively to about 45% and 21% of that corresponding to fully saturated gases. In this particular experiment the power required to reach 100% RH on the anode and cathode streams is about 13.5 W (anode) + 54.5 W (cathode) = 68 W, roughly the residual heat available at full humidification. At 60°C the power reduction is to about

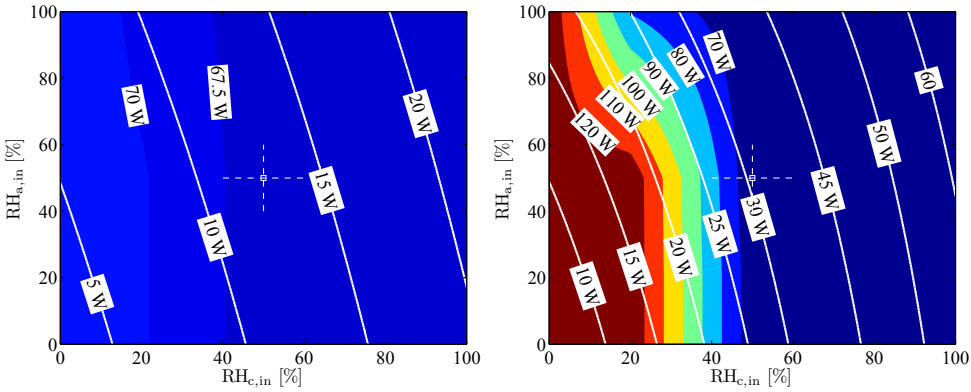

Figure 6.6: White contour plots show the total condition heat Q_{HUM} in Watts at a) 60°C and b) 80°C. The color map represents the residual heat Q_{RES}. The reference conditions (50% RH at both anode and cathode) are indicated by a white cross. Due to the stability of operation at low humidification conditions, Q_{RES} remains approximately constant at 60°C, whereas it shows a large increase at low cathode RH due to the reduction of the voltage efficiency of the cell, accompanying severe cell dehydration. Q_{HUM} is significantly lower at 60°C than at 80°C, being dominated by the cathode side in both cases.

54% and 29% of that corresponding to fully humidified gases, but the power required to reach this condition is only 4.6 W (anode) + 18.7 W (cathode) = 23.3 W, which is about one third of the available residual heat.

Unlike the global balance of water, the quantitative results of the energy balance presented in this section could not be easily extrapolated to commercial stacks due to the particular experimental setup used in our study. However, a similar methodology could be applied to assess whether the available heat at certain operating conditions would be sufficient or not to condition the anode and cathode feeding streams.

6.4 Dimensionless BOW

Equations (6.11), (6.14), (6.21) and (6.24) show that all the mass flow rates involved in the global balance of water (6.1) are proportional to the water production rate $\dot{m}_{W,P}$ given by (6.4). This suggests that a dimensionless analysis could be carried out to extend the BOW model to more general conditions.

6.4.1 Dimensionless anode advection capacity

As previously discussed, the anode advection capacity is the difference between the water mass flow rate supplied by the anode inlet and removed by the anode outlet. Using the water production rate as a convenient scale, a dimensionless anode advection capacity

can be defined as

$$\hat{\mathrm{A}} = \frac{\dot{m}_{\mathrm{W,a,in}} - \dot{m}_{\mathrm{W,a,out}}}{\dot{m}_{\mathrm{W,p}}} \tag{6.35}$$

Using (6.4), (6.11) and (6.14) in (6.35) leads to the following expanded expression for the dimensionless anode advection capacity

$$\hat{\mathrm{A}} = \frac{X_{\mathrm{W,a,in}}}{1-X_{\mathrm{W,a,in}}}\phi_{\mathrm{a}} - \frac{X_{\mathrm{W,a,out}}}{1-X_{\mathrm{W,a,out}}}\left(\phi_{\mathrm{a}}-1\right) = \phi_{\mathrm{a}}\left(\frac{X_{\mathrm{W,a,in}}}{1-X_{\mathrm{W,a,in}}} - \frac{X_{\mathrm{W,a,out}}}{1-X_{\mathrm{W,a,out}}}\right) + \frac{X_{\mathrm{W,a,out}}}{1-X_{\mathrm{W,a,out}}} \tag{6.36}$$

in terms of the anode stoichiometry ϕ_{a}, the relative humidity of the anode inlet and outlet gases, the cell temperature T_{cell} and the anode pressure p_{a}. Remember that a positive/negative value of $\hat{\mathrm{A}}$ represents net water addition/removal to/from the cell.

Figure 6.7 shows the dimensionless anode advection capacity as a function of the relative humidity of the inlet gases for two cell operating temperatures (columns) and three different pressures (rows). Each panel includes three different stoichiometries, including the dead-end operating mode, $\phi_{\mathrm{a}} = 1$, as limit case. The curves of advection capacity are lower at 100% $\mathrm{RH_{a,out}}$ than at 70% $\mathrm{RH_{a,out}}$, implying that the water removal rate increases with the relative humidity of the outlet gases; obviously a more saturated outlet stream removes more water. However, this is not the case for $\phi_{\mathrm{a}} = 1$ because in the dead-end mode there is no gas coming out from the cell, and $\hat{\mathrm{A}}$ is independent of the assumed $\mathrm{RH_{a,out}}$. It is interesting to note that when the relative humidities of the outlet and inlet streams are equal, the anode advection capacity $\hat{\mathrm{A}}$ does not depend on the stoichiometry, as can be seen from Eq. (6.36). As a result, in all the plots the curves corresponding to 70% $\mathrm{RH_{a,out}}$ intersect exactly at 70% $\mathrm{RH_{a,in}}$, with lower/higher anode advection capacities being obtained for increasing stoichiometries below/above the crossing point. Temperature and pressure are probably the variables that most affect the advection capacity, with lower pressures and higher temperatures resulting in stronger gradients of $\hat{\mathrm{A}}$ with the inlet relative humidity. As a result, superatmospheric pressures are often used in PEMFCs in order to reduce the impact of the variations of relative humidify within the cell on the cell BOW, and therefore on its performance stability.

6.4.2 Dimensionless cathode advection capacity

The dimensionless cathode advection capacity is defined as the difference between the water mass flow rate supplied by the cathode inlet and removed by the anode outlet, measured with the water production rate

$$\hat{\mathrm{C}} = \frac{\dot{m}_{\mathrm{W,c,in}} - \dot{m}_{\mathrm{W,c,out}}}{\dot{m}_{\mathrm{W,p}}} \tag{6.37}$$

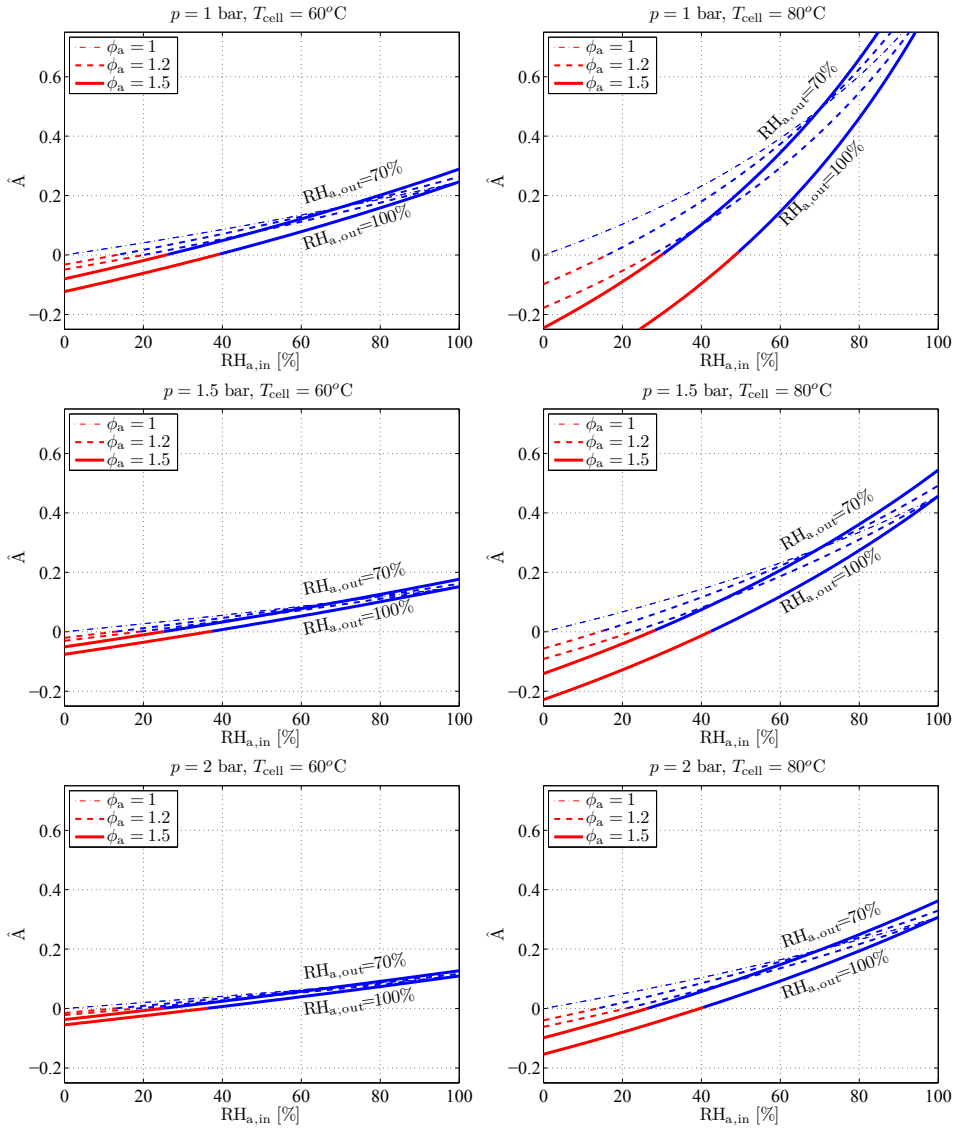

Figure 6.7: Anode advection capacity. Form left to right: T_{cell} =60°C and T_{cell} =80°C. From top to bottom: $p_a = p_c = 1$ bar, $p_a = p_c = 1.5$ bar and $p_a = p_c = 2$ bar. It is shown that when the relative humidity of the outlet is equal to the relative humidity of the inlet ($X_{W,a,out} = X_{W,a,in}$), $\hat{A}$ does not depend on the stoichiometry. For $\phi_a = 1$, $\hat{A}$ does not depends on the outlet relative humidity (no gas outlet).

Upon substitution of (6.4), (6.21) and (6.24) the above expression becomes

$$\hat{C} = \frac{X_{W,c,in}}{1-X_{W,c,in}} \frac{\phi_c}{2}\left(1+\frac{X^{air}_{N_2}}{X^{air}_{O_2}}\right) - \frac{X_{W,c,out}}{1-X_{W,c,out}} \frac{1}{2}\left[\phi_c\left(1+\frac{X^{air}_{N_2}}{X^{air}_{O_2}}\right)-1\right] =$$
$$\frac{\phi_c}{2}\left(1+\frac{X^{air}_{N_2}}{X^{air}_{O_2}}\right)\left[\frac{X_{W,c,in}}{1-X_{W,c,in}} - \frac{X_{W,c,out}}{1-X_{W,c,out}}\right] + \frac{1}{2}\frac{X_{W,c,out}}{1-X_{W,c,out}} \quad (6.38)$$

As in the anode side, the dimensionless cathode advection capacity is function of the cathode stoichiometry ϕ_c, the relative humidity of the inlet and outlet gases, the cell temperature T_{cell} and the cathode pressure p_c. Similarly, a positive value of $\hat{C}$ represents net water addition at the anode while a negative value means net water removal. As main novelty, the presence of nitrogen as passive species introduces the factor $X^{air}_{N_2}/X^{air}_{O_2}$ which significantly increases the magnitude of the cathode advection capacity with respect to that of the anode. There is also a $1/2$ that appears due to the ORR stoichiometry.

Figure 6.8 shows the dimensionless cathode advection capacity as a function of the relative humidity of the inlet gases for different pressures, temperatures and cathode stochiometries. The qualitative behavior is analogous to that of the anode side but the variations are quantitatively larger by the higher mass flow rates due to the presence of nitrogen. Remember that factor $X^{air}_{N_2}/X^{air}_{O_2}$ is close to 4; so by each oxygen molecule introduced, 4 nitrogen molecules are introduced as well.

6.4.3 Dimensionless BOW

Expressed in terms of dimensionless variables, the balance of water expressed in Eq. (6.28) takes the form

$$\widehat{BOW} = \hat{A} + \hat{C} + 1 \tag{6.39}$$

Figure 6.9 shows $\widehat{BOW}$ isocontours in the $RH_{c,in}$—$RH_{a,in}$ plane for 80°C and 60°C. Different subplots correspond to different anode and cathode pressures, assumed to be equal. At both temperatures, increasing the pressure favors a smoother $\widehat{BOW}$ distribution, with a shift of the marginal isocontour ($\widehat{BOW} = 0$) towards lower humidity conditions. This leads to a significant reduction of the drying region, an effect that may be considered undesirable when drying conditions are required, e.g., when purging the cell between freeze-thaw cycles (St-Pierre *et al.*, 2005; Wu *et al.*, 2008). As done in Fig. 6.4, the negative BOW isocontours have been substituted by isocontours of the relative humidity of the outlet gases (assumed equal for anode and cathode) that gives zero BOW, with lower humidity levels of the outlet streams being required to shift the marginal isocontour to lower inlet humidities.

The main difference between operation at 80°C and 60°C is that at lower temperatures the drying capacity of the outlet gases is significantly smaller. As a result, at 60°C the dimensionless balance of water is positive for nearly all conditions except for very low inlet humidities and low pressures. Moreover, the gradient of $\widehat{BOW}$ with the inlet relative humidities is also smaller. The pressure affects in the same way at 60°C than at 80°C, but due the lower temperature at the changes 60°C are also smaller. It is also remarkable that at 60°C the operation under dry conditions reveals a slightly positive $\widehat{BOW}$ for superatmospheric pressures. Under dry conditions the inlet streams do not provide water to the cell, which must be self-humidified by the water produced at the ORR (which turns out to be slightly larger than the combined removal capacity of the outlet streams). As

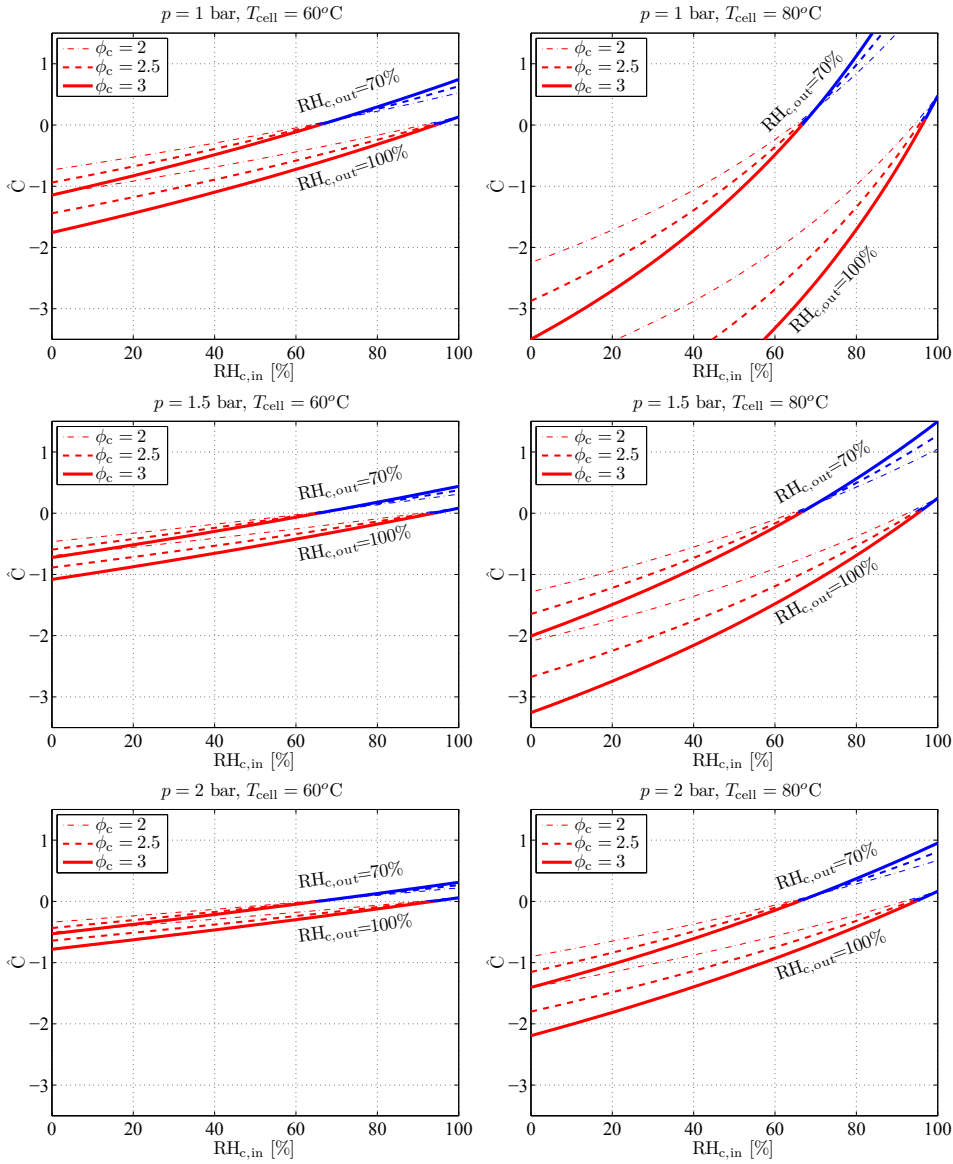

Figure 6.8: Cathode advection capacity. Form left to right: T_{cell} =60°C and T_{cell} =80°C. From top to bottom: $p_a = p_c = 1$ bar, $p_a = p_c = 1.5$ bar and $p_a = p_c = 2$ bar. It is shown that when the relative humidity of the outlet is equal to the relative humidity of the inlet ($X_{W,a,out} = X_{W,a,in}$), Â does not depend on the stoichiometry.

shown in the experiments of the Chapter 5, this is a feasible working point for the cell under self-humidification conditions without any external system. However, the spatial distribution of water should be carefully studied to guarantee an adequate membrane

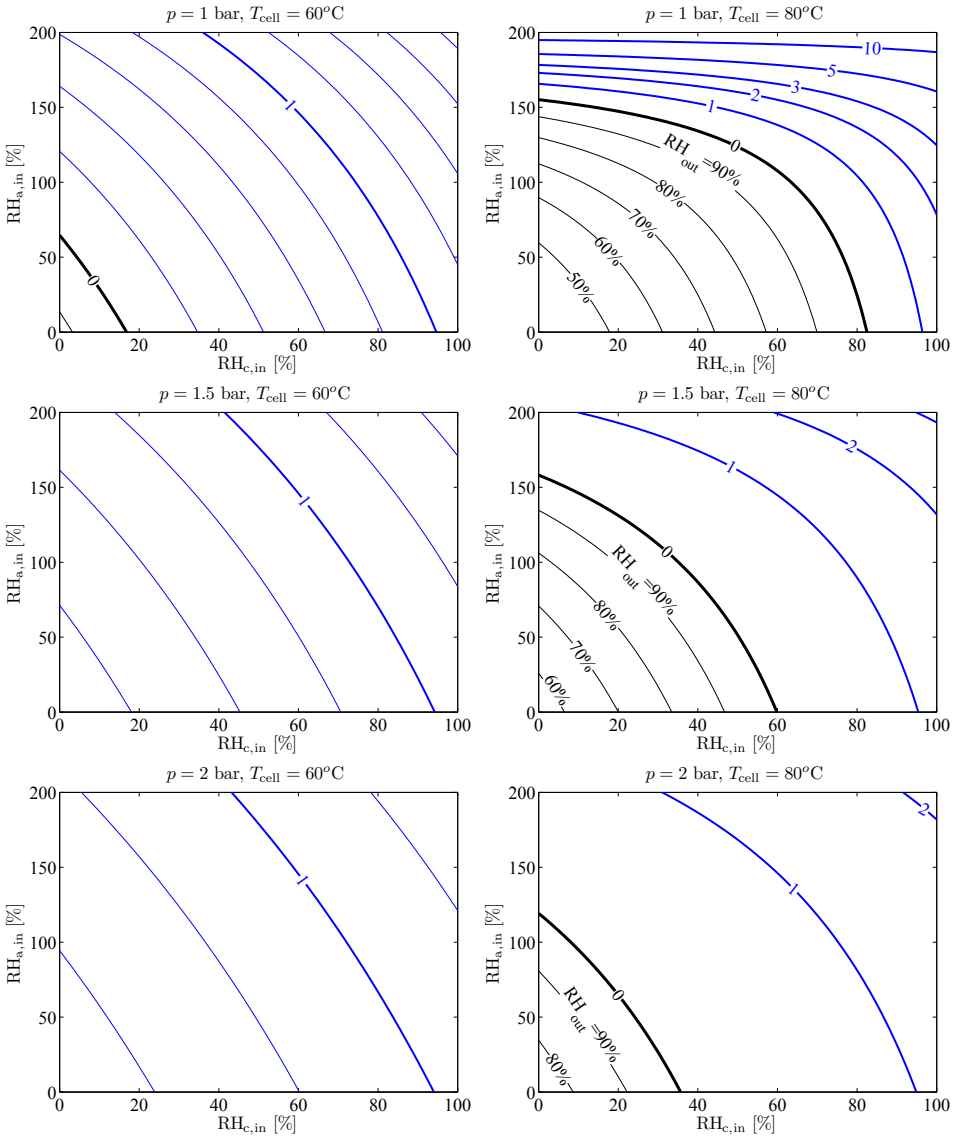

Figure 6.9: Dimensionless . Form left to right: BOW T_{cell} =60°C and T_{cell} =80°C. From top to bottom: $p_a = p_c = 1$ bar, $p_a = p_c = 1.5$ bar and $p_a = p_c = 2$ bar. Anode stoichiometry $\phi_a = 1.2$ and cathode stoichiometry $\phi_c = 2$.

hydration with the little water available.

6.5 Conclusions

This chapter has investigated the influence of the relative humidity of the inlet gases on PEMFC performance stability at different temperatures, pressures and anode and cathode stoichiometries. The experimental results presented in the previous chapter showed that the relative humidity of the cathode is the main parameter controlling the performance stability of the cell, with RH values on the cathode side between 50% and 20% being critical to obtain a relatively stable behavior at 80°C. The results of a simple global balance of water (BOW) model seem to correlate satisfactorily with the observed stability conditions. Nevertheless, additional tests should be carried out with different current densities and channel configurations to validate the model in more general situations.

An overall energy analysis, which accounts for the sensible heat required to increase the temperature of the feeding streams to the cell operating temperature and for the latent heat of vaporization required to humidify the gases to the desired RH, has revealed a remarkable positive energy balance at 60°C. The total heat used to condition streams at 80°C is almost three times larger than at 60°C, although it could still be provided by the available residual heat. The application of this methodology to commercial stacks could be helpful to asses if the heat available under a given operating condition could be enough to condition the anode and cathode feeding streams.

Taking advantage of the fact that all the mass flow rates involved in the global balance of water (6.1) are proportional to the water production rate, a dimensionless BOW model has been finally presented. This model is readily applicable to any PEMFC operating condition and gives valuable insight on the effect of the different operational parameters involved. The proposed model could be used as a fast evaluation method for predicting the stability at a specified operating condition, or, at least, as an academic tool for illustrating the impact of the different operational parameters on the global water balance of the cell.

Due to operational stability at low humidification at 60°C, this seems to be the most efficient condition for our particular cell configuration, despite the small reduction of approximately 6% in cell power output with respect to 80°C. This is consistent with the prediction of the dimensionless model, where a small positive $\widehat{\mathrm{BOW}}$ is predicted even for dry inlet gases, corresponding to moderately stable cell conditions. At higher temperatures, the instable behavior occurring as a consequence of the high water removal rate of the cathode under low humidification, could be compensated using supersaturated anode feed with sufficiently high $\mathrm{RH_{a,in}}$.

References

AMPHLETT, J. C., MANN, R. F., PEPPLEY, B. A., ROBERGE, P. R. & RODRIGUES, A. 1996 A model predicting transient responses of proton exchange membrane fuel cells. *J. Power*

Sources **61** (1-2), 183–188.

BARBIR, F. 2005 *PEM Fuel Cells: Theory and practice*. Elsevier Academic.

JIAO, K. & LI, X. 2011 Water transport in polymer electrolyte membrane fuel cells. *Prog. Energy Combust. Sci.* **37** (3), 221–291.

JOHNSON, R., MORGAN, C., WITMER, D. & JOHNSON, T. 2001 Performance of a proton exchange membrane fuel cell stack. *Int. J. Hydrogen Energy* **26** (8), 879–887.

NAZAROV, I. & PROMISLOW, K. 2006 Ignition waves in a stirred PEM fuel cell. *Chem. Eng. Sci.* **61** (10), 3198–3209.

NGUYEN, T. V. & WHITE, R. E. 1993 A Water and Heat Management Model for Proton-Exchange-Membrane Fuel Cells. *J. Electrochem. Soc.* **140** (8), 2178.

O'HAYRE, R., CHA, S.-W., COLELLA, W. & PRINZ, F. B. 2006 *Fuel Cell Fundamentals*. Hoboken, NJ, USA: John Wiley \& Sons, Inc.

PICOT, D., METKEMEIJER, R., BEZIAN, J. J. & ROUVEYRE, L. 1998 Impact of the water symmetry factor on humidification and cooling strategies for PEM fuel cell stacks. *J. Power Sources* **75** (2), 251–260.

SANCHEZ, D. G. & GARCIA-YBARRA, P. L. 2012 PEMFC operation failure under severe dehydration. *Int. J. Hydrogen Energy* **37** (8), 7279–7288.

VON SCHROEDER, P. L. 1903 Uber Erstarrungs–und Quellungserscheinungen von Gelatine. *Z. Phys. Chem.* **45**, 57.

SPRINGER, T. E., ZAWODZINSKI, T. A. & GOTTESFELD, S. 1991 Polymer Electrolyte Fuel Cell Model. *J. Electrochem. Soc.* **138** (8), 2334.

ST-PIERRE, J., ROBERTS, J., COLBOW, K., CAMPBELL, S. & NELSON, A. 2005 PEMFC operational and design strategies for Sub zero environments. *J. New Mater. Electrochem. Syst. J. New. Mat. Electrochem. Syst.* **8**, 163–176.

WANG, C.-Y. 2004 Fundamental Models for Fuel Cell Engineering. *Chem. Rev.* **104** (10), 4727–4765.

WEBER, A. Z., BORUP, R. L., DARLING, R. M., DAS, P. K., DURSCH, T. J., GU, W., HARVEY, D., KUSOGLU, A., LITSTER, S., MENCH, M. M., MUKUNDAN, R., OWEJAN, J. P., PHAROAH, J. G., SECANELL, M. & ZENYUK, I. V. 2014 A Critical Review of Modeling Transport Phenomena in Polymer-Electrolyte Fuel Cells. *J. Electrochem. Soc.* **161** (12), F1254–F1299.

WEBER, A. Z. & NEWMAN, J. 2004 Modeling Transport in Polymer-Electrolyte Fuel Cells. *Chem. Rev.* **104** (10), 4679–4726.

WU, J., YUAN, X. Z., MARTIN, J. J., WANG, H., ZHANG, J., SHEN, J., WU, S. & MERIDA, W. 2008 A review of PEM fuel cell durability: Degradation mechanisms and mitigation strategies. *J. Power Sources* **184** (1), 104–119.

YU, X., ZHOU, B. & SOBIESIAK, A. 2005 Water and thermal management for Ballard PEM fuel cell stack. *J. Power Sources* **147** (1-2), 184–195.

Nomenclature BOW

Symbols

A	anode advection capacity [kg s^{-1}]
$\hat{A}$	dimensionless anode advection capacity
BOW	global balance of water [kg s^{-1}]
$\hat{BOW}$	dimensionless global balance of water
C	cathode advection capacity [kg s^{-1}]
$\hat{C}$	dimensionless cathode advection capacity
C_k	molar concentration of specie k [mol m^3]
E_0	standard cell voltage
E_{TH}	thermoneutral standard cell voltage
F	Faraday constant $F = 96480$ C
H_{lv}	enthalpy of liquid vapor phase change [W kg^{-1}]
I	current [A]
$\dot{m}_k$	mass flow rate of specie k [kg s^{-1}]
M_k	molar mass of specie k [kg mol^{-1}]
p	pressure [Pa]
P	water production [kg s^{-1}]
$\dot{Q}_k$	flow rate of specie k [m^3 s^{-1}]
Q	heat [W]
RH	relative humidity [%]
T	Temperature [K]
V_m	molar volume [m^3 mol^{-1}]
X_k	molar fraction of specie k
Y_k	mass fraction of specie k

Greek letters

ε	cell efficiency $\varepsilon = V/E_{TH}$
ϕ	stoichiometry [-]

Subscripts

a	anode
c	cathode
cell	cell
in	inlet magnitude
k	specie k

out	outlet magnitude
sat	saturation property
TOT	total magnitude
W	water (H_2O)

Superscripts

0	initial conditions
sc	standard conditions

Conclusions and future work

Three main goals were established at the beginning of this thesis: i) the development of a detailed multi-species kinetic model for the ethanol oxidation reaction on Pt-based binary catalyst, including a systematic methodology to determine the kinetic constants from experimental product selectivity and cell polarization data, ii) the integration of the EOR kinetic model into a full 1D+1D DEFC model including simple across-the-channel and along-the-channel transport descriptions aiming to evaluate DEFC performance and to analyze the downstream evolution of the various final products involved in the model and iii) the qualitative correlation of the performance stability of hydrogen PEMFCs observed experimentally with a balance of water model considering different relative humidity of the inlet and outlet gases at fixed cell temperatures and anode and cathode pressures. The main conclusions of the analyses carried out in this thesis are summarized below.

Direct Alcohol Fuel Cells model

A novel reaction mechanism has been proposed for the ethanol electro-oxidation on binary Pt-based catalysts used in Direct Ethanol PEM Fuel Cells. The detailed kinetic model involves five adsorbates (CH_3CHOH_{ads}, CH_3CO_{ads}, CO_{ads}, $CH_{3\,ads}$, and OH) and six free species, including two reactants (water and ethanol) and four product species (acetaldehyde, acetic acid, carbon dioxide, and methane). The model has been coupled to a 1D across-the-channel description of the mass transport processes that take place in the anode of a DEFC. A new methodology based on the use of a multi-objective genetic algorithm has been used to optimize the set of kinetic constants that better fits selected results taken from the literature. As a result, the genetically optimized model was able to reproduce experimental anode polarization and product selectivity data for all the current densities under study.

The computation of the global reaction selectivities and the so-called effective electron generation number, n^{eff}, introduced for the first time in this work, have shown that the EOR produces at much four electrons in the binary Pt-based catalyst compositions used in state-of-the-art DEFCs. This explains why previous EOR models with acetic acid as unique final product yielded good results in terms of polarization curves. However, they were unable to predict product selectivity.

In a second step, the anode model has been coupled to a 1D+1D DEFC model. The cathode side has been described by a 1D diffusive model with simple ORR kinetics and

accounting for the parasitic current density due to ethanol and acetaldehyde crossover. A simple advection model has been proposed to describe the along-the-channel evolution which provides results along the channel for concentrations, molar consumption and production rates, overpotentials and current densities. An genetic optimization has been used to optimize the volume specific cathodic exchange current density and the contact resistance that better fit experimental results taken from the literature.

Among the chemical species included in the reaction mechanisms, the main species involved in current generation are ethanol and acetaldehyde, and the main non-reactive products are acetic acid and CO_2, the concentration of secondary species such as methane being negligibly small. The variation of ethanol and acetaldehyde concentrations along the anode channel significantly modifies the EOR reaction rate along the channel length. The role of acetaldehyde as free intermediate specie is particularly remarkable. First it is produced when ethanol is abundant, being transported downstream and accumulating along the channel, which leads to growing acetaldehyde concentrations. Under ethanol limiting conditions, the acetaldehyde produced upstream may be oxidized to acetic acid to sustain high cell current densities. Simulations have even shown that, under extreme starvation conditions, acetaldehyde may be completely consumed before leaving the cell. Finally, an optimum ethanol concentration of 1M has also been observed under the particular model setup tested in our study.

Water management in PEMFCs

The experimental results obtained at DLR-Stuttgart have shown that the relative humidity of the cathode is the main parameter controlling the performance stability of the cell, with RH values on the cathode side between 50% and 20% being critical to obtain a relatively stable behavior. The results of a simple global balance of water (BOW) model seem to correlate satisfactorily with the observed cell performance stability. As a result, the proposed model could be used as a fast evaluation tool for predicting the stability of a certain operating condition. A dimensionless global BOW model has been also presented. This model is easily applicable to most PEMFC working conditions. Nevertheless, additional tests should be carried out using different current densities and channel configurations to validate the model in more general situations.

An overall energy analysis, which accounts for the sensible heat required to increase the temperature of the feeding streams to the cell operating temperature and for the latent heat of vaporization required to humidify the gases to the desired RH, has revealed a remarkably positive energy balance at 60°C. The total heat used to condition streams at 80°C is almost three times larger than at 60°C, although it could still be provided by the available residual heat. The application of this methodology to commercial stacks could be helpful to asses if the heat available under a given operating condition could be enough to condition the anode and cathode feeding streams.

Due to operational stability at low humidification at 60°C, this seems to be the most efficient condition for our particular cell configuration, despite the small reduction of approximately 6% in cell power output with respect to 80°C. The unstable behavior, occurring as consequence of low humidification at the cathode, could be compensated using very high values of RH at the anode side.

Future work

During the course of this work, multiple research lines have been opened, but only a few have been closed. As a result, there are plenty of possibilities for future work:

Simplified EOR kinetics: A simplified solution for the system of equations determining the coverage factors (3.12')–(3.16') could drastically reduce the computational time required for evaluating the molar production/consumption rates at the anode catalyst layer. Similarly, a simplified description of the EOR could be obtained by systematically reducing the detailed reaction mechanism proposed in Chapter 3 based on the introduction of partial equilibrium approximations for some of the intermediate reactions, which may be justified in certain overpotential ranges. In any case, the resulting mechanism should be able to reproduce product selectivity adequately and should include acetaldehyde as intermediate free species due its dual role along the anode channel, upstream as reaction product and downstream as reactant, under ethanol starvation conditions.

Modeling of other complex electrochemical systems: The methodology proposed to investigate the EOR kinetics could be applied to other complex compounds used in direct fuel cells, such as more complex alcohols (glycerol), acids, or glycol compounds (Soloveichik, 2014), or even compound mixtures (ethanol-methanol). In addition, it could be used to investigate alcohol oxidation in PEM electrolysis cells operating with monometallic Pt catalyst at higher overpotentials (Altarawneh & Pickup, 2017; Lamy *et al.*, 2014).

Multiphysics PEMFC model: For gaining additional insight on water management in PEMFCs, separated BOW models for anode an cathode could be considered. The coupling of both water balances would require precise information about the mass of water transferred across the membrane from anode to cathode by electro-osmotic drag (EOD), back diffusion and hydraulic permeation. This information could only be obtained by means of a detailed (i.e., multiphysics, multiphase, and preferably transient) analysis of water transport across the MEA. The resulting 1D across the channel model, when applied to a differential cell element, and coupled to simple one-dimensional convective models of water transport along the channel based on the separated BOW model discussed above, would result in the development of a

transient 1D+1D model that may shed further light on the intricacies of PEMFC water management.

Acknowledgments

This doctoral dissertation has been supported by a 4-year PIPF contract of the Pre-doctoral Researcher Training Program of University Carlos III de Madrid and by research Projects ENE2011-24574 and ENE2015-68703-C2-1-R (MINECO/FEDER, UE) awarded by the Spanish Ministry of Economy and Competitiveness. The experimental results presented in Chapters 5 and 6 were obtained at the *Institut für Technische Thermodynamik* of the *Deutsches Zentrum für Luft- und Raumfahrt* (DLR). The author wishes to express his most sincere gratitude to Prof. Dr. *rer. nat.* K. Andreas Friedrich and Dr. Daniel G. Sánchez for their kind hospitality and support.

References

ALTARAWNEH, RAKAN M. & PICKUP, PETER G. 2017 Product Distributions and Efficiencies for Ethanol Oxidation in a Proton Exchange Membrane Electrolysis Cell. *J. Electrochem. Soc.* **164** (7), F861–F865.

GARCÍA-SALABERRI, P. A., SÁNCHEZ, D. G., BOILLAT, P., VERA, M. & FRIEDRICH, K. A. 2017 Hydration and dehydration cycles in polymer electrolyte fuel cells operated with wet anode and dry cathode feed: A neutron imaging and modeling study. *J. Power Sources* **359**, 634–655.

LAMY, C., JAUBERT, T., BARANTON, S. & COUTANCEAU, C. 2014 Clean hydrogen generation through the electrocatalytic oxidation of ethanol in a Proton Exchange Membrane Electrolysis Cell (PEMEC): Effect of the nature and structure of the catalytic anode. *J. Power Sources* **245**, 927–936.

SOLOVEICHIK, G. L. 2014 Liquid fuel cells. *Beilstein J. Nanotechnol.* **5** (1), 1399–418.

List of Publications

Refereed Journal Articles

1. Sanchez, D. G., Ruiu, T., Biswas, I., Friedrich, K. A., Sanchez-Monreal, J., & Vera, M. (2014). Effect of the Inlet Gas Humidification on PEMFC Behavior and Current Density Distribution. ECS Transactions, 64(3), 603–617.

2. Sanchez, D. G., Ruiu, T., Friedrich, K. A., Sanchez-Monreal, J., & Vera, M. (2016). Analysis of the Influence of Temperature and Gas Humidity on the Performance Stability of Polymer Electrolyte Membrane Fuel Cells. Journal of The Electrochemical Society, 163(3), F150–F159.

3. Sanchez-Monreal, J., Garcia-Salaberri, P. A., & Vera, M. (2016). Mathematical Modeling of Direct Ethanol Fuel Cells Using a Multi-Step Chemical Kinetic Mechanism. ECS Transactions, 72(25), 1–16.

4. Sanchez-Monreal, J., Garcia-Salaberri, P. A., & Vera, M. (2017). A genetically optimized kinetic model for ethanol electro-oxidation on Pt-based binary catalysts used in Direct Ethanol PEM Fuel Cells. Journal of Power Sources , Accepted.

Agradecimientos

Me gustaría acordarme de Alberto, Alejandro Sevilla, Ana, el Autobusillo, los becarios pobres, Carol, Caracol, Caracola, Cristina, Dani el del teletexto, Dani Moreno (y los osos de Sequoia), Dani DLR, Domingo, Dr. Parrales, Eduardo y la grupeta senior, Elena, la Familia, mi Familia, los de Fluidos, Prof. Friedrich, Henar, Imma, Iterate, el Ise, Jesús (mi orgulloso creador), Jose Carlos, los jóvenes, Marcos, Mariano, Mercedes, Miguel Hermanns, los del máster de los listos, Nestor, los nuevos, Pablito, Pablo, los de la Patera, Paula, Sergio, Theresa, Wil y de muchos otros que seguro se me han olvidado en ésta lista. No siempre habéis conseguido que el trabajo fuese más fácil, pero, sin duda, habéis conseguido que fuese más agradable. Gracias.